Year : 2011

Role of ENaC in skin wound healing and Phenotypic analysis of GILZ-deficient mice

SUAREZ Philippe

UNIL | Université de Lausanne
Faculté de biologie
et de médecine

Département de Pharmacologie et Toxicologie

Role of ENaC in skin wound healing

and

Phenotypic analysis of GILZ-deficient mice

Thèse de doctorat ès sciences de la vie (PhD)

Présentée à la

Faculté de Biologie et de Médecine de l'Université de Lausanne

par

Philippe SUAREZ

Master en Biochimie
Université de Genève

Jury

Prof. Peter Vollenweider, Président
PD Dr. Edith Hummler, Directeur de thèse
Prof. Bernard Rossier, Expert
Prof. Sabine Werner, Expert
Prof. Luc Pellerin, Expert

Lausanne 2011

UNIL | Université de Lausanne
Faculté de biologie
et de médecine

Ecole Doctorale

Doctorat ès sciences de la vie

Imprimatur

Vu le rapport présenté par le jury d'examen, composé de

Président	Monsieur Prof. Peter **Vollenweider**
Directeur de thèse	Madame Prof. Edith **Hummler**
Experts	Monsieur Prof. Bernard C. **Rossier**
	Madame Prof. Sabine **Werner**
	Monsieur Prof. Luc **Pellerin**

le Conseil de Faculté autorise l'impression de la thèse de

Monsieur Philippe Suarez

master en biochimie de l'Université de Genève

intitulée

Role of ENaC in skin wound healing and phenotypic analysis of GILZ-deficient mice

Lausanne, le 25 mars 2011

pour Le Doyen
de la Faculté de Biologie et de Médecine

Prof. Peter Vollenweider

ACKNOWLEDGEMENTS

I thank Dr. Edith Hummler for giving me the opportunity to join her group and to work on those interesting and exciting projects. I also would like to sincerely thank the members of my thesis commitee: Prof. Sabine Werner, Prof. Bernard Rossier, Prof. Luc Pellerin and Prof. Peter Vollenweider.

I would like to thank my colleagues from the EH group and the Department of Pharmacology and Toxicology. Specially, Prof. Laurent Schild, Prof. Olivier Staub, Dr. Dmitri Firsov, Dr. Simona Frateschi, Dr. Romain Perrier, Dr. Vincent Bize, Gabriel Centeno, Andrée Porret, Anne-Marie Mérillat and Delphine Huser. The neighbours at the Department of Medical Genetics, mainly Dr. Valerie Verdier, Dr. Diana Marek and Dr. Karim Nadra. External collaborators and friends, Dr. Phillip Shaw, Jean-Christophe Stehle, Dr. Anne Wilson, Dr. Armelle Takeda and Dr Nicolas Wade. I also would like to thank the students that worked with me: Christelle Pahud, Laetitia Monney, Virginie Délèze and Mélanie Salamin.

I would like to thank my father Evélio, the Huser family and all my friends in Geneva, Lausanne and all over the globe for love, support and motivation.

This work is dedicated in loving memory of my beloved Mother who taught me the greatest values.

SUMMARY

In my first project, I analyzed the role of the amiloride-sensitive epithelial sodium channel (ENaC) in the skin during wound healing. ENaC is present in the skin and a function in keratinocyte differentiation and barrier formation has been demonstrated. Previous findings suggested, that ENaC might be implicated in keratinocyte migration, although its role in wound healing was not analyzed yet. Using skin-specific (K14-Cre) conditional αENaC knockout and overexpressing mice, I determined the wound closure kinetic and performed morphometric measurements. The time course of wound repair was not significantly different in knockouts or transgenics when compared to control mice and the morphology of the closing wound was not altered.

In my second project, I studied the glucocorticoid-induced leucine zipper (GILZ, Tsc22d3). GILZ is widely expressed and an important role has been predicted in immunity, adipogenesis and renal sodium handling. Mice were generated that constitutively lack all the functional domains of the *Gilz* gene. In these mice, the expression of GILZ mRNA transcripts and protein were completely abolished in all tissues tested. Surprisingly, knockout mice survived. To test whether GILZ mimicks glucocorticoid action, we studied its implication in T- and B-cell development and in a model of sepsis. We measured cytokine secretion in different inflammatory models, like in peritoneal and bone marrow-derived macrophages, in splenocytes and a model of sepsis. In all our experiments, cytokine secretion from GILZ-deficient cells was not different from controls. From 6 months onwards, knockout mice contained significantly less body fat and were lighter. Following sodium and water deprivation experiments, water and salt homeostasis was preserved. Sterility of knockout males was associated with a severe testis dysplasia, smaller seminiferous tubules, the number of Sertoli and germ cell was reduced while increased apoptosis, but not cell proliferation, was evidenced. The interstitial Leydig cell population was augmented, and higher plasma FSH and testosterone levels were found. Interestingly, the expression of the target gene *Pparγ2* was diminished in the testis and in the liver, but not in the skin, kidney or fat. Tsc22d1 mRNA transcript level was found to be upregulated in testis, but not in the kidney or fat tissue. In most tissue, excepted the testis, GILZ-deficient mice reveal functional redundancy amongst members of the Tsc22d family or genes involved in the same regulatory pathways. In summary, contrarily to the published *in vitro* data, GILZ does not play a crucial role attributed in immunology or inflammation, but we identified a novel function in spermatogenesis.

RESUME

Dans mon premier projet, j'ai analysé le rôle du canal épithélial sodique sensible à l'amiloride (ENaC) dans la cicatrisation de la peau. ENaC est présent dans la peau et il a une fonction dans la différenciation des kératinocytes et dans la formation de la barrière. Des études suggèrent qu'ENaC pourrait être impliqué dans la migration des kératinocytes, cependant, son rôle dans la cicatrisation n'a pas encore été étudié. A l'aide de souris qui surexpriment ou qui sont knockout pour αENaC, spécifiquement dans la peau (K14-Cre), j'ai analysé le temps de clôture de la cicatrice et j'ai aussi étudié la morphologie de la plaie guérissant. Chez les souris qui surexpriment ou chez les knockouts, la vitesse de fermeture et la morphologie de la cicatrice étaient identiques aux souris contrôles.

Dans mon second projet, j'ai étudié le glucocorticoid-induced leucine zipper (GILZ, Tsc22d3). GILZ est largement exprimé et un rôle important a été prédit dans l'immunité, l'adipogénèse et le transport sodique rénal. Des souris ont été générées dont les domaines fonctionnels du gène *Gilz* sont éliminés. L'expression de GILZ en ARNm et protéine a été complètement abolie dans tous les tissus testés. Étonnamment, ces souris knockout survivent. Afin de tester si GILZ imite les effets des glucocorticoïdes, nous avons étudié son implication dans le développement des cellules T et B ainsi qu'un modèle de septicémie. Nous avons mesuré la sécrétion de cytokines à partir de différents modèles d'inflammation tels que des macrophages péritonéaux ou de moelle, de splénocytes ou encore d'un modèle de septicémie. Dans toutes nos expériences, la sécrétion de cytokines de cellules GILZ-déficientes était semblable. Dès 6 mois, les knockouts contenaient significativement moins de graisses et étaient plus légères. Suite à une privation sodique et aqueuse, l'homéostasie du sel et de l'eau était préservée. Les mâles knockouts présentaient une stérilité accompagnée d'une dysplasie testiculaire sévère, de tubules séminifères étaient plus petits et contenaient un nombre réduit de cellules de Sertoli et de cellules germinales. L'apoptose était augmentée dans ces cellules mais pas la prolifération cellulaire. Le nombre de cellules de Leydig était aussi plus élevé, ainsi que la FSH et la testostérone. L'expression du gène cible *Pparγ2* était diminuée dans le testicule et le foie, mais pas dans la peau, le rein ou le tissu adipeux. L'ARNm de Tsc22d1 était plus exprimé dans le testicule, mais pas dans le rein ou le tissu adipeux. Dans la plupart des tissus, sauf le testicule, les souris knockouts révélaient une redondance fonctionnelle des autres membres de la famille Tsc22d ou de gènes impliqués dans les mêmes voies de régulation. En résumé, contrairement aux données *in vitro*, GILZ ne joue pas un rôle essentiel en immunologie, mais nous avons identifié une nouvelle fonction dans la spermatogénèse.

INDEX

ABBREVIATIONS

11βHSD1	11β-hydroxysteroid dehydrogenase type 1
ACTH	Adrenocorticotropic hormone
AMH	Anti-Müllerian hormone
AQP2	Aquaporin 2
AR	Androgen receptor
ASDN	Aldosterone-sensitive distal nephron
ASIC	Acid-sensitive ion channel
Bun	Bunched
C/EBP	CCAAT/enhancer binding protein
CAP	Channel activating protease
cAMP	Cyclic adenosine monophosphate
CD	Collecting duct
CD3	Cluster of differentiation 3
CFTR	cystic fibrosis transmembrane conductance regulator
CNS	Central nervous system
CNT	Connecting tubule
Ctrl	Control
DCT	Distal convoluted tubule
DEX	Dexamethasone
DIP	Delta sleep-inducing peptide immunoreactive peptide
DNA	Deoxyribonucleic acid
dpc	Days post coitum
ENaC	Epithelial sodium channel
ER	Estrogen receptor
ERK1/2	Extracellular signal-related kinase ½
ES	Embryonic stem (cell)
FaNaC	FMRFamide-gated sodium channel
FFA	Free fatty acid
FSH	Follicle-stimulating hormone
GC	Glucocorticoid
GILZ	Glucorticoid-induced leucine zipper
GR	Glucocorticoid receptor
GRE	Glucocorticoid response element
H&E	Hematoxylin and eosin (staining)
HE	Hyperproliferative epithelium
HPA	Hypothalamic-pituitary-adrenal axis
HPG	Hypothalamic-pituitary-gonadal axis
IL	Interleukin
K14	Keratin 14 promoter
K_i	Dissociation constant
KLF5	Krüppel-like factor 5

KO	Knockout
LC	Leydig cell
LH	Luteinizing hormone
LPL	Lipoprotein lipase
mRNA	Messenger ribonucleic acid
MEF	Mouse embryonic fibroblast
MEM	Minimum essential medium
MR	Mineralocorticoid receptor
MSC	Mesenchymal stem cell
Nedd4-2	Neural precursor cell expressed developmentally down-regulated protein 4-2
Nrf2	Nuclear respiratory factor-2
OSTF1	Osmotic stress transcription factor 1
PCR	Polymerase chain reaction
PGC	Primordial germ cell
PHA1	Pseudohypoaldosteronism type 1
PI3K	Phosphoinositide-3 kinase
PKA	Protein kinase A
PMP	Plasma membrane potential
PPAR	Peroxisome proliferator-activated receptor
qPCR	Quantitative PCR
RT-PCR	Reverse transcriptase PCR
RXR	retinoid X receptors
SC	Stem cell
SCN	Suprachiasmatic nucleus
SEM	Standard error of the mean
SGK1	Serum and glucocorticoid inducible kinase 1
SHS	Shortsighted
Slbo	Slow boarder cells
Smad3	Small mothers against decapentaplegic homolog 3
ST	Sertoli cell
TEWL	Transepidermal water loss
Tg	Transgenic
TGF-β	Transforming growth factor β
TM	Transmembrane domain
TNFα	Tumor necrosis factor α
TSC-22	TGF-β-stimulated clone-22
USP2	Ubiquitin specific peptidase 2
VSMC	Vascular smooth muscle cell
WT	Wild-type
WW	Wound width

<u>Part I:</u> Role of the epithelial sodium channel ENaC in skin wound healing

INTRODUCTION

The epithelial sodium channel (ENaC)

Gene structure and function

The epithelial sodium channel (ENaC) belongs to the ENaC/Degenerin gene family (figure 1). In the beginning of the 1990's, the sequence of the ENaC α subunit was identified from epithelial cells of rat distal colon and identified by functional expression in *Xenopus laevis* oocytes (Canessa et al., 1993), quickly followed by the two other β and γ subunits (Canessa et al., 1994). At the same period, genetic screening of *Caenorhabditis elegans* mutants presenting defective mechanosensation allowed to identify *degenerin* genes (Chalfie and Wolinsky, 1990). Later, it has been determined that gain-of-function of these two degenerin ion channel genes results in toxicity for the nematode by causing degeneration of several neurons and rendering mutants incapable of mechanosensation. Neuronal degenerins from human and rat brain were cloned and described as amiloride-sensitive cation channels for which phylogenic analysis indicated that they were equally divergent from all other members of the ENaC/Degenerin family. These channels are activated by rapid extracellular acidification (Waldmann et al., 1997), so they are called acid-sensing ion channel (ASIC). In the snail *Helix aspersa*, it has been found that the FMRFamide-gated sodium channel (FaNaC) could be blocked by amiloride. Despite the low sequence homology with ENaC subunits and degenerins, FaNaC displays the same overall structural organization (Lingueglia et al., 1995). Sequence alignment studies between all members of ENaC/Deg family led to a potential phylogenetic tree proposed in figure 1. Related sequences are organized into subfamilies. Figure 2 shows the conservation of several domains between the main subfamilies (Kellenberger and Schild, 2002; Golubovic et al., 2007).

The highly amiloride-sensitive epithelial sodium channel (*Scnn1*, sodium channel non-voltage-gated) is composed of 3 homologous subunits α, β and γ. The α subunit is required for channel activity, whereas β and γ are necessary for maximal channel activity (Canessa et al., 1994; Rossier et al., 2002). Each subunit consists of two transmembrane helices, a large extracellular loop and short cytoplasmic amino- and carboxy-termini. ENaC is thought to be composed of 2α, 1β and 1γ subunits (figure 3*A*) and showed to be functional by construction of a concatemeric cDNA (Firsov et al., 1998; Kosari et al., 1998; Anantharam and Palmer, 2007). A stoichiometry of 8 to 9 subunits has also been proposed (Snyder et al., 1998; Eskandari et al., 1999).

Figure 1: Quartet-puzzling consensus tree for the DEG/ENaC data set. The tree has been constructed by maximum likelihood analysis with the program TREE-PUZZLE; branch lengths are proportional to the evolutionary distance. Support values below 90% are indicated. The small schematics illustrate the topology and domain organization of different branches of the DEG/ENaC gene family. The ASIC branch is shown also at higher magnification. Abbreviations of species names are as follows: *c*, chicken (*Gallus gallus*); *f*, toadfish (*Opsanus tau*); *h*, human (*Homo sapiens*); *Ha*, *Helix aspersa*; *Ht*, *Helisoma trivolvis*; *Hy*, *H. magnipapillata*; *l*, lamprey (*Lampetra fluviatilis*); *Ls*, *Limnea stagnalis*;*m*, mouse (*Mus musculus*); *r*, rat (*Rattus norvegicus*); *sh*, shark (*Squalus acanthias*); *z*, zebrafish (*Danio rerio*). Other proteins are from *Drosophila melanogaster* or *C. elegans* (Golubovic et al., 2007).

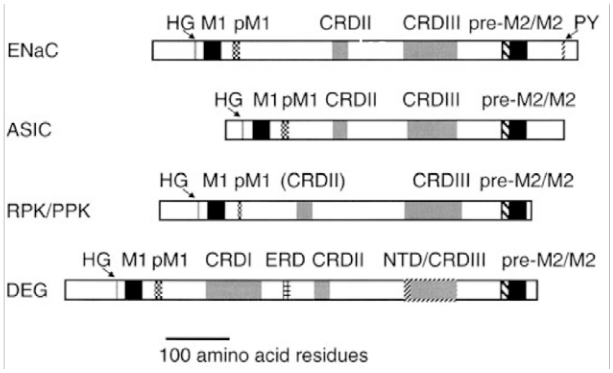

Figure 2: Linear representation of the primary structure shows the conserved regions found in each of the main subfamilies. The length of the domains in the diagram reflects their relative size in the protein. M1, M2, transmembrane segments; HG, conserved His-Gly motif within a conserved NH2-terminal domain; pM1, post-M1, conserved domain directly downstream of M1; CRD, cysteine-rich domain; pre-M2, hydrophobic domain directly preceding M2; ERD, extracellular regulatory domain unique to *C. elegans* degenerins; NTD, neurotoxin domain; PY, PPPxY domain of α, β, and γENaC (Kellenberger and Schild, 2002).

New insights about the molecular organization have been recently given with the low pH crystal structure of a chicken ASIC1 in a desensitized state, suggesting a homotrimeric structure for this proton-sensing ion channel (Jasti et al., 2007; Gonzales et al., 2009). Since ASICs belong to the ENaC/DEG family, ENaC has been proposed to a trimer composed of 1α, 1β and 1γ subunits. However, it is worth to mention that the homotrimeric organization of ASIC1 was determined by crystallography on the truncated protein expressed in SF9 insect cells. This is a cell line having very low cholesterol content and different phospholipid profile compared with mammalian cell lines. Furthermore, only the functionality of the GFP-tagged construct of ASIC, used for the transfection, has been tested. The construct, as it was crystallized, has never been assessed. Thus, the number of subunits composing the functional ENaC is still under debate.

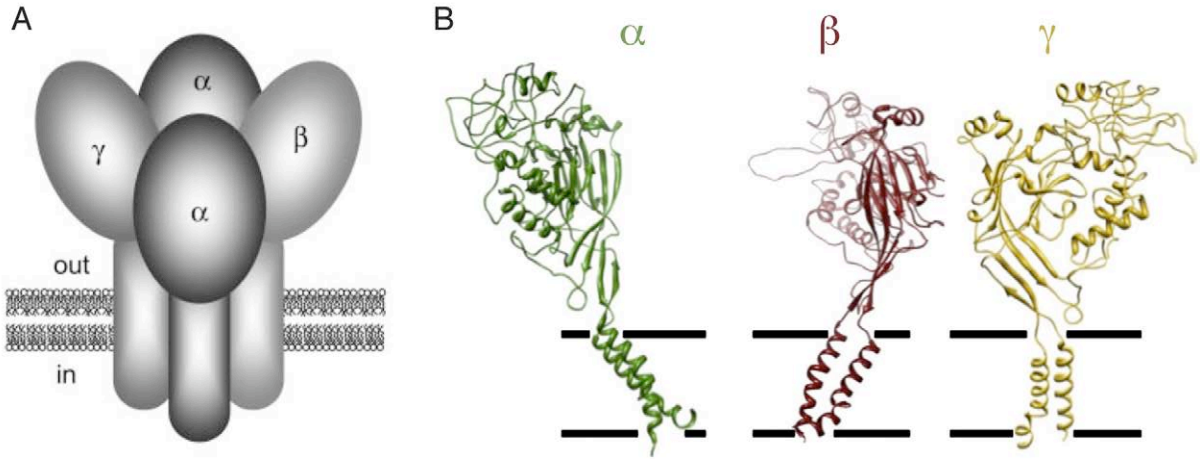

Figure 3: ENaC structure. *A*, Model of the tetrameric assembly of an ENaC channel around the central pore. Functional analyses have shown that α, β and γENaC subunits participate in the formation of the pore and establish the stoechiometry of the channel (Kellenberger and Schild, 2002). *B*, Homology models of α (green), β (red) and γ (yellow) ENaC subunits based on the crystal structure of ASIC channel. These homologous subunits show a large extracellular domain that represents more than half of the mass of the protein. The two transmembrane domains (TM1 and TM2) consist of α helices, and the TM2 is involved in lining the pore. The crystal obtained for ASIC1a did not allow the resolution of the structure of the amino and the carboxy termini, and therefore are absent as well in the present homology models of α, β and γ subunits (Schild, 2010).

ENaC is constitutively active and localized at the apical membrane of tight epithelia. Single ENaC recordings in the cortical collecting tubule show slow kinetics with open and closed times in the range of seconds at room temperature (Palmer and Frindt, 1986). ENaC activity can be pharmacologically inhibited by amiloride and triamterene that bind extracellularly to a common site on the TM2 segment (Kellenberger et al., 2003).

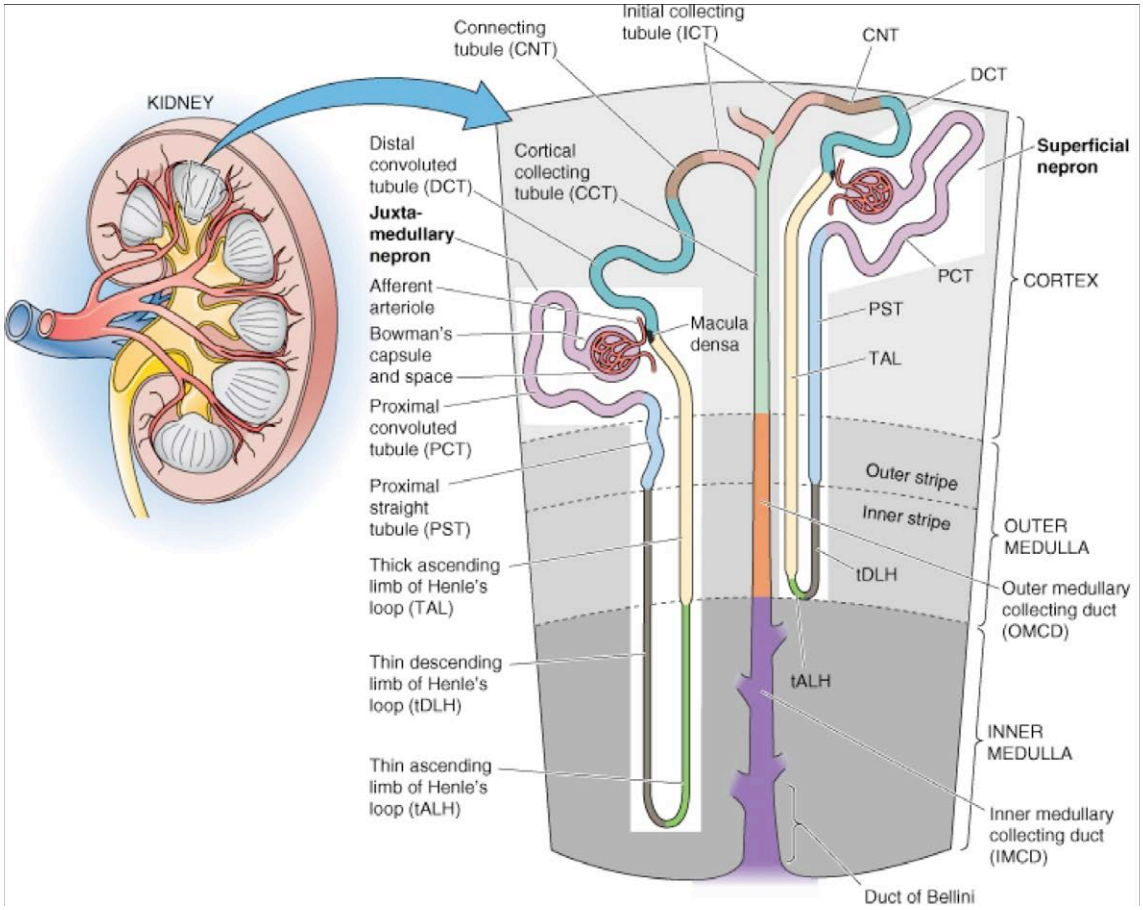

Figure 4: Structure of the nephron (Boron and Boulpaep, 2004)

In the kidney (figure 4), ENaC is expressed in the aldosterone-sensitive distal nephron (ASDN), a region that includes successively, the late portion of the distal convoluted tubule (DCT2), the connecting tubule (CNT) and the collecting duct (CD) (Loffing et al., 2001). In spite of their different embryonic origin (mesenchymal for DCT and CNT, ureteric bud for CD) (Vainio and Lin, 2002), all three nephron segments express ENaC, the mineralocorticoid receptor (MR) and the 11-β hydroxysteroid dehydrogenase type-2, the enzyme that confers to the MR receptor a functional mineralocorticoid specificity (Edwards et al., 1988; Funder et al., 1988). The subcellular location and the level of expression of ENaC subunits change drastically upon the elevation of plasma aldosterone levels in response to sodium diet (Masilamani et al., 1999; Loffing et al., 2000). In rodents under standard Na^+ diet associated with moderate plasma

aldosterone levels, ENaC subunits are detectable by immunohistochemistry in the cytosol of principal cells, with a discrete labelling of the apical membrane of the late DCT and the CNT. Under low Na^+ diet leading to high plasma levels of aldosterone in these animals, ENaC subunits are localized in the apical membrane of principal cells of the CD, with a more prominent expression in the early ASDN compared with the late ASDN. ENaC in the apical membrane of principal cells is the major entry for Na^+ from the tubule lumen into the cell. Na^+ enters the cell across the apical membrane following a favourable electrochemical gradient (Palmer and Andersen, 2008). The vectorial transport of Na^+ across the epithelial cell is ensured by the Na^+/K^+-ATPase located at the basolateral membrane that pumps the sodium ions out of the cell toward the blood.

Regulation of ENaC

Open probability of ENaC

ENaC is a non-voltage-gated sodium channel. Its activity is strongly regulated by sodium itself *via* two distinct phenomena: self-inhibition and feedback inhibition. Self-inhibition reduces ENaC activity by an increase in extracellular sodium concentration (Chraibi and Horisberger, 2002). The feedback inhibition displays slower kinetics compared to the self inhibition due to the increase of intracellular sodium concentration. (Kellenberger et al., 2002; Anantharam et al., 2006). Beside sodium, some molecules have been shown to inactivate the channel at low concentrations, like amiloride, which is the most classical blocker for ENaC activity. Actually, the inhibition of ENaC by amiloride was described in the frog skin and bladder 15 years before the cloning of the channel (Fuchs et al., 1977; Diamond, 1978; Palmer, 1984) Another blocker of ENaC is benzamil, which has a K_i about ten times lower than amiloride (0.01µM), but with a lower specificity to ENaC (Kellenberger et al., 2003).

Protease activation of ENaC

ENaC was found to be stimulated by soluble proteases such as trypsin, kallikrein or thrombin (Vallet et al., 1997; Chraibi et al., 1998; Harris et al., 2007). Serine proteases increase ENaC activity at the cell surface. The channel activating protease 1 (CAP1), the ortholog of human prostasin (Prss8), was the first to be cloned and characterized (Vallet et al., 1997; Vuagniaux et al., 2000). CAP2 (TMPRSS4), CAP3 (matriptase) and elastase were thereafter discovered and described as further activators of ENaC (Vuagniaux et al., 2002).

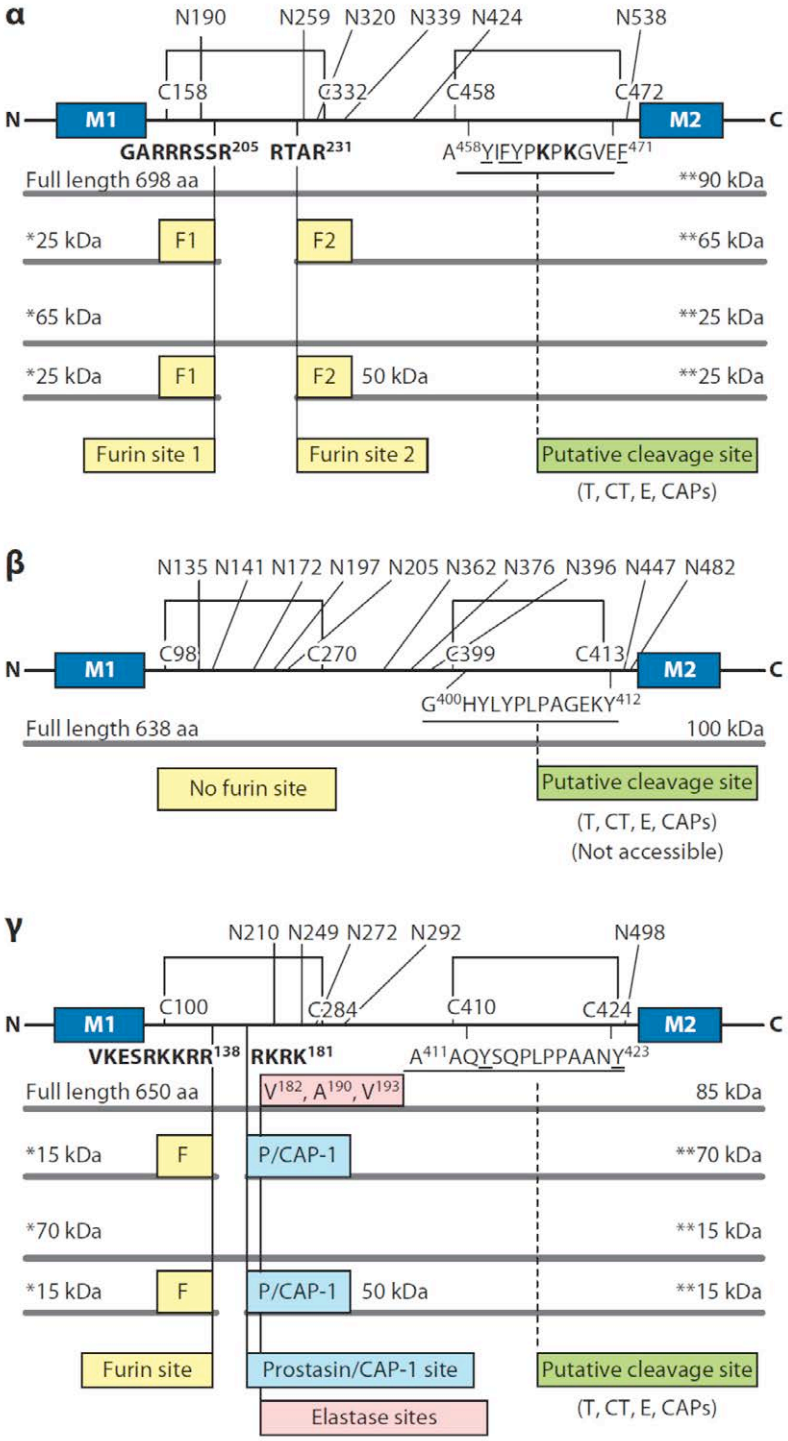

Figure 5: Linear models for ENaC subunit cleavage. Each subunit has common features, including two transmembrane domains (M1 and M2) with short N and C termini, a large extracellular loop with 5–12 *N*-glycosylation sites, and multiple cysteines that participate in disulfides bridges critical for folding, trafficking, and/or activity. Known and suspected sites of ENaC cleavage are indicated. Molecular masses (kDa) of nonglycosylated fragments consistent with cleavage at the indicated sites, and that have been detected by N-terminal (*asterisks*) or C-terminal antibodies (*double asterisks*), are indicated. (*Top*) In the α subunit model, within the first cysteine disulfide bridge (C158-C332) two furin cleavage sites (F) are identified (*yellow boxes*). Putative trypsin (T), chymotrypsin (CT), elastase (E), or SPs within the second cysteine disulfide bridge (C458-C472) are indicated (*green box*). These sites may generate a 65–70-kDa fragment as detected by an N-terminal antibody and as observed in oocytes, kidney, and lung. (*Middle*) In the β subunit model, furin cleavage sites (F) are absent. Putative trypsin (T), chymotrypsin (CT), elastase (E), or CAP-induced cleavage sites are postulated to be protected by heavy glycosylation (ten potential *N*-glycosylation sites) and/or by the absence of conformational changes induced by furin. (*Bottom*) In the γ subunit model, only one furin cleavage site (F) is observed within the first cysteine disulfide bridge (C100-C284) (*yellow*). A CAP-1/prostasin cleavage site (*light blue box*) and elastase cleavage sites (*pink box*) are indicated. Putative trypsin (T), chymotrypsin (CT), elastase (E), or SPs within the second cysteine disulfide bridge (C410-C424) are indicated, but there are no experimental data confirming that they exist *in vivo* or *in vitro* (Rossier and Stutts, 2009).

As illustrated in figure 5, it has been speculated that ENaC activation by proteases results from the release of an inhibitory peptide from the α and γ subunits (Hamm et al., 2010). Cleavage by furin of the α subunit leading to activation of ENaC was first reported (Carattino et al., 2006). A cleavage site by furin was also proposed for the γ subunit (Hughey et al., 2004; Bruns et al., 2007). However, more recent studies indicated that mutation of the furin site in the αENaC subunit did not alter the channel activation (Diakov et al., 2008). Moreover, Harris et al., showed from oocyte experiments, that furin-mediated cleavage is not required for participation of α and γ in heteromers (Harris et al., 2008). These proteolytic processes occur within the *trans*-Golgi network, but both cleaved and uncleaved channels are expressed at the cell membrane (figure 6).

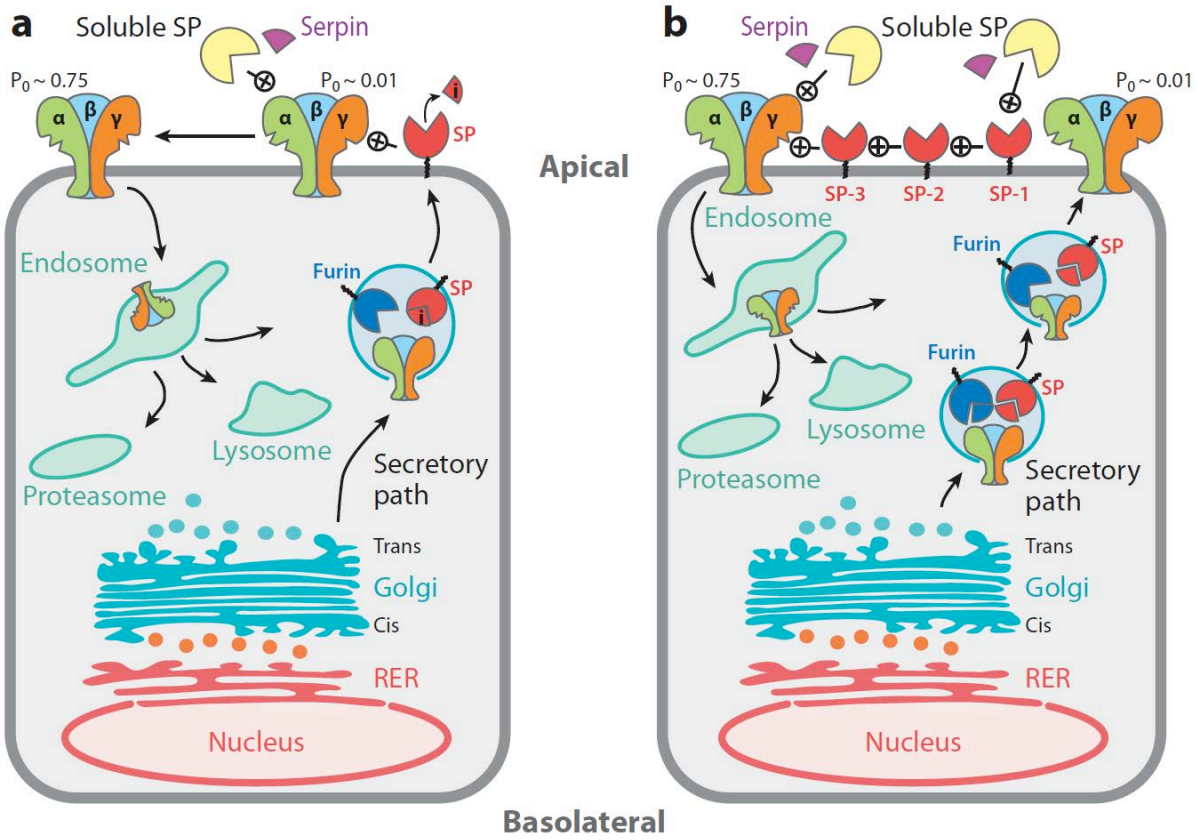

Figure 6: Schematic representation of the proteolytic regulation of ENaC. (*A*) The colocalization model emphasizes the presence of consensus recognition and cleavage sequences for furin and furin-like convertases in α and γ ENaC. Convertase(s) and substrate (ENaC) are expected to cotraffic along the same trans-Golgi path, potentially allowing partially proteolized ENaC heteromers to be delivered to the cell surface. At the cell surface, channel-activating serine proteases (SPs) become activated and, if appropriately colocalized, can complete proteolytic activation. Alternatively, certain soluble serine proteases present in the extracellular milieu can activate near-silent ENaC under the influence of soluble serine protease inhibitors (serpins). (*B*) The sequential model elaborates on the colocalization implicit in proteases directly cleaving ENaC to include the further possibility that a protease or proteases may be essential for activating ENaC but may act indirectly by participating in a protease cascade. As depicted, ENaC may be partially processed by convertases and then fully activated by a protease that requires activation by other membrane-bound or soluble proteases. (Rossier and Stutts, 2009).

This allows a more precise regulation of the activity of the channel by soluble and membrane-associated serine proteases (Rossier and Stutts, 2009). Furthermore, several *in vivo* studies

support the importance of the proteolytic cleavage of ENaC. The γENaC and probably also the αENaC subunits are present in the apical membrane mainly in proteolytically cleaved forms, particularly under conditions of high aldosterone. This was shown directly for γENaC and inferred for αENaC on the basis of the absence of the full-length form of the subunit. Previous work showed that the overall amounts of the cleaved forms correlated with the physiological activity of the channels (Masilamani et al., 1999; Frindt et al., 2001; Ergonul et al., 2006).

Regulation of ENaC activity

To keep the extracellular volume constant, the kidney has to balance precisely the urinary excretion of electrolytes and water with daily salt and fluid intake. This regulation is tightly controlled by aldosterone and vasopressin. The action of these hormones is located in the distal nephron and on the collecting tubules of the kidney. These cells express ENaC, the mineralocorticoid receptor (MR), aquaporin 2 (AQP2) and the vasopressin receptor (V_2R). The correct function of these channels and receptors is crucial to sustain hormonally balanced sodium and water homeostasis (figure 7).

Aldosterone, a mineralocorticoid hormone, principally increases the open probability (Po) and the number of active ENaC channels at the surface (Loffing et al., 2000). Aldosterone induces the phosphatidylinositide 3′-kinase (PI3K)-dependent kinase SGK1 (serum- and glucocorticoid-regulated kinase 1), a Ser/Thr kinase that elevates ENaC level and activity at the cell surface in heterologous expression systems (Alvarez de la Rosa et al., 1999; Chen et al., 1999; Naray-Fejes-Toth et al., 1999). Subsequently, SGK1 was found to phosphorylate Nedd4-2, leading to a decreased interaction and ubiquitylation of ENaC subunits, finally resulting in an increased ENaC activity at the cell surface (Debonneville et al., 2001). Other aldosterone-induced transcripts have been identified, in particular the deubiquitylating enzyme Usp2-45, which also increases ENaC activity at the cell surface *in vitro* (Fakitsas et al., 2007). These observations suggest that the regulation of ENaC activity by aldosterone is mediated at least in part by inhibition of Nedd4-2-dependent ubiquitylation of ENaC, that ultimately tends to increase the number of active channel at the cell surface (Verrey et al., 2008).

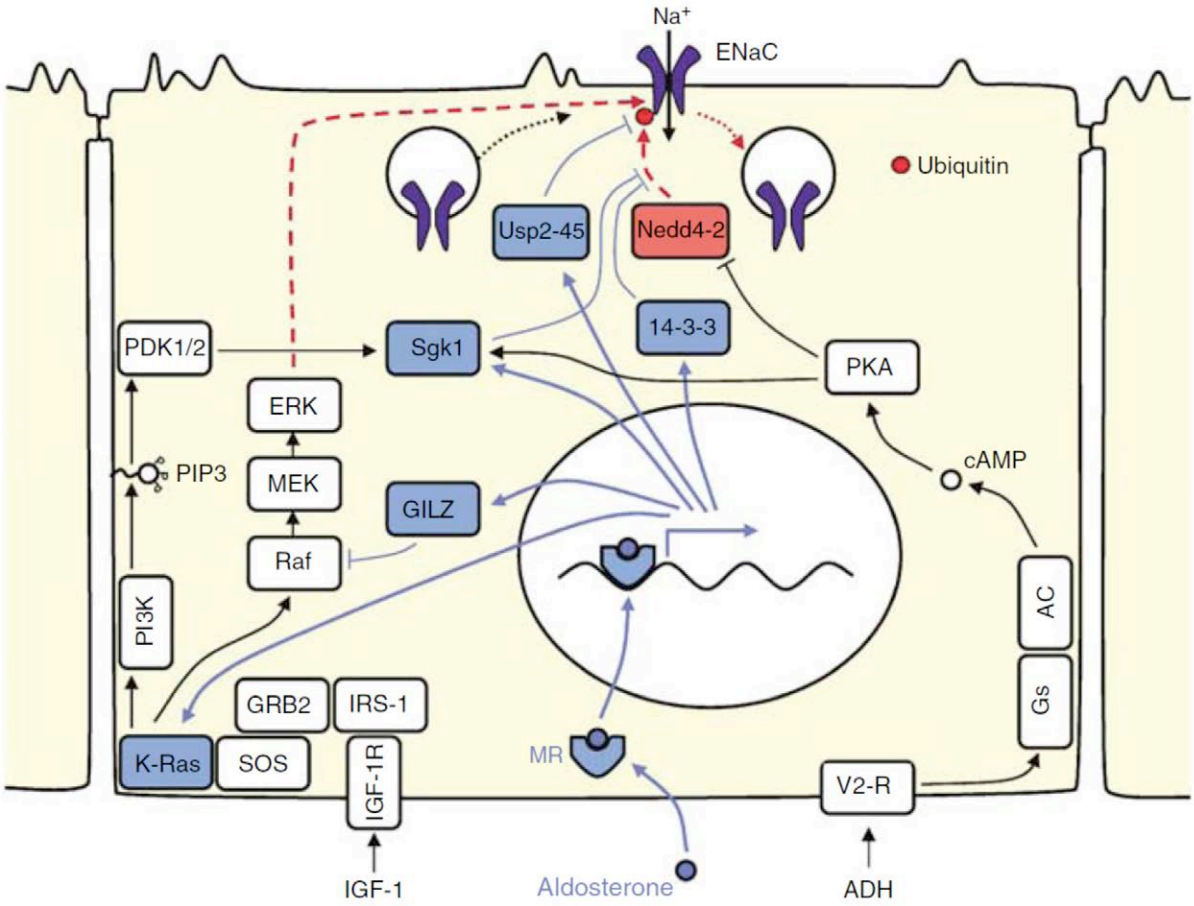

Figure 7: Model for the early transcriptional action of aldosterone on ENaC function. The ubiquitin ligase Nedd4-2 that tonically inhibits ENaC surface expression is highlighted in red, and red dashed arrows indicate pathways downregulating ENaC that are antagonized by aldosterone. Blue boxes represent the regulatory proteins implicated in the early aldosterone action that are rapidly induced via activated MR. The blue lines terminated by a dash indicate at what level these regulatory proteins interfere with ENaC inhibition (Verrey et al., 2008).

Additionally, vasopressin also increases ENaC activity in the ASDN. Binding of vasopressin to the V_2R, stimulates the release of cAMP, which in turn increases the density of ENaC channel at the cell surface (Canessa and Schafer, 1992; Auberson et al., 2003). *In vitro* studies indicate that PKA, much like SGK1, also phosphorylates Nedd4-2, providing a cellular mechanism for the positive regulation of ENaC by vasopressin (Snyder et al., 2004). PKA and SGK1 phosphorylate the same residues of Nedd4-2. Thus, the converging phosphorylation of Nedd4-2 by these two kinases does not explain the additive effects of vasopressin and aldosterone on ENaC-mediated Na^+ absorption in the ASDN (Bugaj et al., 2009); therefore, other mechanisms are most likely involved in the regulation of ENaC by PKA.

The regulation of Nedd4-2 remains poorly understood. As shown in figure 8, the phosphorylation of Nedd4-2 by SGK1 and PKA stabilizes the interaction of Nedd4-2 with 14-3-3 scaffolding proteins, preventing the Nedd4-2 dependent ubiquitylation of ENaC (Bhalla et al., 2005). Interestingly, 2 isoforms of the 14-3-3 proteins are induced by aldosterone, as

SGK1. Another 14-3-3 binding protein has recently been identified that controls the trafficking of ENaC from an intracellular compartment to the cell surface: this binding partner, AS160, is a Rab GTPase-activating protein (Rab-GAP) known to play a role in GLUT4 transport to the plasma membrane in response to insulin (Liang et al., 2010). In CCD cells, AS160 phosphorylation, possibly by SGK1, allows ENaC trafficking to the cell surface, providing a mechanism for endocytosed ENaC to recycle to the cell surface (Liang et al., 2010).

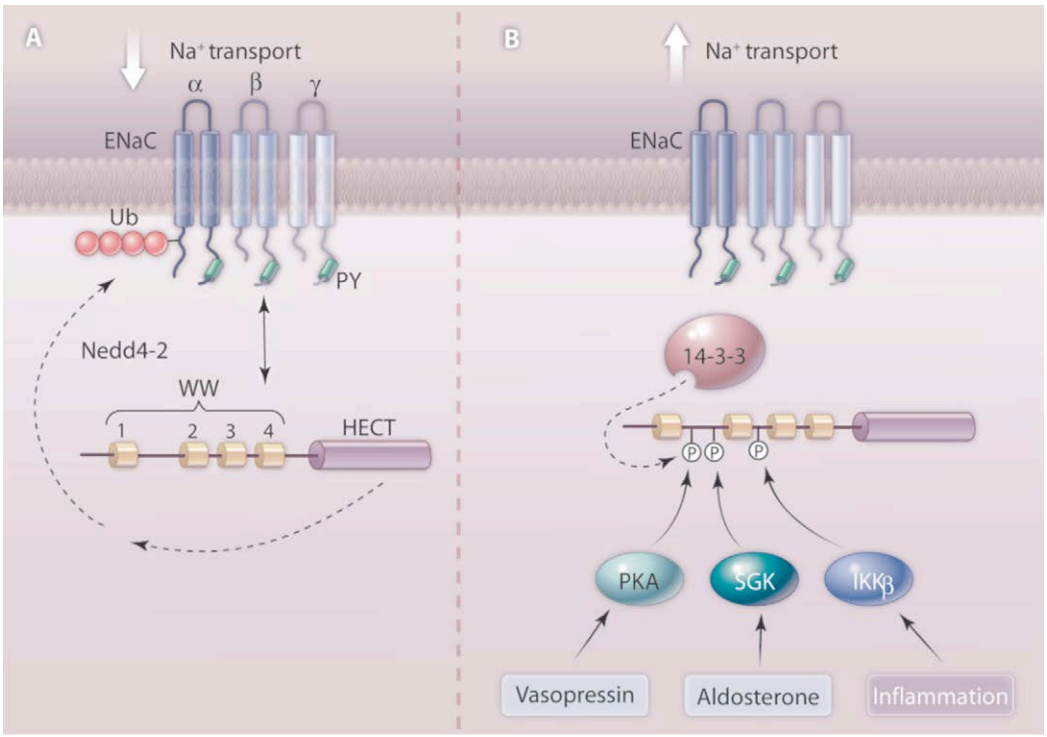

Figure 8: Phosphorylation regulates Nedd4-2 activity. *A*, To reduce the rate of epithelial Na^+ transport, Nedd4-2 binds to ENaC PY motifs and catalyzes its ubiquitination. This induces ENaC endocytosis and lysosomal targeting, resulting in fewer channels at the cell surface. *B*, To increase Na^+ transport, Nedd4-2 is phosphorylated by kinases, including PKA, SGK, and IKKβ. Phosphorylation induces binding of 14-3-3 dimers, which prevents Nedd4-2 from binding to ENaC. As a result, increased ENaC abundance at the surface enhances epithelial Na^+ absorption (Snyder, 2009).

In parallel to the SGK1/Nedd4-2 pathway that stabilizes ENaC at the cell surface, a signaling cascade involving the Raf-1-MAPK/ERK kinases acts to inhibit the cell surface expression of ENaC by stimulating the interaction between Nedd4-2 and ENaC (Nicod et al., 2002; Falin and Cotton, 2007). These studies essentially performed *in vitro* on heterologous expression systems or in cortical collecting duct cell lines, identify Nedd4-2 as a critical convergence point for the regulation of ENaC at the cell surface. Interestingly, the activation of ERK could be inhibited by another aldosterone-induced protein in a cortical collecting cell line, the glucocorticoid-induced leucine zipper protein (GILZ) (Soundararajan et al., 2010).

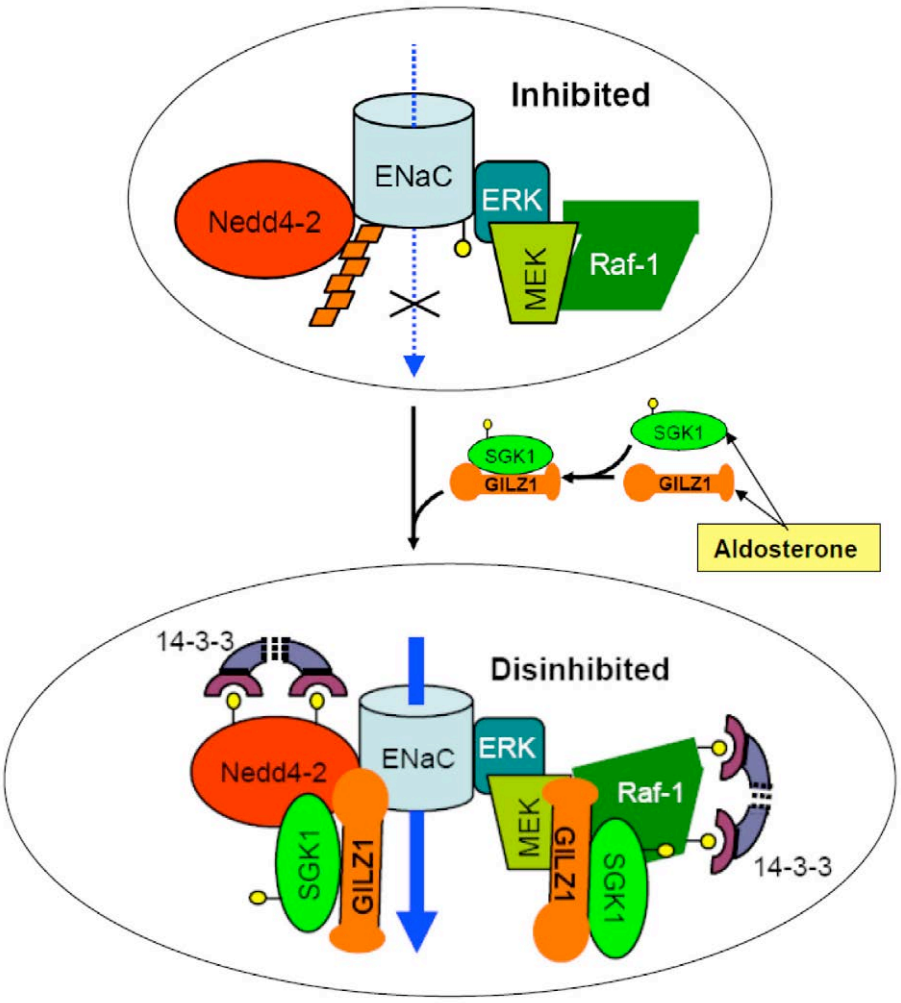

Figure 9: The ENaC-regulatory complex. In the "basal/no-hormone" state, ENaC is associated with and inhibited by an ENaC regulatory complex (ERC), which contains Nedd4-2, as well as Raf-1, MEK, and ERK. ERK phosphorylates the channel (small yellow circles), which in turn stimulates recruitment of Nedd4-2, and hence channel ubuiquitination (orange trapezoids). ENaC internalization, endocytic trafficking, and lysosome-mediated degradation are thus augmented. Aldosterone coordinately induces the expression of SGK1 and GILZ1. GILZ1 in turn: a) recruits SGK1 to the ERC, b) increases interaction of SGK1 with its substrates Nedd4-2 and Raf-1, c) augments SGK1 inhibition of Nedd4-2 and Raf-1 within the ERC, which results in the recruitment of inhibitory 14-3-3 proteins, and d) synergizes with SGK1 to selectively stimulate its ENaC specific functions. The net effect is "dual disinhibition" of ENaC (by SGK1 and GILZ1) resulting in increased channel surface expression and activity. Blue arrows represent Na^+ movement through the channel, while black arrows represent proteins recruited to the complex. Top ellipse shows ENaC in the "*inhibited*" state, in which endocytosis and degradation are favored, while bottom ellipse shows the activated or "*disinhibited*" state, favoring accumulation at the plasma membrane (Soundararajan et al., 2010).

The Pearce group recently showed that GILZ1 physically interacts with Nedd4-2 and with SGK1. There is a synergistic effect with SGK1 in the inhibition of Raf-1 and Nedd4-2 (Soundararajan et al., 2009). GILZ1 physically interacts with and inhibits Raf-1 (Ayroldi et al., 2002; Ayroldi et al., 2007), leading to ENaC activation. All of these factors are associated with ENaC within an ENaC-regulatory complex (ERC), the composition of which is controlled by GILZ1 (figure 9). In the absence of aldosterone with low levels of GILZ1 and SGK1, the complex is likely comprised of Nedd4-2 and Raf-1, along with other components of the Raf-MEK-ERK signalling pathway that are known to be tightly associated with Raf-1. In the presence of aldosterone, GILZ1 recruits SGK1 into the complex. Together they cooperatively

inhibit Nedd4-2 and Raf-1, and synergistically stimulate ENaC surface expression and activity (Soundararajan et al., 2009).

ENaC and human pathophysiology

Liddle's syndrome is an autosomal dominant form of salt-sensitive hypertension with early onset of elevated blood pressure during adolescence; this hypertension is usually associated with hypokalemia, metabolic alkalosis, low plasma aldosterone, and suppressed plasma renin activity (Botero-Velez et al., 1994). The elevated blood pressure in Liddle's syndrome can be normalized by salt restriction and amiloride treatment. The mutation identified in the index case, is a 45 amino acid deletion in the cytosolic C-terminus of the β ENaC subunit. Despite the fact that Liddle's syndrome is a very rare condition, subsequent genetic analysis of other Liddle's syndrome families revealed corresponding deletion mutations in the C-terminus of the γ ENaC subunit, but none in the α subunit (Shimkets et al., 1994). Furthermore, missense mutations causing Liddle's syndrome identified the target amino acid sequence in the β and γ C-termini that involves the conserved proline-rich motif, the canonical PPXY motif (Hansson et al., 1995b; Hansson et al., 1995a; Snyder et al., 1995; Firsov et al., 1996; Schild et al., 1996). Experiments using ENaC channels expressed from synthetic RNA and carrying the mutations associated with Liddle's syndrome exhibit an increased channel activity in *Xenopus* oocytes and in a cortical collecting duct cell line (Schild et al., 1995; Auberson et al., 2003). This gain of function of the mutated channels results from both, an increased number of active channels at the cell surface, and a higher probability for the channel to remain open (Firsov et al., 1996).

The PPXY motifs of β and γENaC bind the ubiquitin ligase Nedd4-2 that is responsible for the ubiquitylation of the active channel complex at the cell surface, and the subsequent targeting of the channel for endocytosis and lysosomal degradation. In Liddle's syndrome patients, deletion or missense mutations of PPXY motifs in the β or γENaC subunits impair the ability of Nedd4-2 to bind and thus ubiquitylate the channel, leading to the accumulation of active ENaC channels at the cell surface (Abriel et al., 1999).

Pseudohypoaldosteronism type 1 (PHA1) is characterized in the first week of life by severe dehydration, hyponatremia, metabolic acidosis and hyperkalemia (Chang et al., 1996). There are two clinically distinct forms of (PHA1), an autosomal recessive form affecting multiple organs (systemic form), including the kidneys, colon, salivary glands, skin and sweat ducts (but not the inner ear) and an autosomal dominant form restricted to the kidney (Belot et al., 2008). Patients with a systemic form of PHA1 exhibit mutations in α, β and γ ENaC subunits. Mutations in the α, β or γ ENaC genes include nonsense, frameshift or missense mutations

leading to channel loss of function, and the clinical severity of the syndrome correlates with the extent to which ENaC activity is reduced. The autosomal dominant form of PHA1 is caused by mutations of the mineralocorticoid receptors (Geller et al., 1998). Thus, both Liddle's and PHA1 syndromes clearly indicate the critical role of ENaC in the ASDN for the maintenance of sodium balance.

ENaC mouse models

Several transgenic mouse models have been developed to study *in vivo* the physiological and pathophysiological roles of ENaC in the maintenance of sodium balance and in the control of blood pressure. The phenotypes observed in these mice demonstrate that each subunit is essential for survival and for regulation of sodium transport (Bonny and Hummler, 2000). Inactivation of the for *Scnn1a* gene led to death due to lung clearance defect within 48h after birth (Hummler et al., 1996). Mice with mutations in the *Scnn1b* and *Scnn1g* genes die from dehydration and hyperkalaemia during the first week of life (Barker et al., 1998; McDonald et al., 1999).

To obtain new insights into the pathophysiology of salt-sensitive hypertension, a mouse model of Liddle's syndrome has been developed, with the deletion of the C-terminal end of the βENaC subunit mimicking the human mutation of the index case (Pradervand et al., 1999). Under normal salt diet, these mice develop normally with a blood pressure similar to their wild type counterparts of identical genetic background. However, under high salt diet the Liddle mice develop high blood pressure, hypokalemia, metabolic alkalosis, low plasma aldosterone, recapitulating clinical features in Liddle's syndrome patients.

The mouse model of Liddle's syndrome with the mutation in the PPXY motif of β ENaC, together with the Nedd4-2 knockout and SGK1 knockout mouse models thereby allow a genetic dissection of the aldosterone-signaling pathway. The Nedd4-2 knockout mice had a slightly elevated blood pressure under normal salt diet that was exacerbated under high salt diet. In these knockout mice, plasma aldosterone level was low (tendency) under normal salt diet and significantly under low salt diet. (Shi et al., 2008). The SGK1 knockout mice were viable and did not display any major phenotype under normal salt diet. Low salt diet induced a significantly higher natriuresis in the knockout mice when compared to controls (Wulff et al., 2002; Fejes-Toth et al., 2008). These Nedd4-2 and SGK1 knockout mouse models show that these genes are not absolutely required for aldosterone-mediated control of ENaC.

Since constitutive deficiency of a gene/protein may lead to embryonic or early perinatal lethality, conditional knockouts have been developed to study a gene deletion in a given cell

type or in a timely controlled manner. The development of site-specific recombinases and recognition sites from bacteriophages (Cre/loxP-mediated recombination) or yeast (Flp/frt-mediated recombination) was a prerequisite for this technique. These strategies have already helped to understand the physiological role of proteins implicated in salt and water balance in the ASDN (Rubera et al., 2003; Rubera et al., 2009; Christensen et al., 2010a; Christensen et al., 2010b).

The skin and ENaC

Skin structure and function

The skin is a complex organ. It is also the largest of the human body (about 4-5 kg). During mammalian embryogenesis the epidermis develops from the surface ectoderm, which initially consists of a multipotent single-layer epithelium. Once these epithelial cells receive the appropriate developmental signals, they become committed to stratify, initiate a massive expansion program, and finally result in terminal differentiation to produce the morphologically distinct layers of the epidermis. The end result is the formation of an impervious cornified envelope *via* a highly specialized form of programmed cell death, termed "cornification" (Candi et al., 2005), which is distinct in many ways from the classic apoptotic pathways (Mack et al., 2005).

To prevent water loss, the skin provides a relatively dry and impermeable barrier. The regulation of water release from the organism into the atmosphere is defined as trans epidermal water loss (TEWL), which is the constitutive steady-state water loss from the skin, excluding sweat gland activity (Rogiers, 2001). Another important skin function is somatosensation. The skin contains a variety of nerve endings that reacts to heat and cold, touch, pressure, vibration and tissue injury (Bressler and Bressler, 1989; Willis, 2007). The skin is involved in heat regulation since it contains a blood supply, far greater than its requirements, which allows precise control of energy loss by radiation, convection and conduction. Dilated blood vessels increase perfusion and heat loss, while constricted vessels greatly reduce cutaneous blood flow and conserve heat (Rowell, 1974). The skin exhibit pigmentation, or melanin, provided by melanocytes that adsorb some of the potentially dangerous sunlight ultraviolet (UV) radiations (Brenner and Hearing, 2008). The skin can act as a storage for lipids (Schmitz and Muller, 1991) and water (Verdier-Sevrain and Bonte, 2007), as well as a means of synthesis of vitamin D by the action of UV (Poduje et al., 2008). A continual self-renewal of cells occurs to compensate the loss of damaged tissue.

The skin is composed of three parts: the epidermis which provides waterproofing and serves as a barrier to infection; the dermis which serves as a location for skin appendages, like hair follicles, and the hypodermis which is a subcutaneous adipose layer (figure 10*A*). Hair follicles consist of an external epithelial envelope (outer root sheath) that is continuous with the epidermis, ensheaths the shaft and its thin internal envelope (inner root sheath) and embedded in it there is a distinct group of specialized dermal cells, the papilla. This core is surrounded by mesenchymal tissue, the dermal sheath (Paus and Cotsarelis, 1999). The hair follicle displays a remarkable ability for self regeneration, undergoing a regular succession of growth (anagen) and regression (catagen) phases associated with replacement of the old hair shaft by a new one (Hardy, 1992). Epidermis ("epi" coming from the greek meaning "over" or "upon") is the outermost layer of the skin. It forms the protective wrap over the surface of the body, and it is made up of stratified squamous epithelium (Blanpain and Fuchs, 2009). The dermis is the layer of skin beneath the epidermis consisting of connective tissue and it cushions the body from stress and strain (figure 10*B*).

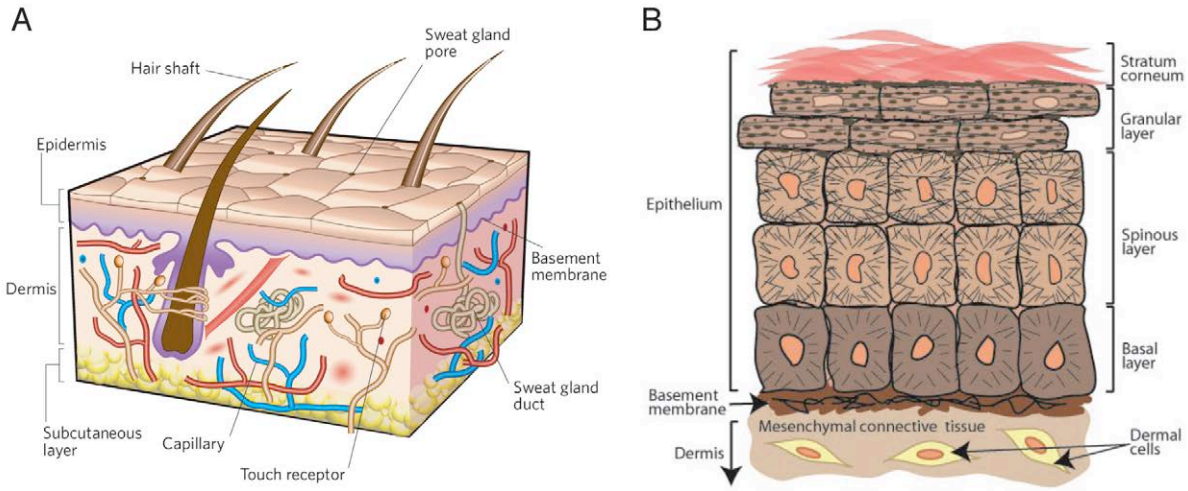

Figure 10: The skin. *A*, Structure of the human skin (MacNeil, 2007). *B*, Epidermis and the different layers forming this pluristratified epithelium (Fuchs, 2008).

The epidermis is tightly connected to the dermis by a basement membrane. It also harbours many mechanoreceptor nerve endings that provide the sense of touch and heat (Boulais and Misery, 2008). It contains the hair follicles, sweat glands, sebaceous glands, apocrine glands, lymphatic vessels and blood vessels. The blood vessels in the dermis provide nourishment and waste removal to its own cells as well as to the stratum basale of the epidermis. The hypodermis lies below the dermis. Its purpose is to attach the skin to underlying bones and muscles as well as supplying them with blood vessels and nerves. It consists of connective

tissue and elastin. The main cell types are fibroblasts, macrophages and adipocytes. The hypodermis contains about 50% of the body fat which serves as padding and insulation for the body (Wajchenberg, 2000).

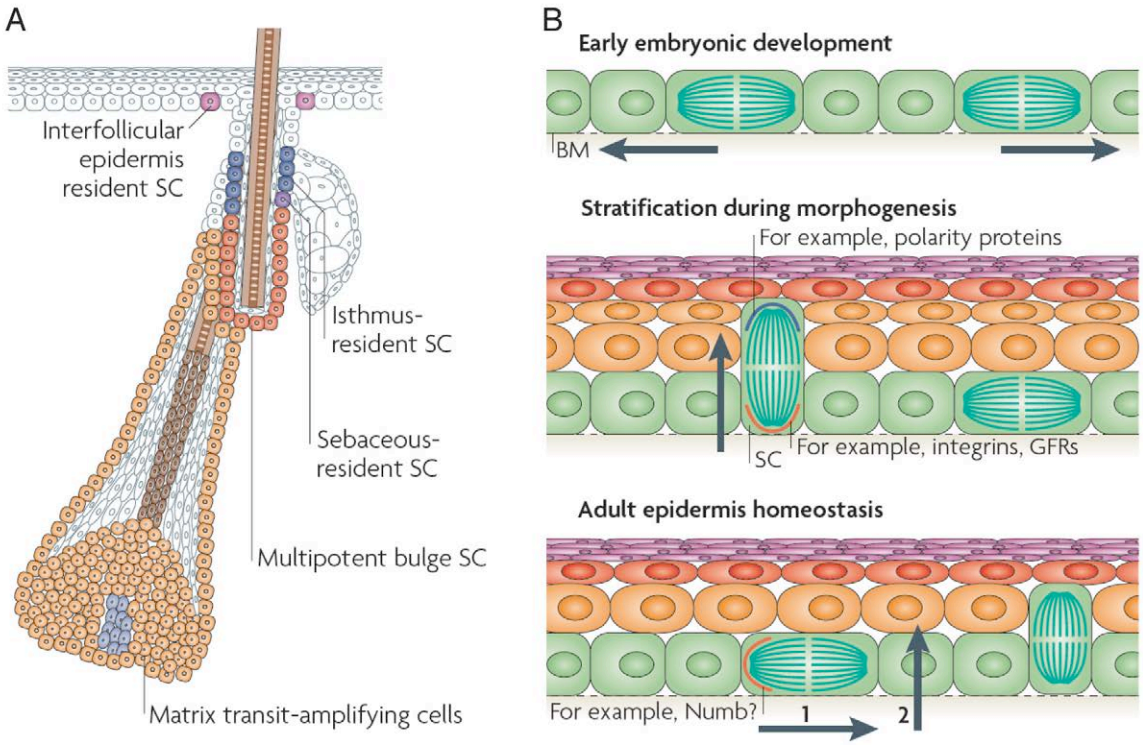

Figure 11: Stem cells (SC) of the skin. *A*, Schematic representation of the skin epidermis with the different resident SC compartments and transit-amplifying progeny identified. Bulge SCs are multipotent, residing in the permanent portion of the hair follicle (HF). Interfollicular epidermis SCs reside in the basal layer of the epidermis. Resident progenitors of the isthmus and sebaceous glands (SG) reside in the outer root sheath that is above the bulge and below the SG. It is not clear whether these two resident progenitors are equivalent. *B*, During the early stages of embryonic skin development, most cell divisions are symmetric and parallel to the basement membrane (BM), which ensures the growth of the surface of the developing embryo and maintains the epithelium as a single layer (top pannel). During epidermal stratification, ~70% of the cell divisions become asymmetric, such that the mitotic spindle is perpendicular to the basement membrane. This allows the development of suprabasal cells that terminally differentiate and establish the skin barrier (indicated by the arrow). In this mode of asymmetric cell division, different cell fate determinants are segregated unequally between the two daughter cells. The basal cell segregates the integrins and growth factor receptors (GFRs), which provide survival and proliferative cues to the SC. Polarity proteins are concentrated to the apical surface and presumably become preferentially distributed to the suprabasal cell (middle pannel). During epidermal homeostasis in the adult tail skin, asymmetric cell divisions occur with the plane of division parallel to the BM, such that only one daughter cell inherits a cell fate determinant, such as Numb, and remains a SC (step 1), whereas the other becomes committed to terminal differentiation, and probably undergoes delamination to reach the suprabasal layers (step 2; lower pannel). Adapted from: (Blanpain and Fuchs, 2009).

The epidermis is a rapidly self-renewing tissue. It contains no blood vessels, and cells in the deepest layers are nourished by diffusion from blood capillaries extending to the upper layers of the dermis. The epidermis is mainly composed by keratinocytes with melanocytes, Langerhans cells and Merkels cells are also present. It can be further subdivided into the following strata (beginning with the innermost layer): stratum basale, stratum spinosum, stratum granulosum, stratum lucidum (present only in palms of the hands and sole of the foot) and stratum corneum (figure 10*B*).

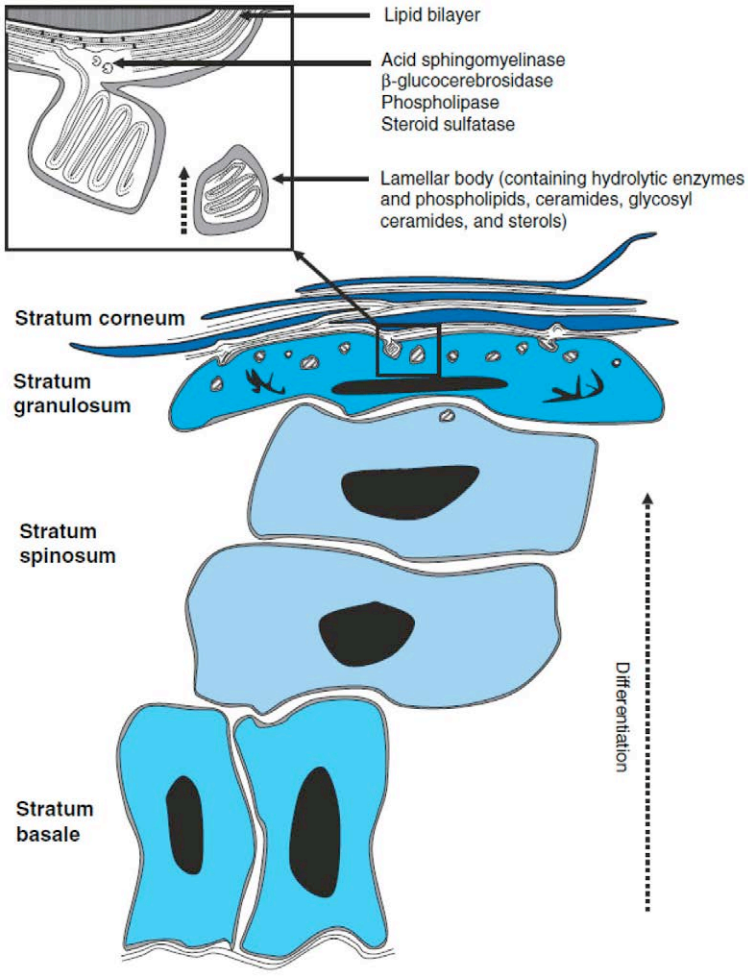

Figure 12: Detailed structure of the epidermis. At the stratum granulosum/stratum corneum interface, the content of the lamellar bodies is extruded to the interface, thus forming continuous bilayers (Proksch et al., 2008).

The epidermis maintains homeostasis by constant proliferation of rapidly dividing progeny of stem cells (figure 11*A*). Cutaneous stem cells or keratinocyte stem cells, which reside in the stratum basale, represent about 10% of the stratum basale population. As shown in figure 11*B*, stem cells generate daughter cells by asymmetry-division mitosis by either stem cells themselves or keratinocyte cells that move up from the suprabasal layers to the skin surface (Blanpain and Fuchs, 2009). While keratinocytes move from one stratum to the upper one, they mature and express different proteins (e.g. keratins; figure 12). Then the cells loose their nuclei, flatten and slough off from the stratum corneum in a process called desquamation. The final steps in keratinocyte differentiation are associated with profound changes in their structure, resulting in their transformation into the flat and anucleated corneocytes of the stratum corneum, which are loaded with keratin filaments and surrounded by a cell envelope composed of cross-linked proteins (cornified envelope proteins) as well as a covalently bound lipid

envelope (Houben et al., 2007). Extracellular non-polar lipids surround the corneocytes to form a hydrophobic matrix. This phenomenon, in which keratinocytes divide in the basal layer, produce keratins, differentiate and migrate to the upper layers as they mature, is known as keratinization and takes place within about 27 days. In normal epidermis, the proliferation rate in the basal layer is precisely balanced by desquamation of the cornified layer at the skin surface (Candi et al., 2005).

Melanocytes originate in the neural crest and migrate to the stratum basale of the epidermis and the hair matrices. Through a process called melanogenesis, these cells produce melanin pigment that determines the skin color and provides protection against harmful UV (Yuji Yamaguchi, 2009). The major determinant of the skin color is not the number, but rather the activity of the melanocytes (Rees, 2003). Merkel cells are scattered in the basal layer of the epidermis and in the outer root sheath of hair follicles. They are located near areas of well-vascularised, richly innervated connective tissue. Each Merkel cell is intimately associated with an afferent nerve terminal, forming a structure known as a Merkel cell-neuron complex, or a Merkel disc (Boulais and Misery, 2007). Their structure is characteristic of transducer sensory cells that act as intermediates between an initial stimulus and the afferent neuron impulse. Langerhans cells also known as dendritic cells that are potent antigen-presenting cells with important immunostimulatory and migratory activities also populate epidermis and dermis. Langerhans cells serve to fix and process cutaneous antigens. To present foreign antigens to naive T cells, dendritic cells must migrate from inflamed or injured peripheral tissues to the closest draining lymph nodes through afferent lymphatic vessels (Martin-Fontecha et al., 2009). Immature Langerhans cells that reside in the periphery in the steady state are highly specialized in antigen uptake. Langerhans cells form a dense network in the epidermis where they constantly scan the environment by extending and retracting their dendrites and are ideally positioned to detect any pathogen breaching the skin barrier. Langerhans cells transport antigen to skin draining lymph nodes, which is essential to ensure interaction with rare antigen-specific naive T cells. During this process, they undergo maturation and produce proinflammatory cytokines, which leads to efficient antigen presentation and activation of the innate and acquired immune systems. Thus, by the time Langerhans cells arrive in the lymph nodes, they have acquired the surface phenotype of ‘functionally’ mature dendritic cells capable of activating naive T cells and thereby initiating an adaptive immune response specifically tailored to fight off the invading cutaneous pathogen (Kaplan et al., 2008).

Skin wound healing

Disruption of the skin following injury exposes the body to dehydration and infection. To avoid this, a number of events aim the restoration of an intact epidermal barrier through wound epithelialization (also called re-epithelialization). Wound healing is a complex process that involves 3 different phases: inflammation, proliferation and remodelling (figures 13).

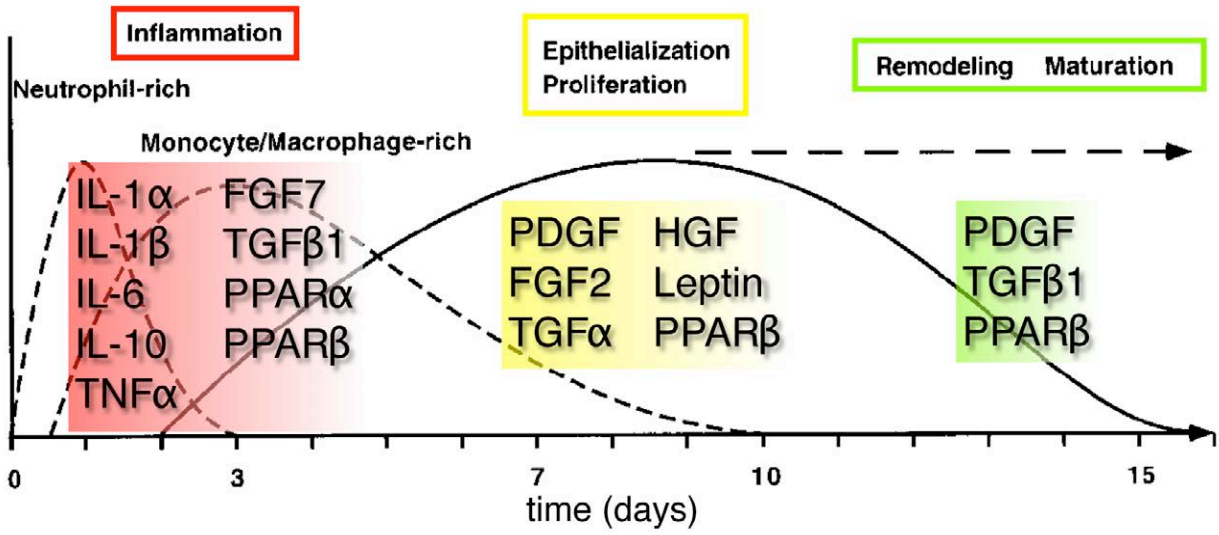

Figure 13: Summary of time sequence of the major overlapping phases of skin wound healing and expression pattern of several genes involved in these processes. Modified from (Michalik et al., 2001).

Shortly after injury, the formation of a platelet plug and a blood clot results in a temporary sealing of the wound. Inflammatory cells, which are subsequently attracted to the wound site, are important for the defence against invading bacteria. The inflammatory cells also produce growth factors, cytokines and proteinases, which are required for the phase of new tissue formation. This phase involves migration and hyperproliferation of keratinocytes at the wound edge, which finally leads to coverage of the wound with a new epidermis. Concomitantly, repair of the injured dermis is initiated. Blood-vessel sprouting occurs at the wound edge, and new vasculature develops. Fibroblasts migrate into the wound, where they proliferate and produce large amounts of extracellular matrix (ECM).

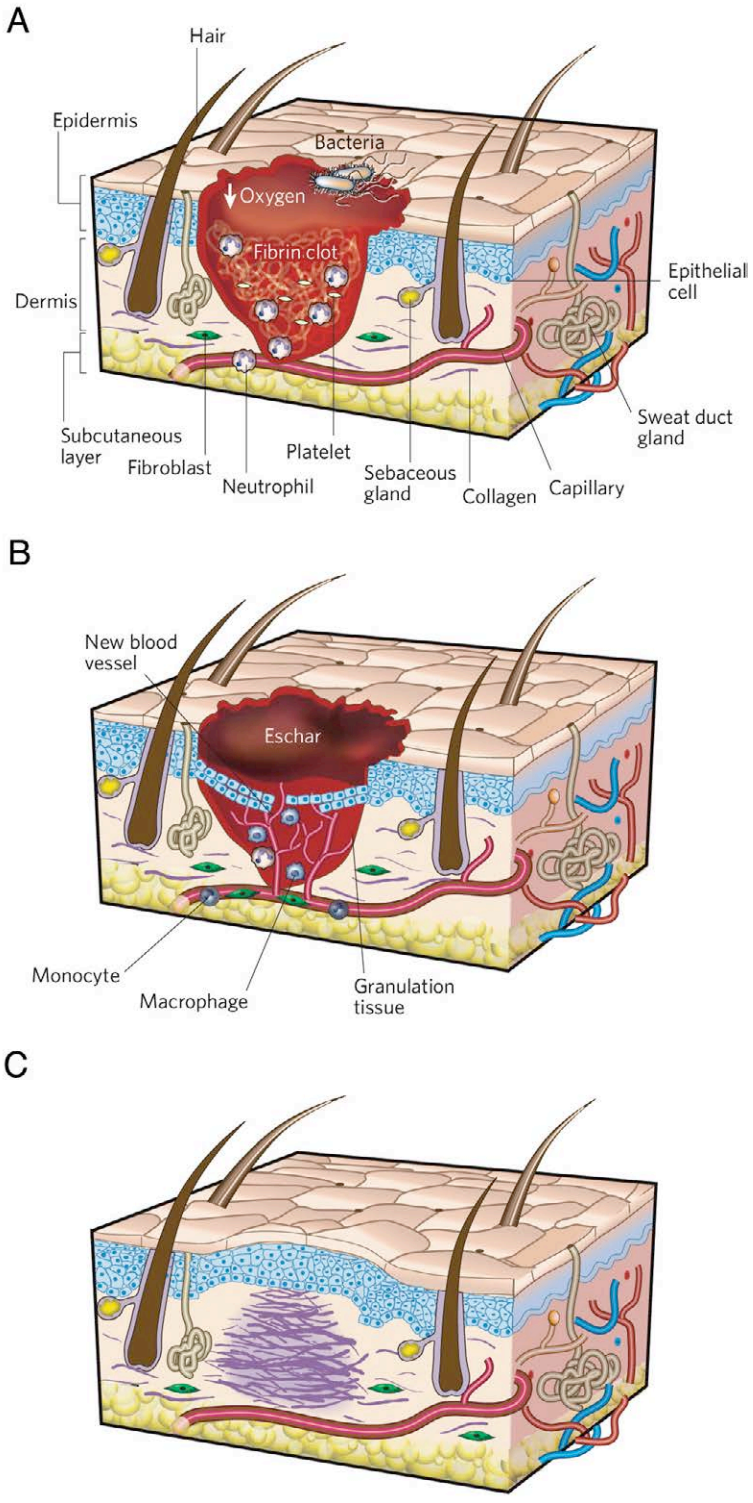

Figure 14: The three classic stages of wound repair: inflammation (*A*), new tissue formation (*B*) and remodelling (*C*). *A*, Inflammation. This stage lasts until about 48 h after injury. Depicted is a skin wound at about 24–48 h after injury. The wound is characterized by a hypoxic (ischaemic) environment in which a fibrin clot has formed. Bacteria, neutrophils and platelets are abundant in the wound. Normal skin appendages (such as hair follicles and sweat duct glands) are still present in the skin outside the wound. *B*, New tissue formation. This stage occurs about 2–10 days after injury. Depicted is a skin wound at about 5–10 days after injury. An eschar (scab) has formed on the surface of the wound. Most cells from the previous stage of repair have migrated from the wound, and new blood vessels now populate the area. The migration of epithelial cells can be observed under the eschar. *C*, Remodelling. This stage lasts for a year or longer. Depicted is a skin wound about 1–12 months after repair. Disorganized collagen has been laid down by fibroblasts that have migrated into the wound. The wound has contracted near its surface, and the widest portion is now the deepest. The re-epithelialized wound is slightly higher than the surrounding surface, and the healed region does not contain normal skin appendages (Gurtner et al., 2008).

Some fibroblasts differentiate into myofibroblasts, which are responsible for wound contraction and the deposition of additional matrix. The new tissue that forms at the wound site is called granulation tissue because of the granular appearance of the numerous capillaries. In the final phase, a transition from granulation tissue to mature scar tissue occurs. Matrix remodelling and a reduction in cellularity characterize this process. The scar tissue shows reduced mechanical stability and elasticity compared with uninjured skin, and it lacks appendages, including hair follicles, sebaceous glands and sweat glands (figure 14).

During all these phases, various cell types and proteins are involved (Raja et al., 2007; Schafer and Werner, 2007). Recent studies have shown that many are essential for normal wound healing. Deletion of some genes such as c-Met (Chmielowiec et al., 2007), TGFβ1 (Brown et al., 1995), Nrf2 (Beyer et al., 2007), PPARα and PPARβ (Michalik et al., 2001) causes an impaired wound healing. On the other hand, the knockout of certain genes provokes an accelerated wound closure rate like in the case of Smad3 (Ashcroft et al., 1999) or IL-10 (Eming et al., 2007). Interestingly, nicotine not only affects skin aging but also causes wound healing delay (Misery, 2004). Several key mediators of wound healing and their function are presented in figure 15.

Ligand	Receptor	Type of receptor	Signalling proteins	Role in re-epithelialization
HGF	MET	Receptor tyrosine kinase	Unknown, possibly ERK1 and ERK2, AKT, GAB1, PAK1 and/or PAK2	Stimulation of keratinocyte migration and probably proliferation
FGF7, FGF10 and FGF22	FGFR2-IIIb, possibly FGFR1-IIIb	Receptor tyrosine kinase	Unknown, possibly ERK1, ERK2, AKT and/or STAT3	Stimulation of keratinocyte proliferation and migration
Heparin-binding EGF and other EGF-family members	EGFR (also known as ERBB1), possibly ERBB2, ERBB3 and/or ERBB4	Receptor tyrosine kinase	Unknown, possibly ERK1 and ERK2, AKT and/or STAT3	Stimulation of keratinocyte proliferation and migration
TGF-β	TGF-β receptor I and TGF-β receptor II	Receptor serine/threonine kinase	SMAD3 and others, including SMAD2 and MAPK	Inhibition of keratinocyte proliferation and survival
Acetylcholine	M3 receptor	G-protein-coupled receptor	Ca^{2+}-dependent guanylyl cyclase, cyclic GMP and PKG, leading to inhibition of RHO	Inhibition of keratinocyte migration
	M4 receptor	G-protein-coupled receptor	Adenylyl cyclase, cyclic AMP and PKA, leading to activation of RHO	Stimulation of keratinocyte migration
Catecholamines, including adrenaline	β_2-Adrenoceptor	G-protein-coupled receptor	Activation of phosphatase PP2A, resulting in dephosphorylation and inhibition of ERK1 and ERK2	Inhibition of keratinocyte migration
Polyunsaturated fatty acids	PPAR-α and PPAR-β*	Nuclear receptor	Direct activation of target genes by binding to the promoter/enhancer of these genes	Stimulation of keratinocyte migration and survival

Figure 15: Soluble mediators of re-epithelialization (Gurtner et al., 2008).

Role of ENaC in the skin

The three ENaC subunits are present in the epidermis (figure 16*A*), hair follicles and sweat glands (Roudier-Pujol et al., 1996; Oda et al., 1999). The expression of ENaC increases following keratinocyte differentiation (Brouard et al., 1999). The application of amiloride blocks calcium-induced keratinocyte differentiation (Mauro et al., 1995; Mauro et al., 1997).

Furthermore, studies involving αENaC-deficient mice showed that their skin was hyperplasic (figure 16*B*). It was also demonstrated that ENaC modulates ionic signalling for specific aspects of epidermal differentiation, such as synthesis or processing of differentiation-specific proteins, and lipid secretion (Mauro et al., 2002). Recent studies in our laboratory have shown that ENaC is required for the postnatal maintenance of the epidermal barrier function (Charles et al., 2008).

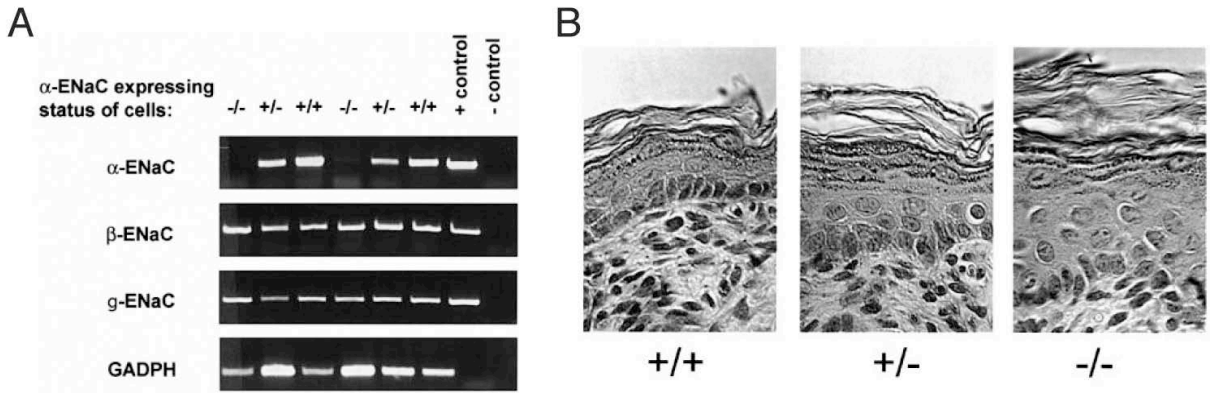

Figure 16: αENaC complete knockout mice exhibit a thicker epidermis. *A*, Detection of mRNA transcripts for α, β, and γENaC in ENaC wild-type (αENaC +/+), heterozygous (+/-), and homozygous mutant (-/-) mouse keratinocytes. In αENaC -/- mice, no change in mRNA expression of the β, and γENaC subunit was detected. The RT-PCR was controlled by detection of GAPDH message. Positive control (+) : αENaC cDNA; negative control (-) : PCR reaction without DNA. *B*, αENaC -/- mice exhibit thickening of the epidermis. Light microscopy of mice skin samples, taken from a-ENaC +/+, +/-, and -/- mice soon after birth and stained with hematoxylin and eosin. Magnification : 400x. Light microscopy demonstrated hyperplasia, nuclear atypia, and abnormal keratohyalin granules in αENaC -/- mice. Adapted from (Mauro et al., 2002).

Injury that disrupts an epithelial layer instantaneously generates endogenous electric fields, which were detected at human skin wounds over 150 years ago. Recent data combining molecular, genetic and imaging techniques have provided significant insights into cellular and molecular responses to this “unconventional” signal. One unexpected finding is that the electric fields play an overriding guidance role in directing cell migration in epithelial wound healing. In experimental models where other directional cues (e.g., contact inhibition release, population pressure, etc.) are present, electric fields of physiological strength override them and direct cell migration (Zhao, 2009). The figure 17 shows the concepts concerning the directional guidance during wound healing. There is evidence that ENaC might play a role in creating these electric fields (Zhao, 2009). Unfortunately, the precise localization of this channel in the different epidermal layers has not been reported yet.

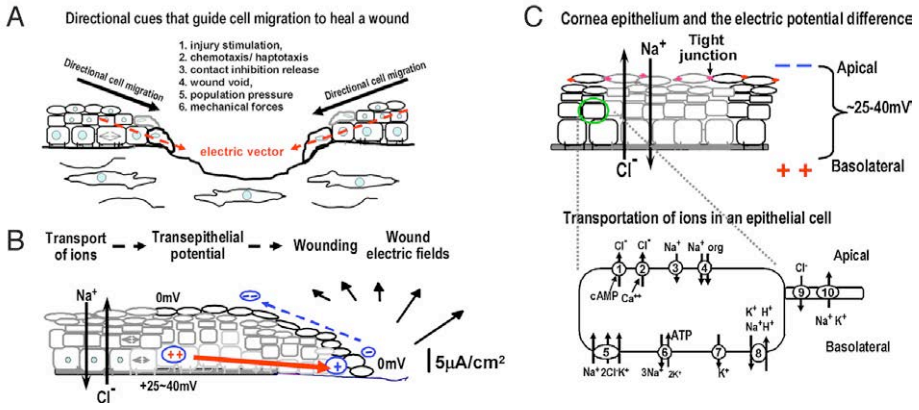

Figure 17: Directional cues that guide the epithelial cells to migrate directionally at a wound. *A*, The following are generally accepted cues: injury stimulation, chemotaxis, contact inhibition release, presence of wound void, population pressure, stress/tensile. The endogenous wound electric fields are a vector that constantly points to the wound center (red dashed arrows), thus could guide the migrating cells into the wound. *B*, The mechanism of generation of wound electric fields. *C*, Molecular basis : directional ion transportation generate electric potential difference. An electric potential difference, positive at the basal side relative to the apical side (upper part) is generated and maintained by net directional electrogenic movement of ions through pumps and channels (lower part). Adapted from (Zhao, 2009).

Vascular smooth muscle cell (VSMC) migration plays a key role in tissue repair after arterial wall injury. VSMC migration requires integration of chemical and mechanical signaling mechanisms (Grifoni et al., 2006).

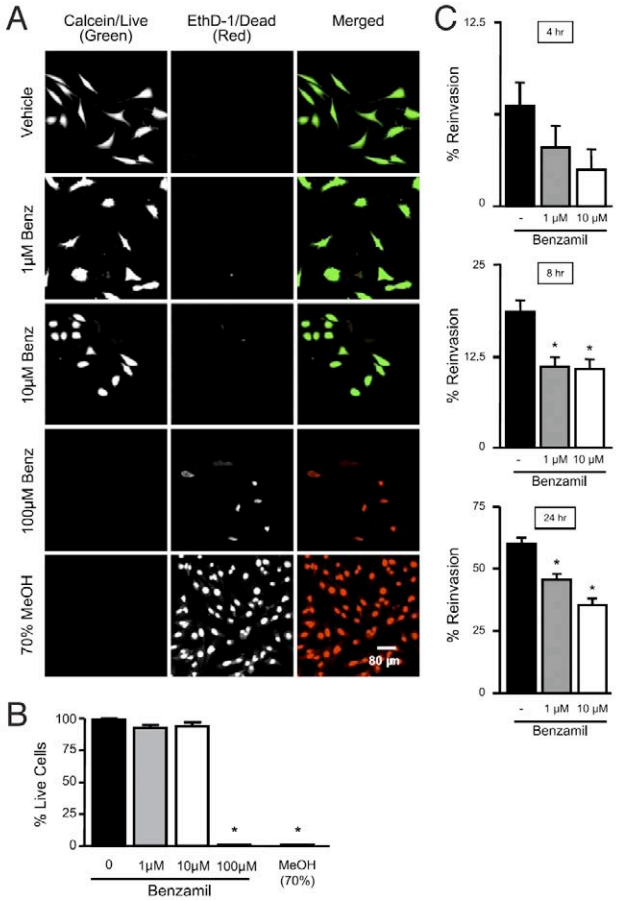

Figure 18: ENaC inhibition reduces VSMC wound healing. *A* and *B*, Effect of benzamil (Benz) on SV40-LT VSMC viability. *A*, Metabolically active cells stained with calcein-AM and dead cells stained with ethidium homodimer-1 (EthD-1). Methanol (MeOH, 70%) was used as a control for dead cells. *B*, Group data. Benzamil at 1 and 10 _M did not alter viability compared with vehicle; 100 μM benzamil elicited a cytotoxicity effect similar to that elicited by 70% MeOH. *C*, VSMC wound healing 4, 8, and 24 h after ENaC inhibition with 1 and 10 μM benzamil. ENaC inhibition blocked healing 8 and 24 h after wound generation. Values are means ± SE (*n* = 5–8), **P* < 0.05 (Grifoni et al., 2006).

Recently, it has been shown (figure 18) that ENaC proteins are expressed in VSMCs and that ENaC inhibition abolishes pressure-induced constriction in isolated artery segments (Grifoni et al., 2006).

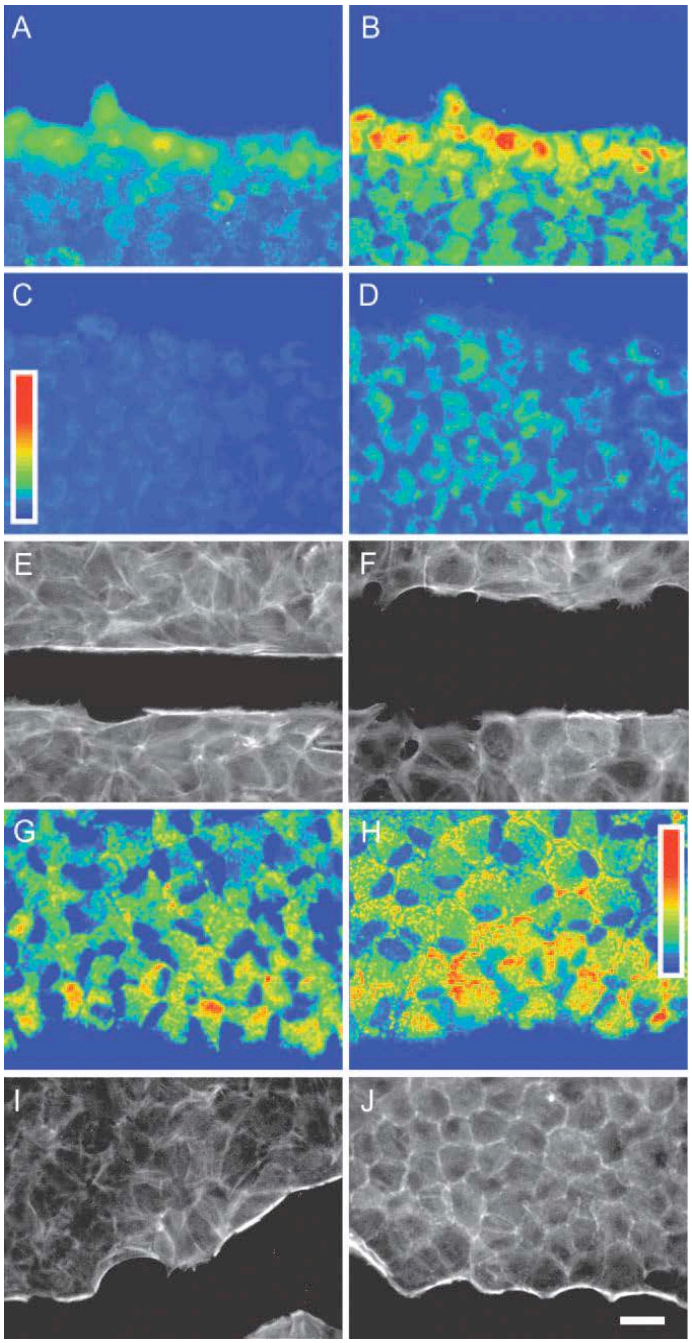

Figure 19: Epithelial Na^+ channel (ENaC) participation in membrane depolarization during the course of wound healing. *A–D*, Wounded monolayers were left in the tissue culture incubator (37°C, 5% CO_2) for 1 h in minimum essential medium (MEM; *A* and *B*) and in MEM containing 50 μM phenamil (*C* and *D*), and afterward they were loaded with Oxonol V, Sodium Green, and PI in CS and photographed for Sodium Green (*A* and *C*) and Oxonol V (*B* and *D*) fluorescence. Shown are pseudocolor images of the original monochromatic ones. Note that phenamil determined a decrease in both the Sodium Green (*C*) and Oxonol V (*D*) fluorescence intensities at the wound borders. *E* and *F*, Wounded monolayers were left for 6 h in the tissue culture incubator in MEM supplemented with 5% serum without (*E*) and with (*F*) 50 μM phenamil, and afterward they were fixed and stained for actin. Note the marked difference in the wound width between the two images. *G* and *H*, Wounded monolayers were left for 1 h in the tissue culture incubator in CS (*G*) and in Li^+ (*H*), loaded with Oxonol V and PI, and photographed. Images and intensity scale are the same as in *B* and *D*. Note that in both cases, an increase in oxonol fluorescence occurred at the wound borders. *I* and *J*, Same as *G* and *H*, but labeled for actin. Note that in both images (*I* and *J*), the actin cable is present. Bar, 30 μm (Chifflet et al., 2005).

Membrane potential depolarization occurs at the leading edge of linear narrow wounds produced on cultured bovine corneal endothelial monolayers and gradually extends inward toward the neighboring cells. The replacement of extracellular Na^+ by choline and the incorporation of phenamil, an inhibitor of ENaC, provokes a decrease in the actin cable and depolarization areas and in the lamellar activity of the wound edges. To the contrary, extracellular Li^+ can successfully replace Na^+ in the determination of the depolarization and cytoskeletal responses. This finding supports the idea that membrane depolarization, not the increase in intracellular Na^+ concentration, is responsible for the formation of the actin cable, a result that is in agreement with previous evidence showing that nonspecific depolarization of the plasma membrane potential (PMP) of epithelial cells may promote characteristic cytoskeletal rearrangements per se (figure 19). This suggests that spontaneous depolarization of the PMP of the cells at the wound borders determined by a rise in the ENaC activity of these cells constitutes an additional factor in the intermediate cellular processes leading to wound healing in some epithelia (Chifflet et al., 2005).

In collaboration with our group, the laboratory of Dr. Rivkah Isseroff (UC Davis, USA), has studied the process of galvanotaxis, the directional migration of cells in an electric field, in human keratinocytes, which are responsible for wound re-epithelialization (unpublished data). These cells respond to electric fields equivalent to those found in human skin wounds (50-100 mV/mm) with persistent directional migration toward the cathode. To analyze whether ENaC is involved in galvanotaxis, keratinocytes from wild type (αENaC +/+) and knockout (αENaC-/-) mice, in which channel activity is abolished, were isolated. They utilized time-lapse imaging to record the speed and the directional route of the galvanotaxis of keratinocytes in a 100 mV/mm electric field. Whereas keratinocytes from αENaC knockout mice migrated at same rate as cells from wild type mice, the directionality of the knockout keratinocytes was lost and cells migrated randomly instead of moving toward the cathode (as did the control cells) in the electric field ($P<0.005$). A similar decrease in the directional migratory response to the electric field was observed when normal human keratinocytes were treated with phenamil. Treated with 10mM phenamil in galvanotaxis, human keratinocyte migrated at 1mm/min as control, but the directionality of the cells, which is measured by the cosine value to the cathode, decreased by 30% from 0.86 to 0.6 ($P<0.005$). Since directional keratinocyte migration is required for wound re-epithelialization, they examined what effect ENaC inhibition by phenamil would have on wound re-epitheliazation of human skin wounds in an *ex vivo* wound healing assay. Application of 10mM phenamil decreased the re-epithelialization by 85%, while control wounds, incubated in 10%FCS-containing medium, healed completely. These results

demonstrate that ENaC has a potentially important function to mediate the directional migration and wound healing in keratinocytes (Yang et al., 2007).

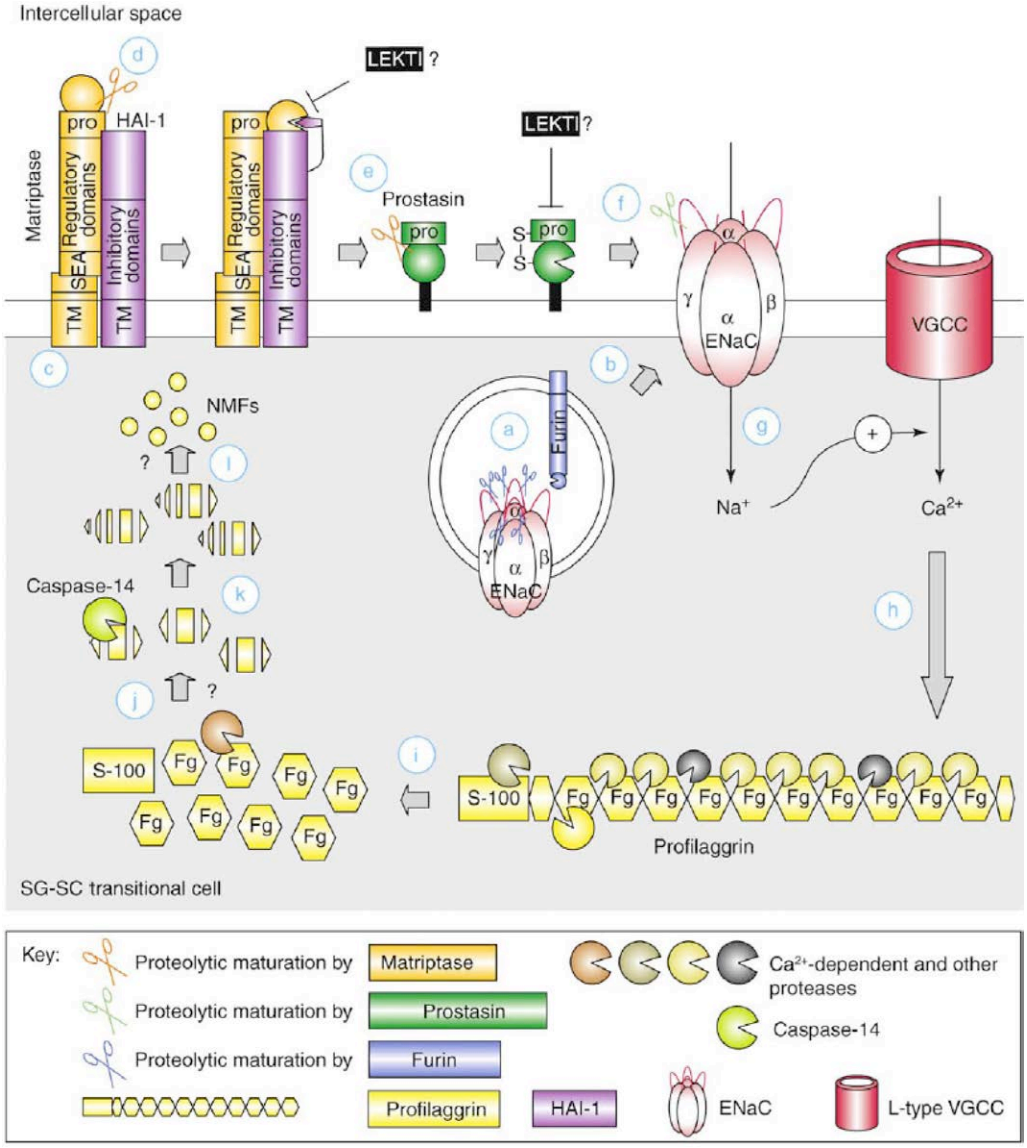

Figure 20: Hypothetical model for the matriptase–prostasin signaling cascade leading to epidermal barrier formation and hydration. This figure illustrates a suggested mechanism for the signaling cascade in which matriptase and prostasin are involved. (a) Furin auto-activates during transport from the ER to the trans-Golgi network, where it cleaves ENaC in the extracellular loops of the a and γ subunits and thereby pre-activates it. (b) The pre-activated ENaC resides in the cytoplasmic membrane because the trans-Golgi vesicles fuse with the cytoplasmic membrane. (c) During transport towards the plasma membrane, HAI-1 associates with matriptase to prevent premature matriptase activation. Once inserted into the cytoplasmic membrane, matriptase, despite its association with HAI-1, can activate (d) itself and (e) prostasin. (f) The activated prostasin cleaves the extracellular loop of the ENaC γ-subunit to fully activate the channel. (g) This is followed by a Na^+ influx, which causes plasma membrane depolarization and increases the Ca^{2+} influx through VGCCs. (h) The increased concentration of Ca^{2+} activates Ca^{2+}-dependent proteases. (i) These proteases cleave profilaggrin into functional filaggrin (Fg) monomers (this probably occurs in conjunction with other, non-Ca^{2+}-dependent proteases). (j) In the SC, the Fg monomers are further cleaved by unknown proteases. (k) These Fg fragments can be further cleaved by Caspase-14. (l) Finally, the fragments are degraded by an unknown subset of proteases to generate free amino acids, some of which are hygroscopic (such as glutamine that is converted to pyrrolidonic carboxylic acid) and contribute to the NMFs. The increase in the concentration of Ca^{2+}, by activating the Ca^{2+}-dependent transglutaminases, is important also for the formation of the CE (not shown). The matriptase–prostasin signaling cascade is regulated by inhibition of matriptase and prostasin by HAI-1. LEKTImight be an inhibitor of these proteases. The inhibition of this signaling cascade by HAI-1, the activation of prostasin by matriptase, and the involvement of Caspase-14 in the degradation of Fg fragments have been genetically proven. Other steps in the cascade are more speculative (see the text for details). CE, cornified envelope; ENaC, epithelial sodium channel; Fg; HAI-1, hepatocyte growth factor activator inhibitor 1; LEKTI, lympho-epithelial Kazal-type related inhibitor; NMFs, natural moisturizing factors; pro, prodomain; SC, stratum corneum; TM, transmembrane domain; VGCC, voltage-gated Ca^{2+} channel (Ovaere et al., 2009).

It has become clear in recent years that serine proteases have an important role in epidermal homeostasis, and the signaling cascades are gradually being identified. CAP3, CAP1 and furin are implicated in a cascade that could activate ENaC, leading to epidermal barrier formation and hydration, maybe in part through their involvement in filaggrin processing (Ovaere et al., 2009). The consecutive cleavages of ENaC remove the inhibitory domains in the extracellular loops. Upon activation, ENaC allows Na^+ influx, which could depolarize the plasma membrane to increase the open-probability of voltage-gated Ca^{2+} channels, such as the L-type voltage-gated Ca^{2+} channels (Denda et al., 2006), leading to influx of Ca^{2+} (figure 20).

The functional relationship between Na^+ and Ca^{2+} channels and keratinocyte differentiation has been shown by treating cells with the ENaC blocker amiloride, which prevents the increase in intracellular Ca^{2+} and thereby limits other Ca^{2+}-dependent processes such as transglutaminase activation and cornified envelope formation (Guitard et al., 2004).

Profilaggrin processing in keratinocytes can be induced by treatment with Ca^{2+}, whereas generation of the filaggrin monomer can be prevented by synthetic calpain inhibitors (Yamazaki et al., 1997). It has been proposed that, in matriptase or prostasin-deficient mice, the absence of prostasin-induced activation of ENaC might result only in intermediate open probability of the channel, and the Ca^{2+} influx could be sufficient for corneocyte formation but not for profilaggrin processing (Ovaere et al., 2009).

WORKING HYPOTHESIS

ENaC is expressed in the skin and a function in keratinocyte differentiation and barrier formation has been demonstrated. Previous studies also suggested that it might be implicated in keratinocyte migration. This process is essential for remodelling of the skin following injury.

The aim of the first part of my thesis project was to investigate the role of ENaC in skin wound healing. We wanted to study this process *in vivo* in two mouse models either deficient for αENaC specifically in the skin or over-expressing the αENaC subunit in the skin. By performing analyses of the time course and the morphology of the closing wound we may be able to define the role of ENaC in the skin repair.

MATERIAL AND METHODS

Mouse models

To investigate the role of ENaC during the wound healing process, we studied whether the skin specific deficiency or the overexpression of the channel alpha subunit can have an influence.

Skin-specific αENaC knockout mice

Since the constitutive αENaC knockout mice die within 48h after birth, it was not possible to investigate the skin development and the role of ENaC in these adult mice. αENaC knockout pups dehydrate due to water loss through the skin. The figure 21 illustrates the breeding strategy to generate conditional αENaC knockout mice. Previously, our laboratory generated mice with the *Scnn1a* (αENaC) floxed gene (Hummler et al., 2002). When this mouse is crossed with a mouse that expresses the Cre recombinase under the keratin 14 promoter (K14), the recombination should only occur in cells from the basal layer of the epidermis and other K14 expressing cells (Huelsken et al., 2001). Noteworthy, the K14 promoter also targets corneal and thymic cells, meaning that the conditional knockout mice also lack the expression of αENaC in these cells.

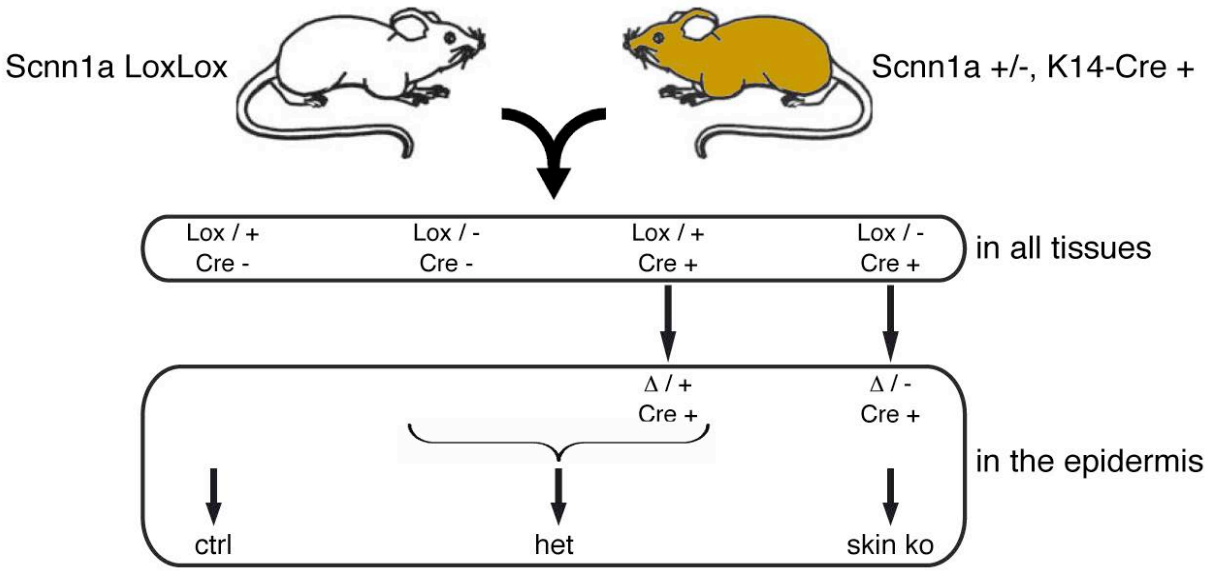

Figure 21: Scheme of the breeding in order to obtain skin specific αENaC knockout mice.

Skin specific αENaC transgenic mice (Tg**)

Simona Frateschi, in our group, developed this transgenic mouse model. The mouse αENaC gene is directed to the basal layer through the human K14 promoter (the basal vector was kindly provided by Prof. Sabine Werner, ETH Zürich). The construct furthermore contains a rabbit β-globin intron, the Scnn1a encoding sequence and a human growth hormone polyA.

Figure 22: Scheme of the αENaC::K14 construct (Frateschi, 2009).

Pronuclear injection was performed into FVB mouse oocytes and two strains were obtained that exhibit two different levels of overexpression of *Scnn1a*. The transgenic mice used in the following experiments exhibit a 20 times increased mRNA transcript expression level over nontransgenic mice. The αENaC protein was also increased in Tg** mice (figure 23).

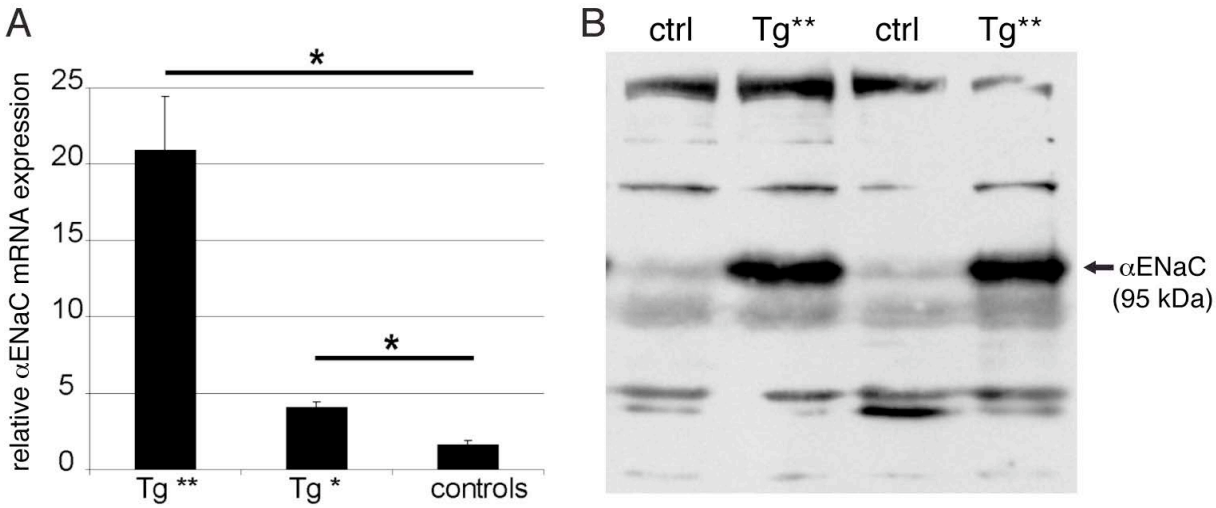

Figure 23: Molecular analysis of the skin specific αENaC overexpression model. *A*, αENaC mRNA transcript expression quantification from skin samples. *B*, Western blot analysis for αENaC on skin lysates of Tg and control mice (Charles, 2007).**

Molecular analysis

Following dissection, skin samples were snap frozen, lysed using the TissueLyser (Qiagen) and homogenized with the QIAshredder (Qiagen). RNA extraction was performed with the RNeasy kit (Qiagen) according to the manufacture's instructions. Reverse transcriptase polymerase

chain reaction (RT-PCR) was then performed. Finally, the αENaC mRNA was quantified by quantitative real-time PCR (Applied Biosystems).

Kinetic parameters of wound healing

To study wound healing, the classical first experiment consists in following the kinetics of wound closure. Full-thickness wounds were performed on the back of the mice, then we measured the surface of the wounds regularly until closure. The results were compared the experimental groups (knockout or transgenic vs. control mice).

Two days preceding the setting the wound, the back of the mice was shaved. First, mice were anesthetized with Ketanarkon/Rompun, then using a biopsy punch pipette (Stiefel), a full-thickness skin wounds (2 per animal) were set on the back of the mice according to the protocol of the laboratory of Prof. Sabine Werner (ETHZ)(Eming et al., 2007). The wounds were measured every two days until complete closure. The perimeter of the wound was drawn on a transparent sheet, then scanned and the surface of the wound was measured with the ImageJ software (http://rsbweb.nih.gov/ij/).

Morphometric analysis of healing skin

Histology was performed to measure various parameters of an unclosed wound (day 5 post-wounding). The same method as described above was used to perform wounds. In this protocol, the piece of skin that contains the unclosed wound was dissected out and put in paraformaldehyde for fixation prior to perform paraffin blocks and hematoxilin and eosin (H&E)-stained sections for further analysis.

On the H&E-stained sections, see figure 24, following parameters can be measured (Thorey et al., 2004), the surface of the hyperproliferative epithelium (HE) and the wound width (WW).

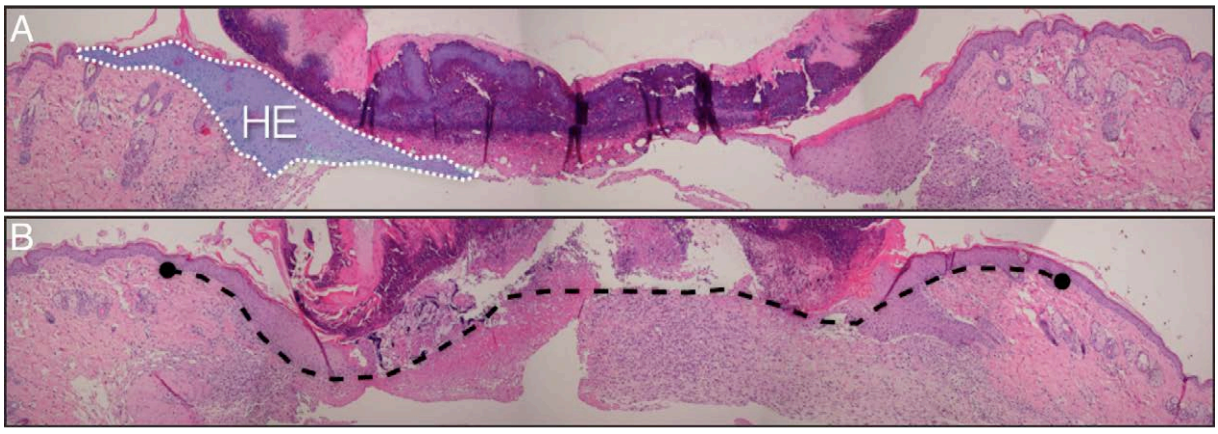

Figure 24: Image reconstitution of hematoxilin and eosin staining of wounded (at day 5 post-wounding) skin sections for morphometrical analysis. *A*, The purple area corresponds to the measured hyperproliferative epithelium (HE) for one side of a wound. *B*, Measurement of the wound width (black dotted line).

CONTRIBUTIONS

For this project, I used the following mouse lines: αENaC::K14 ko and Tg**. I performed all the dissections and *in vivo* experiments. I also performed the molecular analyses. The sections were imbedded in paraffin and stained by Jean-Christophe Stehle. Dr. Samuel Rotman performed histopathological analyses of the skin.

RESULTS

The aim of this study was to investigate the role of ENaC in wound healing. For this purpose, we used a conditional knockout mouse model, which lacks the expression of the αENaC subunit in K14 expressing cells. Thus, we expected that the channel mRNA transcript expression was abolished in the whole epidermis. In the αENaC transgenic mouse model, the transgene was targeted to the basal layer, thus specifically overexpressing the α subunit in the epidermis.

Molecular analysis of the skin-specific αENaC knockout mouse model

The K14 promoter targets Cre expression to the cells of the basal layer of the epidermis and hair follicles. The strategy to verify if the recombination occurred successfully was to extract RNA, perform reverse transcription (RT) and finally perform semi-quantitative RT-PCR and quantitative real-time PCR (qPCR) analyses.

RNA extraction was performed followed by reverse transcriptase polymerase chain reaction (RT-PCR). Finally, the αENaC mRNA was quantified by quantitative real-time PCR (TaqMan® - Applied Biosystems). Figure 25*A* shows the localization of the primers for the semi-quantitative RT-PCR for Scnn1a (αENaC). In figure 25*B*, the product of a RT-PCR is shown. The qPCR result demonstrates that the recombination occurred with nearly 100% efficiency in knockout mice (figure 25*C*).

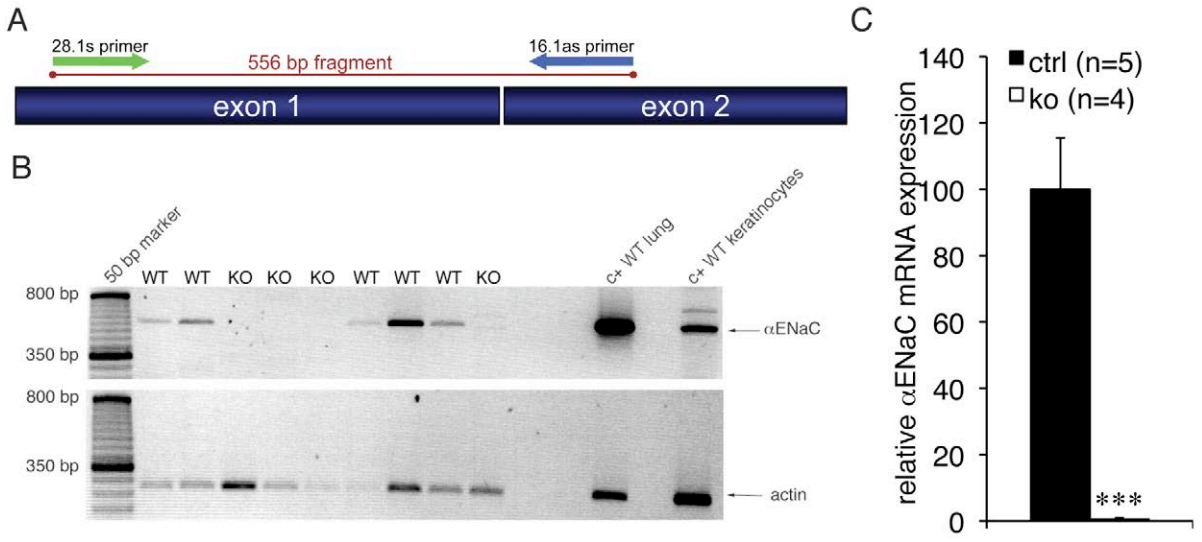

Figure 25: Lack of αENaC gene expression in skin biopsies. *A*, Localization of the primers used for the semi-quantitative RT-PCR. *B*, Semi-quantitative RT-PCR of αENaC and actin. *C*, Quantitative real-time PCR for αENaC from 5 control (black column) and 4 conditional knockouts (white column). Bars represent the SEM, ***$P < 0.001$.

TEWL experiments on skin conditional αENaC mutants

To test the skin outward barrier function we performed transepidermal water loss (TEWL) analysis. The figure 26 presents the results obtained from two groups (figure 26*A*, 6-8 month-old females and 26*B*, 3 month-old males). We measured the TEWL on normal and healed skin. There is an overall tendency for increased TEWL in the repaired skin, independently of the genotype. Comparison of control with conditional αENaC knockout did not show significant differences in all experiments.

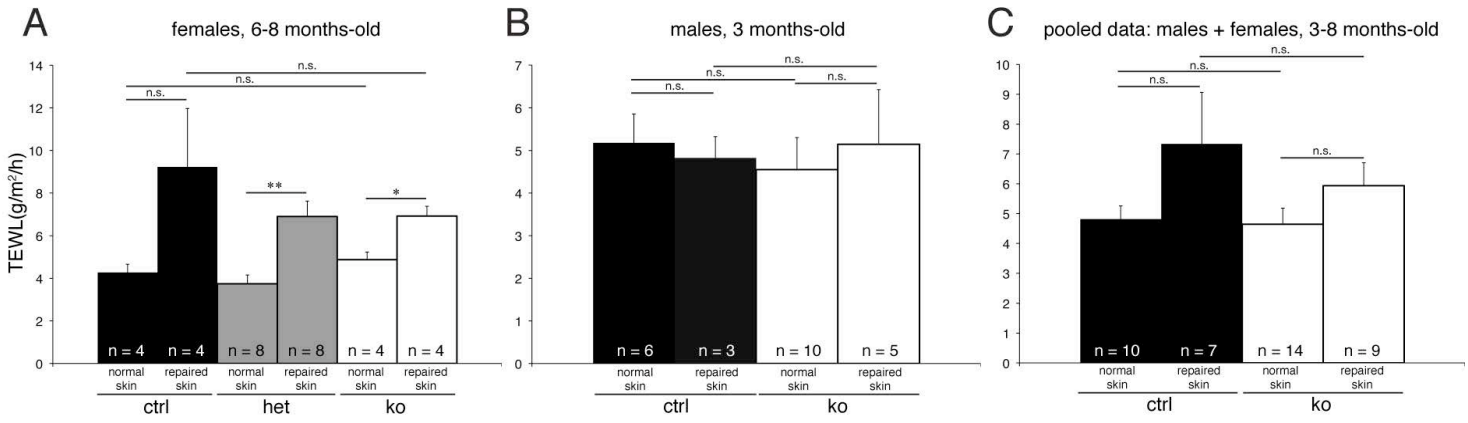

Figure 26: Transepidermal water loss (TEWL) analysis on αENaC skin specific knockout mice. *A*, Control (ctrl), heterozygous (het) and knockout (ko) female mice of 6-8 months of age. *B*, Control (ctrl) and knockout (ko) male mice of 3 months of age. *C*, Data of both experiments were pooled. Bars represent the SEM, the number of mice used is indicated in each column, n.s. = not significant, *$P < 0.05$ and **$P < 0.01$.

Analysis of the wound closure kinetics

Skin-specific αENaC knockout mice

We performed two 0.6 cm full-thickness excisions on the back of the mice and the closure rate in function of time was determined. The figure 27 presents the results for 6 individual experiments. None of these data showed significant differences.

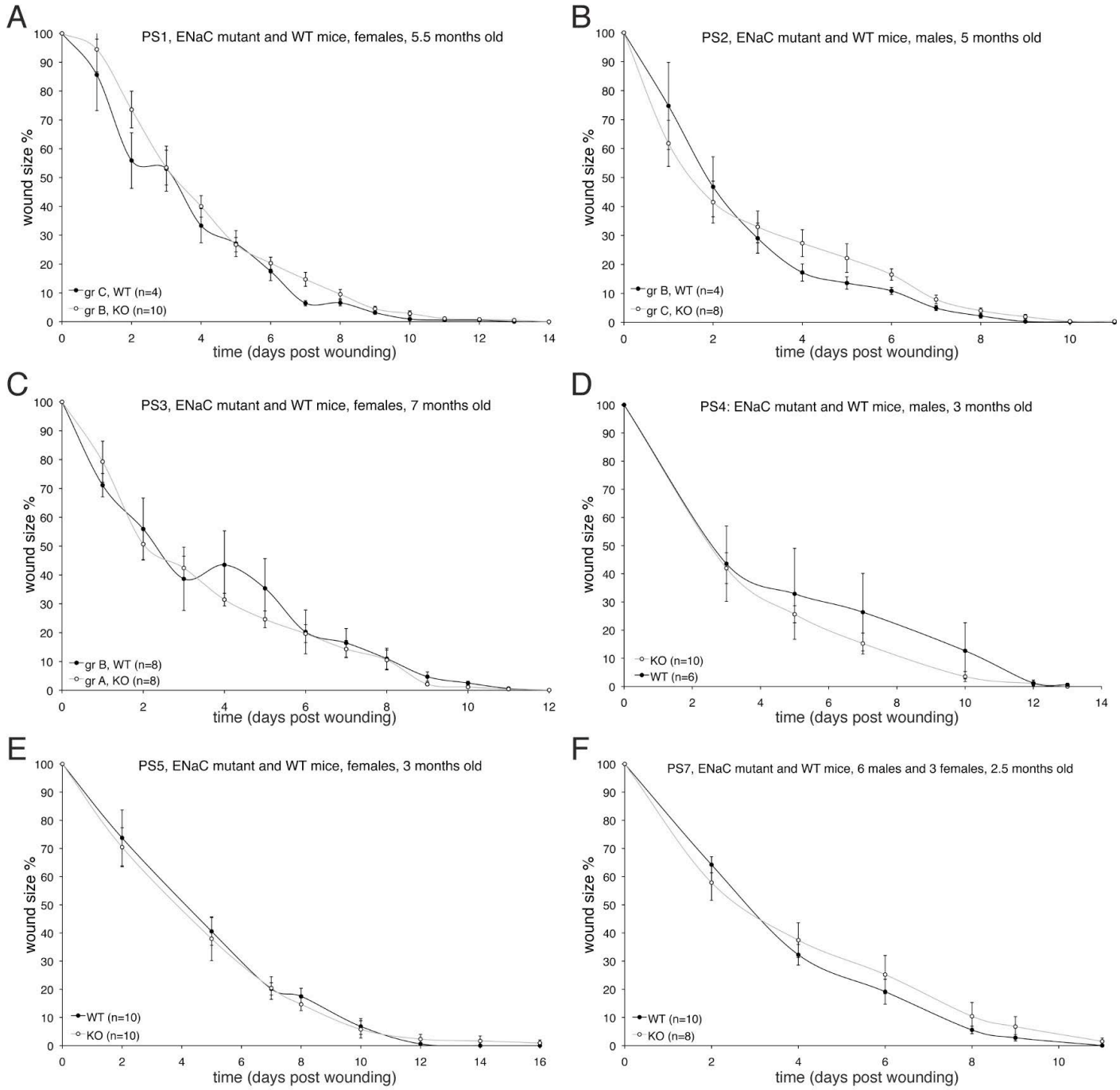

Figure 27: Wound healing kinetics in αENaC skin conditional KO mice. *A*, PS1: 5.5 month-old females. *B*, PS2: 5 month-old males. *C*, PS3: 7 month-old females. *D*, PS4: 3 month-old males. *E*, PS5: 3 month-old females. *F*, PS7: 2.5 month-old males and females. Control (black dots) and KO mice (white dots). Bars represent the SEM.

Although the pooled data (figure 28*A*) revealed a tendency of delayed wound closure in conditional skin-specific knockout mice, it did not reach statistical significance. Figure 28*B* illustrates the wound closure from day 0 to day 12 after wounding.

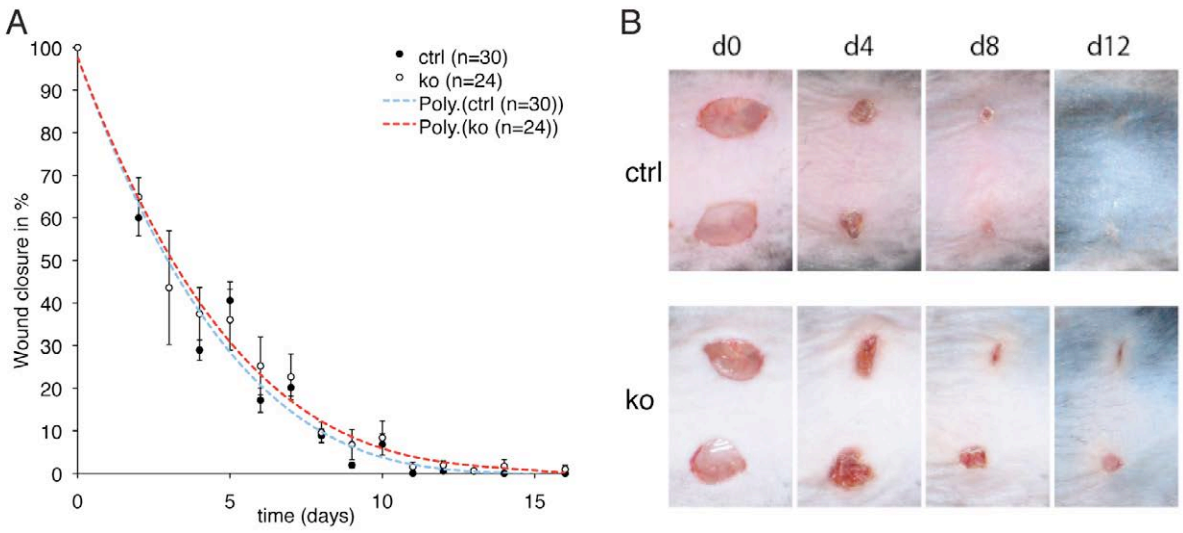

Figure 28: Wound healing kinetics in αENaC skin-specific knockout mice. *A*, Control (filled circles) and knockout mice (empty circles), and polynomial (Poly) regression curves for control (blue dotted line) and knockout (red dotted line) mice. Bars represent the SEM. *B*, Representative images taken between day 0 and 12 showing the progression of wound healing in control (upper panel) and αENaC skin-specific knockout (bottom panel) mice.

Skin-specific αENaC transgenic mice

We performed the same experiment with mice from the αENaC transgenic model. In this case (figure 29), the wound healing process was slightly accelerated in a first phase, but the wounds finally closed at the same time in transgenic mice.

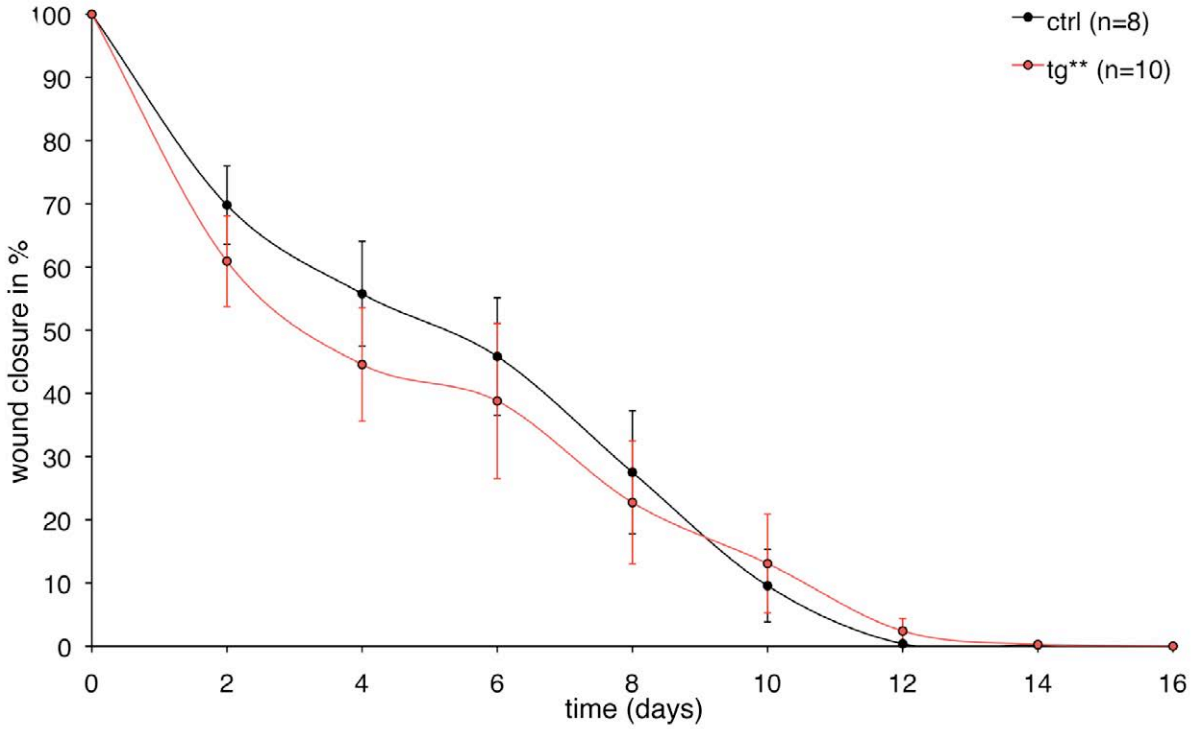

Figure 29: Wound healing kinetics in αENaC skin specific transgenic mice. Control (black) and Tg mice (red). Bars represent the SEM.**

Morphometry of the full-thickness wound healing

Morphometrical analyses of the hyperproliferative epithelium as well as the wound width (figures 30*A* and *B*, respectively) show no statistical difference between the groups in the αENaC skin conditional KO model. The distance between the tips of the wounds is slightly longer in the KO, but did not reach statistical significance (figure 30*C*).

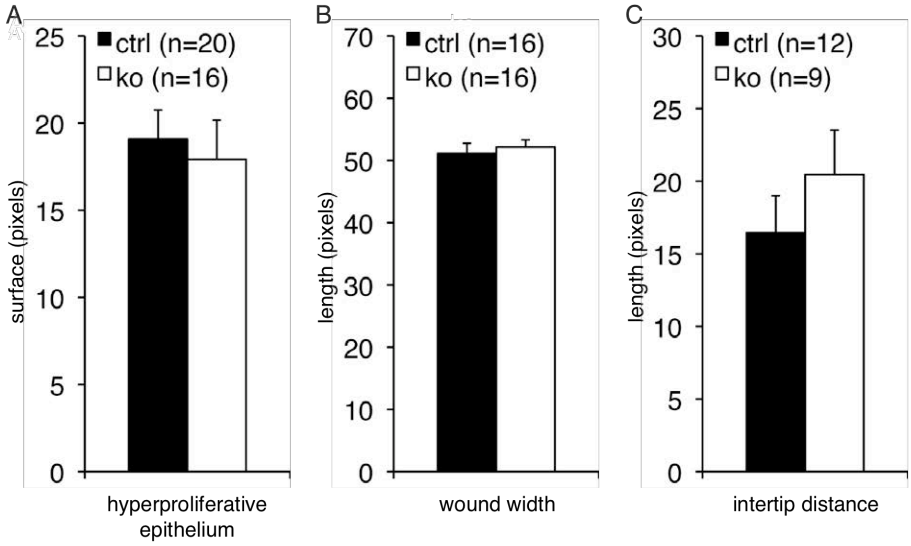

Figure 30: Morphometrical analysis of the skin. *A*, Hyperproliferative epithelium surface quantification. *B*, Wound width. *C*, Distance between the tips of the wound. Control (black column) and αENaC skin conditional KO (white column) mice. Bars represent the SEM.

In the mouse model overexpressing αENaC in the skin, the hyperproliferative epithelium surface and the wound width parameters show only a small difference between transgenic and control (figure 31*A* and *B*, respectively), that is not statistically significant.

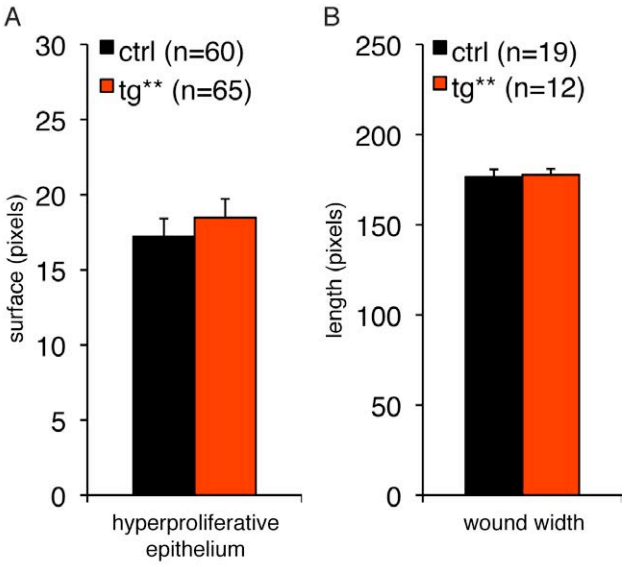

Figure 31: Morphometrical analysis. *A*, Hyperproliferative epithelium surface quantification. *B*, Wound width. Control (black column) and αENaC skin specific TG (red column) mice. Bars represent the SEM.**

All together, theses data indicate that mice lacking the expression of the αENaC gene in the skin present no wound healing defect. Mice overexpressing the αENaC subunit specifically in the skin show slight wound healing acceleration when compared to control mice, but none of these data reached statistical significances.

Corneal and skin defect in 15-month-old αENaC::K14-Cre knockout mice

We found several old (15 months) mice presenting eye abnormalities; indeed, their cornea was opaque (white) and thicker. The skin was scaly. These animals are listed in table I. There were 3 skin-specific αENaC knockout mice out of 17 mice analyzed. Five of these mice were females. All of them presented this phenotype. It is noteworthy, that 2 control mice also had a scaly skin and one animal missed one eye.

Table I. *Phenotypical quantification of more than 1 year old conditional αENaC knockouts*

	ctrl		**ko**	
Phenotype	mice	%	mice	%
Eye lost or whitened and thicker than normal	1/14	7	2/3	66
Thicker and scaly skin	2/14	14	3/3	100

At the histological level, these mice presented thicker corneal and epidermal epithelia (figure 32).

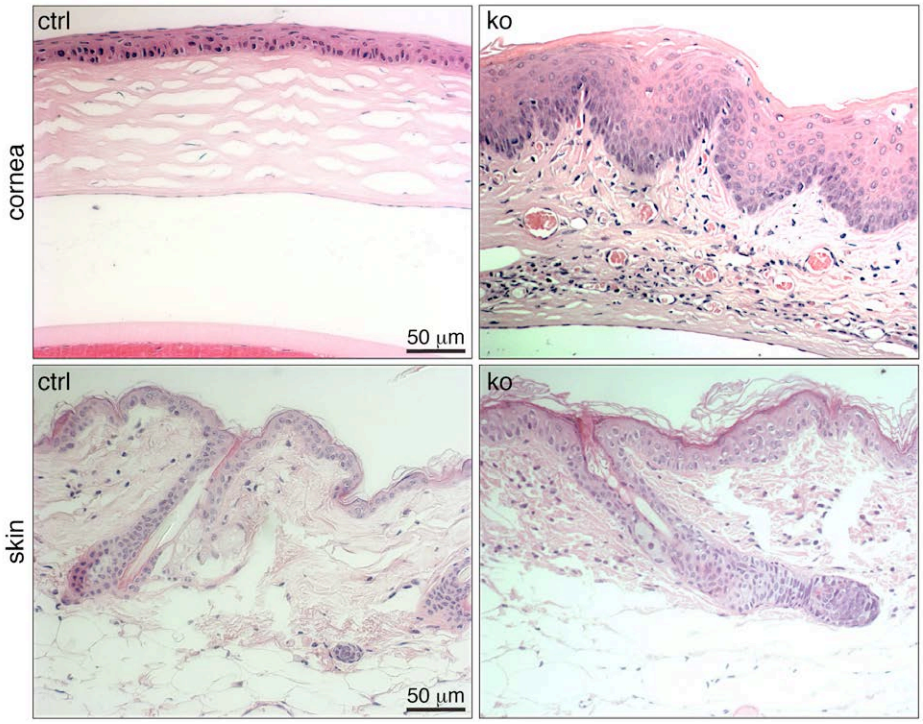

Figure 32: Histology (H&E) of the corneal epithelium (up) and the skin (bottom) of 15 month-old αENaC::K14 control and knockout mice.

DISCUSSION

To study the role of ENaC in wound healing, we used two mouse models: one lacking (skin-specific αENaC knockout mice) and one overexpressing (skin-specific αENaC transgenic mice) the *Scnn1a* gene specifically in the skin. Using these mice, we performed TEWL analysis, wound healing kinetics and morphometric experiments. The αENaC skin conditional knockout mice did not present altered water loss. These data confirmed preliminary experiments from Dr. Roch-Philippe Charles performed during his thesis work (Charles, 2007). In this study, the αENaC skin overexpressing mice were also analyzed and did not display a different TEWL than for the control littermates. However, these mice seem to have a tendency for a retarded wound closure and a less extended hyperproliferative epithelium, which was not significative in comparison with control littermates. The distance between the tips of the wound seemed longer in the knockout mice constant with the slight delay in wound closure observed with these mice. Interestingly, we found a mirrored effect in the αENaC transgenic mice with a slightly accelerated wound healing, at least in the early phase (until day 6 post-wounding), compared to nontransgenic animals. These mice showed a larger hyperproliferative epithelium surface, which was the opposite of knockout mice. Although, in the two models, the wound width measurements did not show any statistical significance between the groups.

It might be possible that in the skin-specific αENaC knockout mice, some residual "wild-type" cells that did not recombine, infiltrated the epidermis during wound closure and rescued the wound. We analysed by qPCR the wounded skin and the skin that recovered the injury completely. It was arduous to obtain a clear result, since the more fibrotic tissue might have rendered the RNA extraction difficult. From our data (not shown), it does not seem that these "wild-type" cells have conquered the knockout skin. This experiment has to be repeated to definitely exclude this possibility.

Our hypothesis was that ENaC might play a role in wound healing, since it is involved in epidermal differentiation and proliferation. As mentioned above, wound healing involves many complex cascades of events including a number of genes and cell types. The fact that only slight effects could be observed with the αENaC knockout model might be due to compensatory effects of other proteins like calcium channels, although we did not investigate this so far. Calcium has an established role in the normal homeostasis of mammalian skin and serves as a modulator in keratinocyte proliferation and differentiation (Lansdown, 2002). Overexpression of αENaC does not significantly affect the wound healing process. A possible reason might be that the overexpression of only one of the three subunits is not sufficient to

induce an increased number of active ENaC channels at the surface of the epidermal cells. An interesting experiment would be to cross these αENaC transgenic mice with the "Liddle" mice that carry a mutation at the βENaC gene locus and that is causative for increased sodium transport as observed in Liddle's syndrome (or pseudoaldosteronism) patients (Pradervand et al., 1999).

We observed that in several 15 month-old αENaC::K14 skin-specific knockout mice, the skin was scaly and the cornea was thicker and not translucent. It is possible that in these epithelia, this channel plays a more critical role with age.

Changes in ion channel expression during development of cancer have been frequently observed (Kunzelmann, 2005). Disturbances in Na^+ absorption have been observed in colonic cancer, and ion channels such as ether a go-go (Eag) or Ca^{2+}-sensitive BK channels have been recognized for their oncogenic potential (Ousingsawat et al., 2008; Koehl et al., 2010). Colonic inflammation like in ulcerative colitis has been shown to reduce electrogenic Na^+ transport and ENaC expression (Amasheh et al., 2004; Barmeyer et al., 2004). Other studies (microarray data) showed that in some cancers, ENaC is overexpressed (Bhoumik et al., 2008; Tripathi et al., 2008). Consequently, ENaC-deficient mice might be protected against cancer development. We have not tested this in our mice.

To conclude, ENaC plays an important role in the keratinocyte differentiation and proliferation, as well as in the skin barrier function of young postnatal mice. But surprisingly, we could not present a clear effect of either the lack or overexpression of ENaC in the healing skin. This does not exclude that ENaC might play a role in this process. Nevertheless, the activity of the channel in the skin is not crucial for the normal physiological response to the injury. The severe skin phenotype (e.g, higher TEWL) observed in the constitutive knockout, might be due to mechanisms secondary to the lung phenotype. Nevertheless, to investigate the precise role of ENaC during wound healing, complementary experiments must be performed. Structural analysis (other morphometrical parameters e.g., the granulation tissue surface (Thorey et al., 2004), or the orientation of keratinocytes in the hyperproliferative epithelium) of the skin of these mice with the help of various markers for differentiation or proliferation might help us to elucidate the role for ENaC in skin wound healing. *In vitro* experiments on primary keratinocytes (cell scrapping or artificial wound healing) may also help us to understand the function of ENaC in wound healing. The pharmacological use of ENaC inhibitors may clarify the role of ENaC in these processes.

<u>Part II:</u> Phenotypic analysis of mice deficient for the glucocorticoid-induced leucine zipper GILZ

INTRODUCTION

The glucocorticoids

Glucocorticoid effects and mechanism of action

Glucocorticoids (GC) are a class of steroid hormones that bind to the glucocorticoid receptor (GR), which is present in almost every vertebrate animal cell. Cortisol (or hydrocortisone) is the most important human GC. In the mouse, it is mainly corticosterone that is effective. These hormones are essential for life, and they regulate or support a variety of important cardiovascular, metabolic, immunologic, and homeostatic functions.

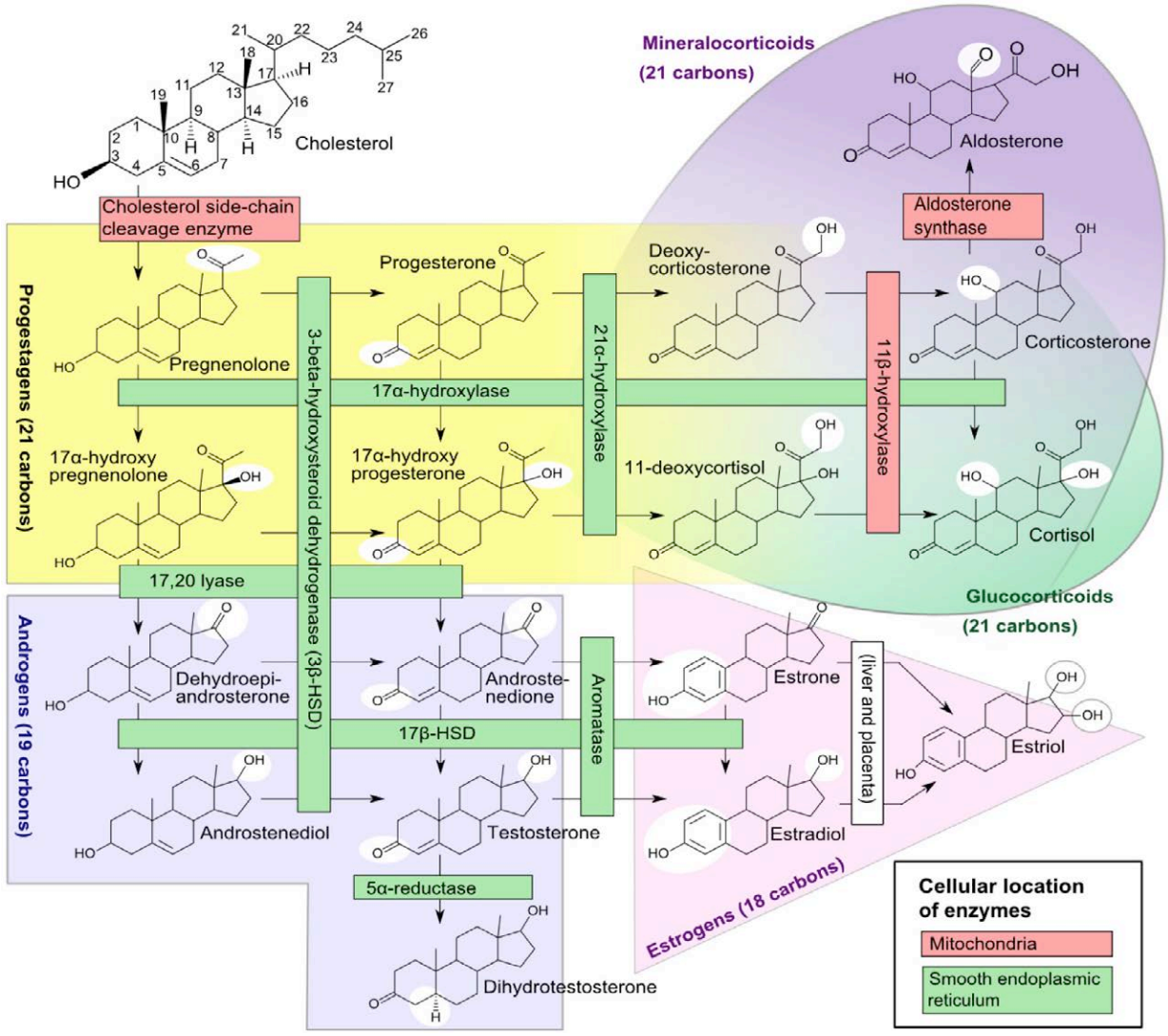

Figure 33: Steroidogenesis (credits : Mikael Häggström; www.wikipedia.org).

The name glucocorticoid (glucose + cortex + steroid) derives from their role in the regulation of the metabolism of glucose, their synthesis in the adrenal cortex, and their steroidal structure. GCs are distinguished from mineralocorticoids and sex steroids by their specific receptors, target cells, and effects. The precursor of all steroids is cholesterol and can be enzymatically processed to produce protestagens, androgens, estrogens, mineralocorticoids or glucocorticoids (figure 33). In technical terms, "corticosteroid" refers to both glucocorticoids and mineralocorticoids (as both are mimics of hormones produced by the adrenal cortex), but is often used as a synonym for *glucocorticoid* (figure 34)

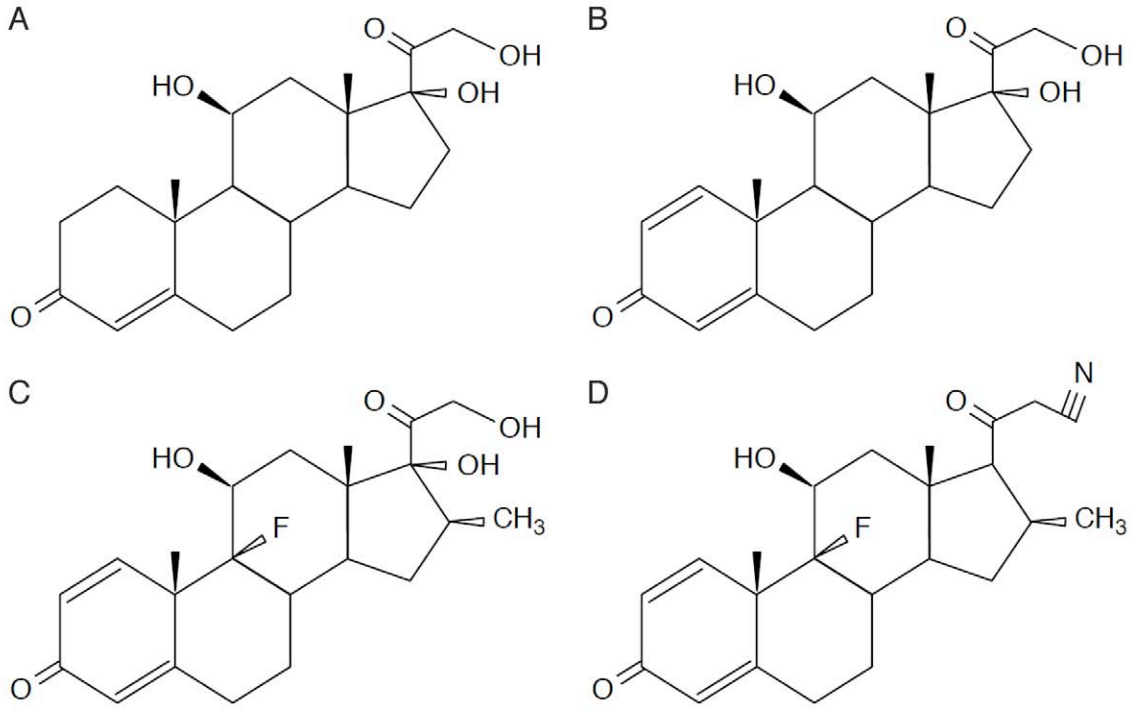

Figure 34: Chemical structures of (*A*) cortisol, (*B*) prednisolone, (*C*) dexamethasone and (*D*) RU24858 are shown. Cortisol is the major endogenous anti-inflammatory GC, whereas the others are synthetic. Prednisolone is widely used in the treatment of inflammation; dexamethasone is often used experimentally to investigate GC function; and RU24858 is a representative dissociated GC, which transactivates GRE-dependent reporters relatively poorly but transrepresses NFκB- and AP1-dependent reporters relatively efficiently (in specific cell lines), and exerts antiinflammatory effects *in vivo* (Clark and Lasa, 2003).

GCs are part of the feedback mechanism in the immune system that turns inflammation down (figure 35). They have many diverse (pleiotropic) effects, including potentially harmful side effects. They are therefore used in medicine to treat diseases that are caused by an overactive immune system, such as allergies, asthma, autoimmune diseases and sepsis. They also interfere with some of the abnormal mechanisms in cancer cells, so they are used in high doses to treat cancer (Pui et al., 2004).

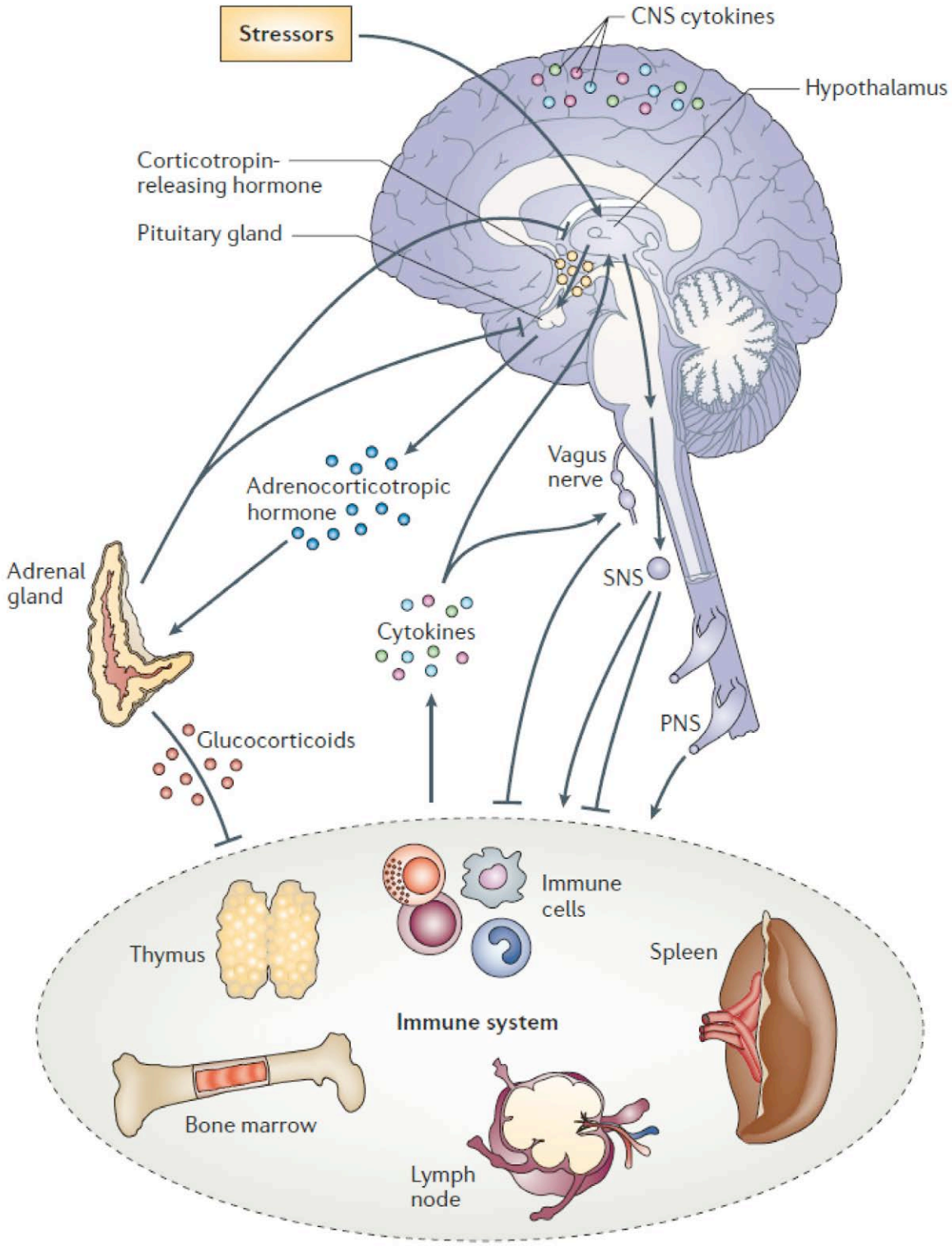

Figure 35: Schematic illustration of connections between the nervous and immune systems. Signalling between the immune system and the central nervous system (CNS) through systemic routes, the vagus nerve, the hypothalamic–pituitary–adrenal (HPA) axis, the sympathetic nervous system (SNS) and the peripheral nervous system (PNS) are shown (Sternberg, 2006).

GCs cause their effects by binding to the GR, a member of the nuclear receptor family of ligand-dependent transcription factors. GR is present in the cells of almost all vertebrate tissues. Like other members of this family, GR possesses a modular structure consisting of

three major domains: an N-terminal, a central DNA binding domain, and a C-terminal ligand binding domain (Beato et al., 1995). The activated GR complex in turn up-regulates the expression of anti-inflammatory proteins in the nucleus (a process known as transactivation) and represses the expression of pro-inflammatory proteins in the cytosol by preventing the translocation of other transcription factors from the cytosol into the nucleus (transrepression; figure 36). The antagonist RU-486 (mifepristone) can inhibit the effects of the GR. This compound, in combination with a prostaglandin analogue, was used as abortifacient in the late 1980s (McKinley et al., 1993). This was also used to treat Cushing's syndrome, also known as hyperadrenocorticism (Johanssen and Allolio, 2007).

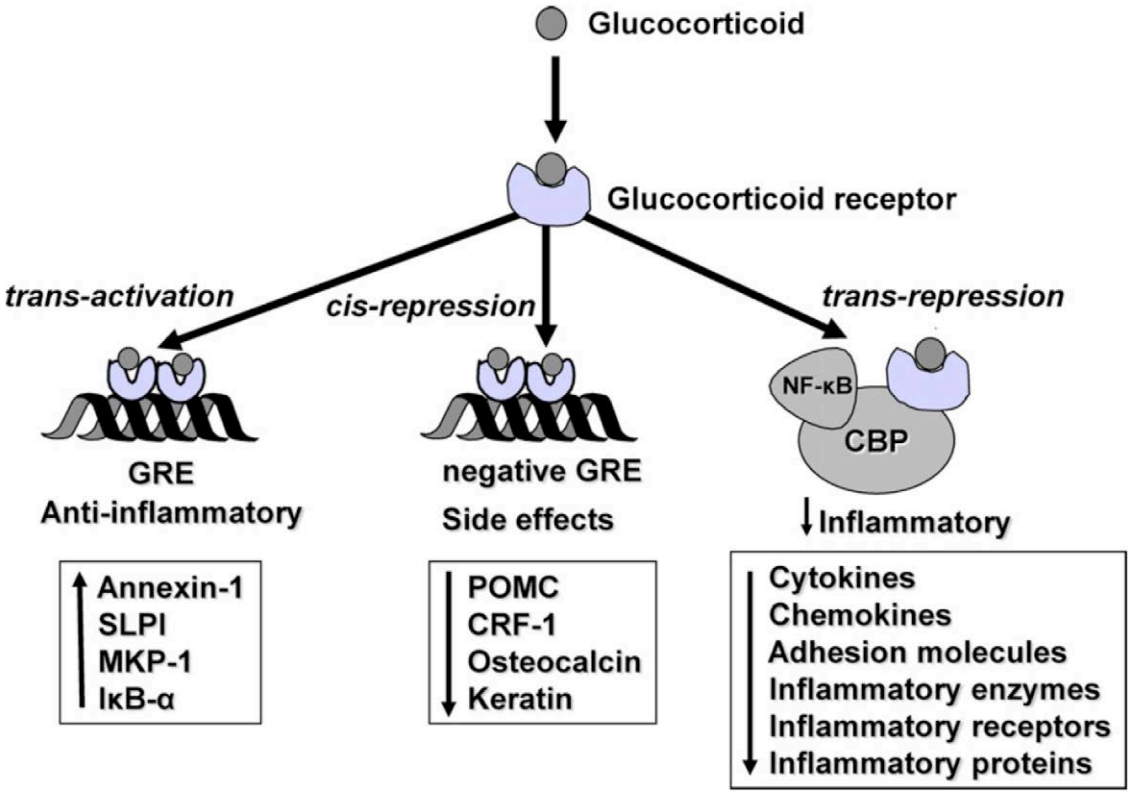

Figure 36: Glucocorticoids regulate gene expression in several ways. Glucocorticoids enter the cell to bind to glucocorticoid receptors (GR) in the cytoplasm that translocate to the nucleus. GR homodimers bind to glucocorticoid-response elements (GRE) in the promoter region of steroid-sensitive genes, which may encode anti-inflammatory proteins. Less commonly, GR homodimers interact with negative GREs to suppress genes. Nuclear GR also interact with coactivator molecules, such as CREB-binding protein (CBP), which is activated by proinflammatory transcription factors, such as nuclear factor-κB (NF-κB), thus switching off the inflammatory genes that are activated by these transcription factors. Other abbreviations: SLPI: secretory leukoprotease inhibitor; MKP-1: mitogen-activated kinase phosphatase-1; IκB-α: inhibitor of NFκB; POMC: proopiomelanocortin; CRH: corticotrophin releasing factor (Barnes, 2010).

Various synthetic GCs are available (e.g. dexamethasone); these are used either as replacement therapy in glucocorticoid deficiency or to suppress the immune system (figure 37).

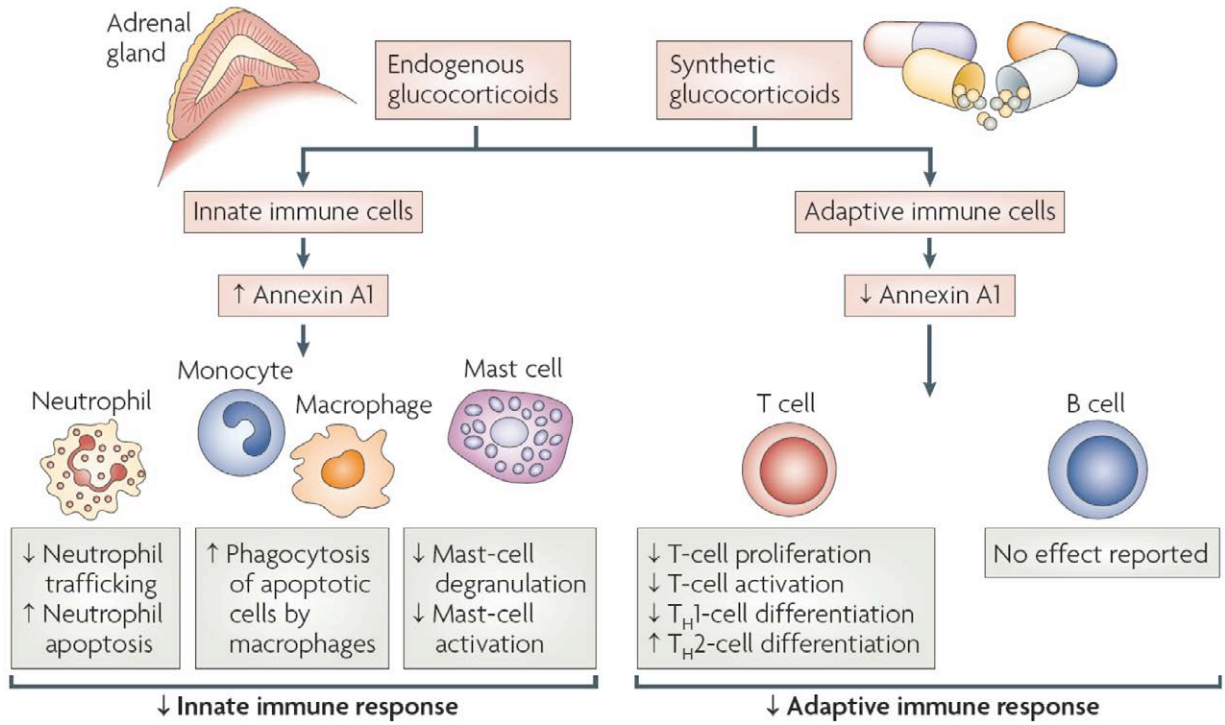

Figure 37: Model of glucocorticoid modulation of the annexin A1 pathway in immune regulation. Endogenous and synthetic glucocorticoids can control innate and adaptive immune responses by modulating the expression and release of annexin A1. Exposure of innate immune cells, such as neutrophils, monocytes, macrophages and mast cells, to glucocorticoids induces the release of annexin A1. This, in turn, acts in a paracrine or autocrine manner to maintain the level (and duration) of cell activation. In a dynamic system such as the inflammatory reaction, in which spatial and temporal factors can influence the final outcome, this could promote the resolution of the inflammatory reaction by actively maintaining homeostatic control of innate immune cells (Perretti and D'Acquisto, 2009).

The circadian clock: regulation and effects

Daily oscillation of physiological and behavioural processes in animals and plants has been reported since the fourth century BC. But it is only from the middle of the last century that the biology of the circadian clock started to be investigated (Pittendrigh, 1954). The first circadian gene, *Period*, was cloned from the fruitflies (Bargiello et al., 1984; Reddy et al., 1984). Circadian rhythms regulate hundreds of functions in the human body, including sleep and wakefulness, body temperature, blood pressure, hormone production, digestive secretion and immune activity (figure 38). Disruption of these rhythms can have a profound influence on health (Fu and Lee, 2003).

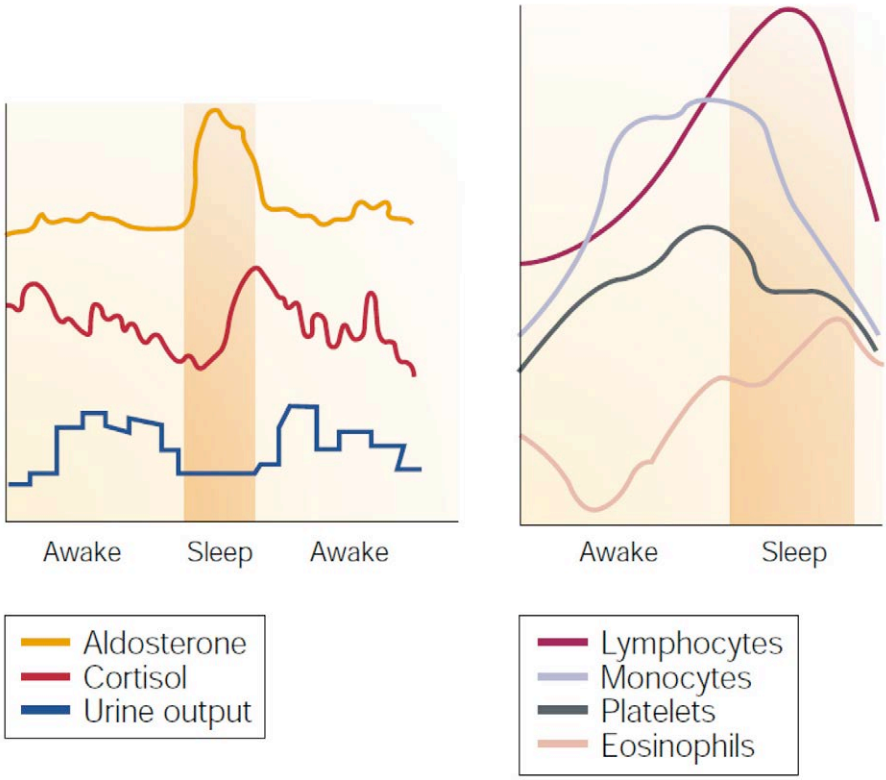

Figure 38: Circadian regulation of hormones, urine and the immune system. The circadian oscillation of hundreds of biological processes enables a human body to adapt to 24-hour light/dark cycles. The serum levels of cortisol and aldosterone, and urine volume, oscillate in circadian cycles in humans. The cortisol level peaks in healthy individuals at early morning and reach their lowest levels before bedtime. Disruption of cortisol circadian rhythm can result in fatigue and restlessness, weight loss, insomnia and coronary heart disease. Aldosterone is a steroid hormone that is secreted by the cortex of the adrenal gland and regulates the body's electrolyte balance. The level of aldosterone is normally low during the day and high during sleep in humans. Disruption of aldosterone rhythms result in sodium and water retention, increased blood pressure and coronary heart disease. Urine volumes have inverted circadian oscillating patterns, compared to that of aldosterone, in healthy humans (left panel). The circadian oscillation of lymphocyte, monocyte, platelet and eosinophil levels in healthy young adults. The activity of the immune system, usually represented by the number of lymphocytes, peaks in the late evening and is lowest in the early morning. Disruption in this circadian rhythm could lead to immune suppression (right panel) (Fu and Lee, 2003).

Several other circadian genes have been discovered. From a molecular standpoint, circadian rhythms are regulated by transcriptional and post-translational feedback loops generated by a set of interplaying clock proteins (figures 39-41).

Circadian clocks are present in almost all mammalian tissues. The master or central clock is located in the hypothalamic suprachiasmatic nucleus (SCN), a small brain region containing 10,000–15,000 neurons. The SCN clock can function autonomously, without any external input, but it can be reset by environmental cues such as light. Clocks outside the SCN are referred to as peripheral clocks and are thought to be synchronized by the master clock to ensure temporally coordinated physiology. The synchronization mechanisms implicate various humoral signals, including circulating entraining factors such as glucocorticoids. Moreover, peripheral clocks, such as the liver, can be synchronized by the availability of metabolites or feeding time. Peripheral clocks are present in almost all mammalian tissues, such as the liver, heart, lungs and kidneys, where they maintain circadian rhythms and modulate transcription

factors in a paracrine fashion to regulate tissue-specific gene expression (Sahar and Sassone-Corsi, 2009).

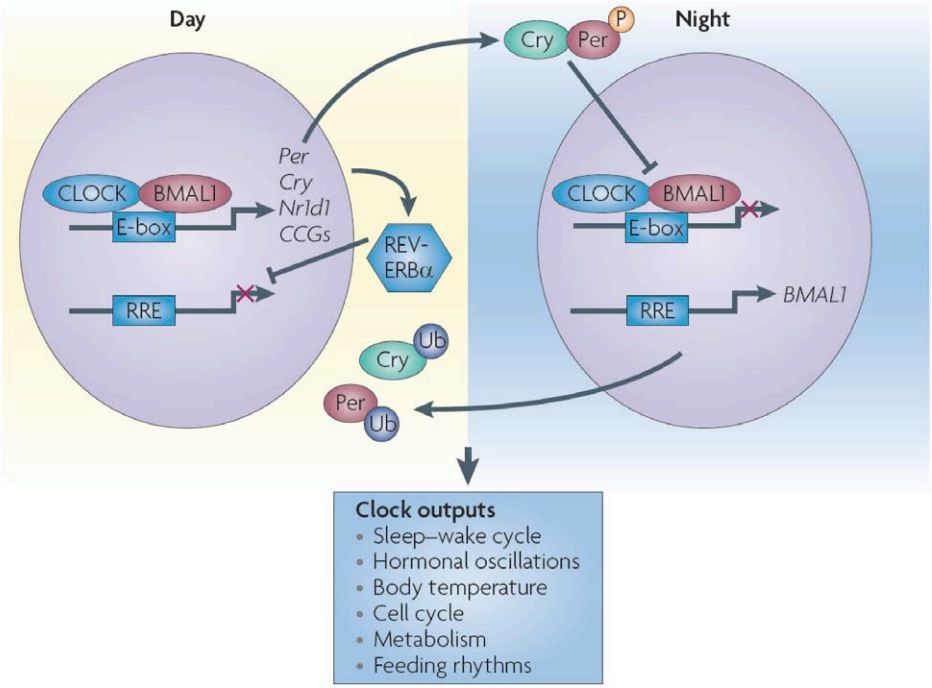

Figure 39: The circadian feedback loop. CLOCK and BMAL1 increase the transcription of Period (Per), Cryptochrome (Cry) and other clock-controlled genes (CCGs) during the day. In the classic view, the levels of Per and Cry proteins increase during the night, after which they dimerize and translocate to the nucleus to repress CLOCK–BMAL1-mediated transcription. Per and Cry proteins are then ubiquitylated and degraded to initiate a new circadian cycle. Conversely, REV-ERBα (encoded by *Nr1d1*) protein levels are high during the day and inhibit *Bmal1* transcription at this time. At night, REV-ERBα protein levels are low, allowing *Bmal1* transcription to take place. P, phosphorylation; RRE, REV-ERB/ROR response elements; Ub, ubiquitylation (Sahar and Sassone-Corsi, 2009).

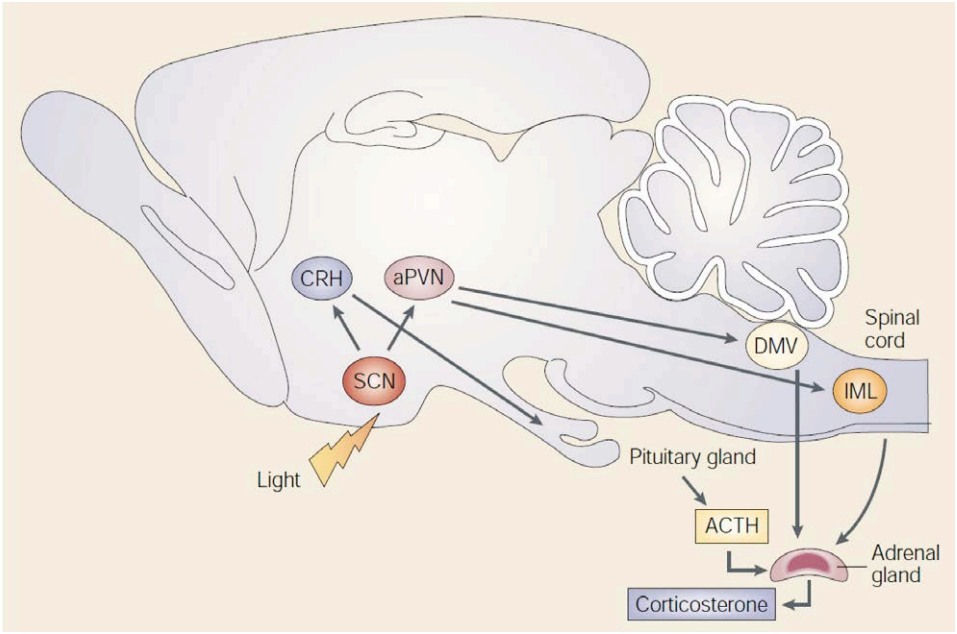

Figure 40: The suprachiasmatic nucleus (SCN) controls the activity of the autonomic nervous system through the autonomic neurons of the paraventricular nucleus (aPVN). These neurons project from the hypothalamus to preganglionic parasympathetic and sympathetic neurons in brainstem nuclei, such as the dorsal motor nucleus of the vagus (DMV) and in the intermediolateral cell columns (IML) of the spinal cord44. The SCN indirectly controls the secretion of adrenocorticotropic hormone (ACTH) from the pituitary gland, through the CRH-producing endocrine neurons in the hypothalamus. Circadian variations in the activity of the autonomic nervous system and in ACTH production result in rhythmic release of corticosterone from the adrenal gland into the blood. So, plasma levels of corticosterone undergo a 24h circadian variation *in vivo* (Fu and Lee, 2003).

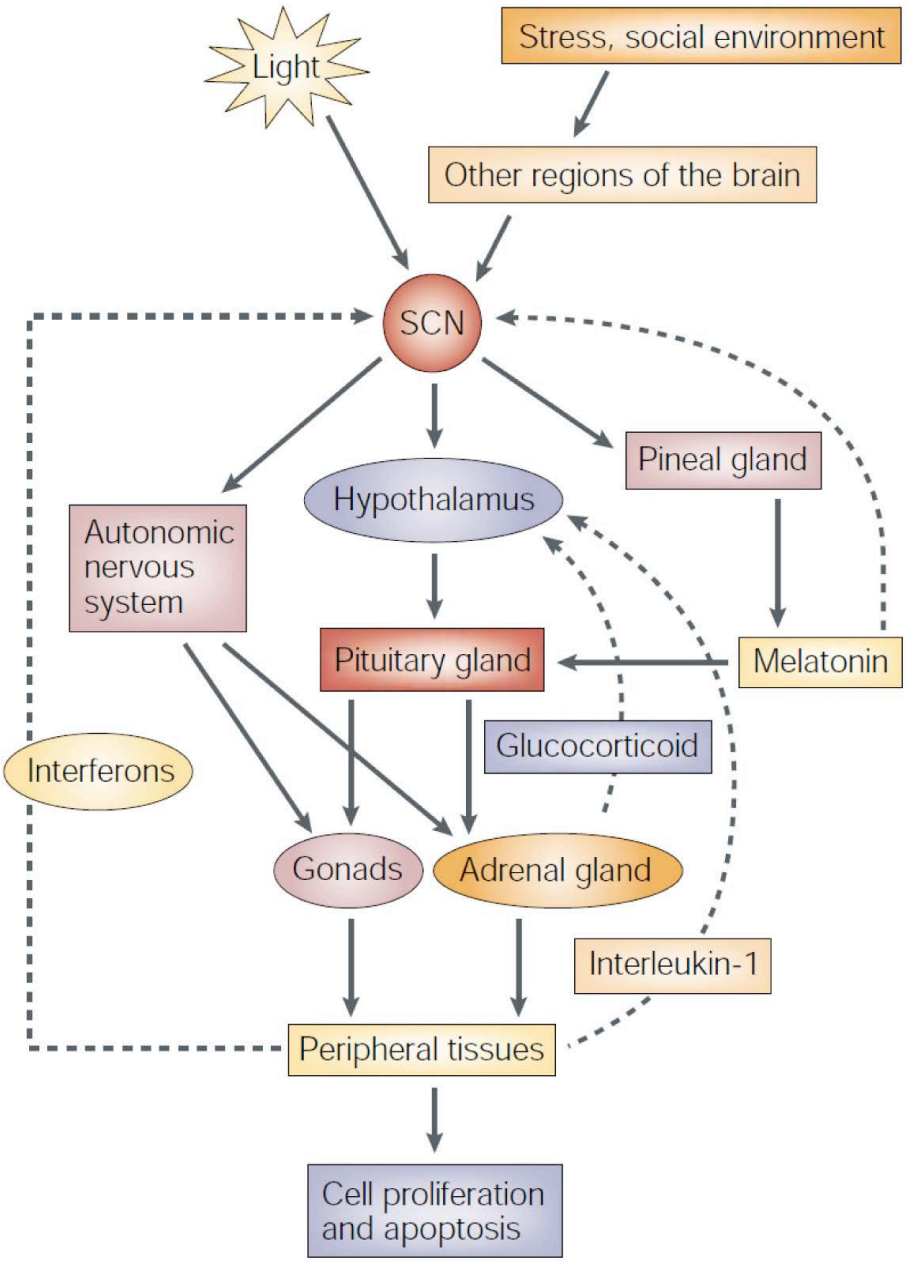

Figure 41: The circadian clock controls cell proliferation and apoptosis at the systemic level. Light and other environmental cues reach the suprachiasmatic nuclei (SCN) through various input pathways. The SCN clock synchronizes with the environment to generate endogenous rhythms, which are transmitted through output pathways to peripheral tissues. Representative output pathways, such as the autonomic nervous system (ANS), the hypothalamic–pituitary–gonadal (HPG) and the hypothalamic–pituitary–adrenal (HPA) axes, are shown. The pineal gland and peripheral tissues can also feed back to SCN or HPA axes, through production of melatonin, to regulate homeostasis. Melatonin binds to receptors on SCN neurons to induce phase shifts. The adrenal glands produce glucocorticoids, which have negative feedback on the hypothalamus to terminate the release of corticotropin-releasing hormone. The products of immune activity, such as interferon-α and -γ, and interleukin-1, can also modulate the activity of SCN, as well as the HPA axis. Feedback pathways are indicated by dashed lines (Fu and Lee, 2003).

The secretion of corticosterone follows the circadian criteria. There is a peak at the onset of the activity phase in human and rodents (figure 42*A*). Experiments performed on mice showed that this oscillation can be attenuated by chronic administration of alcohol (Kakihana and Moore, 1976). Figure 42*B* shows that by knocking down the central circadian machinery, as in *clock* mutant mice, the wave is shifted but not flattened (Oishi et al., 2006).

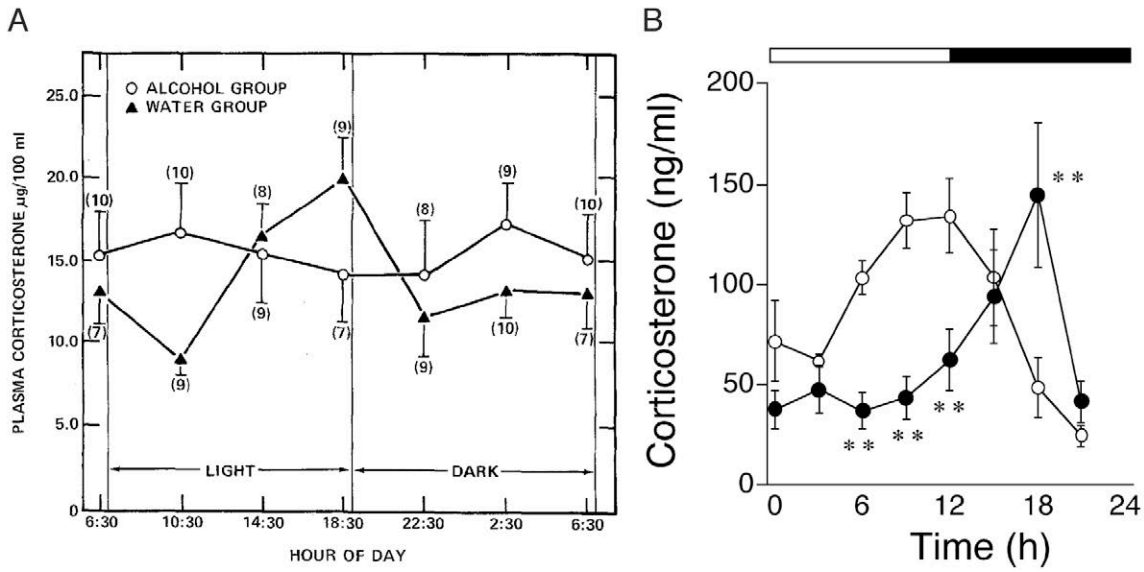

Figure 42: Circadian plasma corticosterone secretion in mouse. *A*, Circadian variations of the plasma corticosterone in the chronically alcohol consuming DBA/2J male mice. Blood samples were collected after 15 weeks of alcohol consumption, 3.8 ~ (w/v) during the first week and 7.5 ~ for the next 14 weeks. Numbers in parentheses represent number of mice assayed for each time point. Vertical bars indicate SEM (Kakihana and Moore, 1976). *B*, Circadian variations in plasma corticosterone levels in *Clock* mutant mice. Open and filled circles indicate values from wild-type and *Clock* mutant mice, respectively. Open and solid bars represent lights on and off, respectively. Values represent means ± SEM (n = 4). Significant differences between genotypes are shown as **$P < 0.01$ (Oishi et al., 2006).

The glucocorticoid-induced leucine zipper (GILZ)

GILZ cloning and role in T-cells

The glucocorticoid-induced leucine zipper (GILZ) was originally described in as a gene induced by dexamethasone (DEX), a glucocorticoid receptor agonist, from a mouse thymocyte subtraction cDNA library (D'Adamio et al., 1997). It is expressed in various tissues and is rapidly induced by glucocorticoids in T lymphocytes, in which it inhibits anti-CD3-induced IL-2 production, IL-2-receptor expression, Fas and Fas-ligand up-regulation, and cell death consequent to CD3-induced activation (Riccardi et al., 2000; Ayroldi et al., 2001; Smit et al., 2005).

In cells of the myeloid lineage, a higher basal expression of GILZ was observed, and both GCs and anti-inflammatory cytokines, such as IL-10, increased this expression (Cannarile et al., 2001; Berrebi et al., 2003). Microarray experiments also demonstrated GILZ induction by GCs in human peripheral blood mononuclear cells and in acute lymphoblastic leukemia cells undergoing GC-induced apoptosis (Tonko et al., 2001; Galon et al., 2002). Direct inhibition of transcription through binding of GILZ to AP-1 or NFκB was suggested to block expression of Fas ligand, IL-2 and various markers of macrophage activation (Ayroldi et al., 2001; Mittelstadt and Ashwell, 2001; Berrebi et al., 2003). GILZ also inhibited ERK signaling by

sequestering the MAPKkinase-kinase Raf (Ayroldi et al., 2002), a mechanism that is presumably selective for the ERK pathway, as Raf does not activate JNK or p38. Raf has been shown to form a cytoplasmic complex with GR; however, the relationship of GILZ to this complex is not known (Widen et al., 2000).

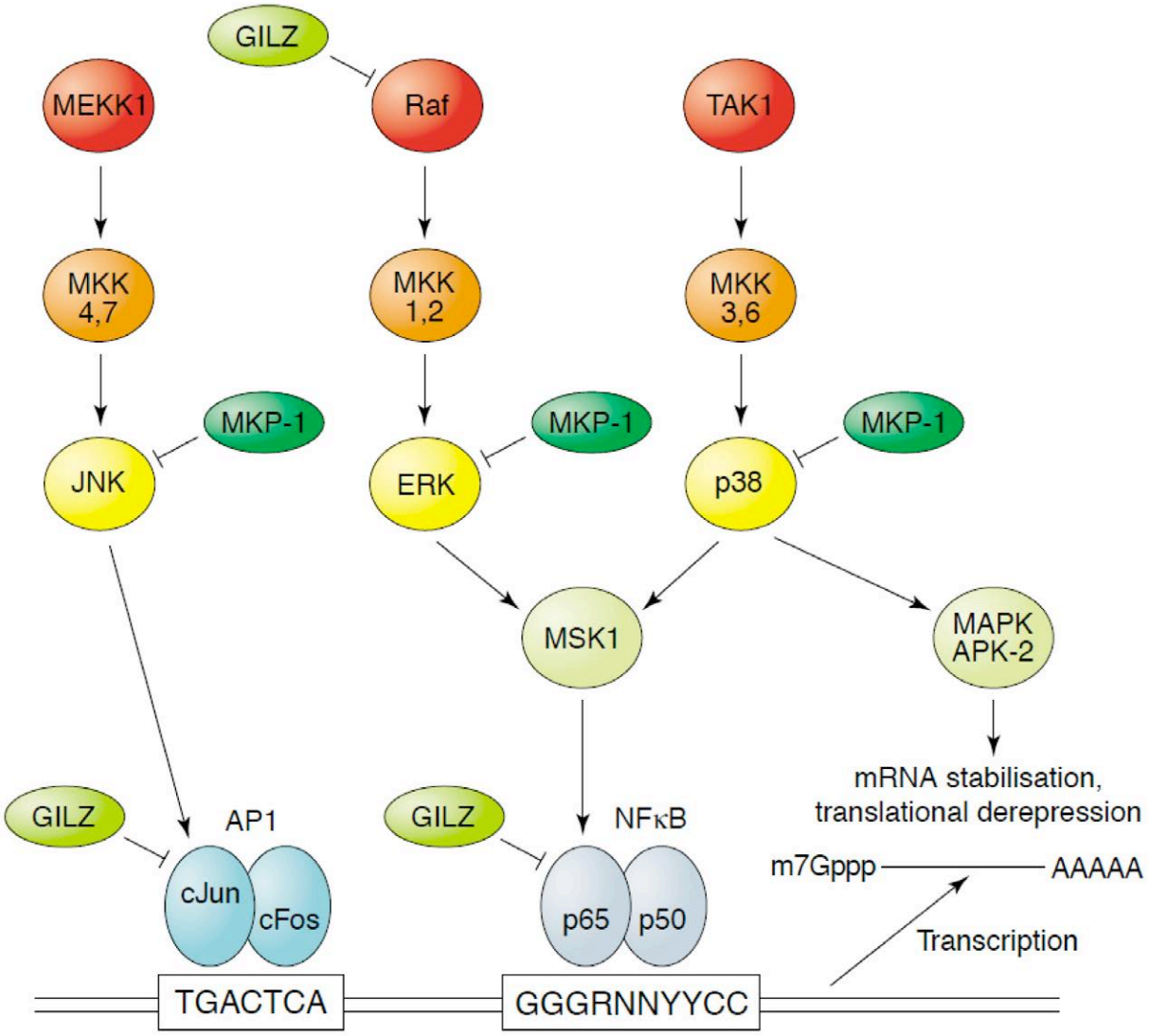

Figure 43: Activation of gene expression by MAPKs, and its inhibition by GILZ or MKP-1. This is an incomplete 'circuit diagram', which omits a number of important signalling molecules of the MAPK cascades. The expression of GILZ and MKP-1 is induced by GCs. MKP-1 dephosphorylates and inactivates the MAPKs JNK, p38 and (under some circumstances) ERK. GILZ acts by sequestering Raf and inhibiting the Raf–MKK1/2–ERK pathway, or by directly interfering with the function of the transcription factors AP-1 and NFκB. MEKK1, MAPK or ERK kinase 1; TAK1, transforming growth factor b-activated kinase-1 (Clark and Lasa, 2003).

GILZ as member of the TSC-22/DIP/BUN family

GILZ is a member of the leucine zipper protein (Ayroldi et al., 2002) and belongs to the TGF-β-stimulated clone-22 (TSC-22) family of transcription factors (figure 44). This family of

leucine zipper proteins lacks the typical canonical DNA-binding domain and has a low molecular weight. GILZ shares between 60-90% identity to the other members of this family at the protein level. A PDZ-binding domain is present at the C-terminus of some members (figure 45).

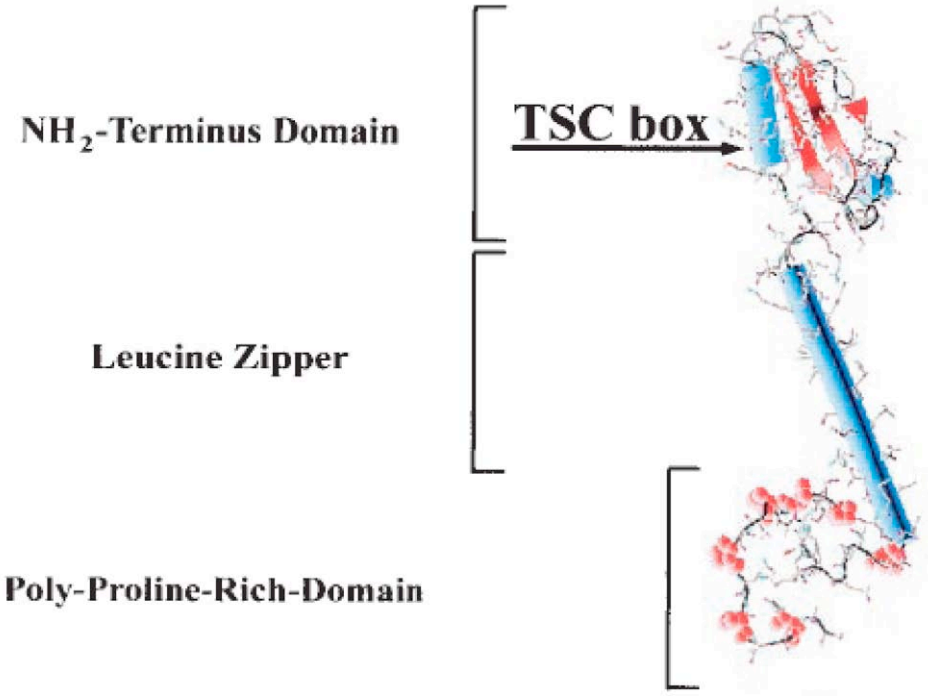

Figure 44: 3D model of the human GILZ. α-Helices are represented as blue cylinders, β-sheet as red ribbons, and proline residues are indicated in red CPK (Ayroldi et al., 2002).

DIP (DSIP immunoreactive protein) shows 95% homology to GILZ from human to mouse and was first isolated from porcine brain (Sillard et al., 1993) and later on from human fetal brain (hDIP) (Vogel et al., 1996). The protein misses a large N-terminal part as compared to other family members and is only 77 amino-acids long. When aligning human DIP against human GILZ protein sequences, the proteins shows 100% homology (nucleotide alignments show 99.1% homology, divergences might be due to sequencing errors and DIP and GILZ might be splice-variants of a same gene). An interesting point about this protein is that its three-dimensional structure has been studied (Seidel et al., 1997). Its high homology to GILZ lets us suppose, that its tertiary structure could in a major extent serve as model for the GILZ tertiary structure within the conserved domains. Biological function of DIP is not yet known.

SHS (shortsighted), alias BUN (bunched), protein was identified in *Drosophila*, where it acts in the pathway leading to photoreceptor differentiation (Treisman et al., 1995). This protein is

longer than the other members of the superfamily with its 224 amino-acids and has, such as TSC22, no PDZ-binding domain.

Osmotic stress transcription factor 1 (OSTF1) was cloned from gills of euryhyaline tilapia (*Oreochromis mossambicus*) as a gene induced by acute hyperosmotic stress (Fiol et al., 2007). OSTF1 is part of the TSC22 family (figure 46).

GILZ was also found in chicken pituitary, Ellestad *et al*. performed sequence alignment and unrooted phylogenetic tree (figure 47).

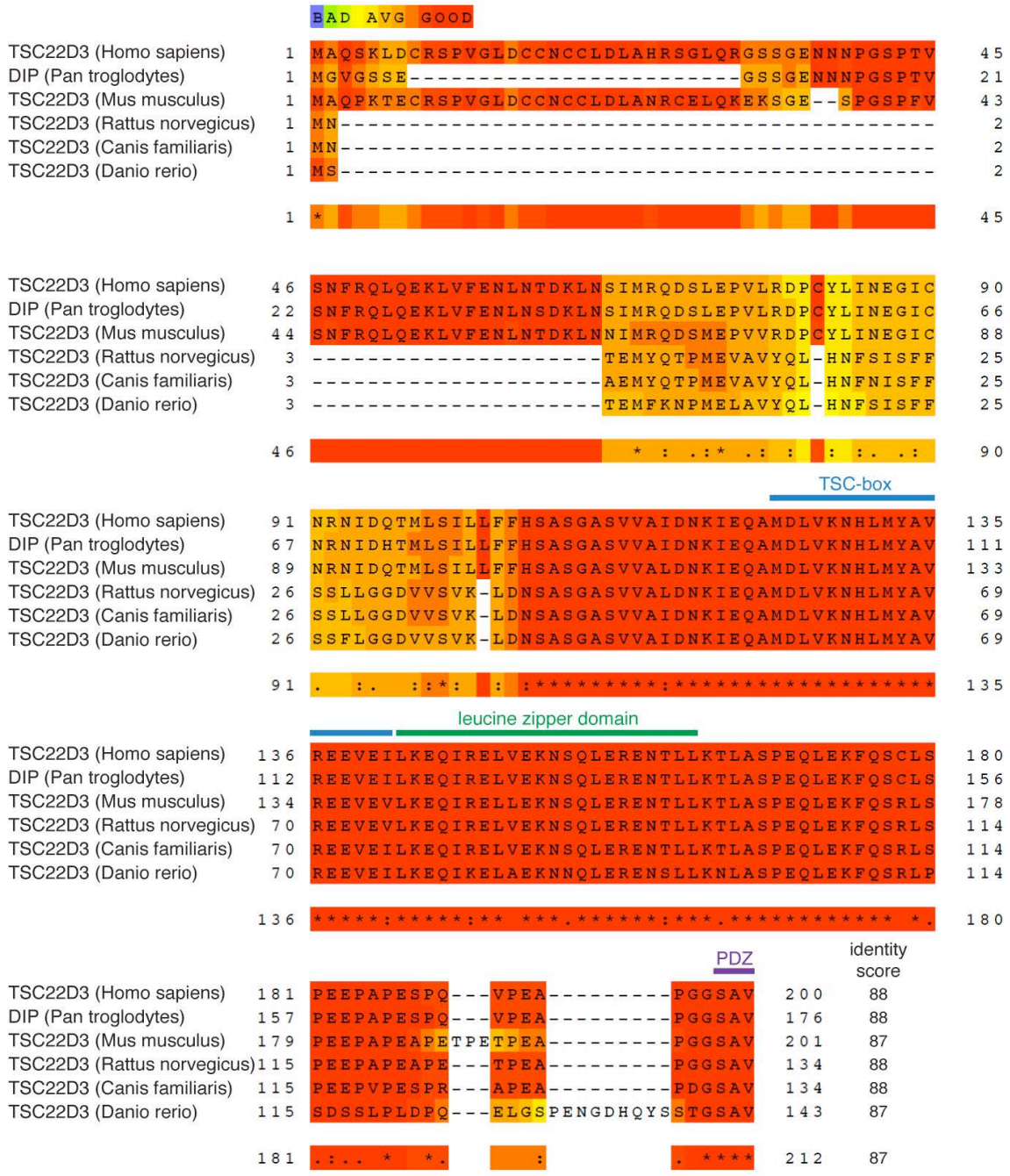

Figure 45: Amino acid sequence alignment of TSC22D3 and DIP orthologs. Human, monkey (DIP), mouse, rat, dog and fish TSC22D3 protein sequences were aligned using the T-Coffee multiple sequence alignment program (http://www.tcoffee.org). Color code for the identity score between residues (top). The conserved domains are indicated: the TSC-box (blue line), the leucine zipper domain (green line) and the PDZ (purple line). The identity score is given (bottom right).

TSC22 is the first isolated and the most studied member of the superfamily. It was isolated in 1992 from TGFβ-treated mouse osteoblastic cells (MC3T3 cells) (Shibanuma et al., 1992). The human homologue was cloned from embryo and shown to have a widespread expression in adult and fetal tissue, which is in concordance with the large number of hormonal factors able to induce TSC22 gene. One probable function of TSC22 is the transcriptional regulation of the C-type natriuretic peptide (CNP) gene and the transmission of signals from cytokines to CNP gene expression (Ohta et al., 1996). Further results suggest that TSC22 may be a negative regulator of proliferation and have tumor suppressor activity (Kester et al., 1997). Given its apparent role as regulatory gene for cell growth, differentiation and apoptosis, TSC22 was proposed to be a good target for diagnosis and therapy of different cancers (Uchida et al., 2000).

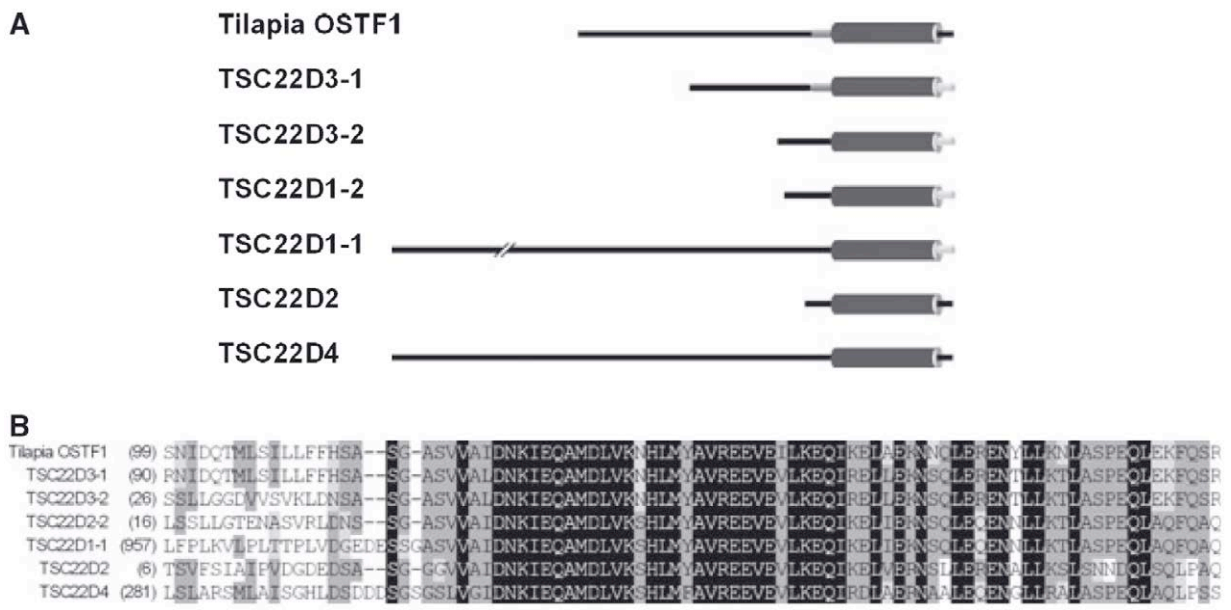

Figure 46: Schematic structure (*A*) and multiple sequence alignment of the TSC22D motif (*B*) of tilapia osmotic stress transcription factor 1 (OSTF1) and mouse TSC22D family members identified by a genome-wide search. Large gray cylinders correspond to the conserved TSC22/leucine zipper motif. Smaller white cylinders represent local regions of high homology. Residues shaded in darker tones correspond to higher level of homology in the alignment (Fiol et al., 2007).

The leucine zipper domain

Leucine zippers contain leucine-rich repeats, all of which appear to be involved in protein-protein interaction (Kobe and Deisenhofer, 1995; Kajava and Kobe, 2002). They are made of coiled coils, which are structures formed by repetition of 7 residues. The amino acid chain forms an α-helix and the coiled coil is formed by mutual winding of these helixes around one another (O'Shea et al., 1989; Lupas, 1996). An important feature for these structures are the

hydrophobic interactions between residues located in the center of the helixes, which are leucines in the case of leucine zippers.

Most identified leucine zippers are implicated in transcriptional mechanisms, however those proteins interact with DNA via a basic DNA binding domain, which is not present in this subfamily, whereas the leucine zipper motif is involved in protein-protein interactions (Moll et al., 2000). Several cytoplasmic membrane or membrane-bound proteins have been reported to contain leucine zipper structures. Examples are postsynaptic density (PSD - defined by an electron dense structure of postsynaptic sites) proteins, such as PSD-Zip45, in which leucine zippers are considered to be one of the common domains, with major importance for multimerization (Sun et al., 1998). Rapsyn is a leucine zipper protein of the neuromuscular PSD and is involved in acetylcholine receptor clustering (AchR). Deletion mutants that lack this motif still interact with the membrane and form clusters of rapsyn itself, but are unable to involve in the AchR clustering (Phillips et al., 1991). A dual leucine zipper bearing kinase (DLK) was reported from synaptic terminals where it was associated with both plasma membrane and cytosolic fractions (Mata et al., 1996). As an example of membrane proteins, a leucine zipper motif was identified in the C-terminus of hSK4, a calcium-activated potassium channel (Joiner et al., 1997). Consistent with these reports leucine zipper proteins seem to be involved in various molecular interactions within nuclear, cytosolic or membrane locations.

As already mentioned, the DIP protein three-dimensional structure was extensively studied (Seidel et al., 1997). The synthetic protein (peptide 9-46) was shown to form dimers through helical structures in the leucine zipper motif. Homodimer formation depending on the coiled coil domain was reported for TSC-22, as well as heterodimerization with a close homologue, the TSC-22 homologous gene-1 (THG-1) (Kester et al., 1999). In this study a yeast two-hybrid screen on a mouse brain cDNA library was performed, using amino acids 38-144 as a bait. The only leucine zipper protein found in the screen was the THG-1, indicating probable high specificity of these interactions, in spite of the well-conserved helical structure. The domain conferring high specificity was not determined and could be located within the leucine zipper domain or in the family signature conserved domain or even in a C-terminal part (containing proline-rich domains).

Given high homology of the leucine zipper of GILZ with the mentioned other members of the subfamily, it is possible that GILZ is implicated in protein-protein interactions with close homologs through its coiled coil structure.

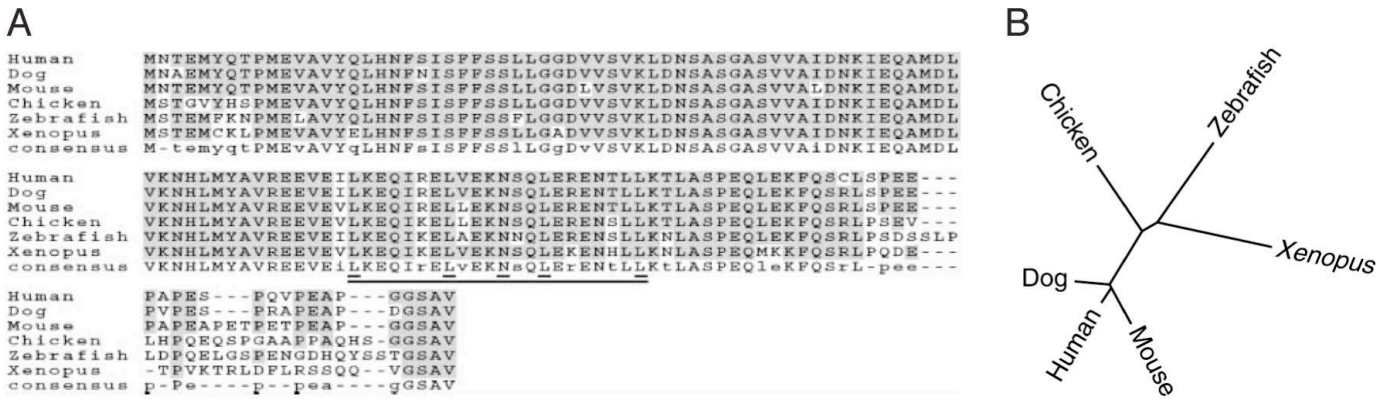

Figure 47: Chicken glucocorticoid-induced leucine zipper (GILZ) is highly homologous with GILZ from other vertebrate species. (*A*) Predicted amino acid sequence for chicken, human, dog, mouse, zebrafish, and Xenopus GILZ were aligned, and the regions of amino acid sequence that are identical with the consensus derived from all species are shaded. The leucine zipper region (black underline) is characterized by four leucine residues at positions 76, 83, 90, and 97 and one asparagine at position 87 (double underlines). (*B*) Unrooted phylogenetic tree of GILZ amino acid sequences from the species listed in (*A*). The length of the lines connecting the species indicates the predicted evolutionary distance (Ellestad et al., 2009).

The PDZ-binding domain

Interactions between PDZ proteins and their targets are known to mediate protein localization, signalling and maintenance of membrane characteristics, mainly by assembling various function entities, including ion channels and other transmembrane receptors, at specialized subcellular sites such as epithelial cell tight junctions, neuromuscular junctions, and PSDs of neurons (Fuh et al., 2000). PDZ domains, originally described as conserved elements in the 95-kDa post-synaptic density protein (PSD-95), the *Drosophila* tumor suppressor discs-large (DLG), and the tight junction protein zonula occludens-1 (ZO-1) (Muller et al., 1995; Craven and Bredt, 1998; Hata et al., 1998), have been observed in a large and diverse set of proteins. They are also named DLG homology region (DHG) and GLGF repeats which is the sequence motif contained in PDZ proteins. The structures reveal that a four-residue C-terminal stretch (X-Thr/Ser-X-Val-COOH or Phe/Tyr-X-Phe/Val/Ala-COOH) engages the PDZ type I and II domains through antiparallel main chain interactions with a β sheet of the domain. Recognition of the terminal carboxylate group of the peptide is conferred by main chain amides provided by the Gly-Leu-Gly-Phe loop as well as by an arginine side chain. Specific side chain interactions and a prominent hydrophobic pocket explain the selective recognition of the C-terminal consensus sequence (Doyle et al., 1996; Fuh et al., 2000). A third type of PDZ domain-ligand interaction involves the recognition of an internal peptide sequence (Fuh et al., 2000).

Events mediated by interactions between PDZ proteins and their targets have been extensively studied in the past few years. These studies have demonstrated that dissociation of such interactions can have profound effects on the spatial distribution and stability of binding

partners (Fanning and Anderson, 1999). A first mutation in a gene encoding a PDZ-containing protein was recently reported lead to sensory disorders (Usher type 1C disease): affected individuals suffer both hearing loss and retinal degeneration (Montell, 2000).

Large number of reports on PDZ interacting proteins are synaptical, where PDZ-domain-containing proteins mainly bind cytoplasmic tails of receptors. They mostly contain several PDZ domains, allowing formation of large protein clusters at the plasma membrane (Garner et al., 2000).

Several reports have now shown that PDZ interactions play an essential role in determining cell polarity (Bhat et al., 1999; Bilder and Perrimon, 2000). A study on apical or basolateral membrane sorting on γ-aminobutyric acid (GABA) receptors (GAT) described that two highly homologous isoforms, GAT-2 and GAT-3, localize to the basolateral and apical surfaces, respectively, when stably expressed in Madin-Darby canine kidney cells (MDCK) (Muth et al., 1998). They showed that removal of the final three amino acids of GAT-3 disrupts its apical sorting. The GAT-3 C-terminal sequence is reminiscent of sequences interacting with PDZ domain (X-Thr-X-Phe-COOH). Similar results were shown for splice variants of the Kv3 K^+ channel (Ponce et al., 1997). The cystic fibrosis transmembrane conductance regulator (CFTR) contains in its C-terminus a PDZ-interacting domain, which is required for apical polarization and CFTR interaction with an apical membrane protein (Moyer et al., 2000). A CFTR-associated protein (CAP70) contains four PDZ domains, three of which are capable of binding to the CFTR C-terminus and might be involved in facilitated intermolecular CFTR interaction, which can potentiate chloride current (Wang et al., 2000).

None of the reports treating with the GILZ/TSC/DIP/BUN family members evoke the PDZ-interacting domains contained in the C terminus of GILZ and DIP proteins. As a consequence no information is available on the role and importance of this functional domain in these proteins. Considering the very rare reports on nuclear PDZ-interactions (Kanai et al., 2000), GILZ might be part of a larger cytoplasmic or membrane bound cluster. Given its probable direct or indirect involvement in the sodium transport machinery, it can not be excluded that this hypothetical cluster is implicated either in regulations of main effectors at the plasma membrane or in membrane trafficking in the polarized CCD cells.

The antiapoptotic motif

The apoptotic program is evolutionarily conserved between yeast and metazoan organisms. A number of mammalian cDNAs capable of suppressing the deleterious effects of Bax expression in yeast have been identified. Such a suppressor, named TSC22[(86)], represents the C-terminal

86 amino acids of the previously characterized leucine zipper (LZ) motif-containing transcriptional regulator TSC22 (Yang et al., 2006). Employing a genome-wide two-hybrid screen, functional genomics, and deletion mutagenesis approaches, it was shown that TSC22[(86)]-mediated antiapoptosis is independent of the LZ motif and is likely independent of effects on gene transcription (figure 48*A*). Rather, a 16-residue sequence within the conserved 56-residue TSC22 domain is necessary for antiapoptosis (Khoury et al., 2008). This motif is conserved in many species and different proteins from the TSC22 family (figure 48*B*).

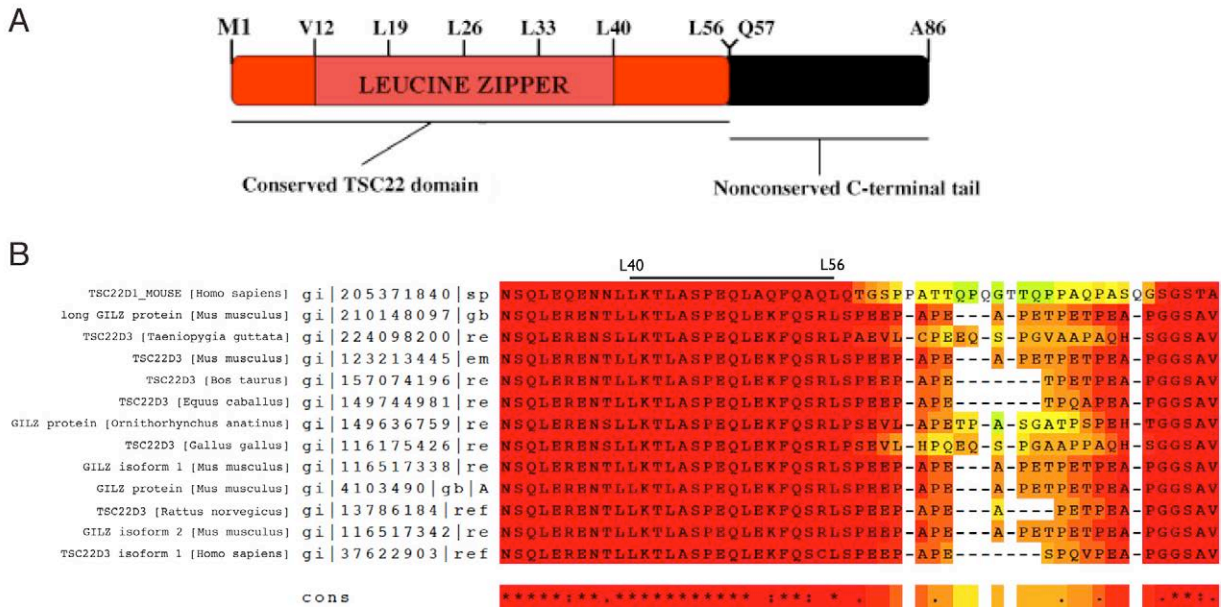

Figure 48: *A*, Schematic representation of the domain organization of Tsc22[(86)]. 'The conserved TSC22 domain' shown in red. The locations of the leucine (L) and valine (V) residues that form the LZ are shown. The domain spans residues Met1(M1)-Leu56(L56), and is succeeded by a variable C-terminal region spanning residues Gln57(Q57)-Ala86(A86). The predicted 'LZ' motif embedded within the TSC22 domain is present between residues V12-L40 (Khoury et al., 2008). *B*, Conservation of the TSC22 antiapoptotic motif across species. Amino acid sequence alignment of Tsc22d3 orthologs using the T-Coffee multiple sequence alignment program (http://www.tcoffee.org).

The Tsc22d3 isoforms

In silico analysis and functional studies revealed that *gilz* exhibits 4 isoforms (Soundararajan et al., 2007). Figure 49 represents the mouse *Tsc22d3* gene, which is located on the X chromosome. Six exons can produce four different transcription products (of ORF lengths 414, 606, 132, and 243 nucleotides each) with translational potential (of 137, 201, 43, and 80 amino acids, respectively). These isoforms are termed GILZ1, -2, -3, and -4, respectively. GILZ1 and -2 share exons 5 and 6, making up the TSC22/dip/bun domain, leucine zipper, and C-terminus, but differ in their N-terminal exon(s) and 5'-untranslated region. Although isoform 4 also shares exons 5 and 6 and has a unique 5'-untranslated region, only its start codon is in exon 5, resulting in a translational truncated variant of isoforms 1 and 2. Isoform 3 consists of exons 3

and 6, skipping exons 4 and 5, resulting in a frameshift and subsequent stop codon, encoding a 43-amino acid long translation product. A CpG island and a series of Sp1 sites appear to define a TATAless promoter, designated as promoter 1 (P1). The large intron B, spanning almost 55 kb, separates exons 1 and 2 from exons 3–6 and contains multiple response elements (six GREs and three FHREs), most of them having been reported as being functional (Asselin-Labat et al., 2004; Asselin-Labat et al., 2005; Cartharius et al., 2005). Four GREs and three FHREs, combined with a TATA-box 32–25 bp 5' from exon 3, form a transcriptionally active cluster, which is designated as promoter 2 (P2).

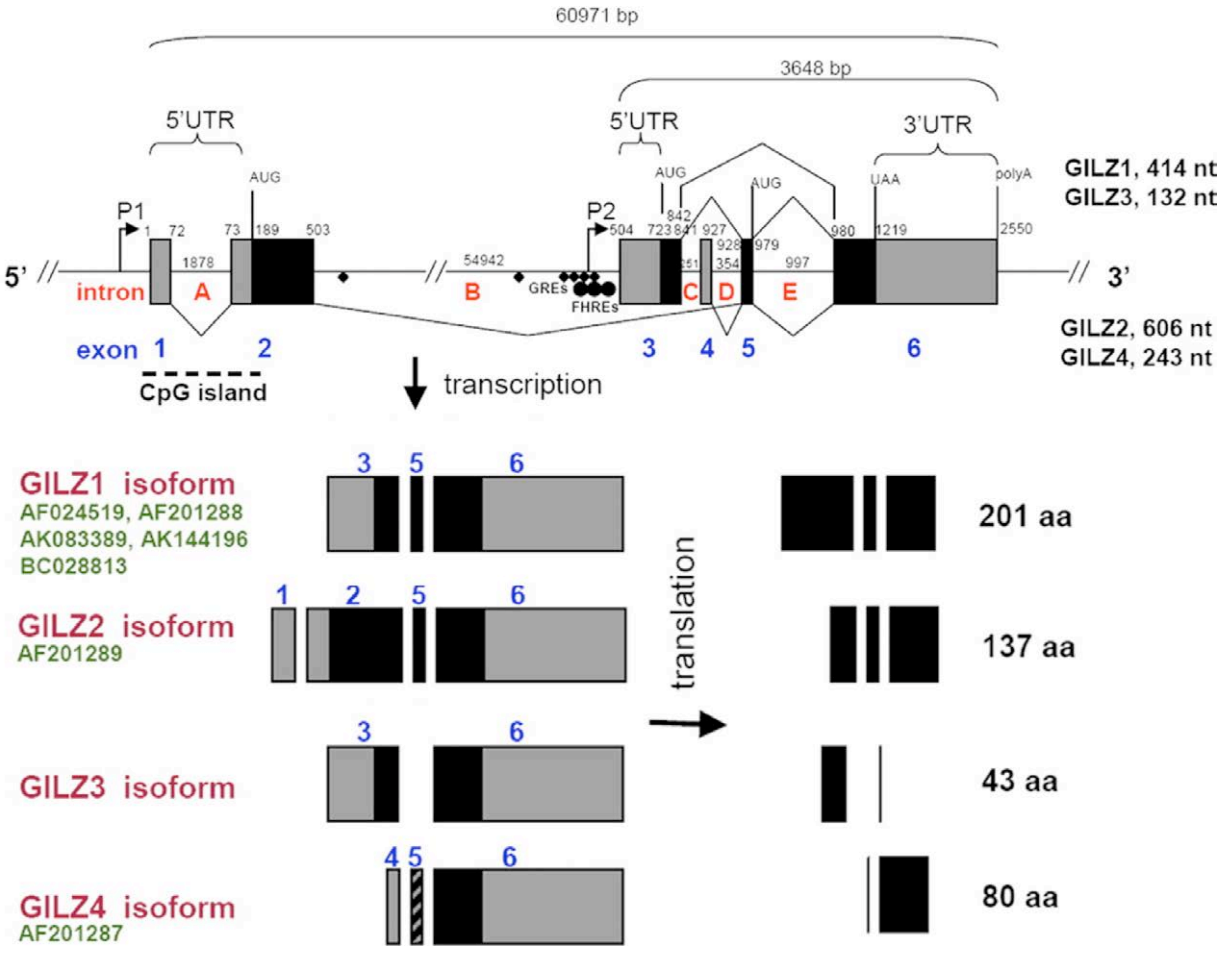

Figure 49: Genomic structure of the mouse *Tsc22d3* gene. A *schematic diagram* shows a region of 60,971 bp on the mouse X chromosome and the *Tsc22d3* gene. Six exons can produce four different transcription products (of ORF lengths 414, 606, 132, and 243 nucleotides each) with translational potential (of 137, 201, 43, and 80 amino acids, respectively). These isoforms are termed GILZ1, -2, -3, and -4, respectively. The *black boxes* represent the translated regions, and the *gray boxes* represent the untranslated regions of the *Tsc22d3* gene. The CpG island locating exons 1 and 2, together with 12 potential Sp1 binding sites is designated as P1. Four GREs and three FHREs in the large second intron B, combined with a TATA-box 32 to 25 bp 5' from exon 3, form a transcriptionally active cluster, which is designated as P2. The *diamonds* in intron B represent potential GREs, and the *black circles* represent potential FHREs. The *numbers* at the *borders* of the *gray* and *black boxes* indicate the nucleotide positions read from 5' to 3', whereas the *numbers above* the *introns* refer to the sizes of the respective introns. The NCBI accession numbers (in *green*) under the different GILZ isoform notations refer to previously reported mRNA transcripts available in the data base (Soundararajan et al., 2007).

It is interesting to note that no GREs were identified upstream of P1, suggesting that the GREs in intron B upstream of P2 mediate glucocorticoid and mineralocorticoid responsiveness of both promoters. It is also of note that there are two Elk-1 binding sites present in the CpG island and two more in exon 6, suggesting regulation of GILZ transcription by Elk-1.

Sequence alignment between the 4 GILZ isoforms shows that they share homology (Figures 50 and 51).

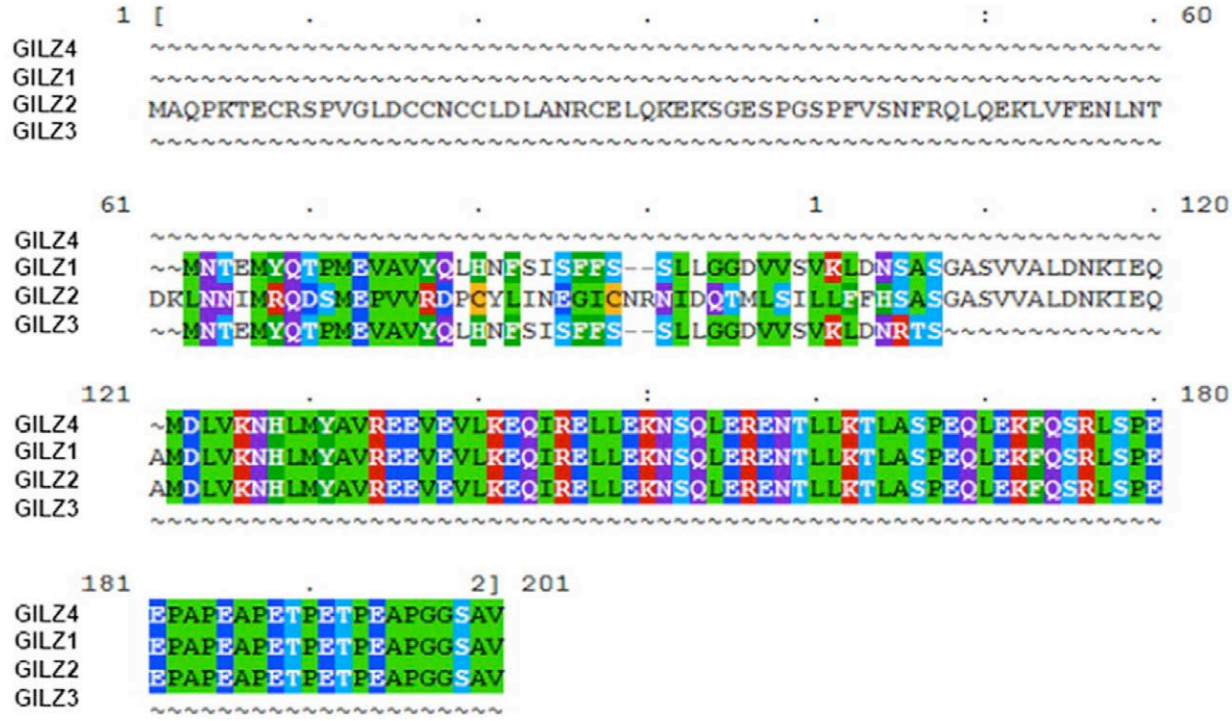

Figure 50: Alignment of the protein sequences of all four mGILZ isoforms, GILZ1, -2, -3, and -4. (Soundararajan et al., 2007).

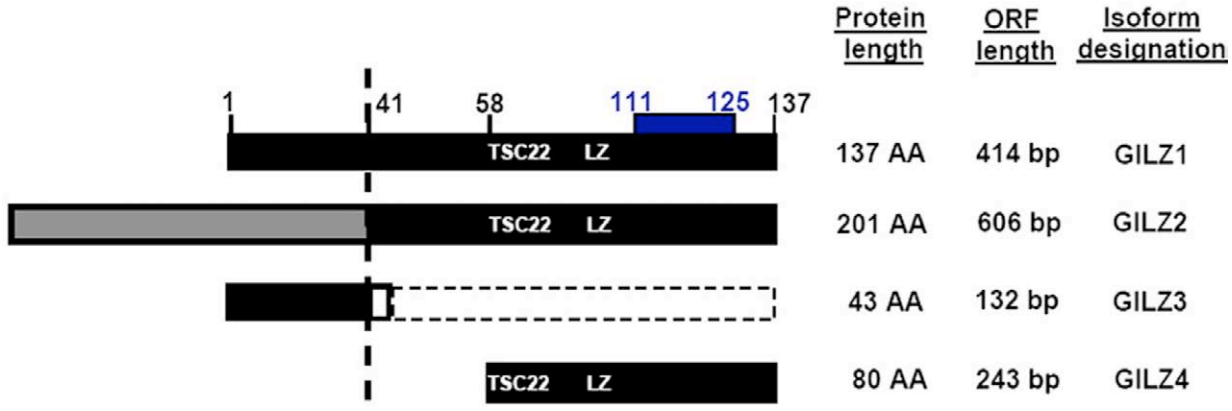

Figure 51: Schematic representation of the above. The *numbers* represent amino acid (*AA*) positions on GILZ1. The *regions* in *black* represent regions of identityamongthe four naturally occurring mGILZ isoforms. The *dotted region* in GILZ3 represents the untranslated portion of the transcript. The *region* in *blue* (GILZ1 residues 111–125) represents the antigenic stretch recognized by our anti-GILZ antibody. The conserved TSC22/dip/bun signature box (*TSC22*) and the leucine zipper domain (*LZ*) are also shown (Soundararajan et al., 2007).

Implications and effects of GILZ

GILZ in the inflammation process

Glucocorticoids are potent modulators of the immune response and inflammatory processes. These hormones are the most commonly used anti-inflammatory and immunosuppressive drugs in the treatment of rheumatic and other inflammatory diseases. As already mentioned, cellular effects of GCs are mediated through the glucocorticoid receptor (GR), which regulates the expression of GC-responsive genes (Payvar et al., 1981; Miesfeld et al., 1984). One of the prominent GC-responsive genes is GILZ (D'Adamio et al., 1997; Ayroldi et al., 2001). GILZ controls T cell activation and development, and inhibits the activities of the key inflammatory signalling mediators NFκB and AP-1 (Ayroldi et al., 2001; Mittelstadt and Ashwell, 2001; Riccardi et al., 2001). When stimulated with GCs, macrophages synthesize significant amounts of GILZ, which subsequently attenuates macrophage inflammatory responses (Berrebi et al., 2003). Moreover, *gilz* gene expression is downregulated in macrophages from inflammatory lesions of delayed type hypersensitivity reactions, and persists in tumor-infiltrating macrophages from Burkitt lymphoma (Berrebi et al., 2003). GILZ mediates the anti-inflammatory effects of GCs via suppressing the activation of NF-κB in human airway epithelial cells (Eddleston et al., 2007) and redirects the maturation of dendritic cells, preventing Ag-specific T lymphocyte responses (Cohen et al., 2006). Annexin-1 (ANXA1), which is a mediator of the anti-inflammatory action of GCs, regulates macrophage IL-6 and TNF secretion *via* GILZ. Interestingly, GILZ induction by GCs was reduced in ANXA1 knockout mice (Yang et al., 2009). A recent study shows that GILZ is upregulated in human epithelial cells upon dose-dependent alcohol exposure (Gomez et al., 2010).

The GILZ promoter contains 6 glucocorticoid responsive elements (GRE), along with binding site for forkhead box class O (FOXO) family proteins, signal transducer and activator of transcription 6 (STAT6), nuclear factor of activated T cells (NFAT), octamer, and c-myc (Asselin-Labat et al., 2004; Wang et al., 2004; Asselin-Labat et al., 2005). The regulation of GILZ expression has been studied in a murine T lymphocyte line where FOXO3 was shown to activate GILZ expression independent of GCs (Asselin-Labat et al., 2004; Asselin-Labat et al., 2005).

These data strongly suggest that GILZ plays a key role in inflammatory inhibition and immunosuppression.

GILZ and ENaC-mediated sodium transport

GILZ was the most significantly increased transcript induced by aldosterone in mpkCCD$_{c14}$ cells (Robert-Nicoud, 2001; Robert-Nicoud et al., 2001). Its kinetics of induction points out to an early-induced gene, suggesting that GILZ could participate to intracellular mechanisms during the first phase of the aldosterone response.

Robert-Nicoud has shown that, in the kidney, GILZ is localised in the proximal tubules, and in the connecting (CNT) and collecting ducts (CD), more precisely in the principal cells (Robert-Nicoud, 2001). GILZ is an early aldosterone-induced gene in the mpkCCD$_{c14}$ cell line: its mRNA expression level increases significantly already 30 min after aldosterone treatment. Its mRNA profile expression during 24 h precedes and is similar to the transepithelial current (I_{sc}) increase (figure 52), and increases in cells treated with aldosterone in a dose-dependent manner. These data strongly suggest that GILZ is a potential mediator of the aldosterone response.

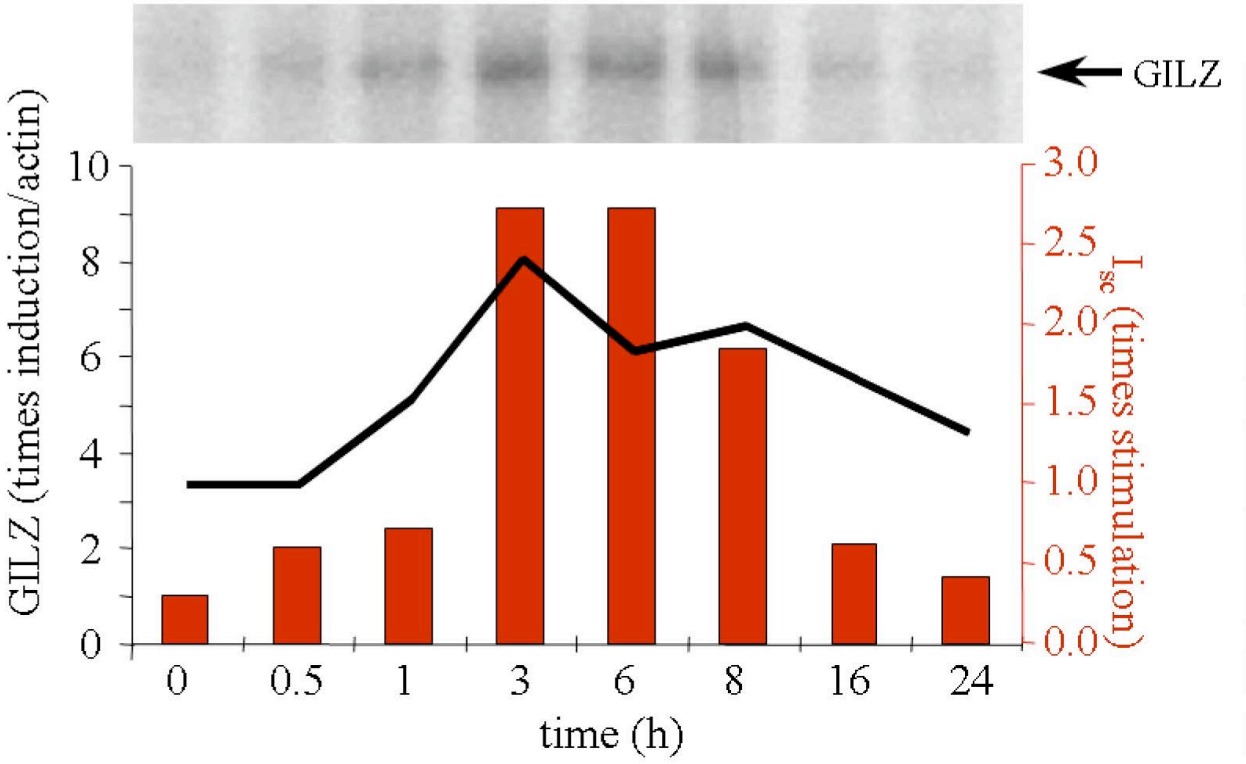

Figure 52: Time-course correlation of transepithelial current (I_{sc}) and GILZ mRNA induction by aldosterone (1 µM) in the mpkCCD$_{cl4}$ cells. GILZ mRNA levels (black line) correspond to the quantification of the shown Northern Blotting (Robert-Nicoud, 2001).

There are several evidences of a putative role for GILZ in the kidney. First, a study on teleosts osmotic stress adaptation showed that OSTF1 (a GILZ ortholog) was rapidly and transiently

induced during hyperosmotic stress after acclimatising from fresh water to seawater (Fiol and Kultz, 2005). Maximal increase at mRNA and protein level was detected after 2 to 4 h transfer to seawater, and was proportional to increasing salinity. The authors conclude that OSTF1 represents the molecular link between the seawater-induced hormone cortisol and transcriptional regulation of ion transport and cell differentiation in teleost gills (Fiol and Kultz, 2005). The gills play the role of the kidney in tilapia adaptation to changes in osmolarity. Cortisol is a central hormone in fish osmoregulation that promotes seawater adaptation by regulating gill cell differentiation, Na^+/K^+-ATPase, cotransporters, and ion channels, resulting in overall salt secretion to maintain body-water and ion homeostasis, and its levels increase very rapidly after transfer of tilapia to seawater (Abo Hegab and Hanke, 1984).

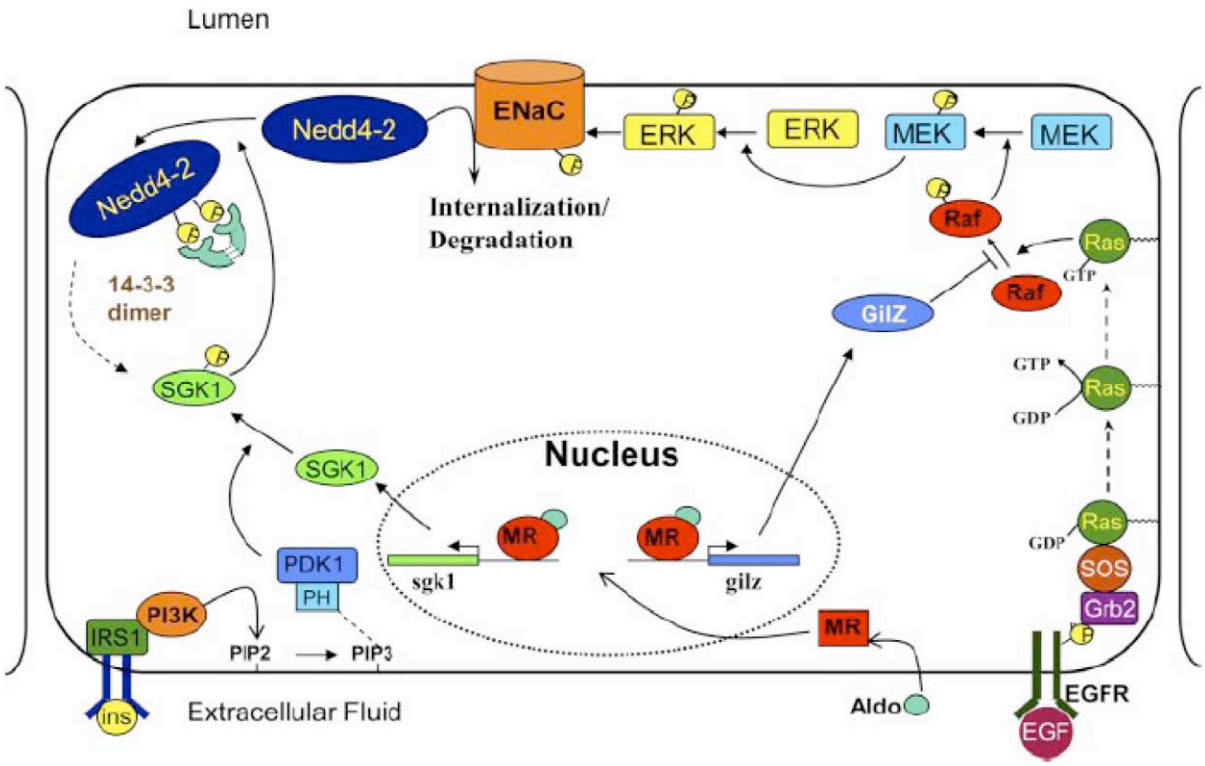

Figure 53: Role of SGK1 and GILZ in hormonal regulation of ENaC activity in an epithelial cell. SGK1 and GILZ abundance is regulated by aldosterone (Aldo). SGK1 activity is regulated by insulin through phosphatidylinositide 3 -kinase (PI3K). GILZ acts in parallel to inhibit ERK signaling. Together, they coordinately block Nedd4-2 inhibition of ENaC (Bhalla et al., 2006).

As shown in figure 53, GILZ seems to negatively regulate tonic inhibition of ENaC and thus use disinhibition to propagate the effects of aldosterone to increase sodium reabsorption in tight epithelia (Soundararajan et al., 2005). It appears to stimulate ENaC cell surface expression at least in part by the extracellular signal-related kinase 1/2 (ERK1/2). ERK1/2 appears to be constitutively active in distal nephron cells (Michlig et al., 2004). Its activation by progesterone in ENaC expressing oocytes, of by the epithelial growth factor (EGF) in MDCK cells, inhibits

Na^+ current (Grossmann et al., 2004; Michlig et al., 2004) and a long-term (>4 h) inhibition of the ERK pathway stimulates it (Shen and Cotton, 2003; Falin et al., 2005), suggesting a tonic inhibition of Na^+ transport by the ERK pathway. The fact that aldosterone induces EGF receptor (EGF-R) expression in renal tissue of adrenalectomized rats and in human renal primary cell cultures (Krug et al., 2003), and that GILZ has been shown to act as an inhibitor of ERK signalling pathway in T-lymphocytes by binding to Raf (Ayroldi et al., 2002) suggested the authors that GILZ might function as a mineralocorticoid-induced inhibitor of ERK signalling implicated in the early induction of ENaC-mediated transport. Indeed, Soundadarajan *et al.* showed that GILZ stimulates ENaC-mediated Na^+ transport in mpkCCD_{cl4} cells by inhibiting ERK, and that similarly aldosterone treatment suppressed phospho-ERK levels with a time course that paralleled the increase of Na^+ transport (Soundararajan et al., 2005). Nevertheless, this model has been recently revisited. Indeed, as shown in figure 9, it seems that GILZ associates with SGK1 to stimulate the ENaC-regulatory complex (Soundararajan et al., 2010). However, no functional *in vivo* study has been published to confirm this hypothesis.

Temporal profile study of DCT/CT and CCD transcriptomes allowed identifying several genes involved in renal circadian rhythms (Zuber et al., 2009). GILZ and USP2 were found to follow a circadian expression profile. These authors further investigated the temporal profile of these genes in the *dbp/hlf/tef* (triple knockout) model (Gachon et al., 2006), and showed that the expression was significantly reduced in kidneys of the triple knockout mice. In *clock* knockout mice, the arterial blood pressure is lower compared to controls, indicating the physiological importance of the clock machinery in the renal function (Zuber et al., 2009). It is probable that the oscillating expression of GILZ plays also a role in this regulation.

As in the pre-adipocytes (mentioned further), GILZ could act as an antagonist of the PPARγ pathway in the ASDN. PPARγ agonists induce sodium and water retention in type II diabetes treated patients. This effect has been shown to be due to an increase in Na^+ reabsorption, probably in the IMCD (Guan et al., 2005; Zhang et al., 2005), either by increasing ENaCγ (Guan et al., 2005) or Sgk1 expression (Hong et al., 2003). More recently, data obtained with mice lacking specifically the expression of αENaC in the collecting duct argue against a primary and critical role of ENaC in thiazolidinedione-induced fluid retention (Vallon et al., 2009).

Role in adipogenesis and bone regulation

Mesenchymal stem cells (MSC) can differentiate towards myocyte, adipocyte, chondrocyte or osteoblast cells in a transcription factor-dependent fashion (figure 54). GILZ inhibits adipogenesis of MSCs. It can bind specifically to a 40-bp DNA fragment containing a unique tandemly repeated C/EBP-binding element present in the promoter of PPARγ2 (Shi et al., 2003). *In vitro*, glucocorticoids are required for osteoblast differentiation of primary bone marrow stromal cells, while *in vivo* bone loss is induced (Clark and Lasa, 2003). Studies on MSC differentiation showed that overexpression of GILZ mediates the shift towards to the osteogenic pathway of the glucocorticoid action in this process (Shi et al., 2007; Zhang et al., 2008).

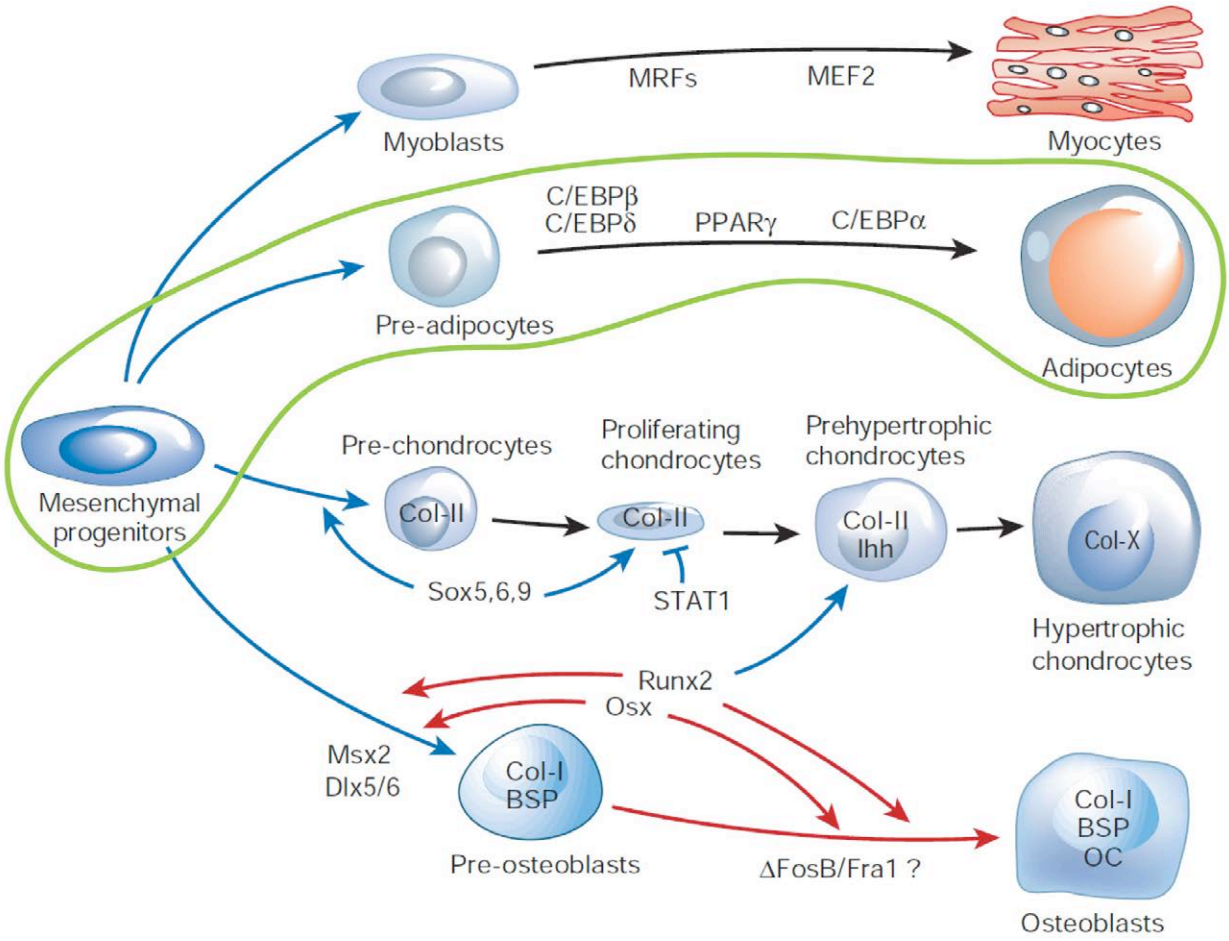

Figure 54: Transcriptional control of osteoblastic, chondrocytic, adipocytic and myocytic differentiation. Osteoblasts differentiate from mesenchymal progenitor cells that also give rise to myocytes, under the control of MRFs and MEF2, to adipocytes under the control of C/EBPα, β and δ and PPARγ, and to chondrocytes under the control of Sox5, -6 and -9 and STAT1. Runx2 is essential for osteoblast differentiation and is also involved in chondrocyte maturation. Osterix (Osx) acts downstream of Runx2 to induce mature osteoblasts that express osteoblast markers, including osteocalcin. Abbreviations: MRFs, myogenic regulatory factors (including MyoD, myogenin, myogenic factor 5 and myogenic regulatory factor 4); MEF2, myocyte-enhancer factor 2; C/EBP, CCAAT-enhancer-binding protein; PPARγ, peroxisome proliferator-activated receptor γ; STAT1, signal transducers and activators of transcription-1; Runx2, runt-related transcription factor 2; Col-I/II/X, type I/II/X collagen; Ihh, Indian hedgehog; BSP, bone sialoprotein; OC, osteocalcin. Modified from (Harada and Rodan, 2003).

A recent study presented the estrogen receptor (ER)-mediated effects on adipogenesis (Xiao et al., 2010). Pseudoprotodiocsin (PPD), a steroid saponin compound found in the Dioscorea plant (Dinchev et al., 2008), has been reported to have an inhibitory effect on some cancer lines (Dong et al., 2001; Ivanova et al., 2009). Treatment with PPD at the onset of adipogenic differentiation resulted is decreased adipogenesis *in vitro* and *in vivo*. This was correlated with increased amount of ERα mRNA, protein and accumulation of ERα in the nucleus. This was accompanied by the decreased expression of several genes involved in adipogenesis, like lipoprotein lipase (LPL), C/EBPα and PPARγ. In contrast, expression of some negative factors of adipogenesis, including pre-adipocyte factor 1 and GILZ, was increased (Xiao et al., 2010).
The GILZ Drosophila homolog is called *bunched* (*bun*) and is required to establish a cell fate boundary in the ovary (Dobens et al., 1997; Wu et al., 2008). A relationship exists between *bun* and *slow boarder cells* (*slbo*) which is the C/EBP Drosophila homolog (Levine et al., 2007), confirming the evolutionary conservation of this interaction.

Peroxisome proliferator-activated receptors (PPARs)

PPARs are ligand-activated transcription factors that belong to the nuclear hormone receptor superfamily. PPARα (NR1C1) was first described as a receptor that is activated by peroxisome proliferators, hence its name (Issemann and Green, 1990). Two additional related isotypes, PPARβ/δ (NR1C2) and PPARγ (NR1C3), were then found and characterized (Dreyer et al., 1992). Each of the PPAR isotypes is encoded in a separate gene and many cellular and systemic roles have been attributed to these receptors, reaching far beyond the stimulation of peroxisome proliferation in rodents after which they were initially named (Desvergne and Wahli, 1999). For effective DNA binding, PPARs require heterodimerization with retinoid X receptors (RXR; figure 55). In line with their various developmental and physiological functions, PPARs exhibit broad, but isotype-specific, tissue expression patterns (Kliewer et al., 1994; Braissant et al., 1996). PPARα is expressed at high levels in organs that carry out significant catabolism of fatty acids such as the brown adipose tissue, liver, heart, kidney, and intestine (Mandard et al., 2004). Interestingly, PPARα expression is upregulated by glucorticoids after skin injury (Lemberger et al., 1994). Of the three isotypes, PPARβ/δ has the broadest expression pattern, and the levels of expression in certain tissues depend on the extent of cell proliferation and differentiation.

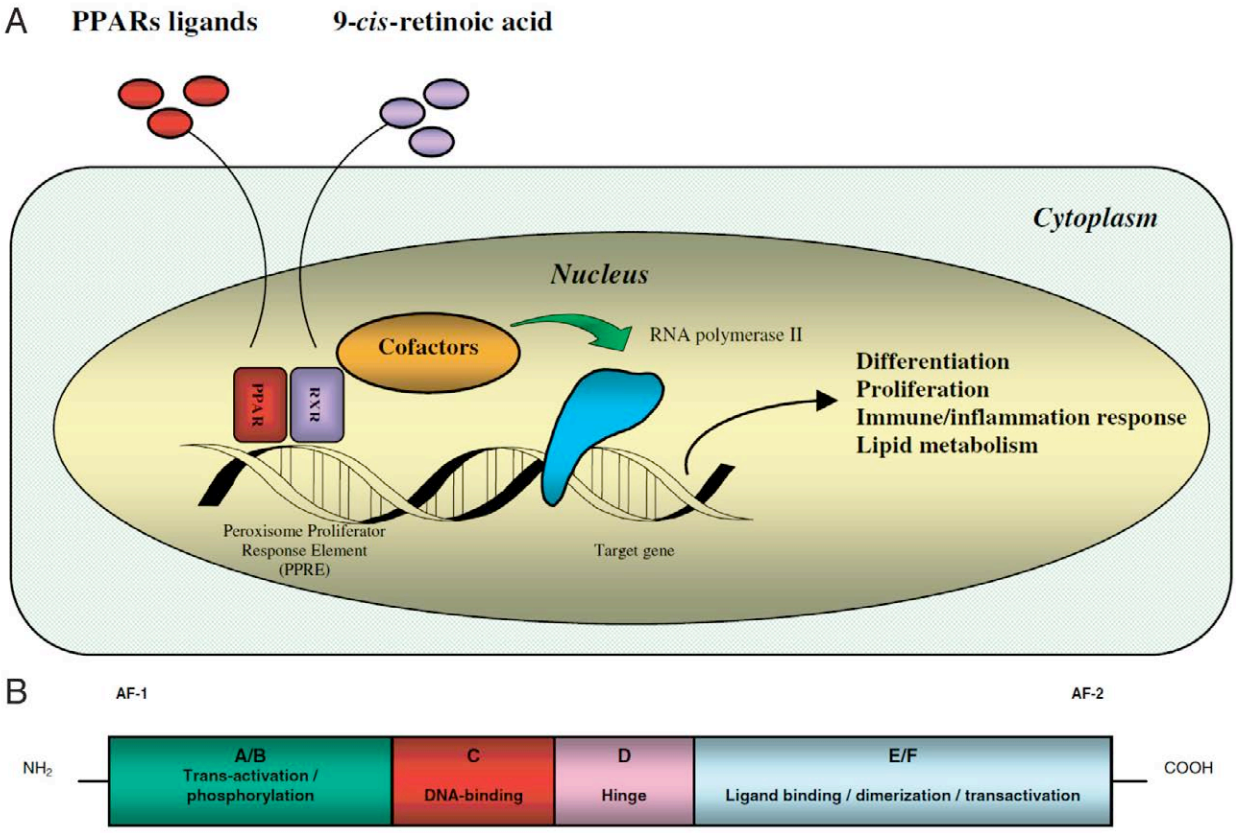

Figure 55: ***A*****, Peroxisome proliferator-activated receptors (PPARs) function as heterodimers with retinoid X receptors (RXRs) and are activated by specific ligands; they then modulate DNA transcription by binding to defined nucleotide sequences (peroxisome proliferator response element, PPRE) in the promoter region of target genes. Several cofactors (coactivators or corepressors) mediate the ability of nuclear receptors to stimulate or repress the transcription process.** ***B*****, The N-terminus A/B domain contains a ligand-independent transcriptional activation domain (AF-1), which can be regulated by mitogen-activated protein kinase (MAPK) phosphorylation in a and c isotypes. The C domain contains two zinc-fingerlike motifs that specifically bind the PPRE in the regulatory region of PPAR-responsive genes. The D domain or hinge region allows conformational changes in the molecule. The E/F domain consists of the ligand-binding domain and the ligand-dependent transcriptional activation domain (AF-2). The ligand-binding pocket appears to be quite large in comparison with other nuclear receptors, allowing the PPARs to interact with a broad range of natural and synthetic ligands (Kuenzli and Saurat, 2003).**

Important functions have been assigned to this isotype in the skin, gut, placenta, skeletal muscle, adipose tissue, and brain (Braissant et al., 1996; Bastie et al., 1999; Peters et al., 2000; Michalik et al., 2001; Barak et al., 2002). PPARγ is expressed as two isoforms, γ1 and γ2, that differ at their N-terminus. PPARγ2 is found at high levels in the different adipose tissues (Dreyer et al., 1992; Chawla et al., 1994; Tontonoz et al., 1994a), whereas PPARγ1 has a broader expression pattern that extends to settings such as the gut, brain, vascular cells, and specific kinds of immune and inflammatory cells (Tontonoz et al., 1994b; Zhu et al., 1995).

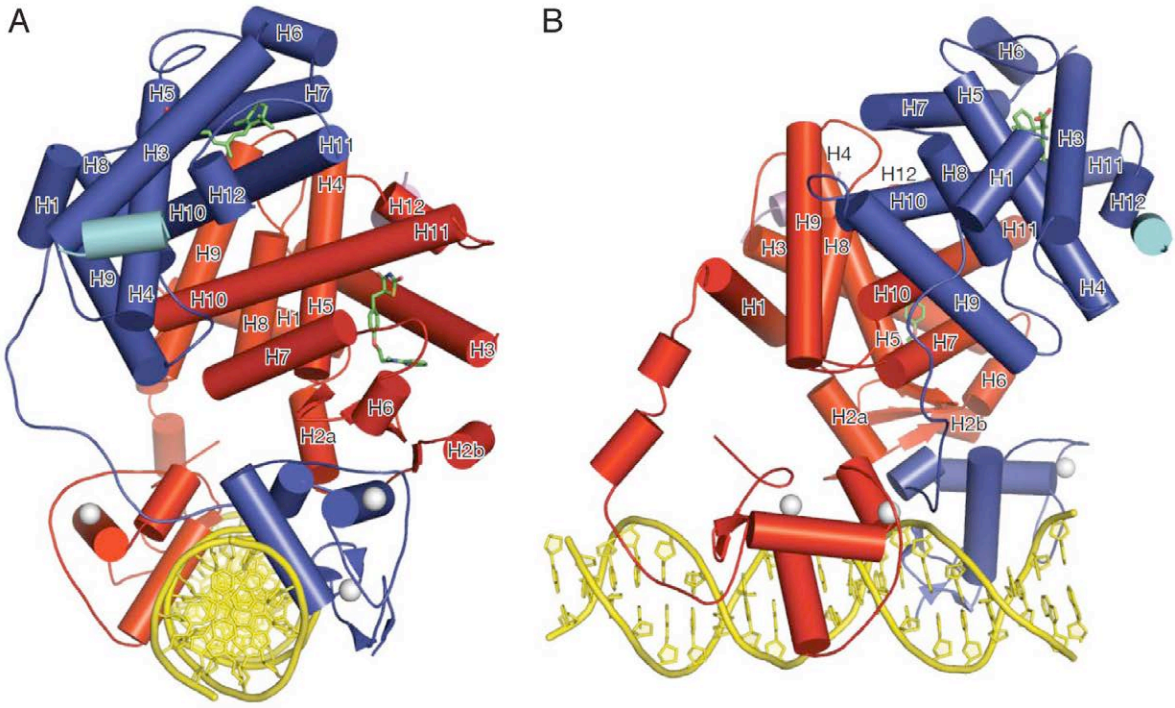

Figure 56: Orthogonal views are shown in which RXR*α* is blue and PPARγ is red. The ligands rosiglitazone and 9-*cis*-retinoic acid are shown in green, the Zn(II) ions are white, and the coactivator LXXLL peptides are in light blue and purple (Chandra et al., 2008).

Figure 56 shows the interaction between the RXRα and PPARγ with DNA. Rosiglitazone, an anti-diabetic compound from the thiazolidinedione class of drug, is a ligand for PPARγ. A ligand for RXRα is 9-*cis*-retinoic acid.

The metabolic syndrome

The metabolic syndrome is a cluster of interrelated common clinical disorders, including obesity, insulin resistance, glucose intolerance, hypertension, and dyslipidemia (hypertriglyceridemia and low HDL cholesterol levels ; figure 57)(Moller and Kaufman, 2005). According to recently defined criteria, the metabolic syndrome is prevalent and is associated with a greater risk of atherosclerotic cardiovascular disease than any of its individual components (Alexander et al., 2003). Primary defects in energy balance that produce obesity (and visceral adiposity in particular) are sufficient to drive all aspects of the syndrome (Despres and Lemieux, 2006). Increased free fatty acids and lipid accumulation in certain organs are mediators of insulin resistance (Howard and Howard, 1994). Obesity also leads to a proinflammatory and prothrombotic state that potentiates atherosclerosis. Pathways leading directly from adiposity to the genesis of dyslipidemia and hypertension have been elucidated. Recent knowledge implies a role for fat-derived “adipokines,” including TNF*α* and adiponectin, as pathogenic contributors or protective factors (Weisberg et al., 2003).

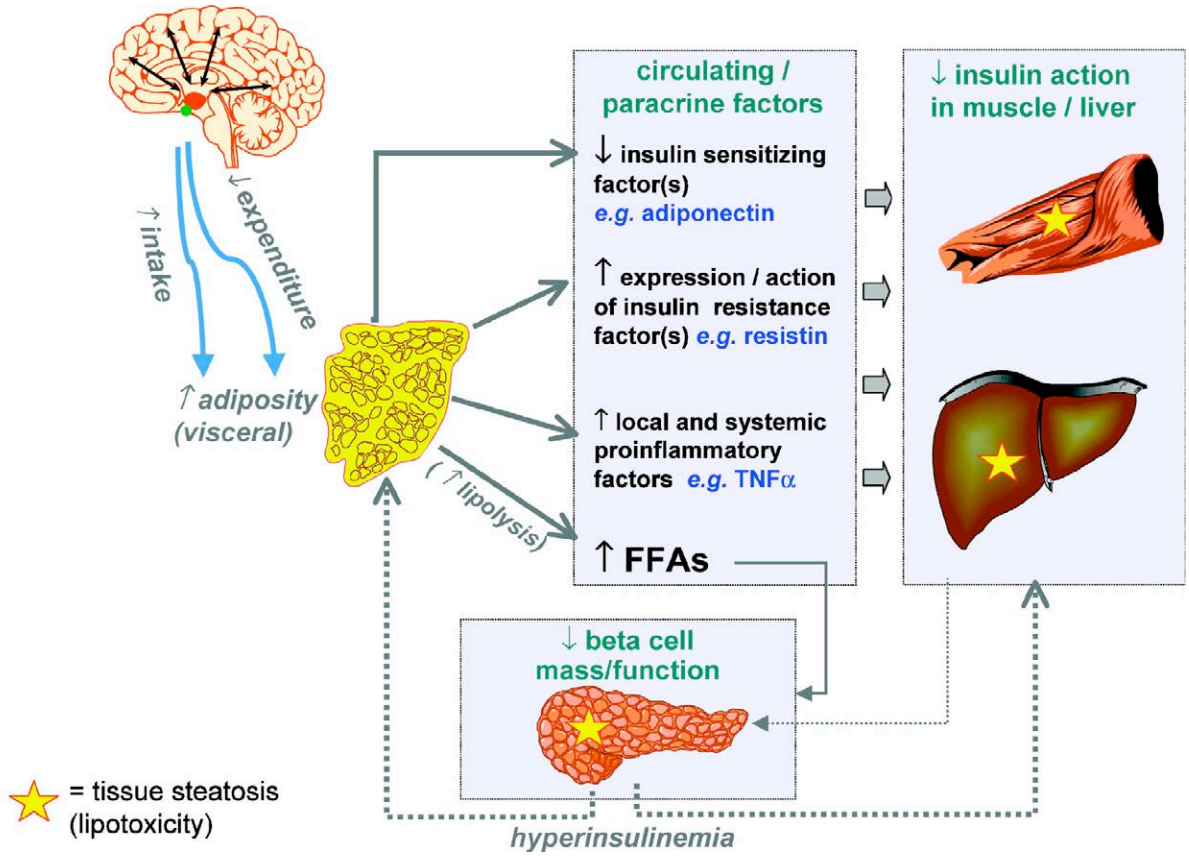

Figure 57: Potential molecular mechanisms for obesity-induced insulin resistance and glucose intolerance. Increased adiposity (obesity), particularly increased visceral adiposity, results from a centrally regulated imbalance in energy intake versus expenditure. Secondary effects of obesity include increased circulating free fatty acids (FFAs), in part resulting from a net increase in lipolysis; reduced adiponectin; a potential increase in insulin resistance factors (e.g., resistin); and increased proinflammatory mediators (e.g., TNFα). Increased lipid flux into peripheral tissues can result in accumulation of triglycerides and long-chain fatty acyl-CoA esters (steatosis), which mediate insulin resistance and pancreatic beta cell "lipotoxicity." Insulin resistance in liver and muscle leads to hyperinsulinemia, which can, in turn, augment adipose tissue accretion and exacerbate tissue resistance to insulin (Moller and Kaufman, 2005).

Current therapies include diet and exercise as well as agents indicated for the treatment of individual components of the syndrome (Moller, 2001; Katzmarzyk et al., 2003). Future therapies may accrue from the aggressive pursuit of newer molecular drug targets that have the potential to prevent or treat multiple aspects of the metabolic syndrome.

A prevailing hypothesis for regulation of insulin sensitivity by PPARγ involves primary effects of PPARγ on gene transcription in adipose tissue (where it is most abundantly expressed), which ultimately lead to improved insulin action in muscle and liver. Direct activation of PPARγ leads to the induction of adipocyte genes such as those for lipoprotein lipase and fatty-acid transporter 1, which in turn contribute to lowering triglyceride and FFA levels, respectively. Similarly, suppression of TNFα gene expression by PPARγ in adipose tissue has been reported. As FFAs and TNFα are both potential systemic mediators of insulin resistance, such effects are likely to contribute to the efficacy of PPARγ activation in increasing insulin sensitivity (Oakes et al., 1994; Moller, 2001).

GC excess (Cushing's syndrome) causes visceral obesity, insulin resistance, diabetes mellitus, dyslipidaemia, hypertension and premature vascular mortality (Fraser et al., 1999). In peripheral tissues, 11β-hydroxysteroid dehydrogenase type 1 (11βHSD1) catalyses the conversion of cortisone to the active glucocorticoid, cortisol (figure 58). On the basis of the apparently insulin-sensitive phenotype of 11βHSD1-null mice, inhibition of this enzyme has been suggested as a potential drug target for metabolic syndrome (Seckl and Walker, 2001). Furthermore, in obese subjects, increased 11βHSD1 expression in subcutaneous adipose tissue, but not in visceral adipose tissue, is associated with the worsening of metabolic conditions. Higher glucocorticoid production in adipose tissue may favor the development of metabolic disorders through a decrease in adiponectin release (Alberti et al., 2007).

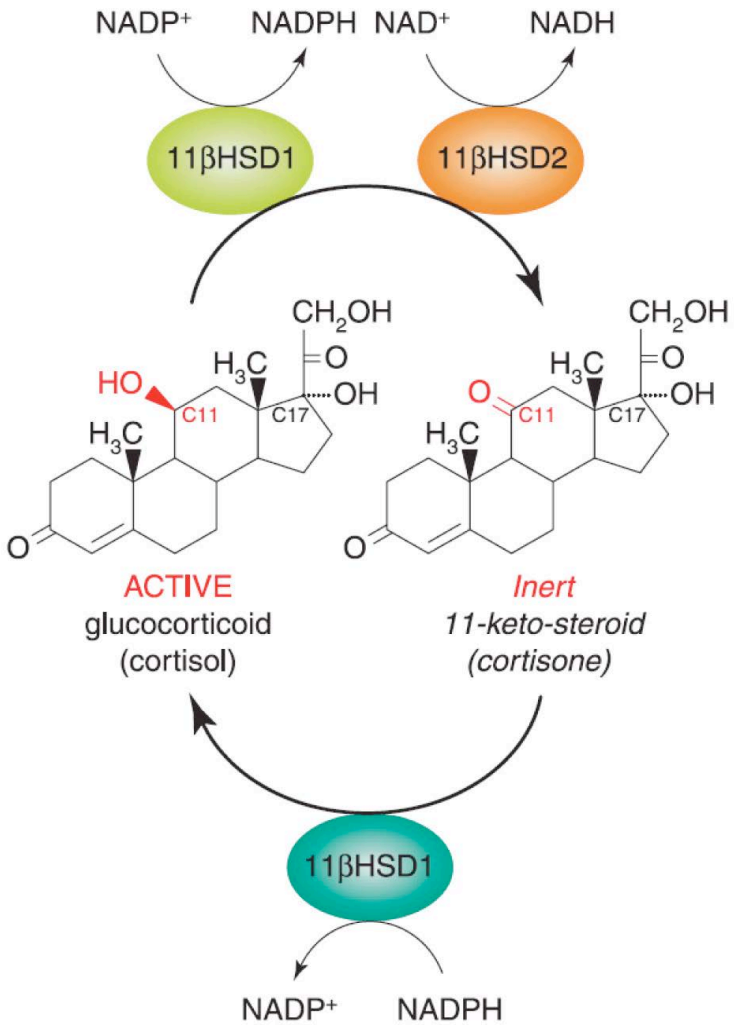

Figure 58: Interconversion of cortisol and cortisone by enzymatic oxidation or reduction at carbon position 11 (C11), catalysed by the two cloned isoforms of 11β-hydroxysteroid dehydrogenase (11βHSD). By convention, bonds below the plane of the molécule (α bonds) are represented by dotted lines; bonds which have no definitive orientation are represented by solid lines; and bonds above the plane of the molecule (β bonds) are represented by solid triangles. Corticosterone and 11-dehydrocorticosterone have similar structures to cortisol and cortisone, respectively, but lack the α-hydroxyl groups at position C17 (Michael et al., 2003).

Several reports indicate that adipose tissue regulation depends on the circadian clock. Plasma concentrations of the adipose tissue hormone leptin show a clear circadian rhythm (Sinha et al., 1996), which is not controlled by circulating glucocorticoid levels, but which disappears after SCN lesions (Kalsbeek et al., 2001). In addition, the circulating plasma levels of a number of other adipocytokines (as well as their adipose mRNA levels) show clear day/night rhythms (Gavrila et al., 2003; Rajala et al., 2004; Ando et al., 2005). BMAL1 knockout mice embryonic fibroblast cells failed to be differentiated into adipocytes, indicating a functional role for the circadian clock machinery in this process (Shimba et al., 2005).

Metabolic syndrome is often associated with infertility. Obesity or overweight may result in hypogonadism, increased scrotal temperature, impaired spermatogenesis, decreased sperm concentration and motility, and increased sperm DNA damage (Pasquali et al., 2007; Kasturi et al., 2008).

Sexual development and fertility

Sexual differentiation

The first step in the establishment of the fertility of a higher organism is the determination of its sexual identity, which is ultimately determined by the sex chromosomes (figure 59). Developmentally, male and female fetuses are essentially indistinguishable until midgestation in the mouse and approximately six weeks of pregnancy in humans. Thus, the formation of primordial germ cells (PGCs) at the base of the yolk sac, their tortuous journey along the hindgut to the genital ridge, and the proliferation and migration of the somatic cells and germ cells in the bipotential gonad are independent of which sex chromosomes the fetus harbors (figure 60). The gonad then differentiates along the female or male pathway, and gonadal development, in turn, dictates the development of the secondary sex organs (Gilbert, 2006).

Gonad development

Once a testis or an ovary begins to form, the developmental processes differ. In the testis cords, the differentiating primordial germ cells that will become spermatogonia are destined to undergo proliferation before entering meiosis and undergoing spermiogenesis. Germ cells arise and propagate in an autocrine, paracrine, juxtracrine and endocrine environment that includes factors within the gonads and beyond.

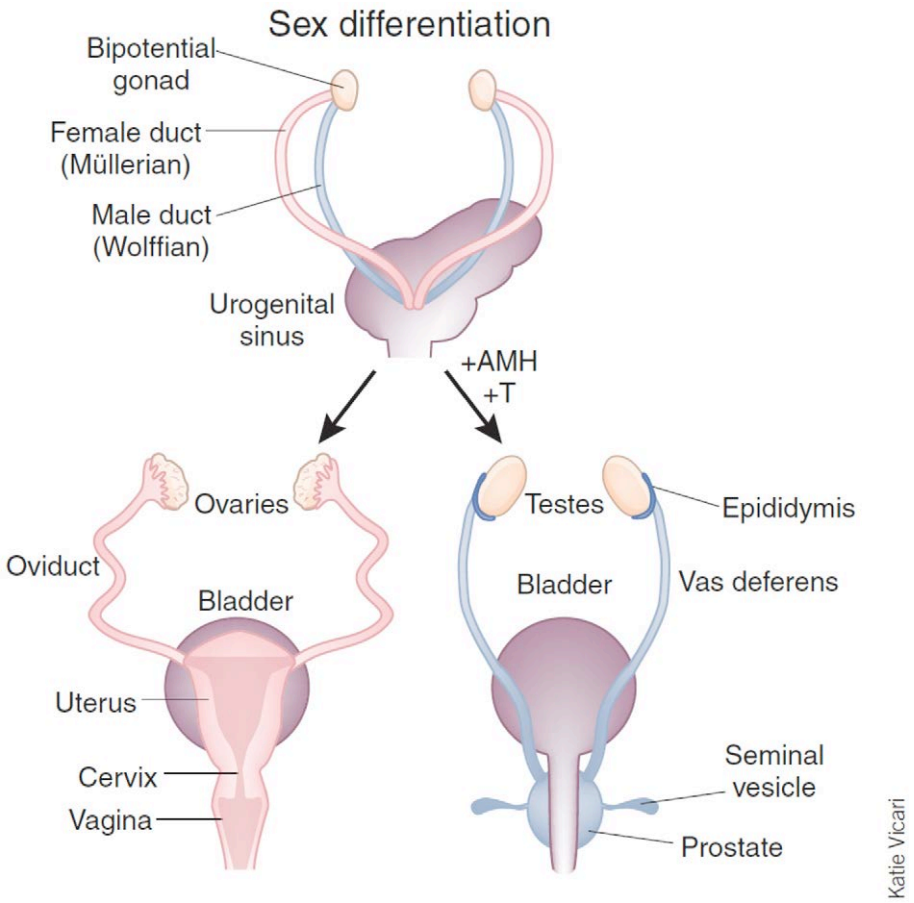

Figure 59: Sex differentiation in humans. The presence of a fetal testis that secretes both testosterone (T) and anti-Müllerian hormone (AMH) results in the induction of the Wolffian duct into the future vas deferens, epididymis, and seminal vesicles and the regression of the Müllerian duct, respectively. In females, the fetal ovary does not secrete either of these substances, so the Wolffian duct regresses, whereas the Müllerian duct gives rise to the fallopian tubes (oviducts), uterus and the upper portion of the vagina. Androgens (including testosterone) have a key role in the development of the male genital tract but are not the only signaling pathways involved. For a sperm and oocyte to meet *in vivo*, millions of spermatozoa leave the seminiferous tubules of the testis to mature in the epididymis before traveling through the vas deferens and urethra to enter the female, where they transverse the vagina, cervix and uterus before typically encountering a single oocyte in one of the fallopian tubes. Surgical contraception involves closing this pathway by removing segments of the two vas deferens (that is, vasectomy) in a man or both fallopian tubes (that is, tubal ligation) in a woman (Matzuk and Lamb, 2008).

In a normal man, spermatogenesis will continue throughout his lifetime and continue to produce millions of sperm in each ejaculate. In contrast, in the ovary, the primordial follicles represent the maximum number of follicles possible in this organ, with subsequent loss occurring during the time between development, birth and puberty, until they are depleted at menopause. In addition, the processes of mitosis and meiosis vary between the ovary and testis, but they are highly regulated by both endocrine and paracrine factors. Epigenetic events are essential to germ-cell development, for example, to maintain genomic integrity in these cells during meiosis or for gene imprinting (figure 60)(Sasaki and Matsui, 2008).

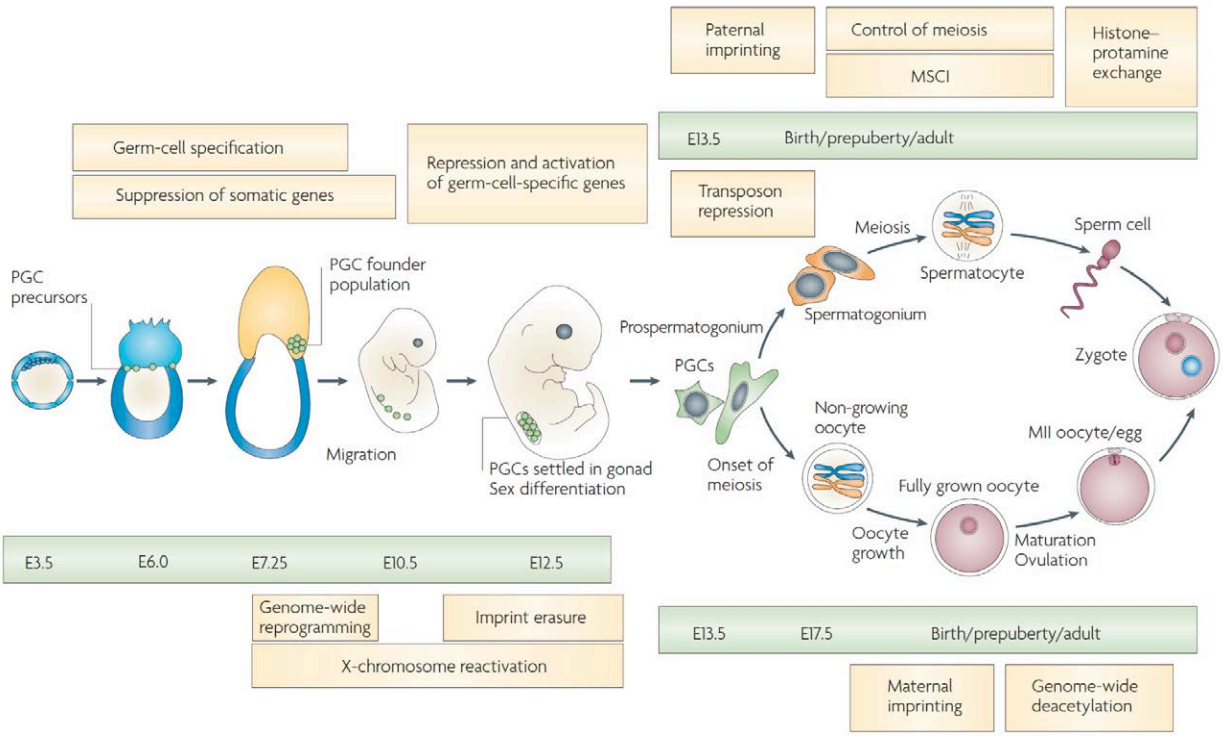

Figure 60: Germ cell development and associated epigenetic events in mice. Chronology of mouse germ cell development and the main epigenetic events that occur. PGCs first emerge at embryonic day 7.25 (E7.25) as a cluster of about 20 cells. Subsequently, they rapidly proliferate with an average doubling time of approximately 16 hours. Before they stop dividing at E13.5, their number reaches up to about 26,000. MSCI, meiotic sex-chromosome inactivation (Sasaki and Matsui, 2008).

The development of the genital tract and secondary sex organs depends upon the occurrence of a testis or an ovary and the presence or absence, respectively, of the sex determining region Y (*SRY*) gene carried on the Y chromosome. The oviducts, uterus and upper portion of the vagina of the female are derived from their embryonic precursor, the Müllerian duct, whereas the epididymis, vas deferens and seminal vesicles of the male differentiate from the Wolffian duct (figure 59)(Kobayashi and Behringer, 2003; Barsoum and Yao, 2006; Gilbert, 2006). The prenatal production of testicular anti-Müllerian hormone (AMH), acting through its receptor AMHR2, induces the regression of the Müllerian duct, whereas testosterone drives the development of these Wolffian duct derivatives. 5-α-reductase has a major role in the metabolism of testosterone to dihydrotestosterone, and this hormone is required for the development of the prostate and male external genitalia.

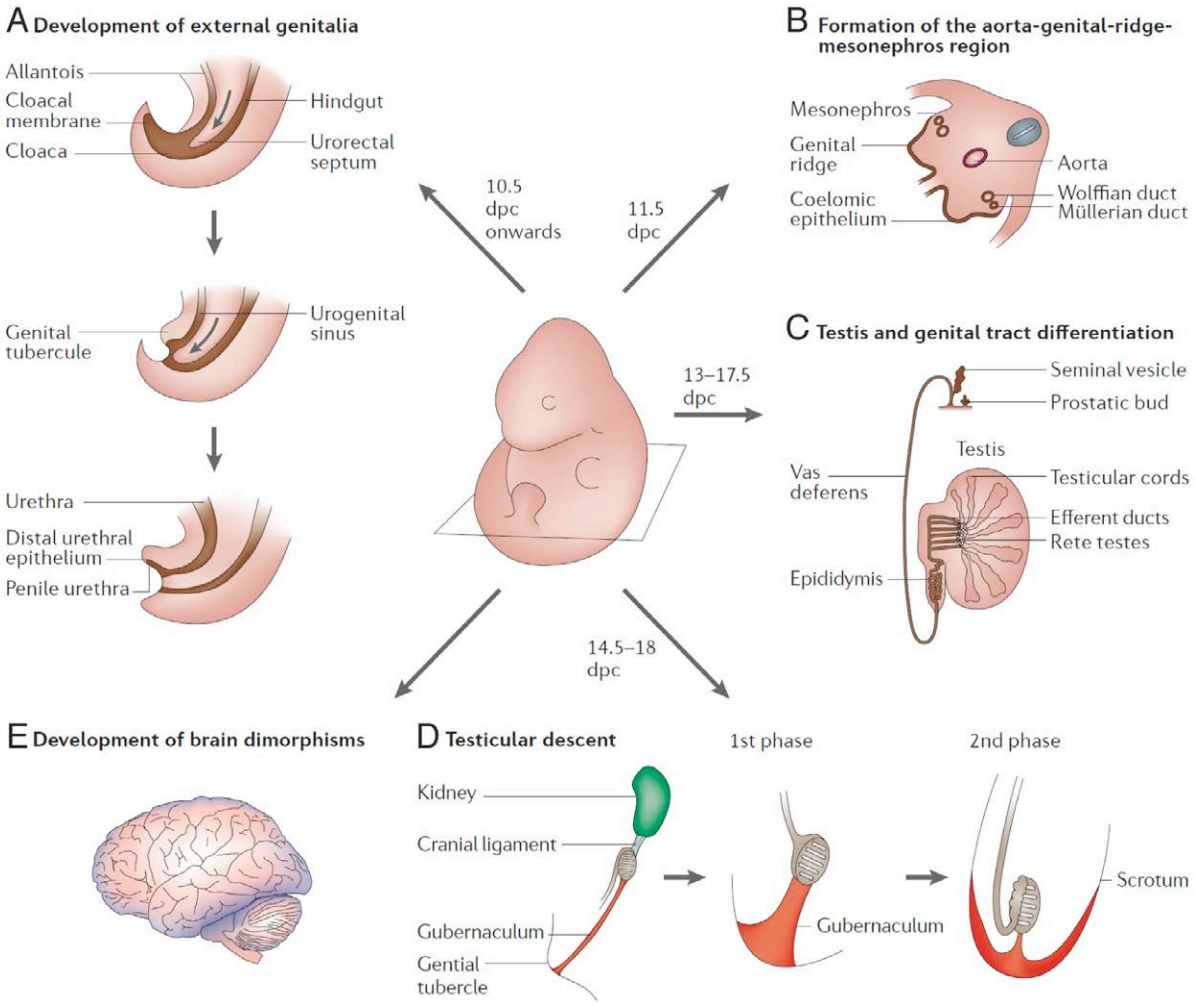

Figure 61: *A*, Major steps in male sexual differentiation. The external genitalia appear as a mesenchymal swelling between the two layers of the cloacal membrane at around 10.5 days post coitum (dpc) and develop further under the influence of testicular androgens. *B*, A transverse section through a mouse embryo at 11.5 dpc shows the developing urogenital ridge, which develops out of the intermediate mesoderm on either side of the aorta and is composed of the mesonephros and genital ridge. Within the mesonephros the Wolffian (male) and Müllerian (female) ducts form. At 11.5 dpc males cannot be distinguished morphologically from females. *C*, However, expression of the male-determining gene Sry induces a cascade of gene expression that results in the differentiation of the genital ridge and the Wolffian duct into the testis and male genital tract (rete testes, epididymis, vas deferens and seminal vesicle), respectively. *D*, At 13 dpc, the bipotential urogenital sinus develops and at 17.5 dpc the prostatic bud is formed by the urogenital sinus under the influence of testicular androgens. Between 14.5 and 18 dpc the testis migrates into the developing scrotum in two phases. *E*, The first phase is due to an enlargement of the gubernaculum, whereas during the second phase the gubernaculum migrates into the scrotum, guided by calcitonin-related peptide that is released by the genito-femoral nerve. The brain develops sexual dimorphisms, some of which are due to direct genetic effects, although most are caused by sex hormones (Wilhelm and Koopman, 2006).

In parallel with the steps of sex determination and differentiation, key developmental and physiological pathways (for example, the gonadotropin and kisspeptin signaling pathways) are being controlled by the hypothalamus and pituitary, foreshadowing puberty and, eventually, reproduction, which are crucially controlled by these organs (figure 61). These developmental and overriding influences allow for highly regulated gene expression at every stage of ovarian folliculogenesis, ovulation, fertilization, implantation and early embryonic development.

Testis structure

Almost healthy male vertebrates have two testes. In mammals, the testes are often contained within an extension of the abdomen called the scrotum. Under a tough membraneous shell, the tunica albuginea, the testis of amniotes, and some teleost fish, contains very fine coiled tubes called seminiferous tubules (figure 62*A*).

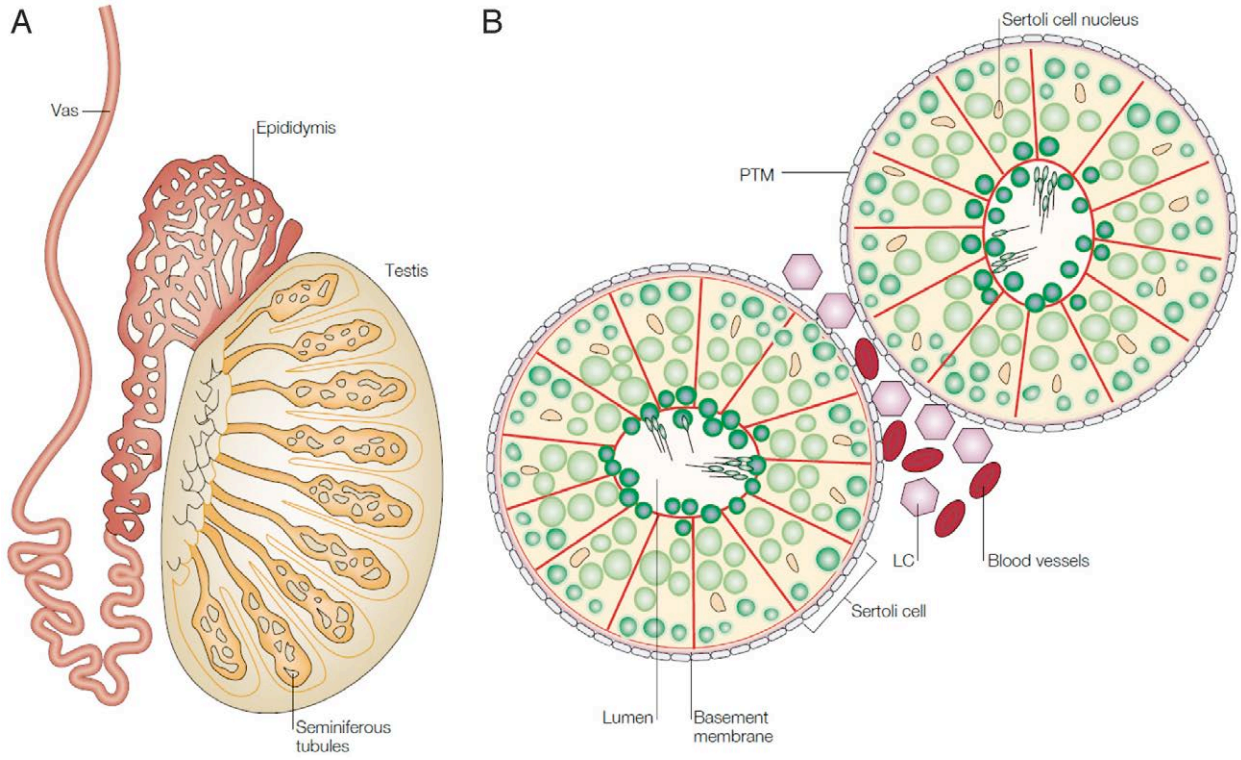

Figure 62: Organization of the testis. *A*, Cross-section through a testis, showing the location of the seminiferous tubules, the vas deferens and the epididymis. *B*, A diagrammatic cross-section through a testicular tubule, showing the germ cells (green) at different stages of maturation developing embedded in somatic Sertoli cells (each Sertoli cell is outlined in red). Leydig cells (LC) — where testosterone is synthesized — are present in the interstitium. Maturing sperm are shown in the lumen of the tubules. PTM, peritubular myoid cell (Cooke and Saunders, 2002).

The tubules are lined with a layer of cells (germ cells) that from puberty to old age, develop into sperm cells (also known as spermatozoa or male gametes). The developing sperm travel through the seminiferous tubules to the rete testis located in the mediastinum testis, to the efferent ducts, and then to the epididymis where newly-created sperm cells mature (see spermatogenesis). The sperm move into the vas deferens, and are eventually expelled through the urethra and out of the urethral orifice through muscular contractions (Marieb, 2009). Leydig cells (LC; also known as interstitial cells of Leydig) are located between seminiferous tubules. They produce testosterone in the presence of luteinizing hormone (LH). Sertoli cells (SC) have the important function to maintain and to nurture the developing sperm cells (figure 62*B*). A single SC extends from the basement membrane to the lumen of the seminiferous tubule. Once

fully differentiated, the SC is unable to proliferate. Therefore, once spermatogenesis has begun, no more SCs are created. The tight junctions of SCs form the blood-testis barrier, a structure that partitions the interstitial blood compartment of the testis from the adluminal compartment of the seminiferous tubules (Mruk and Cheng, 2004). These cells are also responsible for establishing and maintaining the spermatogonial stem cell niche, which ensures the renewal of stem cells and the differentiation of spermatogonia into mature germ cells that progress stepwise through the long process of spermatogenesis, ending in the release of spermatozoa (de Rooij and Grootegoed, 1998; Hess et al., 2006). SCs bind to spermatogonial cells via N-cadherins and galactosyltransferase (via carbohydrate residues)(Akama et al., 2002). Epithelial cells and macrophages are also present in testis.

Spermatogenesis

Spermatogenesis produces mature male gametes, commonly called *sperm* but specifically known as *spermatozoa*, which are able to fertilize the counterpart female gamete, the oocyte, during conception to produce a single-celled individual known as a zygote.

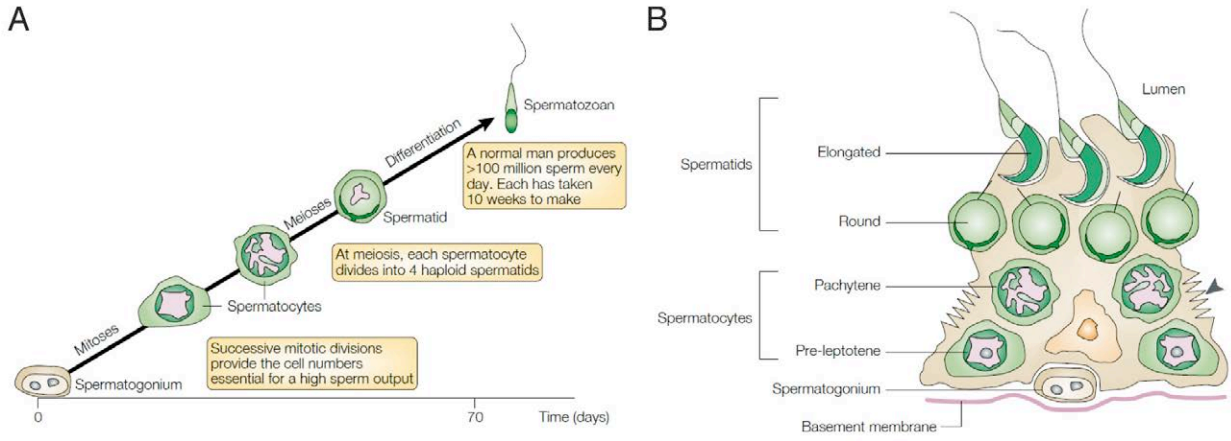

Figure 63: Stages of spermatogenesis. *A*, During the process of spermatogenesis, the mammalian germ cell undergoes mitosis, meiosis and structural remodelling into the mature spermatozoa (cytoplasm is indicated in green, DNA in pink). The time course shown is that for a human male (in mice, spermatogenesis takes 35 days). *B*, A single Sertoli cell with its associated germ cells. Note that tight junctions between Sertoli cells (arrowhead) define two compartments: the stem cells and the pre-meiotic cells (spermatogonia) are found on one side of the junction, whereas the meiotic (spermatocytes) and the post-meiotic (round and elongating spermatids) cells are found organized in strict order of maturation towards the lumen (cytoplasm is shown in dark green, DNA is shown in pink, Sertoli cell nucleus is shown in orange) (Cooke and Saunders, 2002).

Here is the cornerstone of sexual reproduction and involves the two gametes both contributing half the normal set of chromosomes (haploid) to result in a chromosomally normal (diploid) zygote. In humans, spermatogenesis takes about 70 days (figure 63*A*). The spermatogonia development starts from the basement membrane and continues towards the lumen of seminiferous tubule (figure 63*B*).

To preserve the number of chromosomes in the offspring (which differs between species) each gamete must have half the usual number of chromosomes present in other body cells. Otherwise, the offspring will have twice the normal number of chromosomes, and serious abnormalities may result. In humans, chromosomal abnormalities arising from incorrect spermatogenesis can result in Down Syndrome, Klinefelter's Syndrome, and spontaneous abortion.

At the beginning, each primary spermatocyte moves into the adluminal compartment (central region of the Sertoli cells) of the seminiferous tubules and duplicates its DNA and subsequently undergoes *meiosis I* to produce two haploid secondary spermatocytes. This division implicates sources of genetic variation, such as random inclusion of either parental chromosomes, and chromosomal crossover, to increase the genetic variability of the gamete (figure 64).

Each cell division from a spermatogonium to a spermatid is incomplete; the cells remain connected to one another by bridges of cytoplasm to allow synchronous development. It should also be noted that not all spermatogonia divide to produce spermatocytes, otherwise the supply would run out. Instead, certain types of spermatogonia divide to produce copies of themselves, thereby ensuring a constant supply of gametogonia to fuel spermatogenesis (de Rooij and Mizrak, 2008).

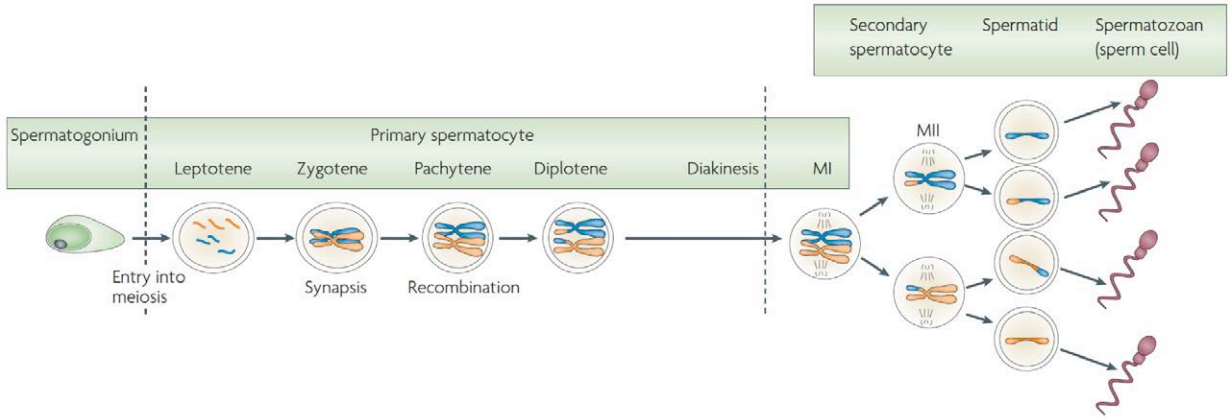

Figure 64: Stages of spermatogenesis. MI, metaphase I; MII, metaphase II (Sasaki and Matsui, 2008).

Spermatidogenesis is the creation of spermatids from secondary spermatocytes. Secondary spermatocytes produced earlier rapidly enter *meiosis II* and divide to produce haploid spermatids. Secondary spermatocytes are rarely seen in histological preparations, meaning that this phase is brief.

During spermiogenesis, the spermatids begin to grow a tail, and develop a thickened mid-piece, where the mitochondria gather and form an axoneme. Spermatid DNA also undergoes packaging, becoming highly condensed. The DNA is packaged firstly with specific nuclear

basic proteins, which are subsequently replaced with protamines during spermatid elongation. The resultant tightly packed chromatin is transcriptionally inactive. The Golgi apparatus surrounds the now condensed nucleus, becoming the acrosome. One of the centrioles of the cell elongates to become the tail of the sperm.

Maturation then takes place under the influence of testosterone, which removes the remaining unnecessary cytoplasm and organelles. The excess cytoplasm, known as *residual bodies*, is phagocytosed by surrounding SCs in the testes. The resulting spermatozoa are now mature but lack motility, rendering them sterile. The mature spermatozoa are released from the protective SCs into the lumen of the seminiferous tubule in a process called *spermiation*.

The non-motile spermatozoa are transported to the epididymis in *testicular fluid* secreted by the SCs with the aid of peristaltic contraction. While in the epididymis the spermatozoa gain motility and become capable of fertilization. However, transport of the mature spermatozoa through the remainder of the male reproductive system is achieved via muscle contraction rather than the spermatozoon's recently acquired motility (Marieb, 2009).

Hormonal influence on spermatogenesis

This endocrine regulation is very complex. As presented in figure 65, signals originate from the brain, more precisely, the hypothalamus secretes gonatotropin-releasing hormone (GnRH), which stimulates the release of follicle-stimulating hormone (FSH) and luteinizing hormone (LH) from the pituitary gland (Sharpe, 1994). They bind to their specific receptors (FSHR and LHR) that are expressed by SCs and LCs, respectively. The paracrine regulation of spermatogenesis is provided by, in one hand, testosterone and oestradiol, that are synthesized by LCs, and on the other hand, the activin and inhibin proteins, that are synthesized by SCs. The primary function of LH is to stimulate the synthesis of testosterone by LCs (Moyle and Ramachandran, 1973; Zhang et al., 2001). FSH acts directly on SCs to stimulate germ cell number and acts to increase androgen production by the LCs (O'Shaughnessy et al., 2010). Testosterone is necessary for normal sperm development. It activates genes in SCs, which promote differentiation of spermatogonia.

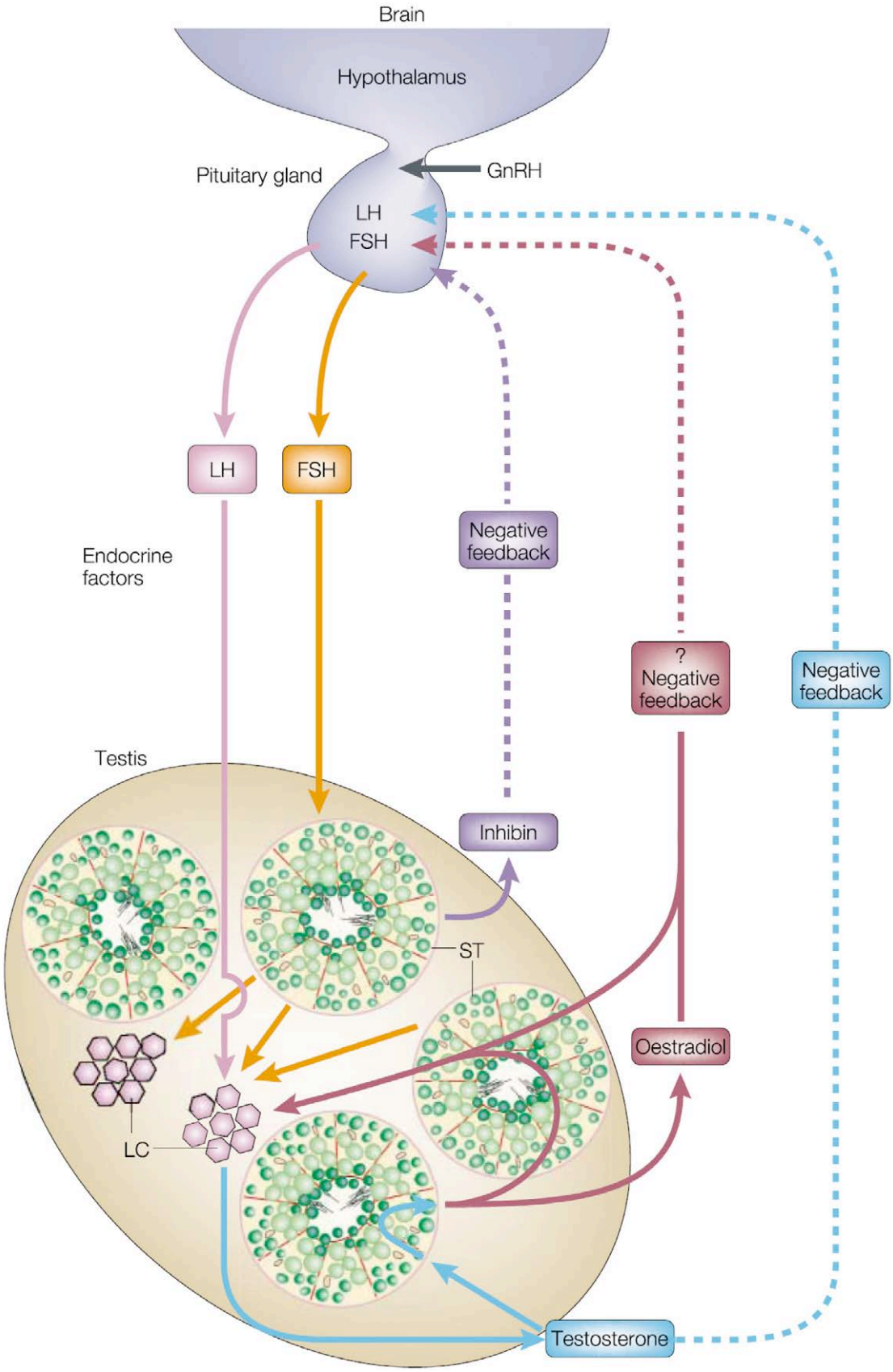

Figure 65: Hormonal regulation of spermatogenesis. Endocrine factors secreted by the pituitary gland (LH, luteinizing hormone; FSH, follicle-stimulating hormone) and local regulators of testis function (such as androgens, oestrogens and inhibins), as well as modulators of gene expression in the pituitary gland (the negative-feedback loops), are involved in the regulation of spermatogenesis. Receptors for LH and FSH are expressed in selected testicular cell populations. GnRH, gonadotrophin-releasing hormone; LC, Leydig cells; ST, Sertoli cells (Cooke and Saunders, 2002).

In this process, the exact role of testosterone is difficult to define. Indeed, it binds to the androgen receptor (AR), and when this gene is not functional (for example, individuals who carry loss-of-function mutations), the male gonad development is impaired and feminization phenotype is observed (Ghadessy et al., 1999). This is also observed with mutations in enzymes involved in androgen biosynthesis (Achermann et al., 2002). The aromatase (*cyp19*) is the enzyme responsible for the irreversible conversion of testosterone to estrogen (Carreau et al., 2006). Correct androgen/estrogen balance is essential for normal sexual development and reproduction (Delbes et al., 2006; Carreau et al., 2007). It has been shown in the rat, that there is an age-related change in cellular distribution of aromatase activity being mainly in SCs of immature animals and then in LCs of adults (Carreau et al., 1999). But, expression in germ cells has also been reported (Nitta et al., 1993). The estrogen receptor (ER) mediates the effects and belongs to the nuclear receptor family. The two ERα and ERβ mRNAs are encoded in the gonad, but their spatio-temporal distribution is different (Saunders et al., 1998; Lambard et al., 2004). Interestingly, mice deficient for ERα are infertile (secondary phenotype), whereas it is not the case with ERβ knockout mice (Eddy et al., 1996; Krege et al., 1998).

GILZ and its role in reproduction

Only few studies show the presence of GILZ in the reproductive organs or along the HPG axis. Cross-species expression profiling analysis of the human, mouse, and rat male meiotic transcriptional program, using enriched germ cell populations, whole gonads, and high-density oligonucleotide microarrays has been performed (Chalmel et al., 2007). From this study, it is possible to point out the relative expression profile of GILZ mRNA transcripts in several tissues and principally in the gonads (figure 66*A*). GILZ is widely expressed throughout the body. It is found in the testis and ovary as well. In the testis, it is mostly expressed in the spermatogonia (figure 66*B*) and mainly during the early phases on spermatogenesis (figure 66*C*).

GILZ is expressed in the anterior pituitary during the second half of embryonic development in the chick. This is consistent with *in vivo* regulation by circulating corticosteroids. Pituitary GILZ mRNA levels increase during embryogenesis to a maximum on the day of hatch, and decreased through the first week after hatch. GILZ expression is rapidly upregulated by corticosterone in embryonic pituitary cells. Exogenous GILZ overexpression increased prolactin mRNA above basal levels, but not as high as that in corticosterone-treated cells, indicating that GILZ may play a small role in lactotroph differentiation. The largest effect

observed was a twofold increase in FSHβ subunit in cells transfected with GILZ but not treated with corticosterone, suggesting that GILZ may positively regulate gonadotroph development in a manner not involving glucocorticoids (Ellestad et al., 2009).

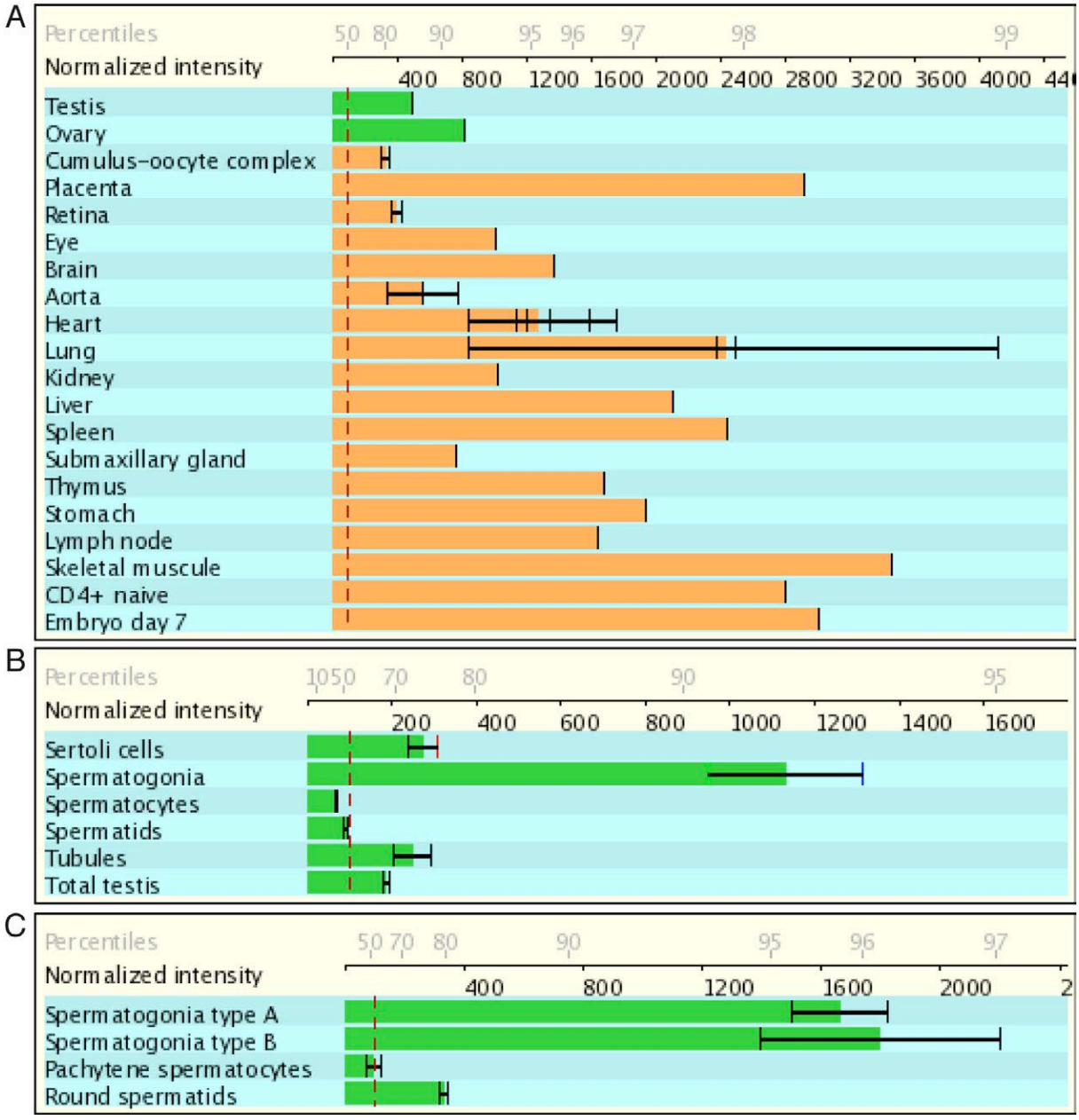

Figure 66: GILZ mRNA transcript expression (from GermOnline database website). Normalized GILZ intensity in various mouse organs (*A*), cells from testis (*B*) and developing spermatogonia (*C*) (Chalmel et al., 2007).

Using microarray analysis, Tynan et al., identified 27 genes that were up-regulated and 20 that were down-regulated by estrogen in MCF-7 human breast cancer cells. GILZ is rapidly down-regulated by estrogen in these cells. Estrogen antagonists block the down-regulation. The region of the GILZ promoter between nucleotides -104 and -69 mediates both basal activity

and estrogen-dependent down-regulation in MCF-7 cells. This region contains a functional Oct-1 binding site and a cAMP response element binding protein (CREB) binding site. The same DNA region mediates up-regulation by estrogen in HeLa and HEK293 cells, indicating that cell-specific factors are involved in estrogen regulation of this gene. The estrogen receptor (ER) is present in GILZ promoter protein complexes, but it does not bind directly to the promoter itself, as the DNA-binding domain of the estrogen receptor is not required for down-regulation. Elimination of the CREB binding site blocks both basal activity and estrogen regulation (Tynan et al., 2004). Estrogen increases near the end of of murine pregnancy, it is plausible that estrogen down-regulates GILZ in the decidua between gestational days 16.5 and 19.0 (Watanabe et al., 2003). Using *in situ* hybridization, GILZ expression has been found at the site of implantation in the later stages of murine pregnancy (Zhao et al., 2006).

TSC22d1 knockout mice are subfertile (personal communication by Dr. Laurel Raftery). Earlier work on cell lines showed that TSC22 transcript is upregulated in response to FSH or progesterone stimulation (Dohrmann et al., 1999). Together, these data suggest that the TSC22 family plays a role in reproduction.

WORKING HYPOTHESIS

Glucocorticoids (GCs) are widely used as therapeutic agents (mainly as anti-inflammatory drugs). They function in every organ and are thus implicated in a variety of physiological processes such as growth development and maintenance of homeostasis. GCs regulate up to 10% of the genes and the glucocorticoid-induced leucine zipper (GILZ, Tsc22d3) has been identified as one of the most expressed genes; thus, GILZ has been proposed to mimick GCs function. Earlier investigations strongly suggested that GILZ might be implicated in the regulation of the epithelial sodium channel (ENaC), consequently having a role in sodium and water handling. We expected that if ENaC was not properly regulated, due to GILZ-deficiency and that the other factors, e.g., SGK1 or Nedd4-2, being part of the described ENaC/GILZ/Nedd4-2/SGK1 complex, could not compensate for the lack of GILZ, we might observe a renal phenotype. We expect, in case of GILZ-deficiency, hypotension, lower blood pressure or salt loosing phenotype. GILZ was proposed to play a role in the differentiation of adipocytes and bone regulation, implying a possible developmental phenotype.

The aim of my thesis project was to analyze the phenotype of GILZ knockout mice. We were interested to investigate the pathways or processes in which GCs play a role, for example in immunity or metabolism. We also wanted to analyze tissues in which less was known about potential GILZ functions, like in skin physiology.

Finally, by dissecting the expression of related genes (like *PPARγ2*) we addressed the question whether GILZ mimics the effects of GCs *in vivo*. Other members of the same family may compensate the lack of GILZ.

MATERIAL AND METHODS

Generation of conditional and null mutant *Tsc22d3* mice

The *Tsc22d3* gene was cloned from a 129/Sv mouse genomic BAC library (Incite Genomics, Inc., USA). For *Tsc22d3* gene information, see GenBank accession number NM_010286.3. The following fragments were then subcloned into a modified lox-targeting vector containing 2 loxP and 2 Frt sites. First, a 10kb (5' region, haboring exon 3) and a 5kb *Eco*RI fragments (3' region, harboring exons 4 to 6), were subcloned into pBSII KS(-) and extracted using *Pac*I and *Stu*I restriction sites. The neomycin resistance gene cassette flanked by *frt* sites and followed by one *loxP* site (Dymecki, 1996), (Rajewsky et al., 1996) was cloned into *Eco*RV (3' of the polyA region). The second *loxP* sequence was introduced in a *Sma*I restriction site created by PCR-based mutagenesis, along with a new diagnostic *Eco*RV restriction site 5' of the third exon. Finally, the thymidine kinase cassette (HSV-tK) was inserted 3' of the homologous region. Further details of cloning are available on request. The targeting vector was linearized with *Pac*I, and transfected into A2 embryonic stem cells (ES cells) of the 129Sv/EV background (Reis et al., 1994; Hummler et al., 2002) as described previously (Hummler et al., 1996). G418 and ganciclovir-resistant colonies were expanded and screened by PCR using the following primers; 5' recombination: sense 5'-ATAGCCTGTGCTCTGGAACT-3', antisense, 5'-TTATGGCGCGGGGATATCTA-3' and 3' recombination: sense 5'-GCCTCCGAGGTTGCAGTGTTT-3', antisense 5'-TCGCCTTCTTGACGAGTTCTTC-3'. Targeted clones were confirmed by Southern blot analysis using two external probes (3' probe: 315 bp fragment isolated from the 3' *Eco*RI clone by *Stu*I and *Bgl*II on *Eco*RI-digested DNA, and 5' probe: 1085 bp fragment isolated from the 5' *Eco*RI clone by *Dra*I on *Eco*RV-digested genomic DNA). PCR-amplified neomycin sequences were used as internal probe. Correctly targeted clones were injected into C57BL/6N blastocyts as described (Porret et al., 2006). Breeding of $Tsc22d3^{loxneo}$ mice with Flp mice (Rodriguez et al., 2000) allowed the excision of the neomycin cassette and with nestin-CRE (Dubois et al., 2006) mice to generate mice haboring the Δ allele. To obtain knockout males ($Tsc22d3^{\Delta/y}$), heterozygous mutant $Tsc22d3^{\Delta/+}$ females were crossed with wildtype males. $Tsc22d3^{\Delta/+}$ and $Tsc22d3^{+/+}$ females, as well as $Tsc22d3^{+/y}$ and $Tsc22d3^{\Delta/y}$ males were genotyped by PCR (sense (s1): 5'-CAGGTCTGAGTAACTTGTCC-3', antisense (as): 5'-CAGTCTGTGGTGACCGTTTC-3', sense (s2): 5'-TGACAGCTGCGTTTCTCAGTG-3'). The s1, s2 and as primers were used for genotyping of lox and wt alleles, and s1 and as for the Δ allele.

All animals were housed in a controlled environment with a 14 h light/10 h dark cycle with free access to water and standard laboratory diet. Males were aged from 3 to 6 months, and were backcrossed to C57BL/6N mice (N4-N6). The control group consisted of age-matched *Tsc22d3*$^{+/y}$ and *Tsc22d3*$^{lox/y}$ littermates. Mouse experiments were conducted under authorization of local authorities and followed Swiss guidelines.

Histology and immunohistochemistry

2-(*n*=2) and 6-(*n*=1) month-old mice were dissected and organs fixed with buffered formalin (pH 7.2) for 12 hours. Tissues were embedded in paraffin (Leica Microsystems, Wetzlar, Germany) and 2-3 μm sections were stained with haematoxylin and eosin (H&E). Testis cellular proliferation was assessed by Ki-67 antibody (monoclonal rat anti-mouse, Dako M7249, Carpinteria, CA, USA; dilution 1:50) with goat anti-rat HRP secondary antibody (Biosource ALI 3404, Camarillo, CA, USA). Apoptosis was analysed using terminal transferase and Biotin-16-dUTP (TUNEL Enzyme, Roche 11 767 305 001; dilution 1:250 and Biotin-16-dUTP, dilution 1:250; Roche 11 093 070 910, Roche Diagnostics GmbH, Mannheim, Germany). Sertoli cells were labelled with the rabbit anti-CTCF (#06–917; Upstate cell signaling, Millipore, Billerica, MA, USA; dilution 1:100); secondary antibody used was EnVision (DakoCytomation, Glostrup, Denmark) as previously described (Jelinic et al., 2006). Pancreas sections were incubated with antibodies against insulin (Linco 4011-01, Linco Research Inc., St. Charles, MO, USA; dilution 1:6000) and glucagon (Linco 4030-01F, Linco Research Inc., St. Charles, MO, USA; dilution 1:6000), and then revealed with Fuchsin (Kit DAKO K0625, Dako, Denmark; dilution 1:50) and DAB (Kit DAKO K3468, Dako, Denmark; dilution 1:50), respectively. GILZ1 and GILZ2 proteins were labelled with the polyclonal Tsc22d3 antibody as described (Soundararajan et al., 2007).

Quantitative real-time PCR

Following sacrifice, tissues were collected and quickly snap frozen in liquid nitrogen and kept at -80° C until used. Total RNA was extracted from tissues with the RNeasy Mini Kit or Qiazol (Qiagen, Valencia, CA, USA). RNA quality was verified on an agarose gel and the concentration was determined by a ND-1000 Spectrophotometer (NanoDrop, Wilmington, DE, USA). Total RNA (1 μg) was subjected to reverse transcription using the SuperScript II First-Strand Synthesis System for RT–PCR (Invitrogen/Life Technologies Corporation, Carlsbad, CA, USA) following the manufacturer's instructions. The resulting cDNA was used as a template for quantitative PCR (qPCR). Results were normalized using the reference genes

glyceraldehyde 3-phosphate dehydrogenase (GAPDH) or RNA polymerase II. Quantitative real-time analysis of selected genes was performed using the ABI Prism 7500 Fast Real-Time PCR System, SYBR Green as DNA binding dye for the detection of PCR products or the TaqMan probe technology (Applied Biosystems/Life Technologies Corporation, Carlsbad, CA, USA). Intron-spanning primers were designed (Microsynth AG, Switzerland) (see table II list for oligonucleotides). The cycling conditions were 95 °C for 10 min, followed by 40 cycles of 95 °C for 15 s, and 60 °C for 1 min. To detect and eliminate possible primer–dimer artifacts, the dissociation curve was generated by adding a cycle of 95 °C for 15 s, 60 °C for 1 min and 95 °C for 15 s. All primer sets produced amplicons of the expected size and their identity was also verified by migration of the PCR products on agarose gel. The quantification was done by measuring the ΔΔCt normalized to the reference gene. All measurements were done at least in triplicate, $n = 3$ mice per group, analysis performed in triplicate, data represent average ± SEM, in all tissues tested.

Western blot analyses

Mice were sacrificed according to standard procedures and various tissue samples were collected from dexamethasone (55 μg/100g body weight)-treated and non-treated, control and knockout mice. The dexamethasone was administred intraperitoneally 3-4 hours before euthanasia. Tissue lysis was performed in ice-cold urea (8M) using the TissueLyser (Qiagen, Valencia, CA, USA). Protein levels were quantified using the Pierce BCA Protein Assay Reagent (Thermo Fisher Scientific, Waltham, MA, USA) with BSA as a standard. Equal amounts of protein extracts were resolved by 12% SDS-PAGE and electro-transferred onto a Protran nitrocellulose membrane (Whatman/GE Healthcare, Piscataway, NJ, USA). Blots were blocked in tris-buffered saline containing 0.1% Tween (TBS-T) supplemented with 4% milk powder and immunoblotted using anti-TSC22d3 antibody, as described previously (Soundararajan et al., 2007). The blots were stripped and reprobed with GAPDH antibody (Chemicon/Millipore, Billerica, MA, USA) as a loading control; $n = 2$ mice per genotype.

Hormone measurements

For plasma aldosterone and corticosterone measurements, mice ($n \geq 7$) were killed by rapid decapitation between 4-6 pm. Blood was collected in EDTA tubes, immediately centrifuged and stored at -20 ^{o}C until assayed for hormone level determination. Plasma aldosterone levels were measured according to standard procedure using a radioimmunoassay (RIA) using the Coat-A-Count RIA kit (Siemens Medical Solutions Diagnostics, Ballerup, Denmark). Mice

samples exhibiting values greater than 1200 pg/ml were previously diluted using a serum pool with a low aldosterone concentration (<50 pg/ml). Corticosterone was measured by RIA (IBL, Hamburg, Germany), FSH was measured by IRMA (IBL, Hamburg, Germany), and LH was measured by RIA (IDS, Liège, Belgium). Testosterone levels were assayed using a kit from MP Biomedicals (Testo DA Kit, Eschwege, Germany). The standard curves ranged between 2 and 200 ng/ml for FSH, 0.25 and 15 ng/ml for LH, and 0.1 and 10 ng/ml for testosterone. Intra- and inter-assay coefficients of variation (CVs) of all three assays were less than 5% and 10%, respectively, n = 10 mice per genotype.

Metabolic parameters

Body weight was measured on a weekly basis over the whole study. Body composition was analyzed on individual 2.5- and 15-month-old mice under light gaz anesthesia (1-2 % isoflurane), by quantitative nuclear magnetic resonance using an EchoMRI Whole Body Composition Analyzer (EchoMedical Systems, Houston, TX, USA). Data for individual mice were obtained by averaging results from two consecutive measurements. Plasma glucose levels in the fed, 15h fasted or 6h-refed states were measured with a glucometer (Ascensia Breeze2, Bayer, Switzerland). Plasma insulin levels were determined from tail-tip bleedings by ELISA (Ultrasensitive Mouse insulin ELISA, Mercodia AB, Uppsala, Sweden).

Glucose tolerance test; after a 15-hour overnight fast period, 6-month-old mice were injected i.p. with 1.5 mg/g glucose. Plasma glucose levels were measured 30 minutes before and punctually during 120 minutes after administration ($n \geq 6$ per group).

Insulin tolerance test; following 4 hours of food removal (9am-1pm), age-matched 7 months old mice were injected i.p. with 0.8 mU/g insulin by intraperitoneal injections. Blood samples were obtained from tail-tip bleedings, and plasma glucose levels were measured with a glucometer (Ascensia Breeze 2, Bayer, Switzerland).

Adipocyte differentiation ; Mouse embryonic fibroblasts (MEFs) were generated from 13.5-day-old embryos obtained from heterozygous mutant female *Tsc22d3*$^{+/\Delta}$ mated to wild type malese (Yang et al., 2003). Briefly, after removal of head and visceral organs (used for genotyping), embryos were minced and trypsinized for 30 minutes at 37°C. Embryonic fibroblasts were then plated and maintained in DMEM (with 10% foetal calf serum (FCS) (Life Technologies), 100 U/ml penicillin and 100 µg/ml streptomycin) at 37°C in an atmosphere of 5% CO_2. All experiments were performed with Tsc22d3 wild-type and knockout MEFs after 15-20 passages. For adipocyte differentiation, 2-day-postconfluent cells (day 0) were transferred to DMEM supplemented with 10% FCS, 8 µg/ml biotin, 4 µg/ml pantothenate, 0.5

mM 3-isobutyl-1-methylxanthine, 1 μM dexamethasone and 10 μg/ml insulin for 2 days (all from Sigma). Medium was renewed every 2 days with DMEM containing 10% FCS, 8 μg/ml biotin, 4 μg/ml pantothenate and 10 μg/ml insulin. LY294002 (Calbiochem) was prepared in dimethyl sulfoxide (DMSO) and added at a final concentration of 50 μM in the medium 20 minutes before, and, every 12 hours after addition of the adipose cocktail. To visualize lipid accumulation, cells were stained with Oil Red O (Ramirez-Zacarias et al., 1992). Briefly, cells were washed with phosphate-buffered saline (PBS), fixed with 3.7% formaldehyde solution for 1 hour and stained with Oil Red O for 1 hour using a 60:40 (v/v) dilution in water of a 0.5% stock solution (in isopropanol). Cells were then washed twice with PBS and twice with water. MEFs were pooled from $n = 2$ per genotype. Experiments were performed in triplicate.

Sodium-restriction diet and water deprivation

Mice (20–24 weeks old) were fed with a standard salt diet (0.17% sodium, Ssniff Spezialdiäten GmbH, Soest, Germany) followed by 12 days with a sodium-deficient diet (<0.01% sodium, Ssniff Spezialdiäten GmbH, GERMANY). The 23 hours water deprivation was performed under normal-salt diet. Body weight, food and water intake were measured during the experiment. Spot urine and serum/blood samples were collected before and after each experiment, and osmolarity as well as sodium, potassium and creatinine composition were analyzed at the Laboratoire Central de Chimie Clinique of the University Hospital (CHUV, Lausanne, Switzerland).

Flow Cytometry and Monoclonal Antibodies

Thymocyte, lymph node and spleen single cell suspensions were prepared by standard methods and stained for FACS analysis at 4°C as follows. Cells were preincubated in 50% anti-mouse FcR (CD16/32; clone 2.4.G.2) culture supernatant and then stained with the following monoclonal antibody conjugates: CD4 (RM-4.5 or GK1.5)-FITC, -PE-Cy5 or PE-Cy7; CD8α (53.6.7)-FITC or Alexa 647; CD11b (M1/70)-FITC, PE-Cy5 or Alexa 647; CD24 (M1/69)-PE; CD25 (PC61.5)-Alexa 700 or APC-Alexa 750; CD41 (MWReg30)-FITC or -PE; CD44 (IM781)-PE-Cy7 or Pacific Blue; CD45R/B220 (RA3-6B2)-FITC, PE-Texas Red or PE-Cy7; CD62L (Mel14)-FITC; CD71 (R17217)-PE; CD122 (5H4)-PE; CD117 (2B8)-APC; F4/80 (BM8)-APC Alexa750, Gr1 (RB6-8C5)-FITC, Alexa 647 or Alexa 700; Ter119-FITC or APC-Alexa 750; TCRβ (H57)-FITC, PE-Cy5 or APC-Alexa750; TCRγδ (GL3)-FITC or PE-Cy5. DN1 ($CD117^+CD44^+CD25^-$), DN2 ($CD117^+CD44^+CD25^+$), DN3 ($CD117^-CD44^-CD25^+$), DN4 ($CD117^-CD44^-CD25^-$), ISP ($CD4^-CD8^+TCR\beta^-$), γδT cells, DP (double positive, $CD4^+CD8^+$),

CD8 SP (single positive, $CD4^-CD8^+$), CD4 SP ($CD4^-CD8^+$). All FITC conjugates were purified and conjugated in the Ludwig Institute with the exception of CD41-FITC, which was purchased from BD Biosciences (San Jose, CA, USA). All Alexa 647 conjugates were prepared in the Ludwig Institute using the Alexa 647 conjugation kit from Invitrogen (Carlsbad, CA, USA). All other monoclonal antibody conjugates were purchased from eBioscience (San Diego, CA, USA). Intracellular staining for TCRβ was performed after first surface staining with all monoclonal antibodies. After fixation and permeabilization in Cytofix/Cytoperm (BD Biosciences, San Jose, CA, USA), the cells were incubated overnight at 4°C in 1x Permwash solution (BD Biosciences, San Jose, CA, USA) containing TCRβ-PE-Cy5 and then washed in 1x Permwash and resuspended in PBS/3% FCS for FACS analysis. Samples were analyzed on either a FACS Canto™ or a FACS LSR II™ (both Becton Dickinson, San Jose, CA, USA) and the data analyzed with FlowJo™ software (TreeStar, Ashland, OR, USA).

Cell Cycle analysis and icBcl2 staining. After surface staining, the cells were fixed and permeabilized (as above). Ki-67 staining and DNA content was performed as previously described (Wilson et al., 2008). Anti-human Ki-67-FITC (BD Biosciences, San Jose, CA, USA) and Hoechst 33342 at 20g/ml were added to the cells in 1x Permwash, incubated at 4°C, then washed and resuspended as above. The cells were analyzed on a LSR II™ Flow Cytometer equipped with a 355nm UV laser to detect Hoechst fluorescence. After surface staining, fixation and permeabilization (see above), the cells were incubated with anti-mouse Bcl2-FITC (BD Biosciences, San Jose, CA, USA), washed and analyzed as above. Data were analyzed with FlowJo™ software.

Inflammation experiments

Three-month-old mice were sacrificed (n = 3, each group) and bone marrow-derived dendritic cells (BMDC), bone marrow-derived macrophages (BMDM) and thioglycolate-elicited peritoneal macrophages (TEPM) were prepared and stimulated as previously described (Gross et al., 2006; Muruve et al., 2008; Gross et al., 2009). Briefly, LPS, MSU, ATP, Candida and CpG stimuli were obtained from InvivoGen (San Diego, CA, USA), ELISA kits from R&D Systems (Minneapolis, MN, USA). Bone marrow-derived macrophages (BMDMs) were obtained as previously described (Roger et al., 2009) and cultured in IMDM containing 10% FCS (Sigma-Aldrich), 100 UI/ml penicillin, 100 μg/ml streptomycin and 50 μM 2-mercaptoethanol. Cells were preincubated for 1 h with dexamethasone (Sigma-Aldrich) prior to stimulation with 10 ng/ml of *Salmonella minnesota* Ultra Pure lipopolysaccharide (LPS) (List Biologicals Laboratories), 10 μg/ml Pam_3CSK_4 lipopeptide (EMC microcollections), 5x 10^7

heat-inactivated *Escherichia coli* (*E. coli*) J5 or 0.1 μM CpG oligodeoxynucleotide (CpG ODN, Coley Pharmaceutical Group). Cell culture supernatants were collected to measure the concentrations of IL-12p40 by ELISA (BD Biosciences) and the concentrations TNF and IL-6 by bioassay (Roger et al., 2001). Splenocytes (5 x 10^5 cells in 200 μl) were seeded in 96-well plates coated with 1 μg/ml anti-CD3 and anti-CD28 antibodies (BD Biosciences) or stimulated with 2.5 μg/ml concanavalin A (Con A, Sigma-Aldrich) in the presence or the absence of dexamethasone. IL-2 in cell culture supernatants collected after 24 h was measured by ELISA (BD Biosciences).

Germ cell and Sertoli cell specific knockout mice

Gilz(lox) and Vasa-Cre (Mvh-Cre) mice were kindly provided by D.H. Castrillon, and were genotyped as described (Gallardo et al 2007). To achieve selective inactivation of Gilz in germ cells, we mated transgenic male mice expressing Cre recombinase under the control of the Mvh promoter with female mice carrying two floxed Gilz alleles in order to generate 50% Vasa-Cre;$Gilz^{fx/y}$ and 50% $Gilz^{fx/y}$ male mice. These males were used to study the depletion of Gilz in the germline. On the other hand, $Gilz^{fx/y}$ males were mated with Vasa-Cre;$Gilz^{fx/wt}$ females in order to produce Vasa-Cre;$Gilz^{fx/fx}$ females as well as $Gilz^{fx/fx}$ and Vasa-Cre;$Gilz^{fx/wt}$ control littermates to assess the depletion of Gilz in the female germ cells. The genetic background of these mice is C57Bl/6J and SV129.

In order to study the depletion of Gilz in the Sertoli cells, we mated Gilz lox females with Mis-Cre (amh-cre) transgenic mice (kindly provided by F.Guillou; lecureuil et al 2002). To achieve selective inactivation of Gilz in Sertoli cells, we mated transgenic male mice expressing Cre recombinase under the control of the Amh promoter with female mice carrying two floxed Gilz alleles in order to generate 50% Mis-Cre;$Gilz^{fx/y}$ and 50% $Gilz^{fx/y}$ male mice.

Sperm analysis

Epididymal sperm count was performed with sperm extracted from the caudal epididymis and ductus deferens of adult (P80) male mice and was analyzed for its concentration as previously described (Guerif et al 2002).

Statistical analysis

Data were analyzed using the Student's *t* test for comparison between the groups. Results are expressed as the mean ± SEM. A P value < 0.05 was considered as statistically significant.

CONTRIBUTIONS

For this project we established many collaborations, because it would have been difficult to make specialized and detailed analyses in immunology, fertility or particular metabolic aspects. I have performed all experiments and measurements, with exception of the paraffin sections and the various stainings (H&E, Ki67, TUNEL, insulin, glucagon) were performed by Jean-Christophe Stehle (Pathology Institute, UNIL). Dr. Elena Gonzalez-Rodriguez and Anne-Marie Mérillat developed the GILZ knockout mouse model in our group. I took care of this mouse line during the period of investigation. The Western blots against GILZ were performed by the group of Prof. David Pearce, because he had the best antibody available. I prepared and sent them the membranes for antibody hybridization. I prepared mouse embryonic fibroblasts from knockout and control animals, and Dr. Karim Nadra performed the adipogenesis differentiation assay. The analysis of the immune system development was performed by FACS by Dr. Anne Wilson. Dr. François Saller performed the blood status. Inflammasome activation and inflammation process analysis were performed by Dr. Virginie Pétrilli, Dr. Olaf Gross and Dr. Thierry Roger. The plasma glucose and insulin measurements, the high fat diet experiments and the echo MRI data were performed at the Mouse Metabolic Evaluation Facility (Dr. Frédéric Preitner). The studies involving the Sertoli and germ cell specific knockouts are done by Yannick Romero. Hormone measurements were done by the groups of Prof. François Pralong and Dr. Marc Maillard.

RESULTS

Analysis of GILZ knockout mice

In order to generate constitutive mutant mice for GILZ we performed 3 different breedings. The aim was to obtain y/Δ (knockout) mice, since *GILZ* is X-linked. In the first breeding, we crossed +/Δ females with y/+ males. In the second breeding, the males were y/lox and the females lox/Δ. In the third breeding, the males were y/+ and the females lox/Δ (figure 67). In all breedings, the Mendelian distribution of genotypes was observed.

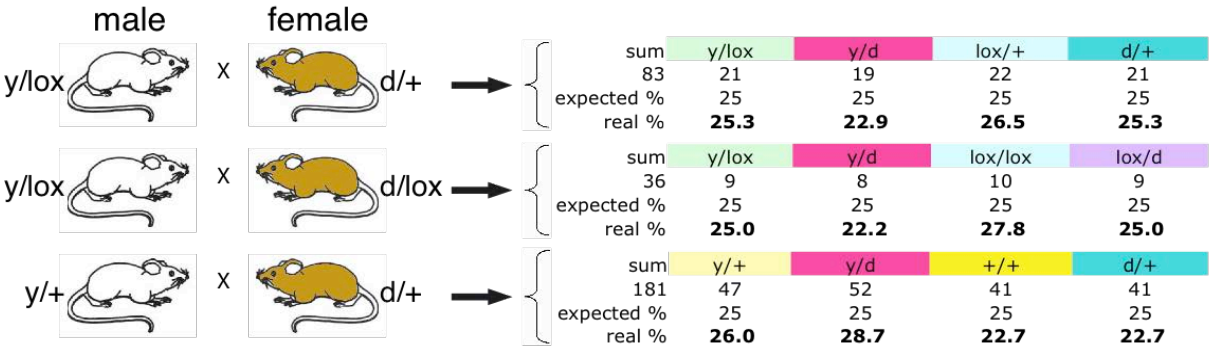

sum	y/lox	y/d	lox/+	d/+
83	21	19	22	21
expected %	25	25	25	25
real %	**25.3**	**22.9**	**26.5**	**25.3**

sum	y/lox	y/d	lox/lox	lox/d
36	9	8	10	9
expected %	25	25	25	25
real %	**25.0**	**22.2**	**27.8**	**25.0**

sum	y/+	y/d	+/+	d/+
181	47	52	41	41
expected %	25	25	25	25
real %	**26.0**	**28.7**	**22.7**	**22.7**

Figure 67: Offspring number values. Breeding strategy to produce control (y/+ or y/lox) and knockout (y/d) male mice. Females are either control (+/+, lox/+ or lox/lox) or heterozygous (d/+ or lox/d). Expected Mendelian ratio is 25%. Obtained ratio for each breeding is give in bold numbers.

When we further bred y/Δ mice with lox/Δ or +/+ mice for a prolonged time, we never obtained offspring. The further analysis of these mice showed that they were sterile. Thus, it was not possible to obtain a Δ/Δ (knockout) female mice for the *GILZ* gene by standard breeding strategy.

Tissue quantitative RT-PCR analysis for GILZ

In order to verify whether the gene locus was inactivated, we quantified the expression of GILZ mRNA in kidney, heart, testis, liver, spleen, skin, brain and lung (figures 68 and 69). This screening confirmed that no mRNA transcript expression could be detected.

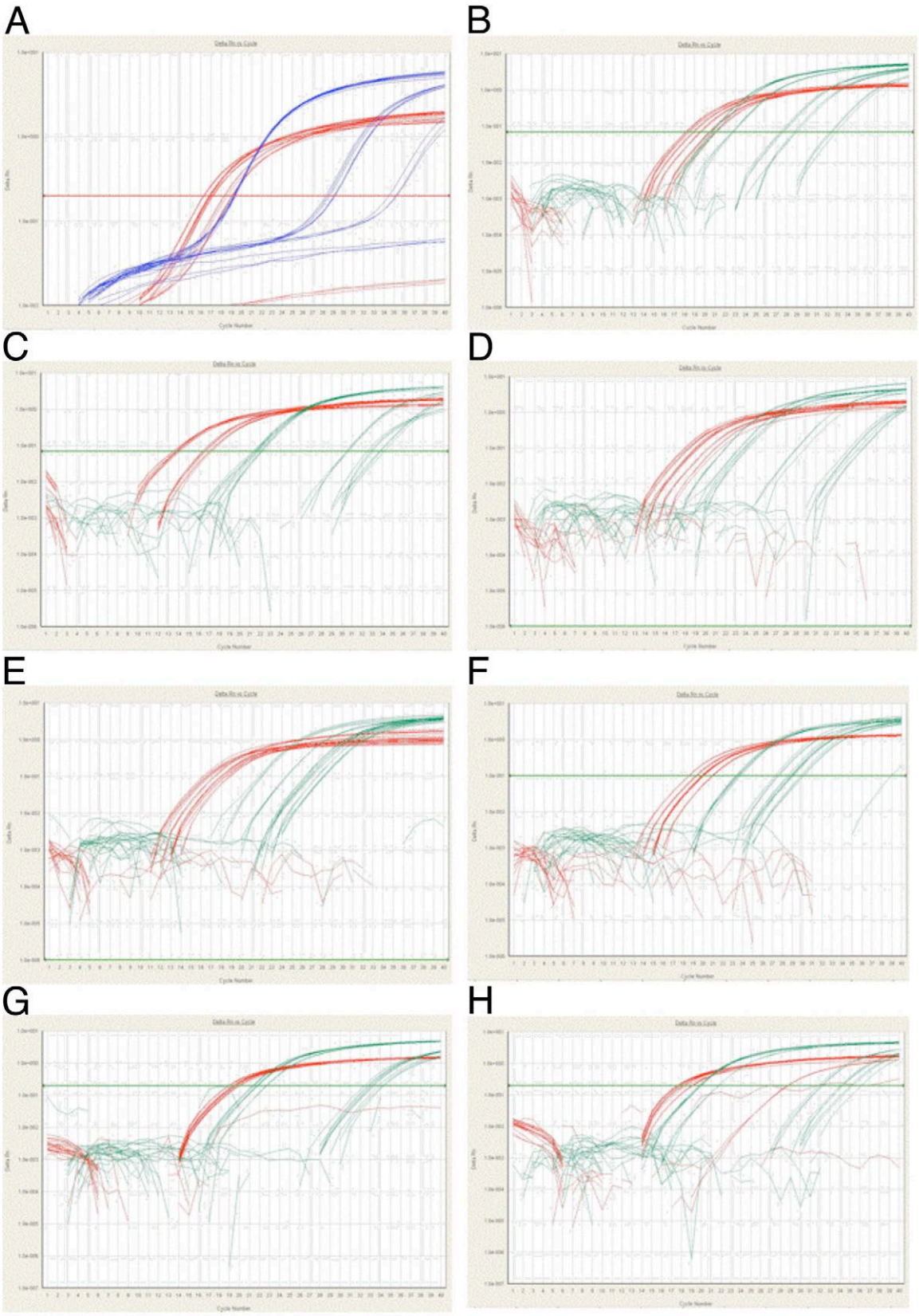

Figure 68: GILZ quantitative real-time PCR profiles. Kidney (a), heart (b), testis (c), liver (d), spleen (e), skin (f), brain (g) and lung (h). Red curves correspond actin, the blue (in a) and green curves correspond to GILZ.

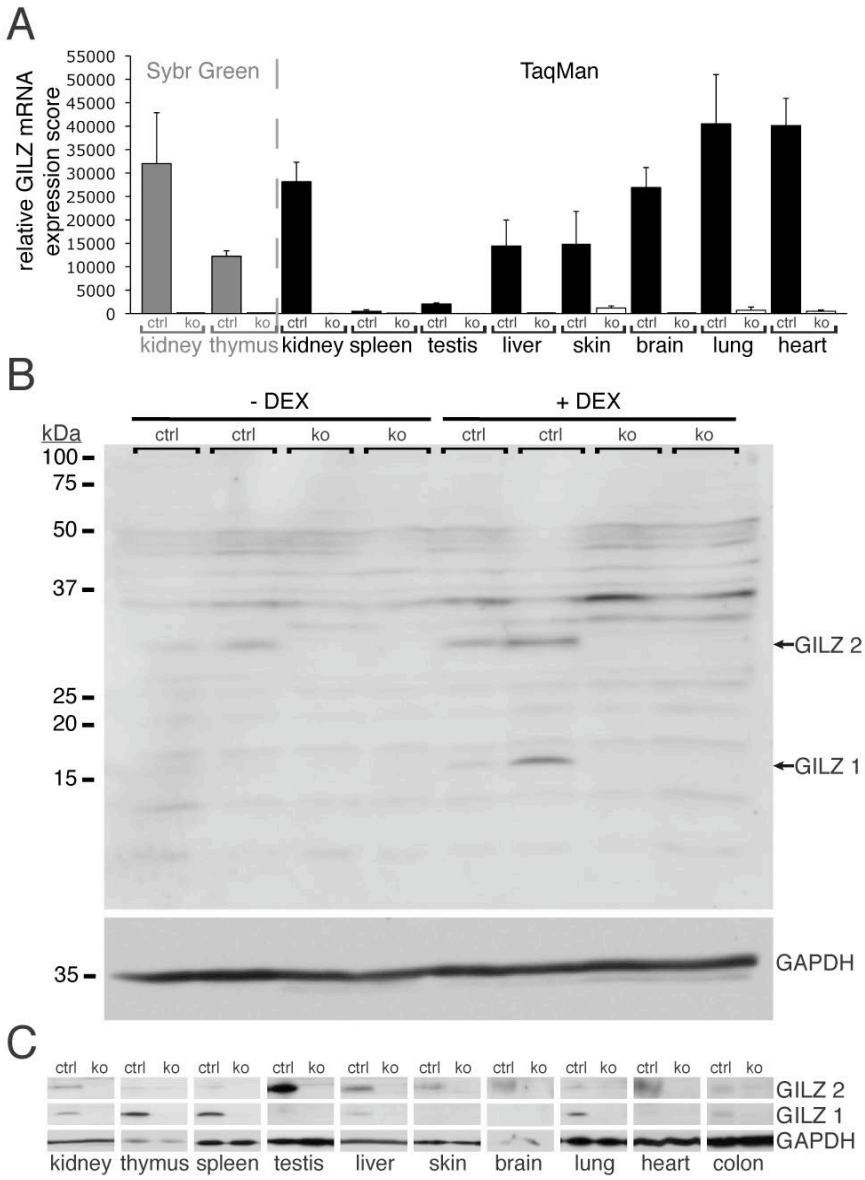

Figure 69. Knockout mice lack Tsc22d3 expression (*A*), Quantitative RT-PCR analysis of kidney, thymus, spleen, testis, liver, skin, brain, lung and heart from *Tsc22d3*$^{lox/y}$ or *Tsc22d3*$^{+/y}$ (control; gray and black columns) and *Tsc22d3*$^{\Delta/y}$ (ko; white columns; *n* = 3 per group; *P* < 0.05) determined by SYBR Green (gray) and TaqMan PCR (black columns). (*B*,*C*) Western blot analyses of kidneys from knockout and control mice (*B*) ± treated with vehicle or dexamethasone (± DEX) and (*C*) kidney, thymus, spleen, testis, liver, skin, brain, lung, heart and colon following dexamethasone stimulation. The polyclonal Tsc22d3 antibody identifies isoform 1 (15 kDa) and 2 (30 kDa). GAPDH (35 kDa) was used as loading control; *n* = 2 per genotype.

We have performed Western blot analysis to verify whether the GILZ protein was present in the knockout (figure 69*B* and *C*). We have used protein lysates from mice that were, or not, stimulated by dexamethasone to induce GILZ protein expression. As shown in figure 56*B*, in the controls, it was possible to detect faintly GILZ2 (30 kDa) but almost not GILZ1 (15 kDa) isoforms from kidney lysates from not dexamethasone-induced mice (-DEX), whereas in dexamethasone-stimulated mice (+DEX) the GILZ1 and GILZ2 proteins were clearly visible. In the knockout samples, we could not detect expression of GILZ1 nor GILZ2, even in the stimulated condition. Loading control was performed with anti-GAPDH (35 kDa) labelling. We

performed this analysis on the following tissues from dexamethasone-stimulated mice: kidney, thymus, spleen, testis, liver, skin, brain, lung, heart and colon (figure 69*C*). In each tissue, we could observe a tissue-specific expression pattern of GILZ1 and GILZ2 isoforms. For example, thymus and spleen exhibited mainly GILZ1, whereas in testis, GILZ2 was detected. In summary, there was no detectable expression of the two GILZ isoforms in all the knockout samples, indicating that the GILZ protein was not present in the organs tested.

Histopathology

We performed histopathological analysis on kidney, thymus, spleen, testis, liver, pancreas, skin, lung, heart, hippocampus, cerebellum, olfactory bulb, cornea, retina, colon, bone and tongue in 2- and 6-month-old GILZ knockout and control mice. With exception of the testis, there was no major defect at the anatomical and histological levels suggesting that organogenesis was not disturbed in the GILZ deficient mice (figure 70).

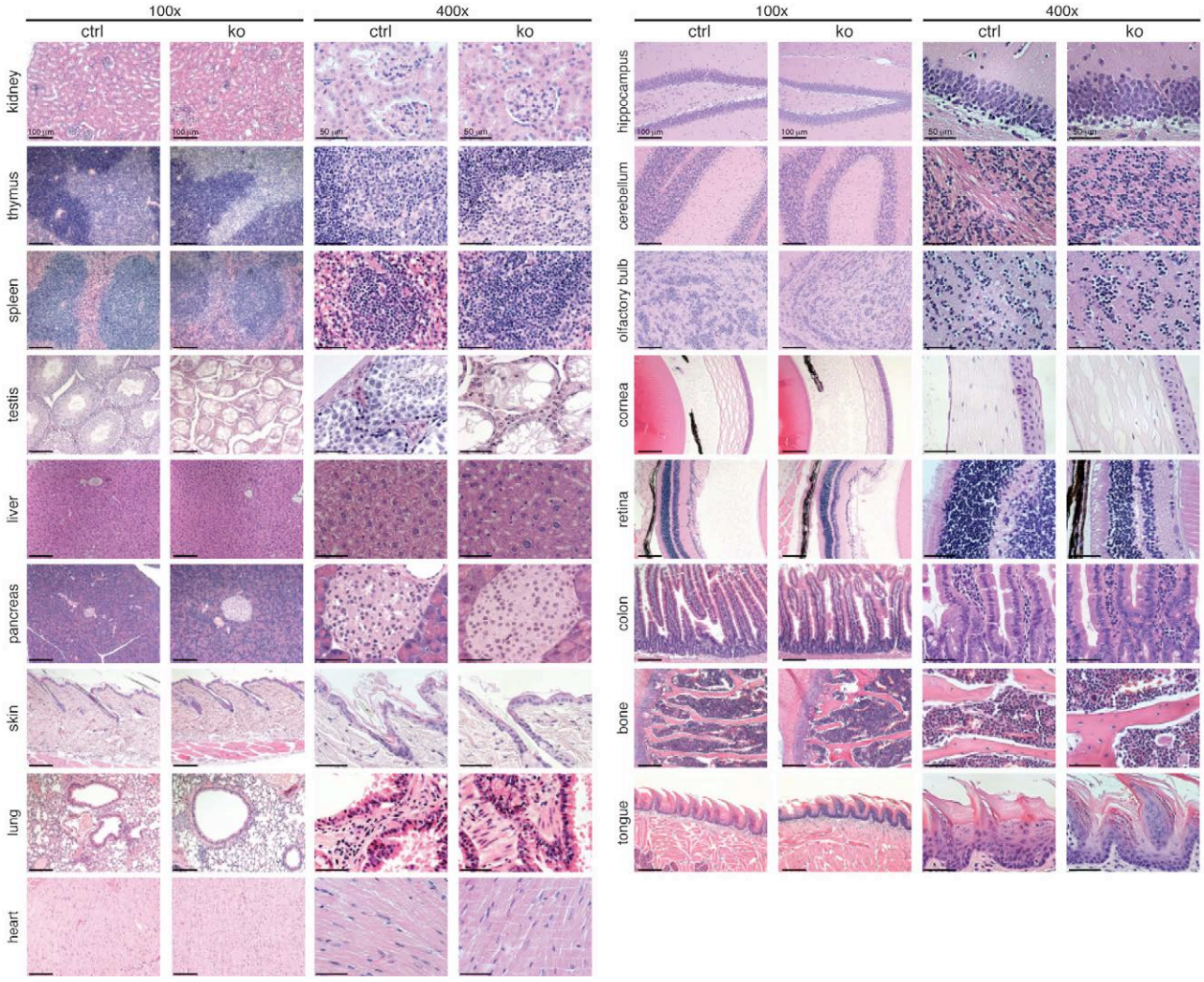

Figure 70: Histopathological analyses of control and Tsc22d3-deficient mice on hematoxylin and eosin stained paraffin sections (magnified 100x (scale bar = 100 µm) and 400x (scale bar = 50 µm)). Representative pictures from 6-month-old control and knockout mice are shown.

We performed more detailed heart, kidney and bone analyses. Although heart weight analyses indicated hypertrophy, it was not obvious from the tissue histology (figure 71). The kidneys of GILZ knockout mice presented no architectural or developmental defects as shown by histopathological analyses (performed by Dr. Samuel Rotman, Institut universitaire de pathologie de Lausanne; figure 72).

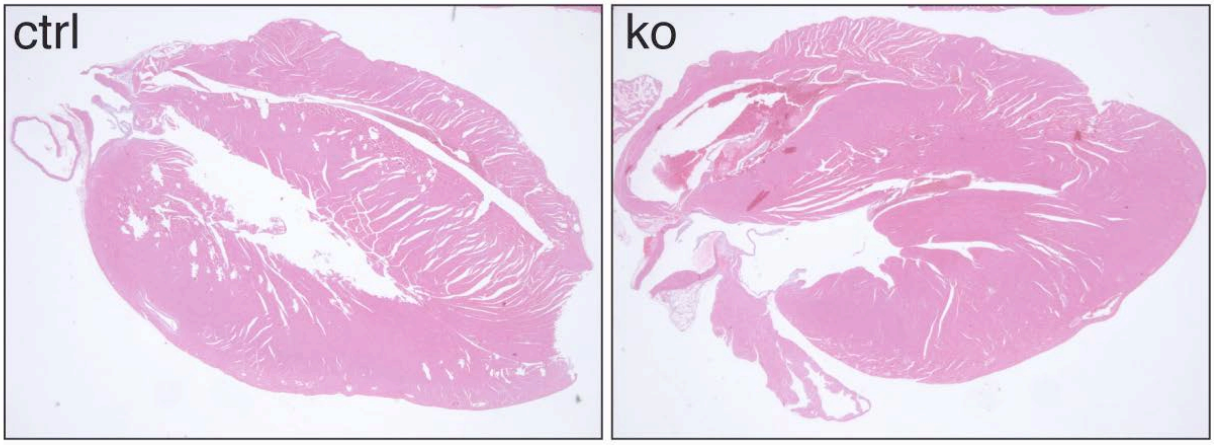

Figure 71: Stereomicroscope view of heart H&E stained sections.

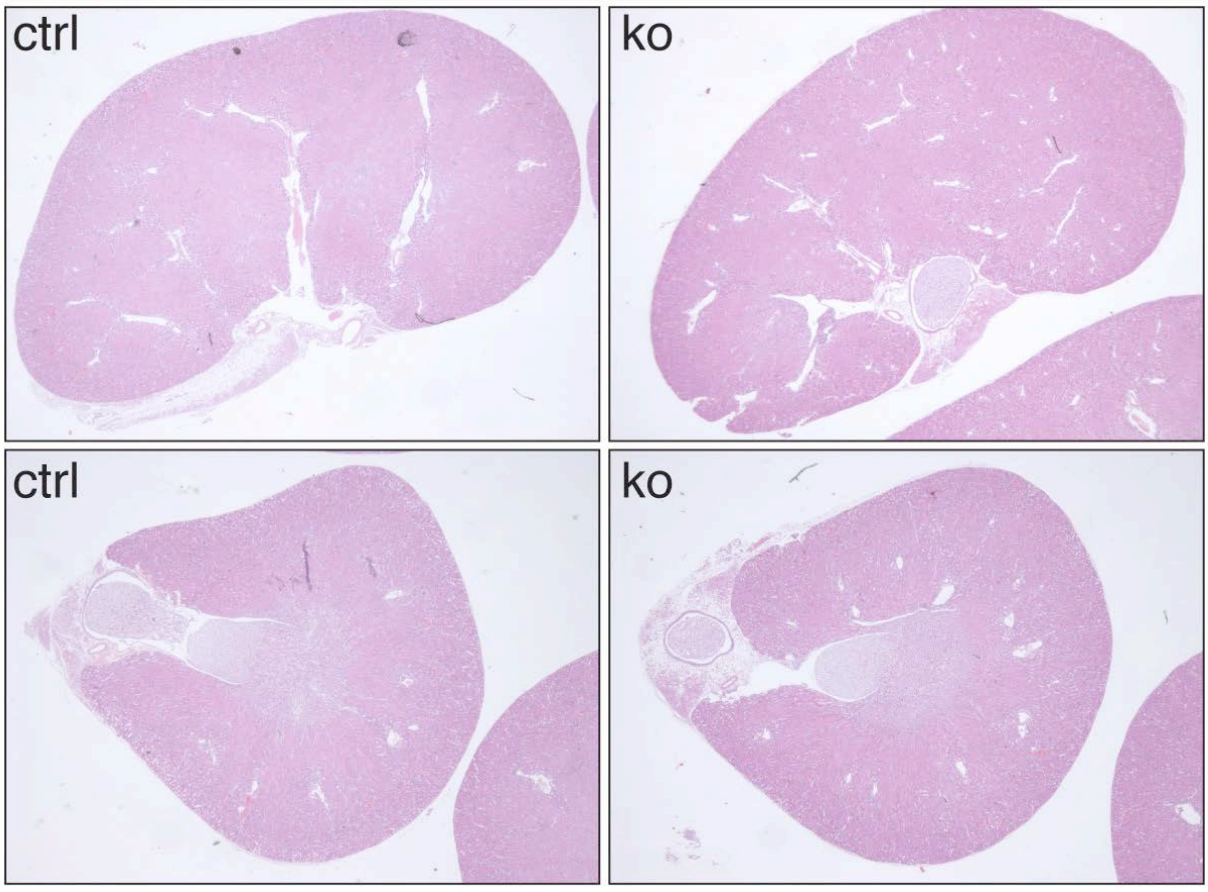

Figure 72: Stereomicroscope view of kidney longitudinal (top) and midtransverse (bottom) H&E stained sections.

Dissections of heart and kidney were performed in mice of 6 and 12 months of age. These organs were subsequently weighed and the mean values are shown in figure 73. Six-month-old knockout mice have a significantly increased heart weight compared to controls at the same age. The kidney weight is not different. In 12-month-old mice, the hearts are of the same weight, whereas the kidneys are slightly lighter ($P = 0.067$) in the knockouts.

The kidney and heart weight values were divided by the body weight or the tibia length. Using these ratios (indexes), no significant changes were observed. Nevertheless, these data indicate a tendency for heart hypertrophy (figure 73).

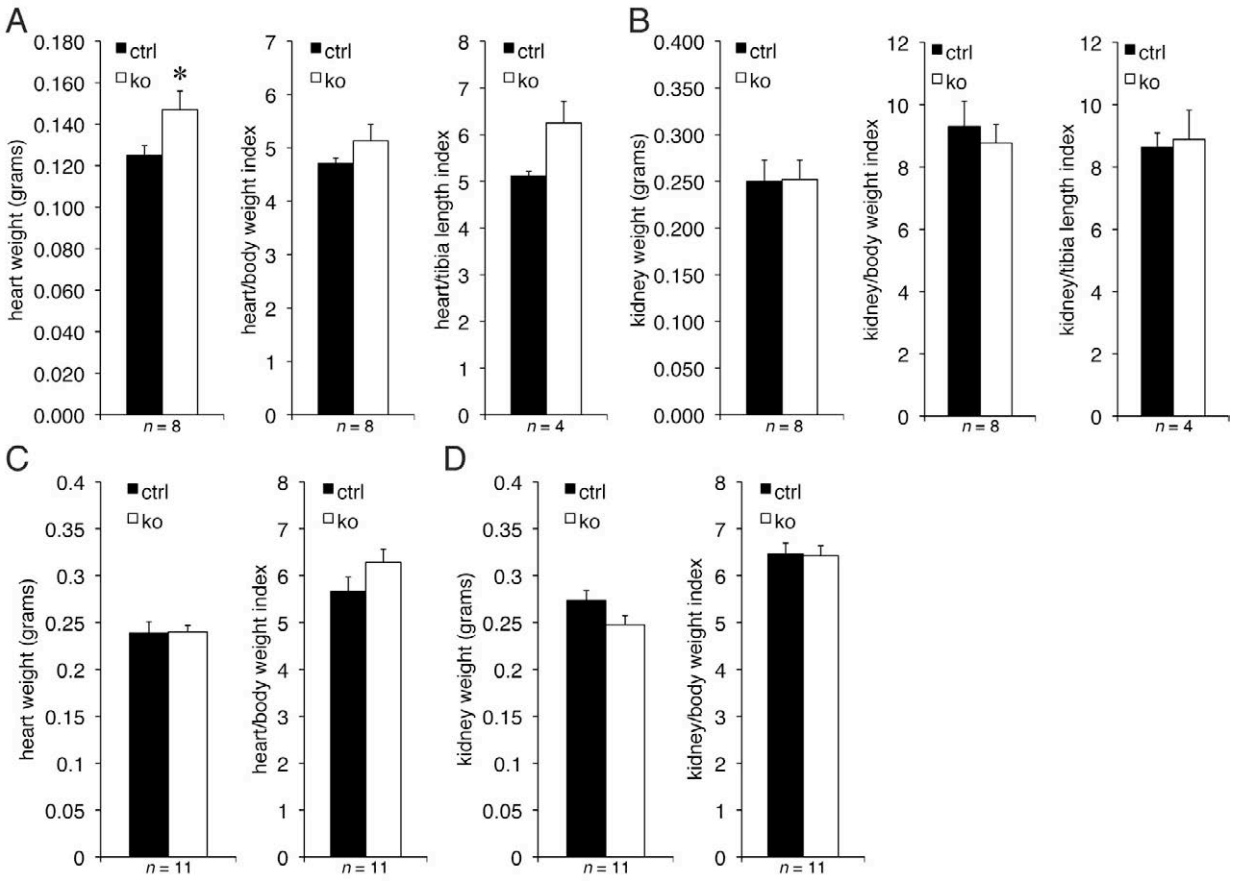

Figure 73: Heart and kidney weight analysis in 6 and 12-month-old mice. Organ weight, organ weight over body weight ratio and organ weight over tibia length ratio for 6-month-old heart (*A*) and kidney (*B*), 12-month-old heart (*C*) and kidney (*D*). Control (black columns) and GILZ knockout (white columns) mice. Number of measurements is indicated. Bars represent the SEM, **P* = 0.05.

We also looked on the bone structure. In knockouts, the length and shape of the tibia bones were undistinguishable from control littermates ($n = 4$; figure 74). Morphology of the bone marrow cells is unchanged as well (cell type and number; $n = 3$) in the knockout mice (figure 75).

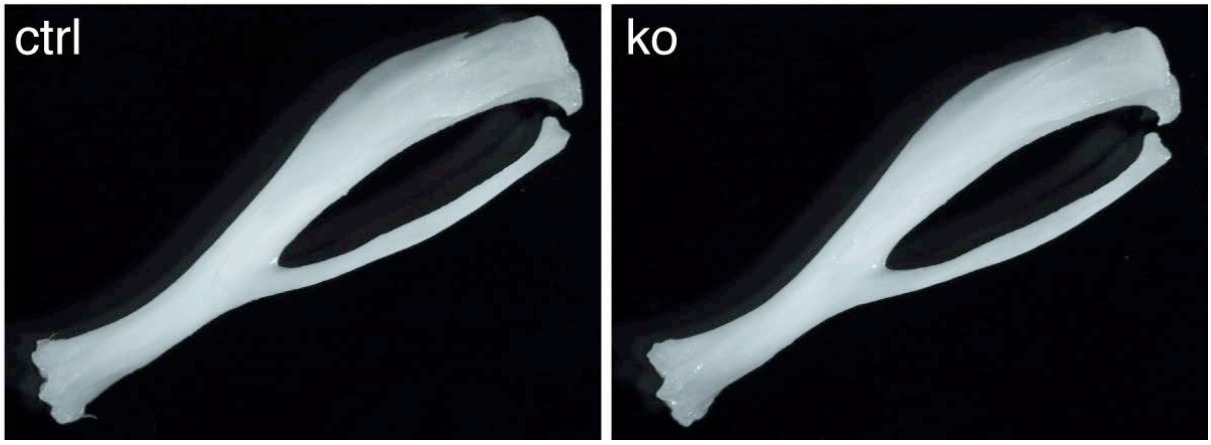

Figure 74: Stereomicroscope view of the tibia bone.

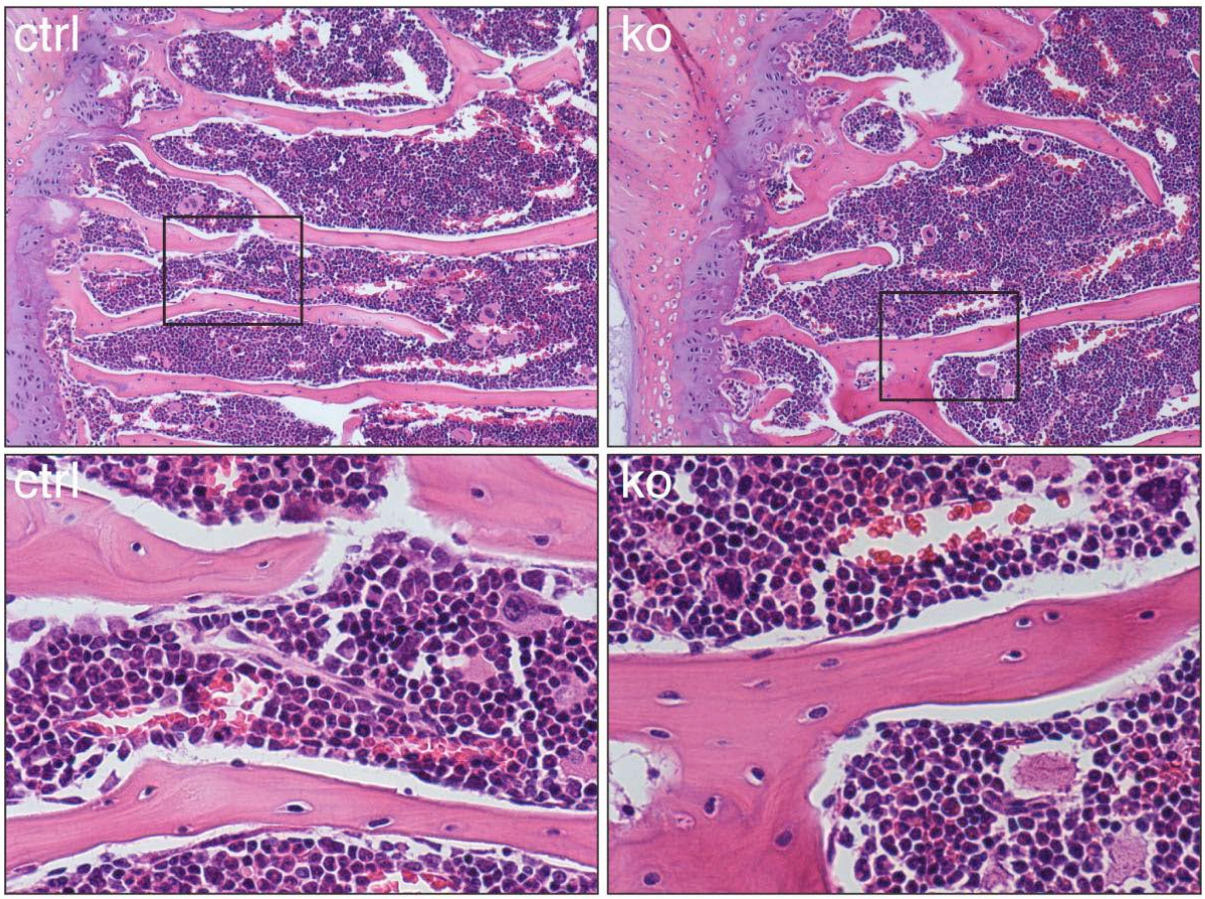

Figure 75: Microscopical pictures of H&E stained sections of bone marrow at 100x (up) and 400x (below) magnification. The rectangles in the top panels correspond to the location of the view at 400x magnification.

Metabolic parameter analyses

Body weight measurements

We further followed the weight gain with time in all the genotypes obtained (male y/+, y/lox and y/Δ; and female lox/+, lox/+, lox/ and +/ mice). We have performed a body weight analysis where we have measured weekly the same male mice ($n \geq 8$) for about ten months (figure 76). We could observe that the growth rate was the same from birth to the age of 6 months. From this moment, the knockouts were significantly lighter.

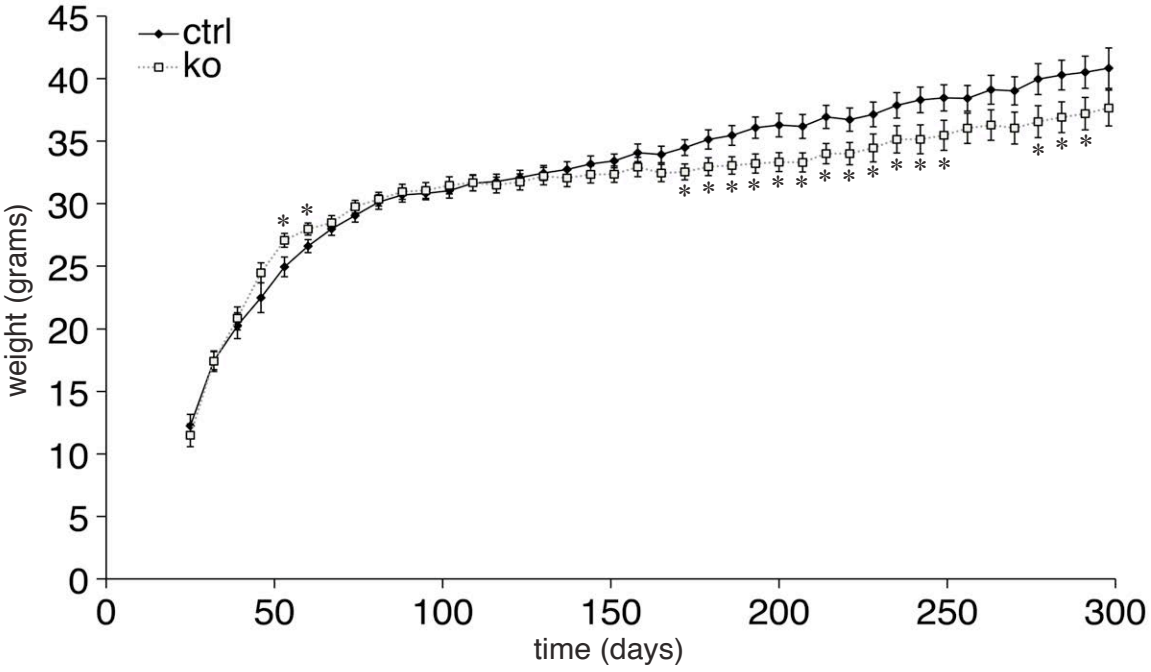

Figure 76. Body weight values of control (black) and knockout mice (white circles; $n \geq 8$ per group; *$P < 0.05$; bars = SEM).

We used Echo-MRI technology to measure the fat, lean and fluid body content of 2.5- and 15-month-old mice (table II). We could observe that the values were the same for controls and knockouts in the younger cohort. In the 15-month-old mice, we could observe a significantly lower body weight and fat content in the knockouts. The other parameters (body length, lean and fluids) were not changed.

Table II. *Mouse body weight and length, echo MRI values*

	2.5 month old mice			15 month old mice		
	ctrl (n=7)	ko (n=8)	*p*-value	ctrl (n=7)	ko (n=9)	*p*-value
Body weight (g)	29.83 ± 0.60	29.98 ± 0.50	0.427	39.57 ± 1.56	35.27 ± 0.10	0.014*
Body length (cm)	9.87 ± 0.10	9.86 ± 0.10	0.454	10.73 ± 0.10	10.53 ± 0.09	0.082
Fat (g)	2.94 ± 2.65	3.37 ± 1.79	0.207	8.31 ± 0.94	6.34 ± 0.44	0.030*
Lean (g)	23.21 ± 0.40	22.73 ± 0.60	0.265	25.95 ± 0.80	24.82 ± 0.57	0.129
Fluids (g)	0.17 ± 0.04	0.12 ± 0.01	0.114	0.47 ± 0.08	0.46 ± 0.06	0.429

Plasma insulin and glucose concentrations

Plasma insulin and glucose were measured under standard, fasting and refed conditions (table III). Under standard condition, insulin is significantly higher in the knockouts. Glucose level is unchanged. In fasted and refed conditions, there were no significant differences.

Table III. *Insulin and glucose measurements upon fasting and refeeding*

feeding state		ctrl (n=7)	ko (n=8)	p-value
fed	insulin (ng/ml)	1.5 ± 0.3	3.5 ± 0.7	0.036*
	glucose (mM)	7.7 ± 0.5	7.7 ± 0.3	0.976
fasted	insulin (ng/ml)	0.6 ± 0.1	0.8 ± 0.3	0.487
	glucose (mM)	3.8 ± 0.1	3.5 ± 0.1	0.052
refed	insulin (ng/ml)	3.9 ± 0.6	4.2 ± 0.8	0.786
	glucose (mM)	10.7 ± 0.5	9.5 ± 0.6	0.129

We performed glucose (GTT) and insulin tolerance tests (ITT; figure 77*A* and *B*). In these experiments, plasma glucose is measured following intraperitoneal administration of glucose or insulin. Both groups responded equally to these tests, suggesting no major dysfunction of glucose or insulin regulation, despite that the plasma insulin concentration is elevated in knockout mice under normal feeding condition (table III).

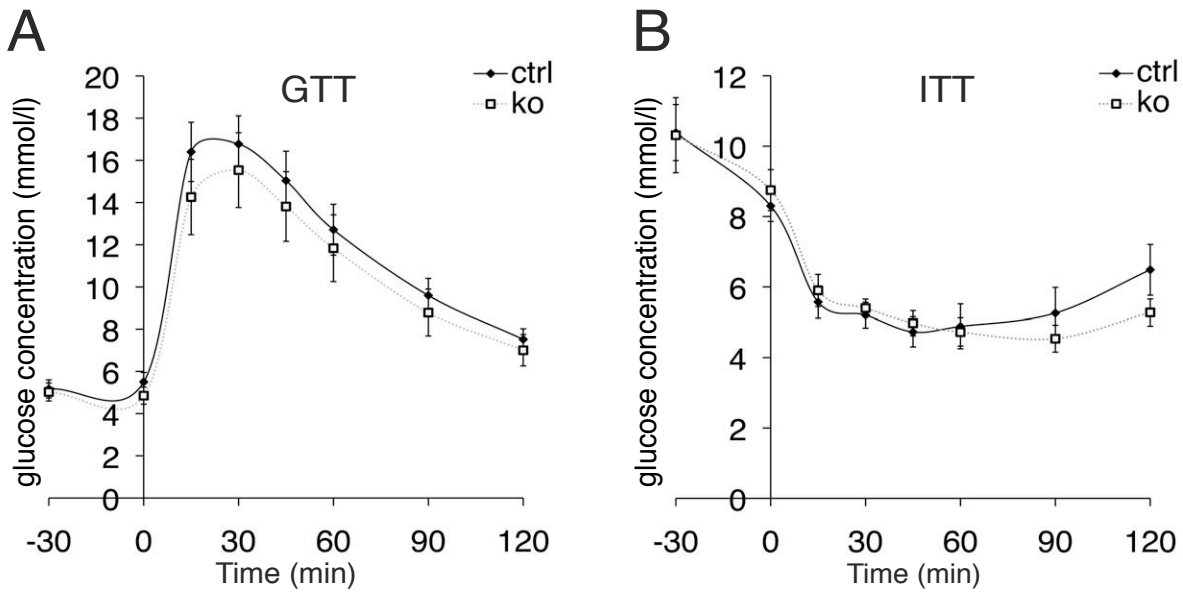

Figure 77. Glucose and insulin sensitivity. (*A*), glucose and (*B*) insulin tolerance tests; plasma glucose concentration was measured 30 min. before and during 120 min. following intraperitoneal administration of 1.5 mg/g glucose (*A*) or 0.8 mU/g insulin (*B*; $n \geq 6$ per group; bars = SEM).

Since insulin is linked to glucagon, we decided to stain pancreas sections for insulin and glucagon (figure 78*A*). We quantified the number of α cells (secreting glucagon) in Langerhans islets. The ratio of α cells/total cells is elevated in knockouts compared to controls (figure 78*B*). The plasma levels of glucagon under standard conditions are not changed (figure 78*C*).

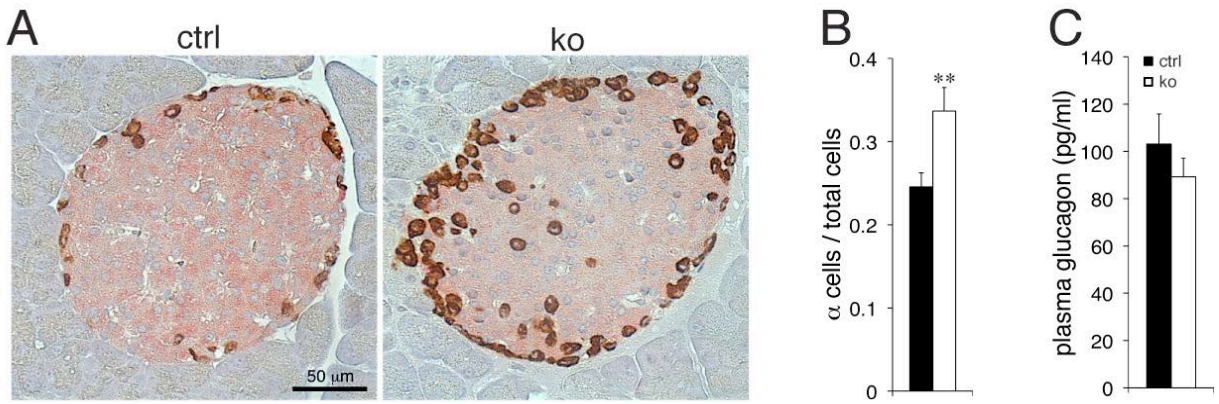

Figure 78. Glucagon secretion. (*A*), Glucagon (brown, α cells) and insulin (rose, β cells) expression in pancreatic islets of Langerhans from control (left) and knockout (right) mice. (*n* = 3 mice per group; scale bar = 50 µm). (*B*), Ratio of glucagon-positive Langerhans cells (*N* = 15-18 images, *n* = 3 mice per group) in control (black) and knockout mice (white columns; ***P* < 0.001; bar = SEM). (*C*), Plasma glucagon by ELISA was measured under standard condition in 4-month-old mice (*n* ≥ 8 mice per group; bar = SEM).

Adipogenesis and high fat diet experiment

We investigated adipogenesis by differentiating mouse embryonic fibroblasts (MEFs) into adipocytes. As shown in figure 79*A* and *B*, in both groups, adipocytes developed when differentiation medium was applied, as revealed by the Oil red O staining. The number and the shape of the adipocytes were not changed. In parallel, at the mRNA level, we measured by qRT-PCR the expression of GILZ, PPARγ2 and fatty acid binding protein 4 (FABP4) from cells that were ± stimulated with differentiation medium (figure 79*C*).

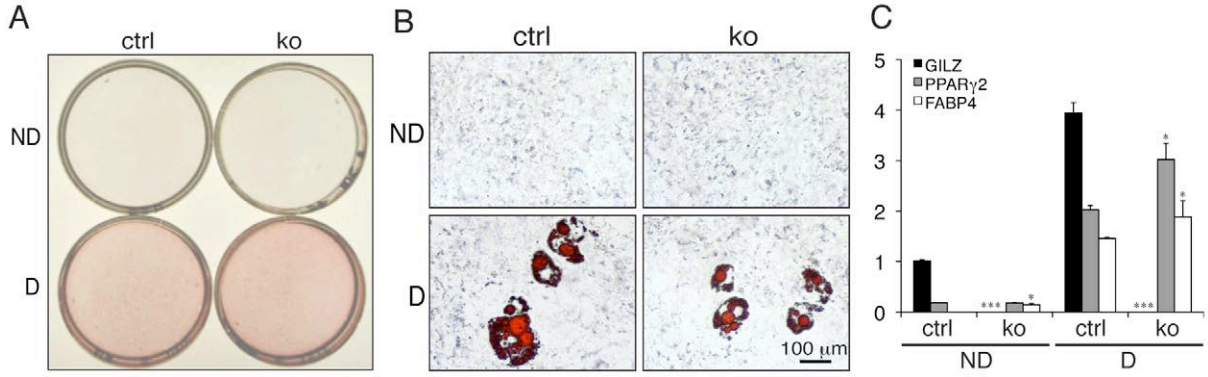

Figure 79. Adipocyte differentiation. (*A*, *B*) Two days after confluence, MEF cells were ± induced to differentiate into adipocytes (ND, not differentiated; D, differentiated MEFs). Cells from control (ctrl) and knockout (ko) mice were stained with Oil-Red O at 8 days post-induction. (*A*), Overview and (*B*), higher magnification on Oil-Red O-stained cells from control (ctrl) and knockout (ko) mice exposed (D, differentiated) and not exposed to adipogenic medium (ND, not differentiated). Note that there is no obvious difference between the two groups. (*C*), Quantitative RT-PCR of GILZ, PPARγ2 and FABP4 from non-differentiated (ND) and differentiated (D) MEF cells from control and knockout mice. Experiments were performed in triplicate; **P* < 0.05, ****P* < 0.001).

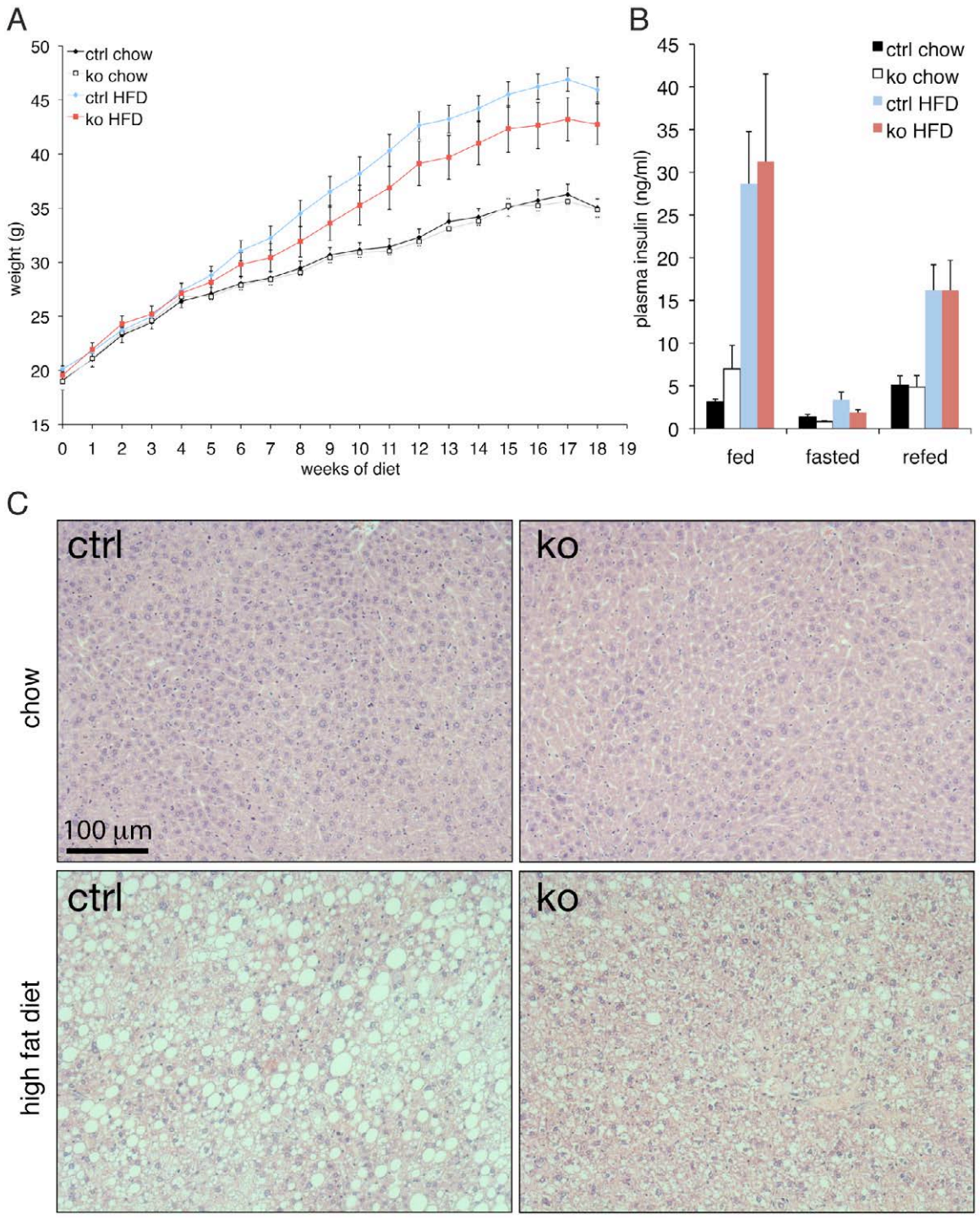

Figure 80. Body weight analysis, plasma insulin measurements and liver histology from chow and high fat diet fed (HFD) mice. (*A*), Body weight values following chow and high fat diets. (*B*), Plasma insulin (ng/ml) measurements in chow and HFD mice under fed, fasted and refed conditions. Control mice (Chow in black; HFD in blue) and knockout mice (chow in white; HFD in red; $n \geq 11$ per group; bars = SEM). (*C*), Liver H&E stained sections following 18 weeks of chow and HFD fed control and knockout mice ($n = 3$; scale bar = 100 µm).

We challenged our mice by feeding them with high fat diet for 18 weeks (starting at 6 weeks of age). We also compared the results with control and knockout groups fed with chow (standard diet). The figure 80*A* shows the results obtained. Under chow diet the knockout and control

mice had the same growth rate, whereas under high fat diet, the knockout group gained less weight than the control (about 8% less body weight, $P = 0.11$ at week 17 of the experiment). We measured plasma insulin levels in fed, fasted and refed conditions (figure 80*B*). As expected, insulin concentration is higher in knockouts under normal feeding conditions. In the fasting situation, knockout mice had lower (but not significant) insulin levels. When the mice were refed, the levels were not different between the groups, in chow and HFD.

Sodium and water handling

Under standard, sodium- or water-deprived conditions, we have analyzed the blood and urine concentrations of Na^+ and K^+, osmolarity and plasma aldosterone (table V). In general, no major changes could be measured. Plasma K^+ is significantly higher in the knockout mice under standard condition. Following 10-day sodium-deprived diet, the GILZ-deficient mice had significantly increased plasma Na^+ and decreased K^+ concentrations. The plasma aldosterone levels are not different between the genotypes under standard and sodium-deprived diets. The knockout mice responded like controls to the sodium-deprived diet, the body weight, food and water intakes were the same (figure 81). The 23-hour water deprivation had no effect on our measurements. The urinary data are not modified under any condition.

Table IV. *Renal sodium and water handling*

Mice upon normal diet					
Plasma	ctrl	n	ko	n	*p*-value
sodium (mmol/l)	148.6 ± 0.90	7	150.3 ± 0.06	7	0.063
potassium (mmol/l)	5.5 ± 0.13	7	5.9 ± 0.18	7	0.046*
osmolarity (mmol/kg H_2O)	318.9 ± 2.65	7	321.9 ± 1.79	7	0.176
aldosterone (pg/ml)	183.9 ± 43.8	8	159.8 ± 44.4	8	0.352
Urine					
sodium (mmol/l)	54.7 ± 8.2	7	59.7 ± 8.75	7	0.684
potassium (mmol/l)	318.6 ± 28.65	7	290 ± 23.95	7	0.46
osmolarity (mmol/kg H_2O)	1911 ± 152	7	1880 ± 183	7	0.897
creatinine (µmol/l)	4887 ± 462	7	5102 ± 529	7	0.765
sodium/creatinine ratio	0.011 ± 0.0008	7	0.0118 ± 0.0011	7	0.6
potassium/creatinine ratio	0.0657 ± 0.0029	7	0.0579 ± 0.0026	7	0.069
Mice upon no sodium diet					
Plasma					
sodium (mmol/l)	147 ± 1	3	150.7 ± 0.33	3	0.013*
potassium (mmol/l)	8.5 ± 0.44	3	7.4 ± 0.21	3	0.043*
osmolarity (mmol/kg H_2O)	327 ± 2.31	3	327.3 ± 0.88	3	0.45
aldosterone (pg/ml)	601.3 ± 125.5	8	543.6 ± 161.6	7	0.39
Urine					
sodium (mmol/l)	19.5 ± 1.5	8	19.3 ± 2.2	7	0.468
potassium (mmol/l)	325 ± 12.90	8	297.9 ± 19	7	0.124
osmolarity (mmol/kg H_2O)	2588 ± 107	8	2445 ± 66	7	0.146
creatinine (µmol/l)	4013 ± 309	8	3577 ± 232	7	0.145
sodium/creatinine ratio	0.0051 ± 0.0001	8	0.0054 ± 0.0005	7	0.32
potassium/creatinine ratio	0.0855 ± 0.0091	8	0.0853 ± 0.0071	7	0.492
Mice upon normal diet, after water deprivation (23h)					
Plasma					
sodium (mmol/l)	167 ± 1.21	6	167.2 ± 1.35	6	0.464
potassium (mmol/l)	5.7 ± 0.21	6	5.83 ± 0.13	6	0.3
osmolarity (mmol/kg H_2O)	357.5 ± 1.98	6	359.0 ± 4.06	6	0.373
Urine					
sodium (mmol/l)	84.4 ± 18.81	5	76.5 ± 13.09	4	0.377
potassium (mmol/l)	474 ± 42.64	5	525 ± 36.57	4	0.204
osmolarity (mmol/kg H_2O)	2110 ± 247	5	2452 ± 124	4	0.146

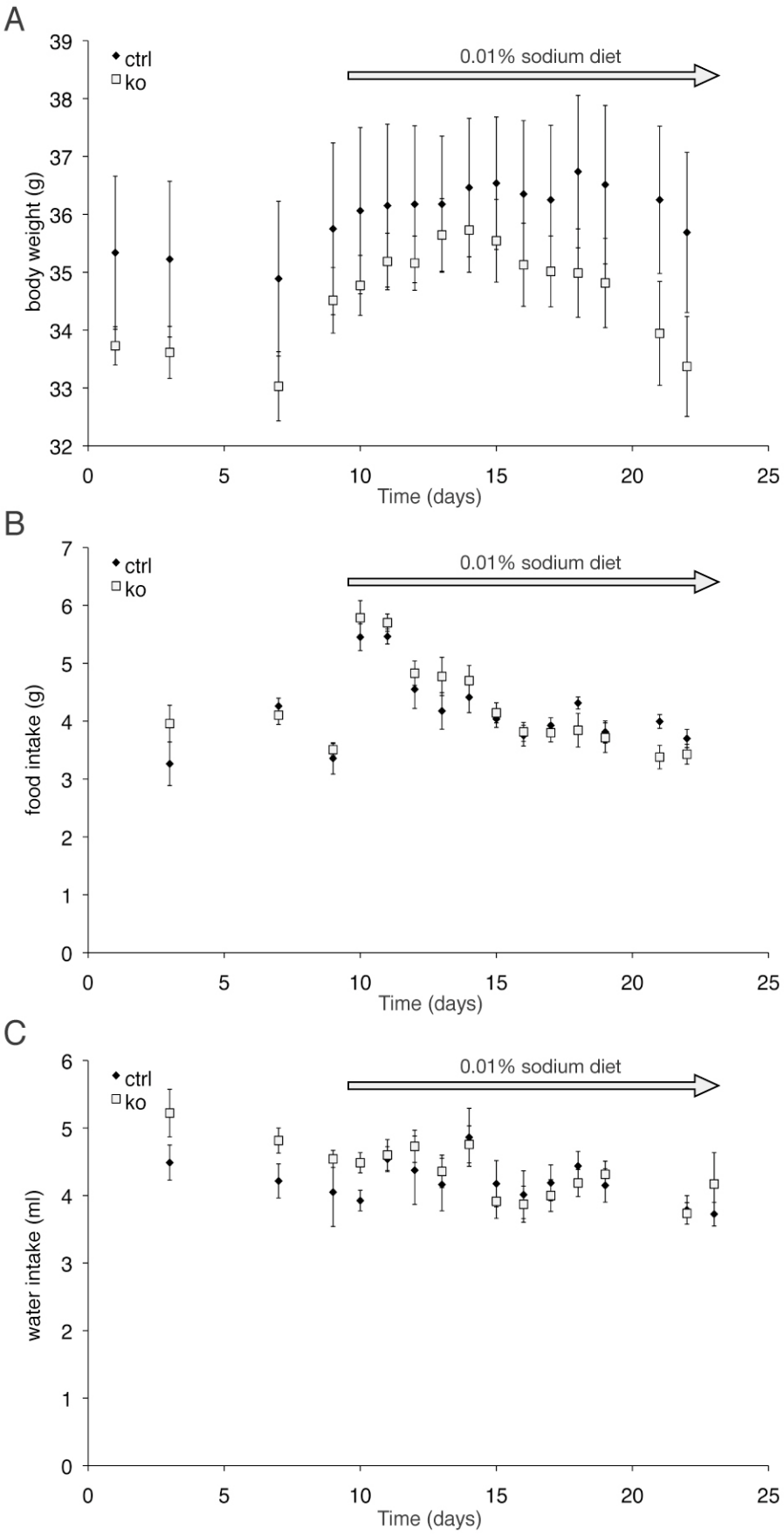

Figure 81. Physiological parameters upon salt-deprived diet. Six-month-old control and knockout mice were analyzed with respect for body weight (*A*), food (*B*) and water (*C*) intake before and following 12 consecutive days of sodium-deprived diet ($n \geq 7$).

Molecular analysis of potentially GILZ target-dependent genes

We investigated by real-time qPCR the levels of mRNA transcripts expressed of several genes that might regulate or be regulated by GILZ in various tissues.

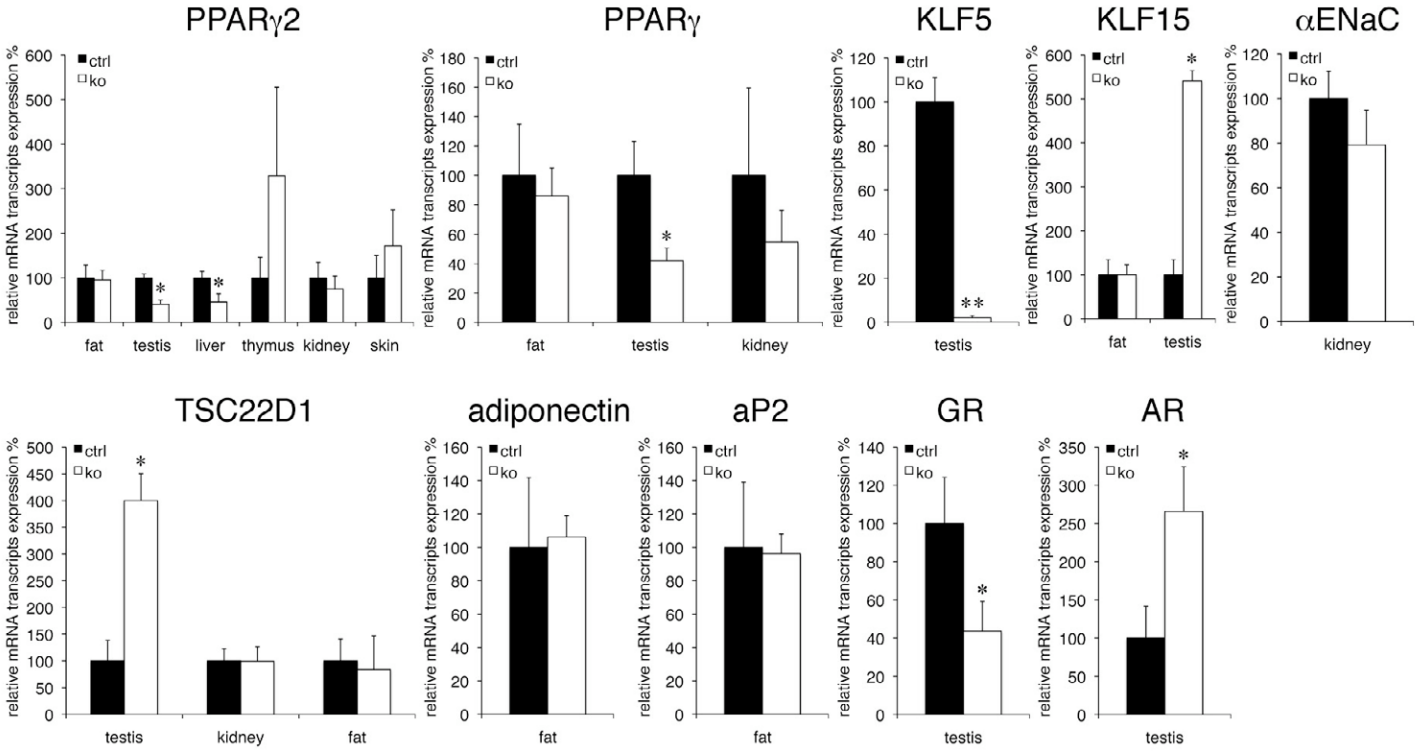

Figure 82: Real-time qPCR results for PPARγ2, PPARγ, KLF5, KLF15, αENaC, TSC22D1, adiponectin, aP2, GR and AR. Data correspond to the mean of relative mRNA transcript expression (in %). Control (black columns) and GILZ knockout (white columns) mice. For each group $n \geq 3$ animals. Bars represent the SEM, *$P < 0.05$ and **$P < 0.01$.

The results of these analyses are given by gene (figure 82) or by tissue (figure 83). The figure 82 shows the results by genes and figure 83 by tissues analysed. Testis of knockout mice was the organ that shows the majority of unbalanced gene expression. Indeed, PPARγ, PPARγ2, GR and KLF5 mRNA transcripts were less abundant, whereas AR and KLF15 were more expressed in knockout male gonads. In the liver, less expression of PPARγ2 was measured.

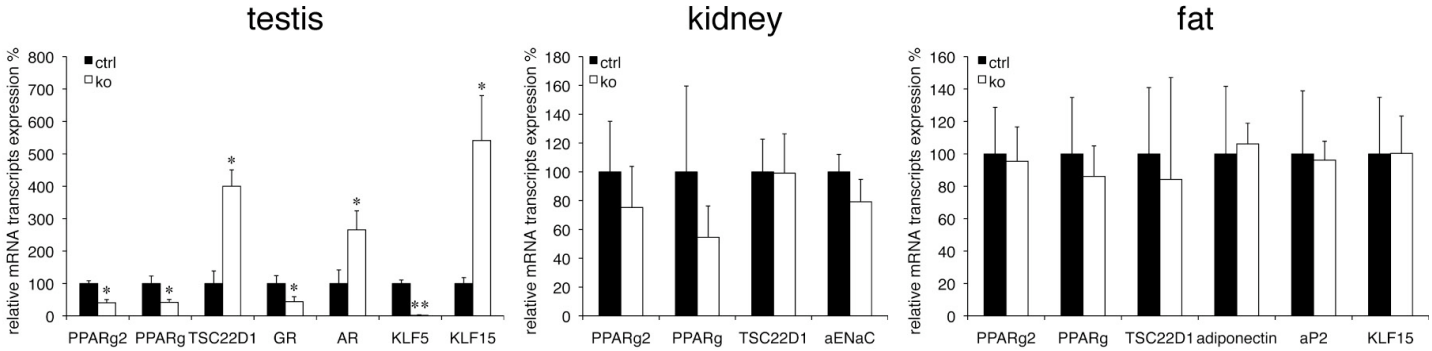

Figure 83: Real-time qPCR results for testis, kidney and fat tissues. Data corresponds to the mean of relative mRNA transcript expression (in %). Control (black columns) and GILZ knockout (white columns) mice. For each group $n \geq 3$ animals. Bars represent the SEM, *$P < 0.05$ and **$P < 0.01$.

At the protein level, we tested the expression of the glucocorticoid receptor (GR) in testis lysates from mice ± stimulated (or not) by dexamethasone (n = 2). These results indicated that dexamethasone treatment induced an increase of GR that was not different in the knockout mice. Quantification of the protein expression did not confirm that GR protein was less abundant in the knockout testis than in the controls, as expected from the qPCR experiments (figure 84).

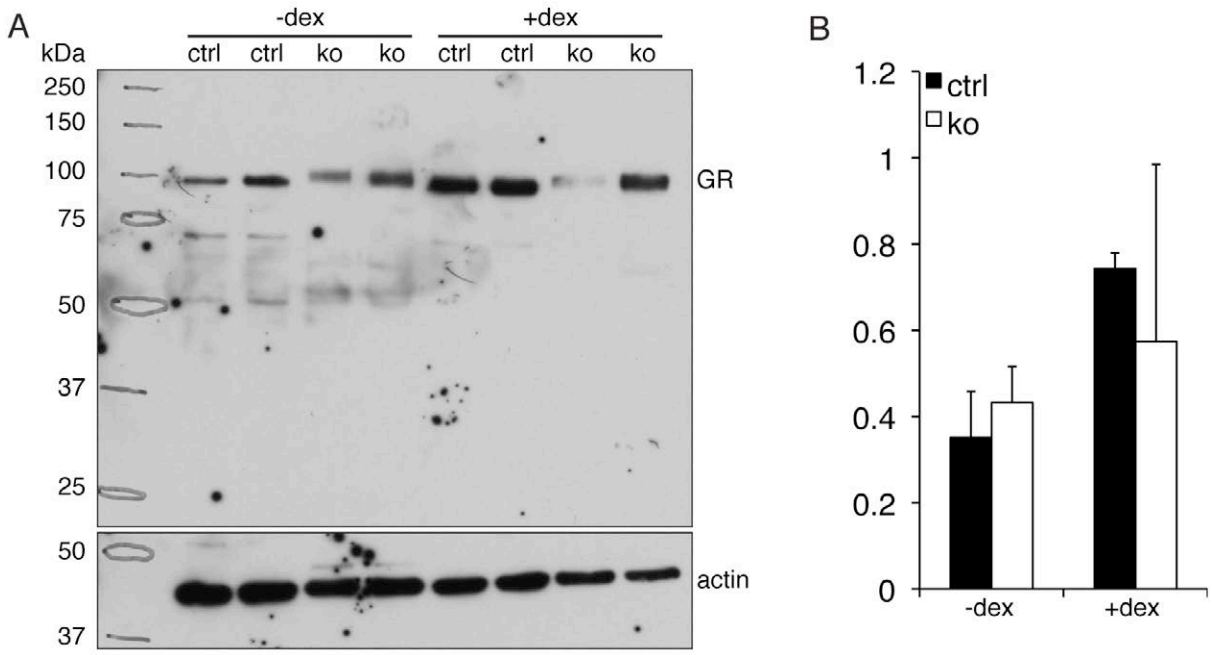

Figure 84: Western blot analysis for GR in testis protein lysates. GR antibody (GRα 95 kDa; GRβ 90 kDa) used against control (ctrl) and knockout (ko) testis lysates from dexamethasone-stimulated (+dex) or not (-dex) mice. Actin (42 kDa) antibody is used as loading control.

Immune development and inflammation

Thymus structure and immune cell development

The architecture of the thymus was analyzed in 3-month-old mice by histology (figure 85). At 100x magnification (upper pictures), it is possible to distinguish clearly the border between the cortex and the medulla regions in both genotypes. The cell population does not seem altered or changed. At higher magnification (400x, lower pictures), no obvious phenotype could be detected.

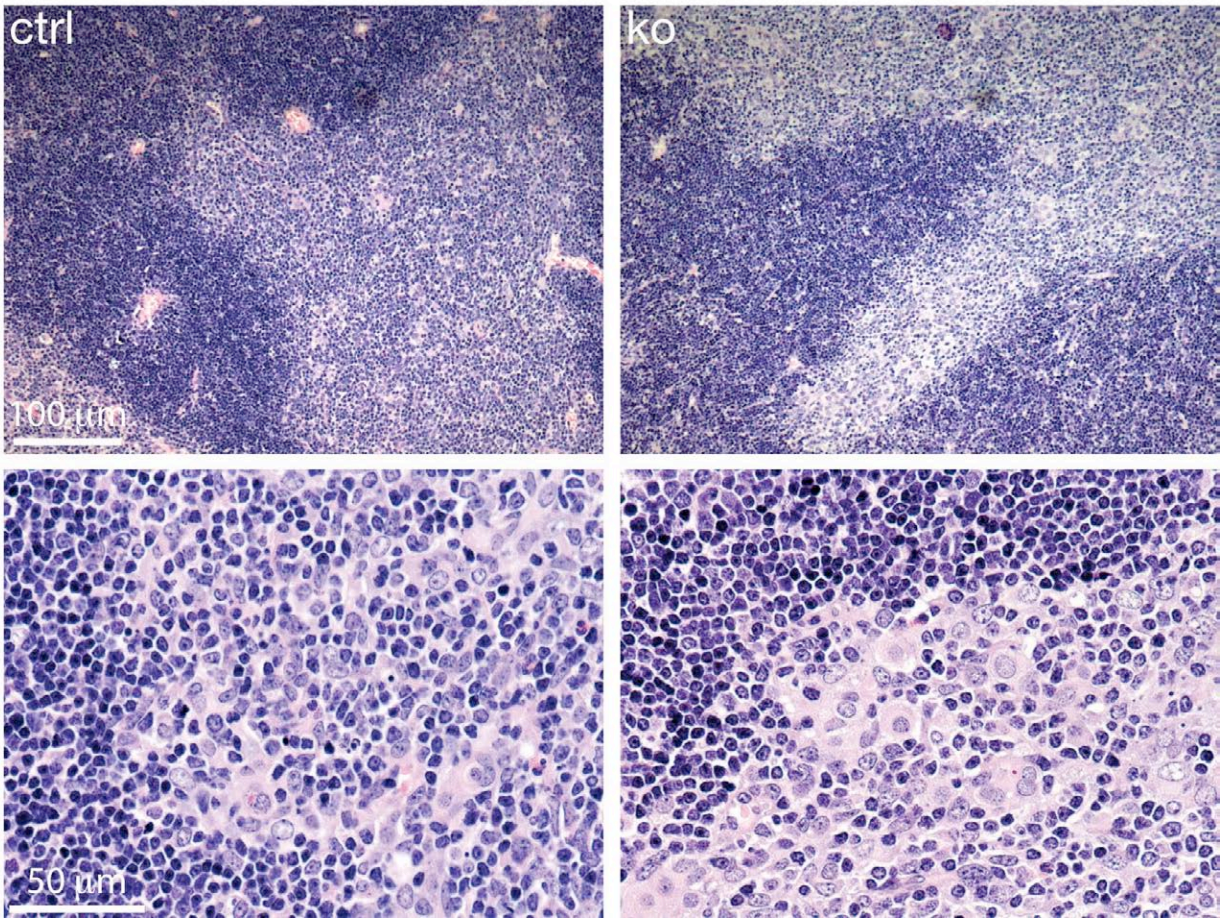

Figure 85. Thymus histology. H&E staining of thymic paraffin sections from 3-month-old mice. Control (ctrl) and knockout (ko) samples at 10x (up; scale bar = 100 µm) and 40x (down; scale bar = 50 µm).

We have measured the weight of the thymus at different ages: 10, 20 days and between 2 and 4.5 months (figure 86*A*). At the age of 10 and 20 days, no differences could be observed, whereas the thymus from knockout mice between 2 and 4.5 months was significantly lighter. We then measured the amount of cells that compose the thymus, spleen and lymph node by flow cytometry (figure 86*B* to *D*). For the thymus, we examined the following subsets: DN1 to 4, ISP, γδT, DP, CD8 and CD4 cells. There were no significant differences between the groups excepted for the DN3 (less cells) and DN4 (more cells) subsets (figure 86*B*). In the spleen, the subsets analyzed were: B, CD8, CD4, RBC, Ebs, Mega, Gran and Mac cells. Only the amount of erythroblast was significantly increased in the knockouts (figure 86*C*). In the lymph node, we measured the number of CD8, CD4 and B cells, and no changes could be observed (figure 86*D*). Together, these data indicated no major impairment of the immune system development.

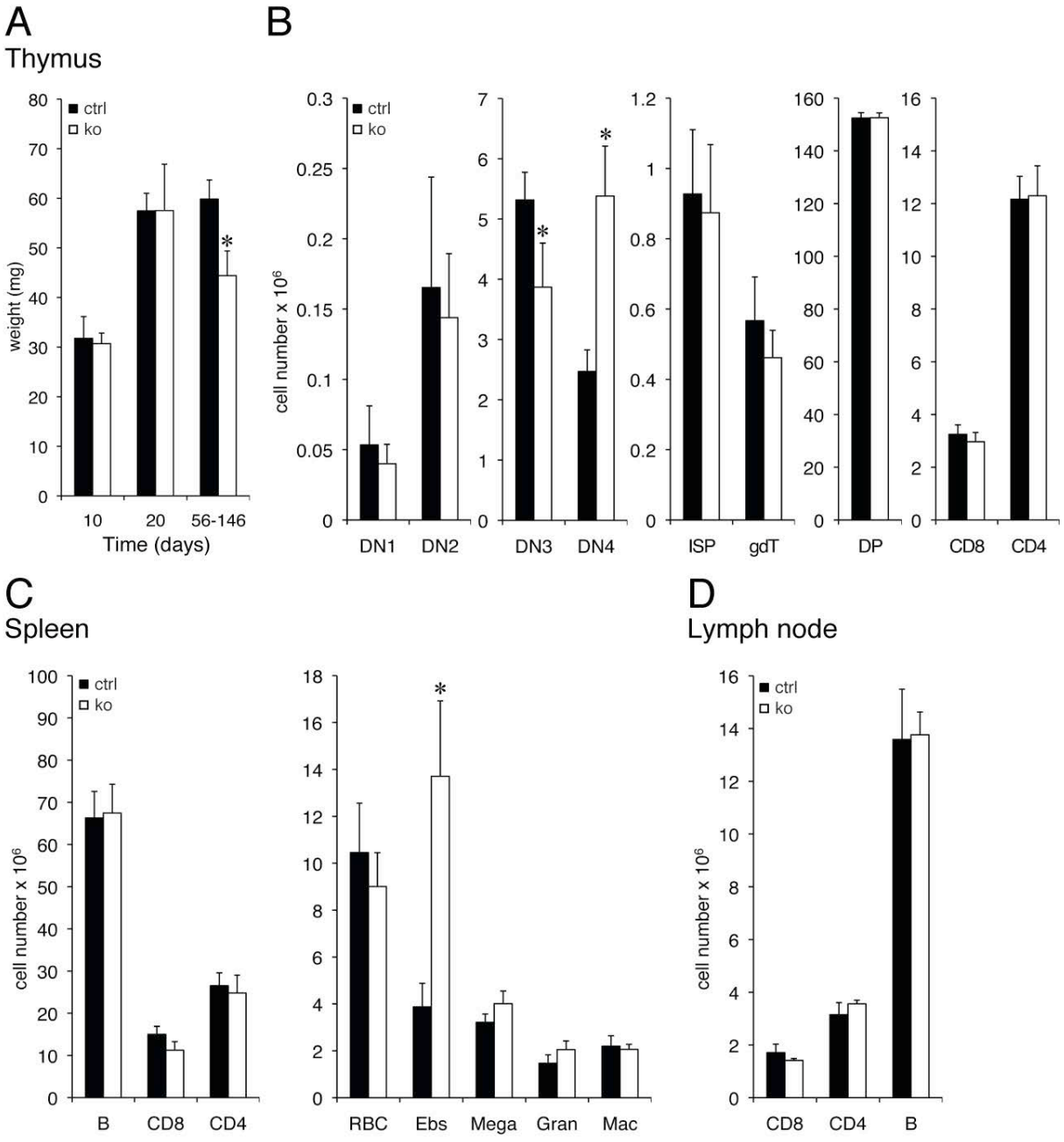

Figure 86. Thymus size and flow cytometric analyses of thymus, spleen and lymph nodes from 10-week-old male control (black) and knockout (white columns) mice. (*A*), The size of the thymus in 10-, 20-day-old and 2-4.5-month-old mice ($n \geq 7$). (*B*), Absolute cell numbers (x10^6) for the following thymocyte subsets: DN1 (CD117$^+$CD44$^+$CD25$^-$), DN2 (CD117$^+$CD44$^+$CD25$^+$), DN3 (CD117$^-$CD44$^-$CD25$^+$), DN4 (CD117$^-$CD44$^-$CD25$^-$), ISP (CD4$^-$CD8$^+$TCRβ$^-$), γδT cells, DP (double positive, CD4$^+$CD8$^+$), CD8 SP (single positive, CD4$^-$CD8$^+$), CD4 SP (CD4$^-$CD8$^+$). (*C*), Absolute cell numbers (x10^6) for the following splenocyte subsets: B cells, CD8 SP, CD4 SP, RBC (erythrocytes) and EBs (Erythroblasts, Ter119$^+$CD71$^+$), Mega (Megakaryocytes), Gran (Granulocytes), Mac (Macrophages). (*D*), Absolute cell numbers (x10^6) for the following lymph node subsets: CD8 SP and CD4 SP cells, B cells. Black bars: control; white bars: knockout mice, data represent average ± SEM. At least 3 mice per group were analyzed. *$P < 0.05$ when compared to control.

We have analyzed the cell cycle, the Bcl2 and TCRβ$^+$ cells in various thymus subsets (figure 87). We could not observe any significant changes in all the subsets tested.

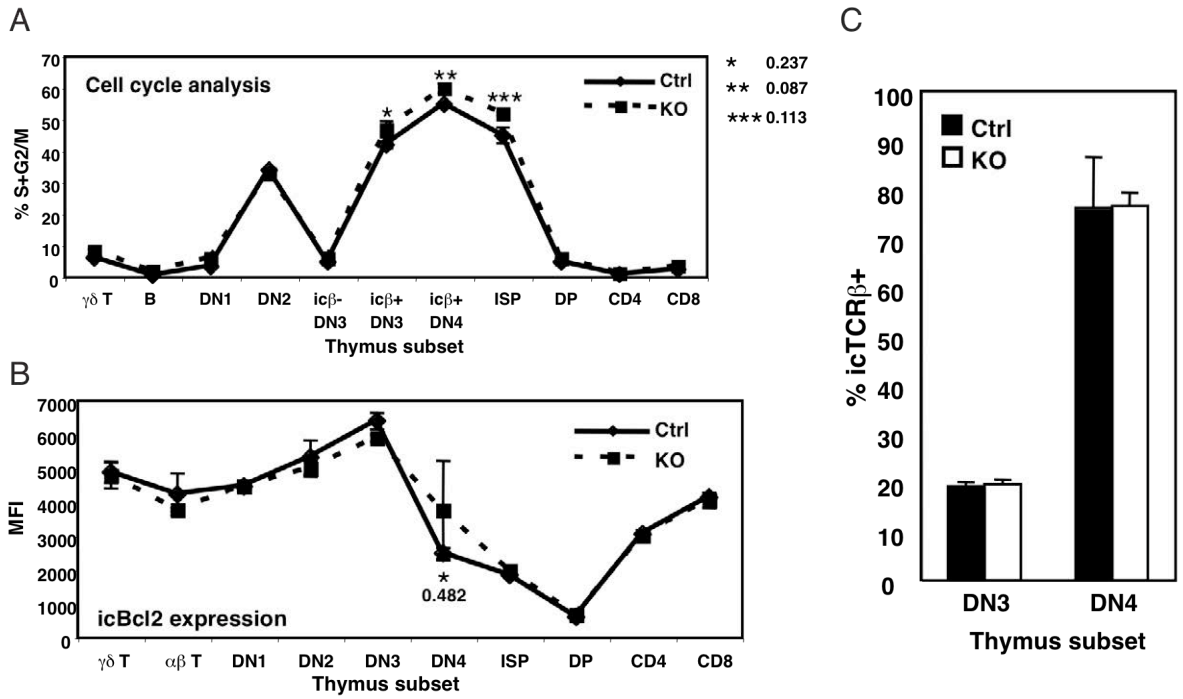

Figure 87. Thymus cell cycle, Bcl2 and TCRβ⁺ analysis. (*A*) Percentage of cells in the S+G2/M. (*B*) Cell count for Bcl2 in the various thymus subsets. (*C*) TCRβ⁺ cells analyzed in DN3 and DN4 subsets. Black lines or bars: control; dotted lines or white bars: knockout mice, data represent average ± SEM. At least 3 mice per group were analyzed.

Inflammatory response experiments

To test functionally the immune system, we have put cells (macrophages or splenocytes) in culture and stimulated them with inflammatory agents and measured the cytokine secretion. We also applied dexamethasone, as anti-inflammatory agent, in the medium and observed if there were genotype-dependent effects.

In the first experiment, we analyzed the role of GILZ in peritoneal macrophages. In all stimulatory conditions tested, we found a tendency for increased RANTES secretion in knockouts, although the overall response was not strikingly different (figure 88).

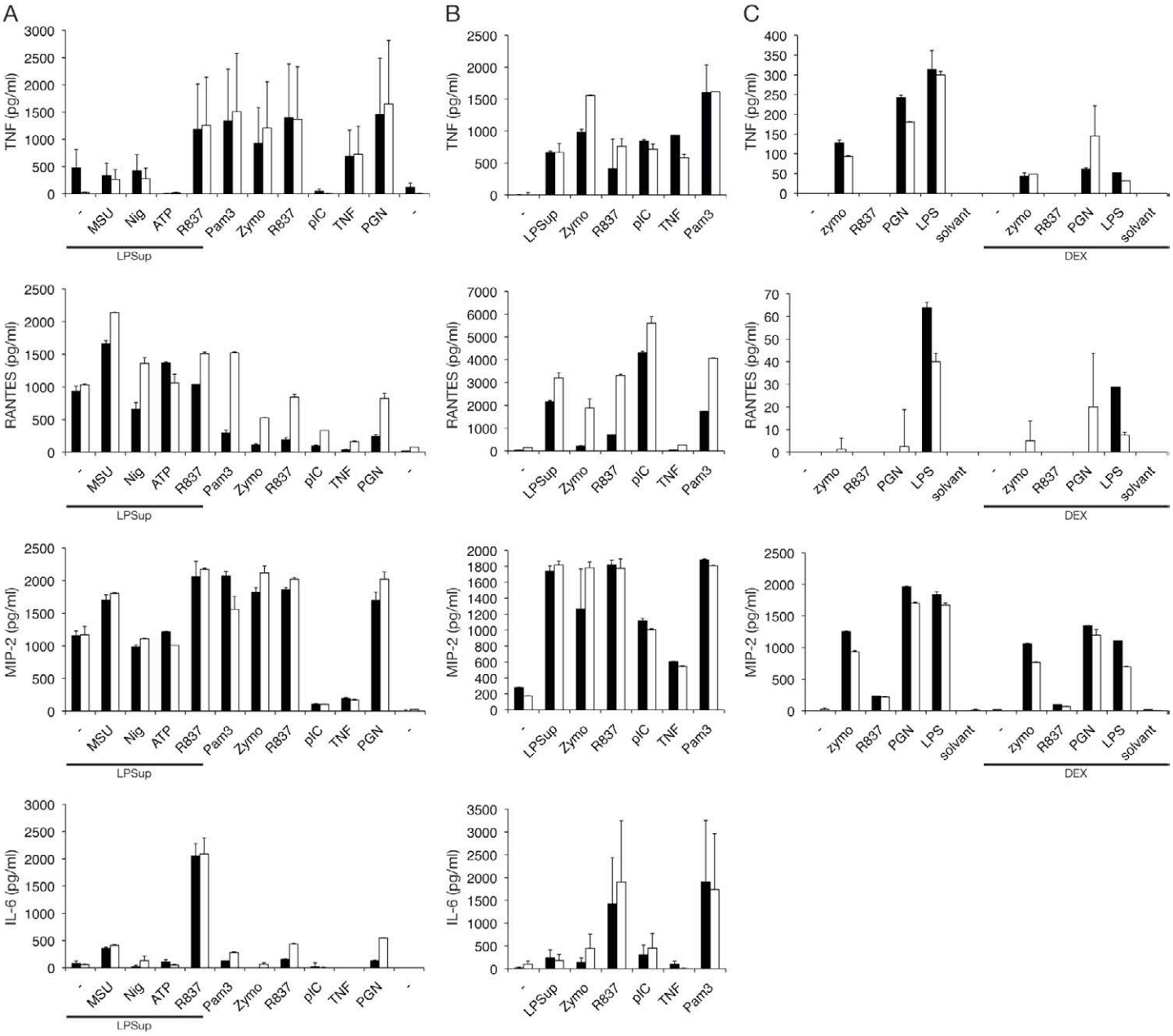

Figure 88 Analysis of peritoneal and bone marrow-derived macrophages cytokine secretion. (*A-C*), ELISA for TNF, RANTES, MIP-2 and IL-6 following (*A*), stimulation of peritoneal macrophages for 6 hours with LPS supplemented by MSU, Nig, ATP, R837 or with Pam3, zymo, pIC, TNF or PGN alone. (*B*), stimulation of peritoneal macrophages for 24 hours with LPS, zymo, R837, pIC, TNF or Pam3 and (*C*), stimulation of bone marrow-derived macrophages with zymo, R837, PGN and LPS with or without dexamethsasone (0.2 µM). Data is shown as mean values of duplicated stimulations ± SEM from 3 mice per group.

In a second series of experiments performed on bone marrow-derived dendritic cells (BMDCs) upon treatment with various stimuli (LPS, MSU, ATP, Candida and CpG), we tested the inflammasome activation and found overall no difference in the secretion of IL-1β, TNF or RANTES between the knockout and the control littermates. Dexamethasone treatment led to an equally reduced cytokine production that was not altered in the absence of Tsc22d3 (figure 89).

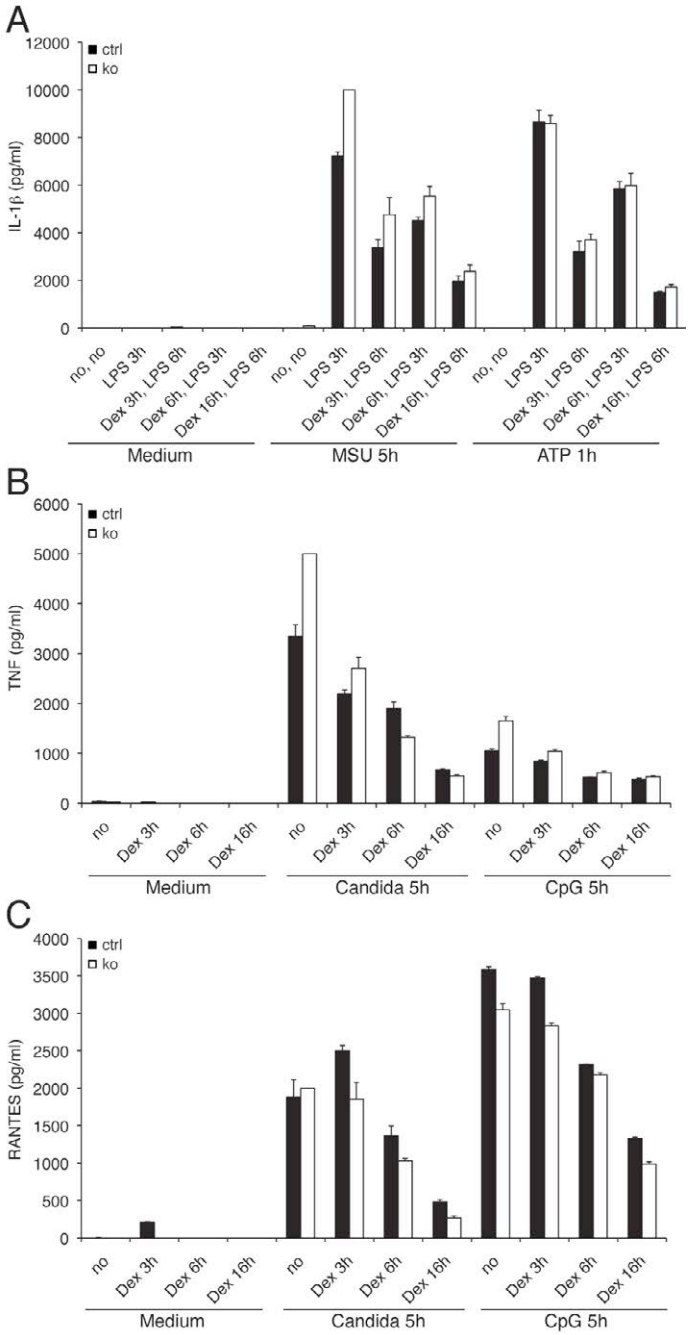

Figure 89. Normal cytokine production by Tsc22d3-deficient bone marrow-derived cells. (*A*), To test inflammasome activation, cells were primed with 10 ng/ml of ultra-pure LPS for the indicated periods prior to inflammasome activation by 100 ng/ml of MSU (for 5h) or 5 mM of ATP (for 1h). Inflammasome activation was quantified by measuring the amount of IL-1β in cell-free supernatants. An influence of dexamethasone on inflammasome activation was addressed by adding dexamethasone to the cells at three different time points prior to ATP or MSU stimulation as indicated. (*B, C*) cells as in (*A*) were pretreated for the indicated periods with dexamethasone and stimulated for 6h with $5x10^6$ heat inactivated Candida cells per ml or 1μM CpG. TNF and RANTES secretion into the medium was measured by ELISA. Data is shown as mean values of triplet stimulations ± SEM and representative for three independent experiments with a total of 6 control and 6 knockout mice.

Furthermore, we tested whether *Tsc22d3* was implicated in a sepsis model and analysed cytokine secretion of IL-6, IL-12, TNF- and IL-2 in bone marrow-derived macrophages upon various stimuli (figure 89). No significant difference could be observed in knockout mice, that responded equally in a dose-dependent manner to dexamethasone administration (figure 89). In addition, experiments performed on splenocytes stimulated by anti-CD3 plus anti-CD28 or

concanavalin A, exibited a dexamethasone dose-dependent response independent on the absence of presence of *Tsc22d3* (figure 90). Altogether, our experiments did not reveal a crucial involvement of *Tsc22d3* in immunology or inflammatory responses upon various stimuli.

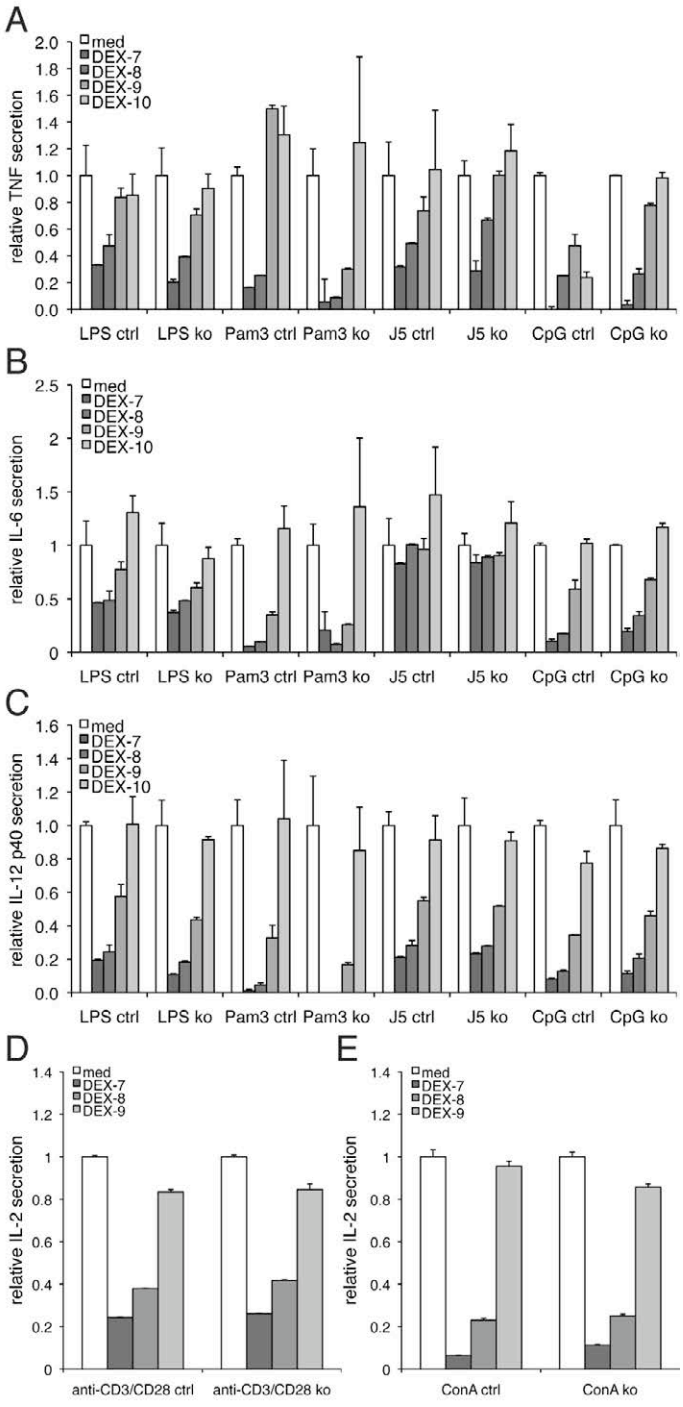

Figure 90. Tsc22d3-deficient bone marrow-derived macrophages (BMDMs) are not particularly susceptible to the immunosuppressive effects of dexamethasone. Control and knockout (*A-C*) and splenocytes (*D-E*) were incubated with or without (med) increasing concentrations of dexamethasone (DEX, 10^{-10}-10^{-7} M) and stimulated with LPS, Pam_3CSK_4 (Pam3), *Escherichia coli* (J5), CpG oligodeoxynucleotide (CpG), anti-CD3 plus anti-CD28 or concanavalin A., IL-6 (*A*), IL-12p40 (*B*), TNF (*C*) and IL-2 concentrations were quantified in cell-culture supernatants collected 4 h (TNF) or 18 h (IL-6, IL-12p40, IL-2) after stimulation. Cytokine concentrations in cells stimulated without dexamethasone were set at 1 for normalization. Data are means ± SD of triplicates samples from one experiment comprising two mice per experimental condition and are representative of two experiments.

Blood parameters

Mice were given to Dr. François Saller (Service and Central Laboratory of Hematology, Centre Hospitalier Universitaire Vaudois and University of Lausanne, Switzerland) to perform blood composition analysis. We could observe a significant decrease in the number of neutrophils and platelets, whereas the lymphocyte number was increased (figure 91). Leukocytes and red blood cells remain unchanged. The monocytes number was decreased, but this difference did not reach statistical significance.

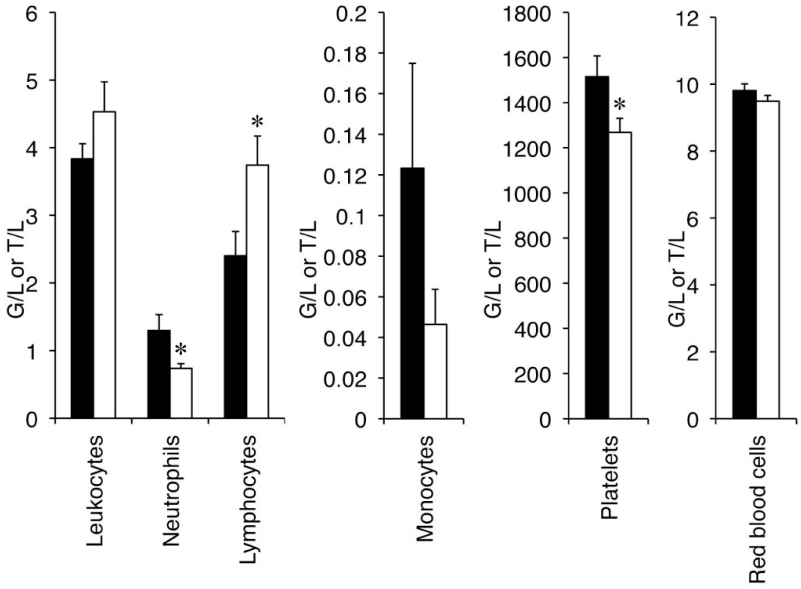

Figure 91: Blood cell count. Values for leukocytes, neutrophils, lymphocytes, monocytes, platelets and red blood cells (erythroblasts). Control (black column) and GILZ knockout (white column) mice (*n* = 9). Bars represent the SEM, ****P* < 0.05.

Gonad development and fertility

The structure on the testis is effected in the GILZ-deficient mice

As mentioned before, male knockout mice were unfertile. In adult animals, testes were drastically reduced in size and they were about 80% lighter (figure 92*A*). Histology revealed important structural changes (figure 92*B*). Indeed, the seminiferous tubules of knockout mice were disrupted and there was an augmented proportion of interstitial Leydig cells (arrow). Figure 92*C*, shows a view from immunostained seminiferous tubules using a CCCTC-binding factor (CTCF) antibody, counterstained with hematoxylin for nuclei (blue). This CTCF antibody labelled Sertoli cells (figure 92*C*, black-filled arrowhead). We could observe the presence of elongated spermatids in the controls (figure 92*C*, white arrowhead), whereas the knockout tubules lacked developing germ cells, where only few residual Sertoli cells remained.

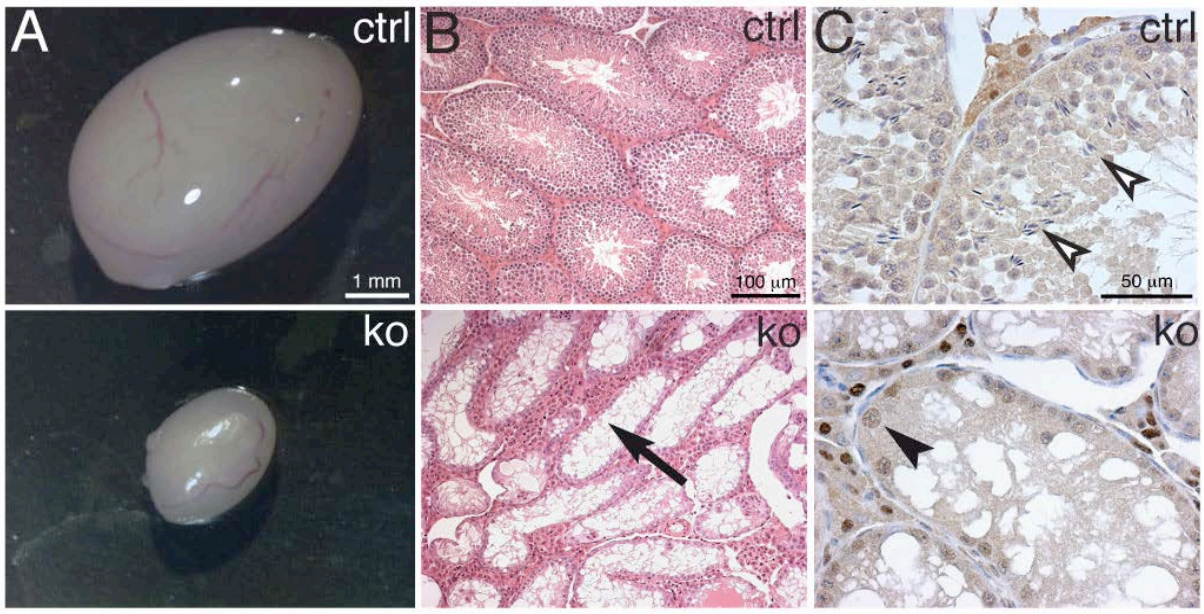

Figure 92. Tsc22d3 knockout males are sterile. (*A*), Representative pictures from control (left) and knockout (right) adult testes. Note the significant decrease in testicular mass in adult knockout. (*B, C*), H&E-stained paraffin sections from control (ctrl) and knockout (ko) testes reveal increased spermatogenic cell apoptosis, absence of mature sperms and hyperproliferation of Leydig cells (black arrow). (*C*), Immunohistochemistry of Sertoli cells (rabbit anti-CTCF antibody; black arrowhead) and counterstaining with hematoxylin reveals blue nuclei. Note the presence of elongated spermatids (white arrowhead) in the control testis, which is absent in the knockout.

We quantified the number of cells per tubule. The knockout tubules have a lower cell population; the ratio is given in figure 93 (left graph). To discriminate whether this difference originated from a lower cell proliferation or an increased cell death, we stained sections with Ki-67 and TUNEL labelling, respectively. We counted positive cells (for Ki-67 and TUNEL markers) and normalized this value to the total number of cell per tubule for each genotype. The ratio of proliferative cells (Ki-67) was the same in both groups, whereas the in the knockout tubules the proportional number of apoptotic cells (TUNEL) was significantly increased (figure 93, right graph). These data were consistent with the anti-apoptotic role proposed for GILZ.

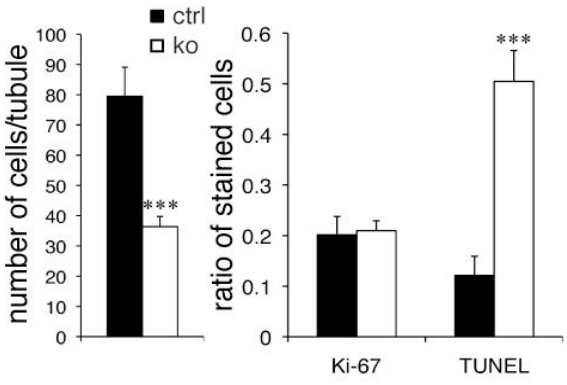

Figure 93. Total number of cells per seminiferous tubule (*N* ≥ 20 tubules per group) in control and knockout mice (left). Ratio of Ki-67 positive cells divided by total cell number, middle) and ratio of TUNEL positive cells divided by total cell number per seminiferous tubule, *N* = 18 tubules, right).

Hormonal measurements and GILZ-target genes analyses

We analysed the plasma levels of several hormones, which are crucial for sexual development and its maintenance (figure 94). Corticosterone levels were significantly lower in the knockouts. FSH and testosterone concentrations were significantly increased. LH levels were not changed.

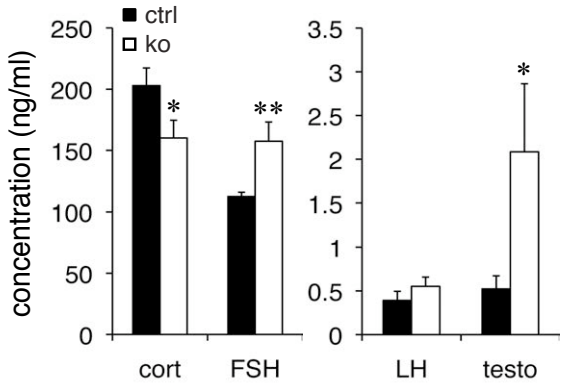

Figure 94. Corticosterone (cort), follicle stimulating (FSH), luteinizing hormone (LH) and testosterone (testo) hormone levels in plasma [ng/mL] from control and knockout males (n ≥ 10 animals per group).

Several mRNA transcripts were abnormally expressed in testis: PPARγ2, PPARγ, Tsc22d1, GR, AR, KLF5 and KLF15. The mRNA level of PPARγ2 was significantly lower in knockouts as shown by RT-PCR and qRT-PCR (figure 95*A* and *B*). We also analyzed the protein level in testis lysates (figure 95*C*). In this experiment, it was only possible to detect the 56 kDa PPARγ2 band in the control samples. This was not surprising, because the expression of mRNA transcripts was low in the knockout testes.

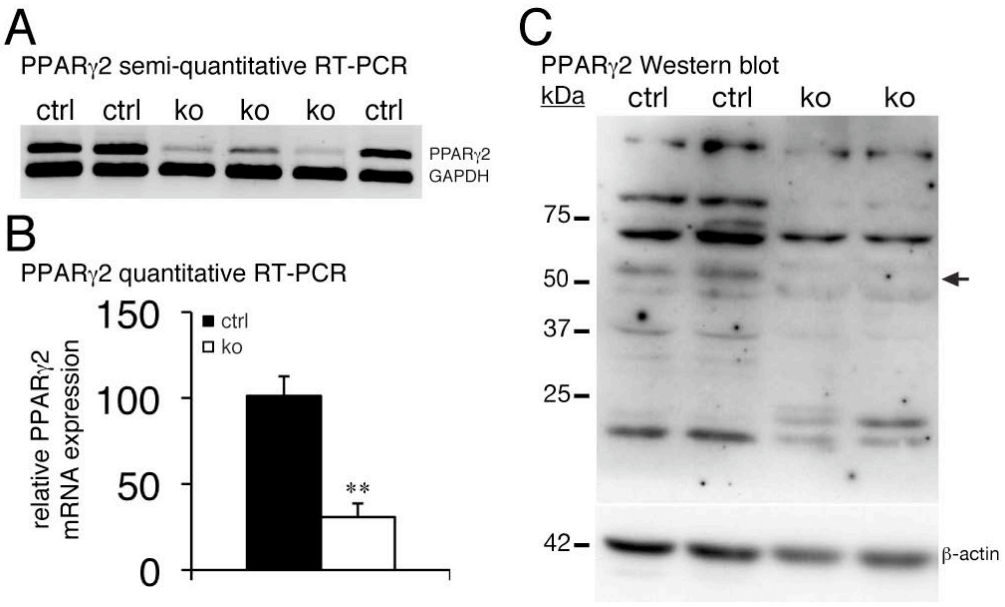

Figure 95. Analysis of PPARγ2 expression in testis. (*A*) Semi-quantitative RT-PCR for PPARγ2. As control, GAPDH mRNA was used. (*B*) Quantitative RT-PCR for PPARγ2 normalized to GAPDH expression. (*C*) Western blot analysis using a PPARγ2 antibody on testis lysates. The arrow indicates the PPARγ2 protein (56 kDa). As loading control β−actin was used. Black bars: control; white bars: knockout mice. Data represent average ± SEM. Statistical analysis was performed using the unpaired Student's t-test, where **P < 0.01 when compared to control.

Sertoli cell and germ cell-specific GILZ knockout mice

In collaboration with Yannick Romero (Department of Genetic Medicine and Development, University of Geneva, Medical School, Switzerland), we generated mice bearing the *gilz* deletion specifically in Sertoli cells or in germ cells.

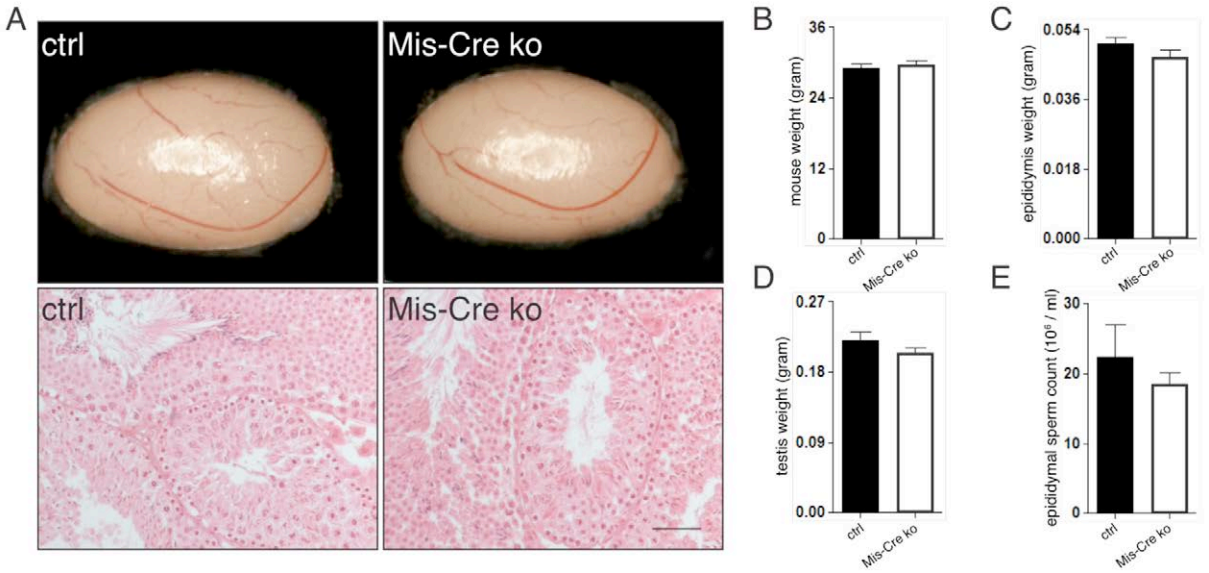

Figure 96: Sertoli cell specific knockout. *A*, Pictures of a whole testis (upper panel) and histological sections (lower panel) from control and GILZ::Mis-Cre knockout littermates (80 days-old mice). The mouse body (*B*), epididymis (*C*) and testis (*D*) weights are given. *E*, Epididymal sperm count. Control (black column, n = 9) and GILZ::Mis-Cre knockout (white column, n = 4) mice. Bars represent the SEM.

Sertoli cell-specific GILZ knockout (Mis-Cre ko (Lecureuil et al., 2002)) mice displayed normal testis size and histology at 80 days of age (figure 96*A*). The mouse body weight, epididymis and testis weights were comparable to the control mice (figure 96*B-D*). The sperm count was also similar to the controls (figure 96*E*).

Germ cell-specific GILZ knockout (Vasa-Cre ko (Gallardo et al., 2007)) mice displayed reduced testis size and the overall organization of seminiferous tubules was similar to the constitutive knockout at 80 days of age (figure 97*A*). The mouse body weight was unchanged, whereas epididymis and testis weights were significantly lower than the controls (figure 97*B-D*). The sperm count was near zero in the Vasa-Cre ko mice (figure 97*E*).

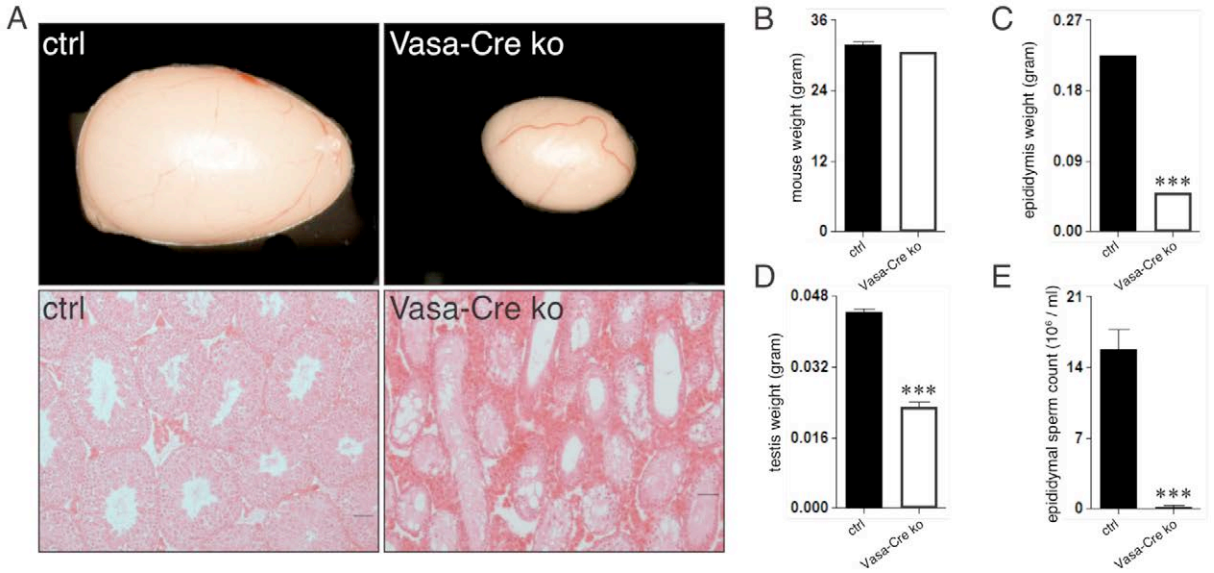

Figure 97: Germ cell specific knockout. *A*, Pictures of a whole testis (upper panel) and histological sections (lower panel) from control and GILZ::Vasa-Cre knockout littermates (80 days-old mice). The mouse body (*B*), epididymis (*C*) and testis (*D*) weights are given. *E*, Epididymal sperm count. Control (black column, *n* = 4) and GILZ::Vasa-Cre knockout (white column, *n* = 3) mice. Bars represent the SEM, ***$P < 0.001$.

Skin analysis

To investigate whether GILZ played a role in the skin we performed barrier function and wound healing experiments. Histologically, the GILZ knockout skin presented no defect (figure 98). The overall structure was preserved (width of the epidermis, no sign of inflammation detected). Obviously, the amount of hair follicles was normal.

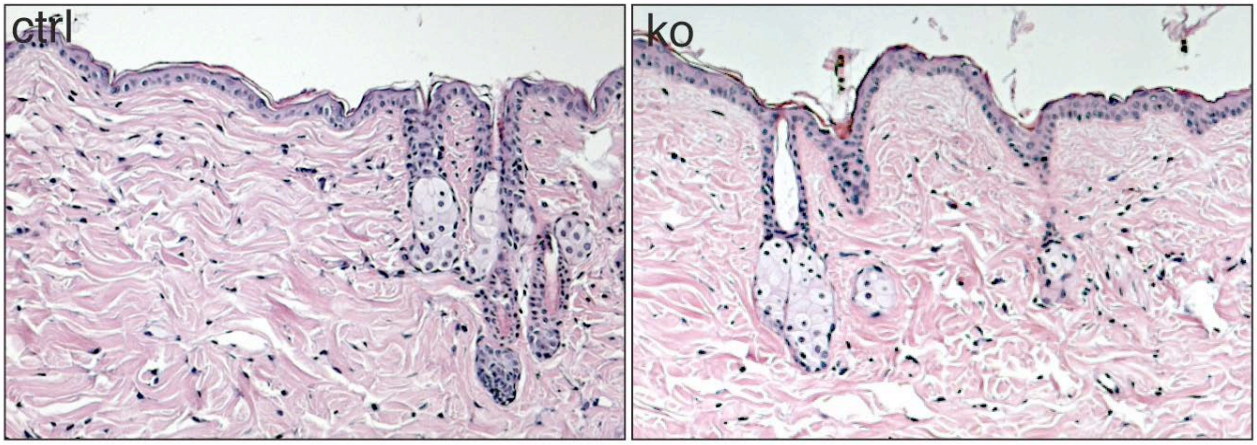

Figure 98: H&E stained skin sections at 100x magnification.

Transepidermal water loss (TEWL) measurements show significantly ($P < 0.001$) increased outwards water loss through the knockout skin compared to controls (figure 99).

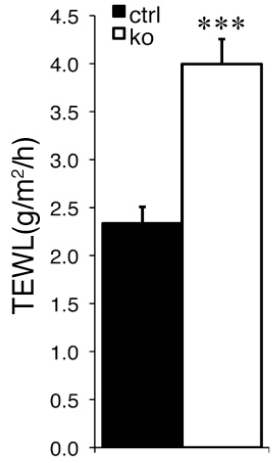

Figure 99: Transepidermal water loss (TEWL) measurements. Control (black columns) and GILZ knockout (white columns) mice. For each group n ≥ 5 animals (with at least 3 measurements per mouse). Bars represent the SEM, ***$P < 0.001$.

To investigate further this skin barrier phenotype, I performed the toluidine blue skin permeation assay with newborn mice (P0). This allowed to control whether there was an inwards barrier defect as well. Figure 100 showed staining of the head and forelimb of several mice after the toluidine blue treatment. The staining with toluidine of the knockout skin was not stronger than for the control littermates. This suggested, that at P0, there was no apparent barrier defect.

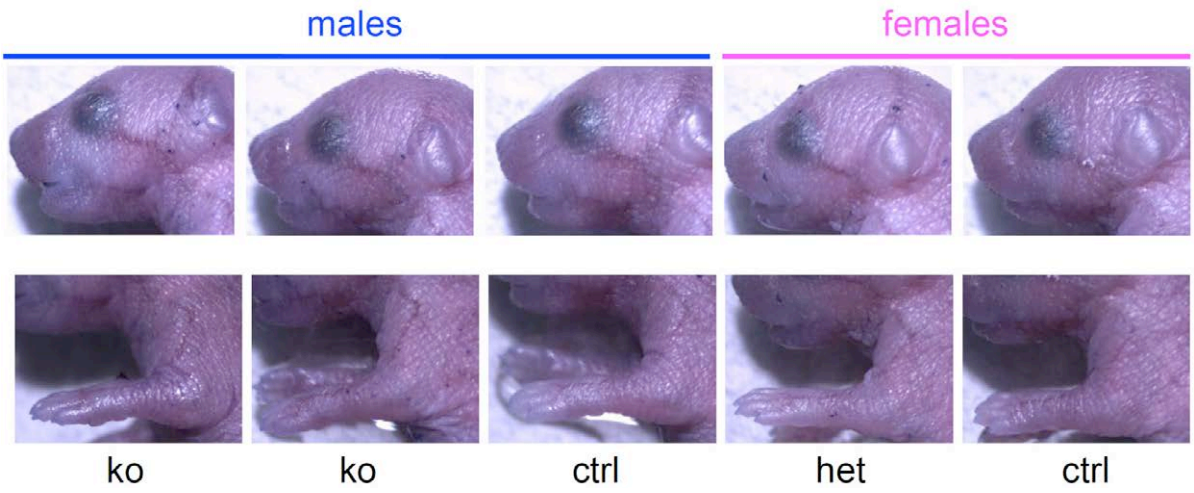

Figure 100: Toluidine blue skin permeability assay. Picture of head and forelimb of P0 mice after immersion in toluidine blue solution.

We analyzed the wound closure rate in control and GILZ-deficient mice. The knockout mice presented no delay nor accelerated wound healing (figure 101).

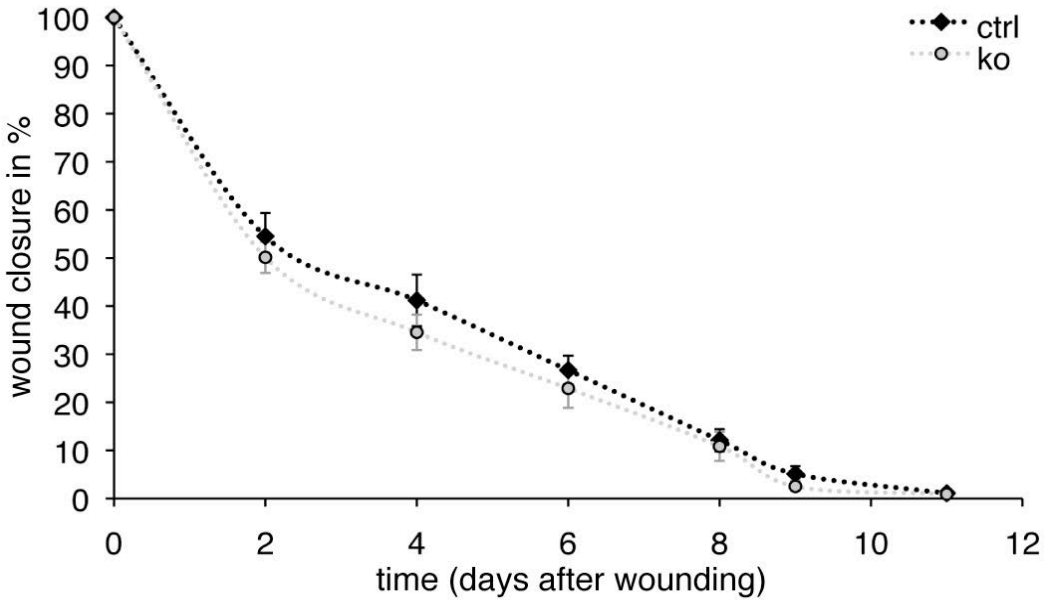

Figure 101: Wound healing kinetics in GILZ-deficient mice. Control (black dots) and knockout (grey dots) mice closure rate after wounding. For each group n ≥ 5 animals (means of 2 wounds per mouse). Bars represent the SEM.

The architecture of the healing skin, and here more specifically, the hyperproliferative epithelium, was similar in both groups as seen in figure 102. The analysis of the morphometrical parameters (the hyperproliferative epithelium surface and the wound width) indicated no defects (figure 103).

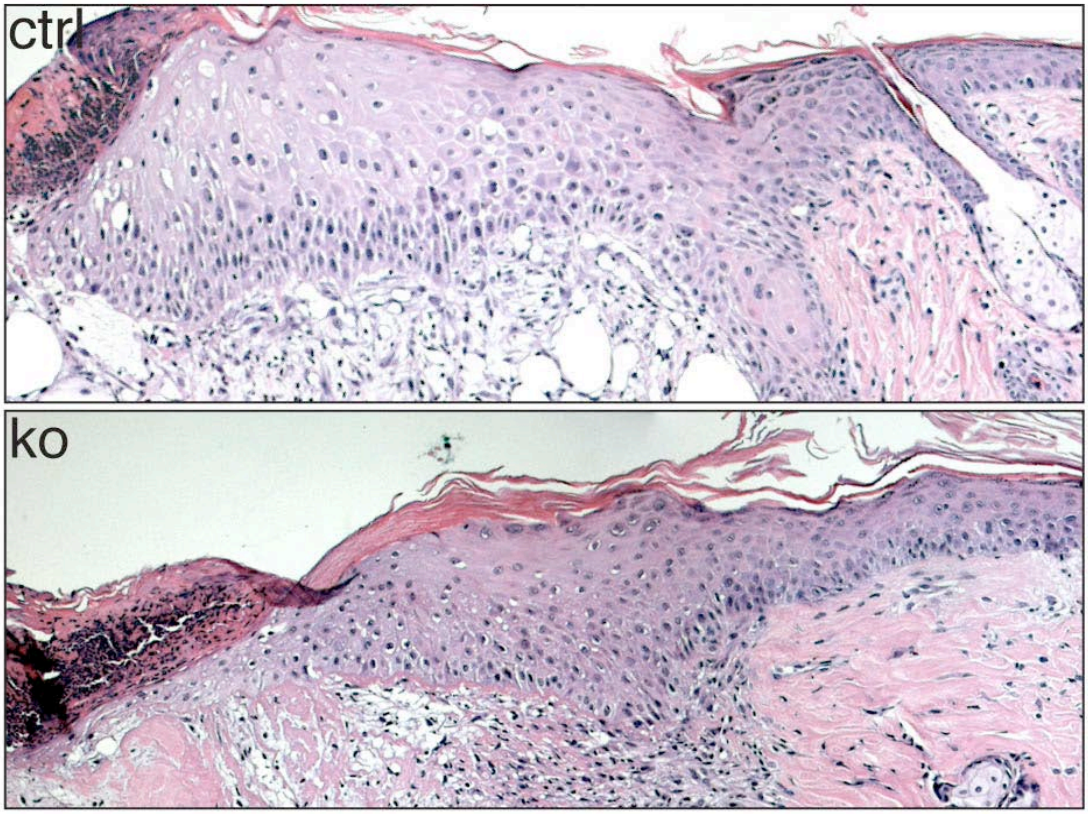

Figure 102: H&E stained skin sections at 100x magnification five days after wounding. Representative pictures of the hyperproliferative epithelium of control (ctrl) and GILZ knockout (ko) mice.

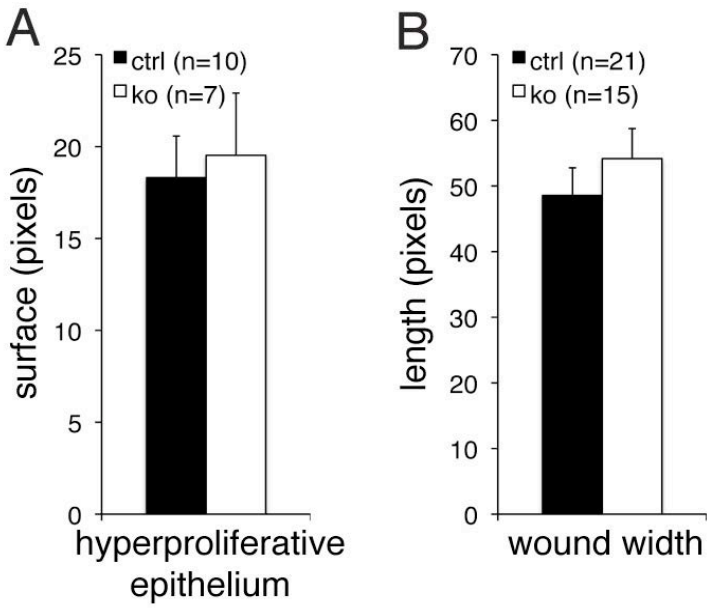

Figure 103: Morphometrical analysis of the skin. *A*, Quantification of hyperproliferative epithelium surface. *B*, Wound width. Control (black column) and GILZ knockout (white column) mice. Bars represent the SEM.

DISCUSSION

The GILZ knockout mouse model

GILZ and its homolog genes have been studied for more than ten years in different species and cell types. These *in vitro* investigations showed that GILZ played a role in immunological and inflammation processes, but also in bone or adipose tissue formation. It has also been suggested that GILZ was a regulator of the ENaC-mediated renal sodium reabsorption *via* the ERK pathway.

Our group generated the first constitutive knockout mice for the *gilz* gene. These mutant mice were viable. Molecular analysis of this mouse model revealed that the Cre-mediated recombination was 100% in the knockout mice. Our qPCR analysis data revealed only residual GILZ mRNA expression in heart, lung and skin tissue. We performed also Western blot analysis to detect the levels of GILZ protein in several tissues (antibody from kindly provided by Dr. David Pearce, UCSF, USA). This allowed to confirm the absence of GILZ protein in all the tissues tested.

Water and sodium handling

Several genes, like *Sgk1* and *Nedd4-2*, were known to regulate the degradation of ENaC (Soundararajan et al., 2010). As already mentioned in the first part of this thesis, mutations in ENaC or its regulator can result in more or less severe renal phenotypes. We have performed electrolyte and aldosterone analysis in GILZ-deficient mice. We found small changes in plasma electrolyte concentration without dramatic physiological effects. These mice adapted normally to 10-day low sodium diet or 23-hour water deprivation. In conclusion, the expected function on the renal salt and water homeostasis is still under debate, or at least, GILZ is not limiting for this regulation.

Immunity in GILZ knockout mice

The activation of cytokine expression and secretion by cells of the innate immune system is essential for early host defence against infections and for subsequent development of adaptive immunity, as well as for the expression of many inflammatory diseases. Endogenous glucocorticoids can modulate the expression of pro- and anti-inflammatory genes, and therefore, they are widely used as anti-inflammatory and immunosuppressive agents (Baschant and Tuckermann; Herold et al., 2006). Following dexamethasone administration, *Gilz* expression was highly up-regulated, suggesting a potential role of GILZ in the immune system

and inflammation processes (D'Adamio et al., 1997). GILZ has been extensively studied *in vitro*, thus we investigated the immune system development and the inflammatory response upon various stimulations.

Immune development and function were also assessed in our GILZ-deficient mice. There, no dramatic abnormalities were found. After puberty, the thymus weight was decreased in the knockouts, but the general architecture was preserved. This suggests that this effect might be due to the high concentration of plasma testosterone. Indeed, androgens influence considerably the size and composition of the thymus. Chemical or surgical castration results in thymic enlargement, whereas androgen replacement reverses these effects (Olsen et al., 1998; Hince et al., 2008; Lynch et al., 2009). The majority of the subsets analyzed from the thymus, spleen and lymph node were not affected in cell number. Exception was found in the thymus with significantly less double-negative (DN)3 and more DN4 thymocytes. Here again, this could be an indirect effect due to the unbalanced testosterone concentration. Castrated rats presented an increased proliferation of DN3 cells (Leposavic and Perisic, 2008). In the spleen, we found more erythroblasts in knockouts. Erythropoiesis has been found to be increased by testosterone treatment in human (Coviello et al., 2008). Thus, we propose that the increased spleen erythroblast value in GILZ knockout mice may be due to the high testosterone concentration. Of interest, the DP thymocyte population, which is known to be glucocorticoid-senstitive, is the same in the two groups (Ashwell et al., 2000).

Functionally, cytokine secretion from macrophages or splenocytes was normal and anti-inflammatory response to dexamethasone treatment was preserved. We found significantly lower number of neutrophils and platelets, but higher number lymphocytes in the blood (figure 72). This indicates an unbalanced haematopoietic stem cell development or regulation in the knockout.

In summary and unexpectedly, in immunity, less difference as expected could be observed between the mutant mice and the control littermates. Together, these data indicate that solely GILZ was not required for normal immune development and response. Indeed, there was probably functional redundancy; there were probably other partners that could compensate the lack of GILZ.

Fat metabolism is mildly altered in GILZ-deficient mice

It has been demonstrated that GILZ could inhibit adipogenesis of mesenchymal stem cells by binding to a tandem repeat of C/EBP binding sites in the PPARγ2 promoter (Shi et al., 2003). This suggests that GILZ might play a developmental role. Under standard conditions, GILZ-

deficient mice did not gain weight like control mice, this difference was significant from 6 months onwards. The body fat composition is significantly lower in 15-month-old knockout mice. This indicates that this metabolic defect is linked to aging, or at least evidenced with time. In 3 to 4-month-old mice, the expression of several adipogenic markers was unchanged at the mRNA level. GILZ deficiency influenced the levels of plasma insulin, thus knockout mice had increased concentrations under standard conditions. Glucose levels were less affected, but were generally decreased (not significantly) in all our experiments. Glucose and insulin tolerance tests did not reveal differences. To uncover the mechanisms by which the GILZ-deficient mice are protected against weight intake, we have put them under a high fat diet (HFD) for about 15 weeks. Echo MRI body composition analysis indicated that the fat content is lower in knockout mice. Liver histology showed that GILZ-deficient mice do not develop hepatic steatosis. Although the analysis is not complete yet, it is clear that knockout mice are protected against HFD-induced obesity.

GILZ knockout males are sterile

The first and most striking phenotype observed was the sterility of y/Δ males. This was observed while the knockout males were used for breeding. Whole body histology has been performed to uncover developmental or pathophysiological defects. All tissues analyzed presented normal histology with the exception of testis characterized by severe dysplasia evident as early as 20 days after birth. We expected that higher corticosterone levels would compensate the lack of GILZ, but this opposite result might be due an inappropriate feedback loop mechanism. Or in the testis, the action of GCs is mediated *via* GILZ. Circulating testosterone and FSH levels are higher, whereas LH is not significantly modified. Histology of knockout testes revealed incorrect maintenance and development of germ cells. FSH and androgen act to stimulate and maintain spermatogenesis. In order to characterize the specific effects of FSH, hypogonadal (*hpg*) mice crossed with either Sertoli cell-specific (*hpg*.SCARKO) or total androgen receptor knockout mice (*hpg*.ARKO), then supplemented with recombinant FSH. This study revealed that FSH, independently of androgens, stimulated spermatogenesis during the initial stages to optimise germ cell number. FSH also indirectly stimulated androgen production by the Leydig cells, that induces proliferation and/or differentiation from precursor stem cells (O'Shaughnessy et al.). This could partly explain the increased Leydig cell population and higher plasma testosterone level. It was also found that the androgen receptor mRNA level in the testis was higher. These data suggested androgen insensitivity. It is not well established whether glucocorticoids could affect AR expression or if

GILZ is involved in its regulation, but crosstalk between hormone receptors cannot be excluded (Yen et al., 1997).

Interestingly, we found significantly lower expression of *Pparγ2* mRNA and protein. It has been reported that PPARγ is expressed in Sertoli cells and in spermatocytes (Froment et al., 2006). PPARs might play a role in reproductive tissues, but their exact function is still under debate (Froment et al., 2006; Huang, 2008).

It is not known, whether the mutation also affects the origin of the hypothalamic-pituitary-gonadal (HPG) axis. GILZ is present in the chicken pituitary and regulates several hormones (Ellestad et al., 2009); this may also explain the increased levels of FSH in knockout mice. Stress effects on reproduction result from abnormal regulation of the hypothalamic-pituitary-adrenal (HPA) and the HPG axes (Kirby et al., 2009). After immobilisation stress in the rat, there is an increase in circulating GCs followed by a drop of the testosterone level. This is further associated with an enhanced testicular germ cell apoptosis (Yazawa et al., 1999). In our GILZ knockout mice, we measured a 20% decrease of plasma corticosterone concentration, but we also find an increased apoptosis rate. It has been reported that a potent GR agonist (mifepristone or RU486) could inhibit the dexamethasone-induced germ cell apoptosis (Yazawa et al., 2000; Sasagawa et al., 2001). Several studies involving *bunched*, the drosophila TSC22 homolog, showed that this gene is important for cellular growth, proliferation and survival (Dobens et al., 1997; Gupta et al., 2003; Levine et al., 2007; Wu et al., 2008). In yeast, an antiapoptotic motif has been described for this gene (Khoury et al., 2008). This sequence is present in the GILZ nucleotide sequence. Hence, the lack of GILZ protein could promote apoptosis. In this study, we only investigated the male phenotype. In collaboration with Dr. Serge Nef, in Geneva, we are currently generating female knockout mice using the Vasa-Cre mice (Gallardo et al., 2007). This germ cell-specific promoter is leaky in the females, meaning that the expression of the targeted gene is partial during a certain time. This allows the generation of knockout females. There are strong indications that the female fertility might be impaired as well. It has been shown that GILZ contains an estrogen response element in the promoter region (Tynan et al., 2004). It is regulated during pregnancy and might play a role in facilitating the detachment of the fetus and the placenta from the implantation site (Zhao et al., 2006).

Summary of the findings

Field of interest	Phenotype / observations
Whole body histopathology	No obvious phenotype at birth until two weeks of age, progressive testis atrophy. The development and morphology of all other organs tested is not different from controls. Heart index increased in adults, kidney index unchanged.
Sodium and water handling	Upon normal salt diet, plasma potassium concentration increased, sodium concentration unchanged. Upon sodium-deprived diet, plasma potassium concentration decreased, sodium concentration increased. Aldosterone concentrations are unchanged upon each condition. Adaptation to 23h water deprivation preserved.
Immunity	Adult thymus decreased in size. With exception of the increased number of erythroblast, the spleen size and cell subsets not different from control. The inflammatory responses in macrophages and splenocytes (cytokine secretion and sepsis +/- dexamethasone treatment) were not different from controls. Blood neutrophils and platelets were decreased, and lymphocytes increased.
Fat metabolism	From 6 months onwards, lower body weight and fat content. Plasma insulin level was elevated under standard diet conditions. Glucagon secreting cells were increased in Langerhans islets despite normal plasma glucagon levels. MEF differentiation into adipocytes was not different from controls. Knockout mice were protected against high fat diet-induced obesity.
Fertility	Knockout males were sterile. Testes were smaller and presented a severe dysplasia most likely due to increased apoptosis. Spermatogenesis was impaired and mature spermatozoa absent. Leydig cell hyperproliferation. Plasma corticosterone levels were lower, whereas FSH and testosterone were higher. Testis from Sertoli cell-specific GILZ knockout mice were not different from controls, whereas testis from germ cell specific GILZ knockout were like in the complete knockout.

Skin	Transepidermal water loss was increased when compared to controls. The inwards barrier function of the newborn skin was intact as evidenced by toluidine blue permeation assay.
Molecular analysis (mRNA)	PPARγ2 decreased in testis and liver. PPARγ decreased in testis. KLF5 decreased in testis. KLF15 increased in testis. TSC22D1 increased in testis. Glucocorticoid receptor decreased in testis. Androgen receptor increased in testis.

PERSPECTIVES AND FUTURE EXPERIMENTS

To unveil the pathophysiology related to the male sterility phenotype, it would be necessary to study the mechanisms in a spatio-temporal way; this can be done by cellular and molecular means. We will have to determine the onset of the phenotype and characterize the pathways or molecules that are deregulated causing sterility. This could be achieved mainly by immunohistochemistry and qRT-PCR analyses. Also further investigations of the Vasa-Cre (germ cell-specific) GILZ knockout mice would help to understand those apoptotic processes, induced by GILZ-deficiency in spermatogonia, that might be responsible for the sterility. By crossing Vasa-Cre female mice ($GILZ^{lox/+}$; Cre+) with Vasa-Cre negative males ($GILZ^{lox/y}$; Cre-), it is possible to obtain female GILZ knockout mice ($GILZ^{lox/lox}$; Cre+). It will be interesting to analyze the phenotype of these female knockout mice.

Protection against high fat diet-induced obesity must be studied more in details. Fat and liver tissue analysis (mRNA expression levels of specific markers and histology). ITT and GTT must be performed under high fat diet. Energy expenditure analyses should also help to uncover certain mechanisms causing this metabolic phenotype.

Since GILZ is part of the same complex with ENaC/SGK1/Nedd4-2, it would be of great interest to cross the GILZ knockout mice with the SGK1 mutant mice (Wulff et al., 2002) to observe an eventual renal phenotype.

It would be interesting to make a double knockout Tsc22d3/Tsc22d1 (L. Raftery laboratory). This would help us to verify whether redundancy occurs in GILZ knockout mice.

GILZ is expressed in neurons of the central nervous system as shown by *in situ* hybridization analyses (Yachi et al., 2007). In this study, Yachi and colleagues established a link between stress and GILZ. Glucocorticoids are released in response to stress stimuli (Muller et al., 2004), therefore cognitive experiments would allow to establish the functional activity of GILZ in the central nervous system and, for example concerning the stress sensibility.

ANNEXES

Manuscript in preparation

VERSION 13-03-2011

Inactivation of the glucocorticoid-induced leucine zipper (Gilz/*Tsc22d3*) gene locus reveals functional redundancy in immunology and physiology but implication in male fertility

Philippe E. Suarez*@, Elena Gonzalez Rodriguez*@, Anne-Marie Mérillat*, Jean-Christophe Stehle†, Samuel Rotman†, Thierry Roger‡, Marie-Jeanne Voirol§, Jian Wang¶, Olaf Gross‖, Virginie Pétrilli‖, Karim Nadra††, Anne Wilson#, Friedrich Beermann≠ François P. Pralong§, Marc Maillard**, David Pearce¶, Jürg Tschopp‖, Bernard C. Rossier*, Edith Hummler*

Affiliations:

*. Department of Pharmacology and Toxicology, University of Lausanne, Switzerland

†. Institute of Pathology, CHUV, Lausanne, Switzerland

‡. Infectious Diseases Service, Department of Medicine, CHUV and University of Lausanne, Switzerland

§. Service of Endocrinology, Diabetology and Metabolism, Department of Medicine, CHUV and University of Lausanne, Switzerland

¶. Division of Nephrology, Department of Medicine, University of California, San Francisco, USA

‖. Department of Biochemistry, University of Lausanne, Epalinges, Switzerland

††. Department of Medical Genetics, University of Lausanne, Switzerland

#. Ludwig Institute for Cancer Research Ltd., Lausanne Branch, 1066 Epalinges, Switzerland

≠. ISREC SV EPFL, Lausanne, Switzerland

**. Service of Nephrology, CHUV, Lausanne, Switzerland.

@. Authors corresponded equally.

Corresponding author:

Dr. Edith Hummler

Department of Pharmacology and Toxicology, Rue du Bugnon 27, CH-1005 Lausanne, Switzerland; Fax: +41216925355; Phone: +41216925357; e-mail: Edith.Hummler@unil.ch

Abstract

The glucocorticoid-induced leucine zipper (Gilz, *Tsc22d3*) is a widely expressed X-linked transcription factor, which was originally identified as a dexamethasone-induced transcript in murine thymocytes. Based on work in cell culture, TCS22D3 has been proposed to be important in immunity, adipogenesis and renal sodium handling. In the present work we have now generated mice deficient for *Tsc22d3* using Cre/loxP-mediated technology. Males deficient for *Tsc22d3* are born according to expected Mendelian distribution. Showing a similar growth curve following birth, male null mutants weight significantly less than their littermate controls from 6 months of age onwards, and their fat content is lower accompanied by an insulin resistance. Expression of PPARγ2, one of the target genes, is downregulated in testis and liver, but unchanged in various tissues and adipogenesis seems not to be impaired. Sodium- and water-deprivation experiments revealed no dysbalance in sodium and water handling of knockout mice. Moreover, T-cell development is not impaired and inflammatory cytokine secretion in peritoneal, splenocyte or bone marrow-derived macrophages, or in sepsis is in the normal range. Strikingly, mating of these *Tsc22d3*-deficient males yielded no offspring, and they proved to become sterile exhibiting a severe testis dysplasia from postnatal day 10 onwards accompanied with significant apoptosis in seminiferous tubules, increased number of Leydig cells, and significantly elevated FSH and testosterone levels. In summary, *Tsc22d3*-deficient male mice are viable, but sterile and do not show severe impairment in metabolism, salt and water balance as well as in immune and inflammatory reactions unveiling partial functional redundancy in mediating glucocorticoid responses.

Introduction

Glucocorticoids are involved in physiological regulation of a variety of processes, including immune responses, metabolism, cell growth, and development. Due to their anti-inflammatory and immunosuppressive role, they are widely used in clinic as to treat inflammation, allergy, or malignancies (see for review Ayroldi and Riccardi, 2009 (1)). The X-linked glucocorticoid-induced leucine zipper (GILZ) was originally identified as dexamethasone-induced transcript protecting T lymphocytes from TCR/CD3-activated cell death (2). GILZ encodes a new member of the TSC22-domain leucine zipper family and is found expressed in lymphocytes from thymus, spleen, and lymph nodes, whereas low or no expression is detected in other non-lymphoid tissues, including brain, kidney, and liver (2). Members of this family,

TSC22D1 to TSC22D4 share a highly conserved TSC- (tuberous sclerosis complex)-box domain and a PDZ (post synaptic density protein (PSD95), Drosophila disc large tumor suppressor (DlgA), and zona occludens-1 protein (zo-1)-binding domain at the C-terminus (see for review Ayroldi and Riccardi, 2009 (1)). Initially thought to function as a transcription factor, Gilz homodimerizes or heterodimerizes by means of its leucine zipper domain (3). In total, four isoforms with have been characterized as splice variants from the TSC22D3-2 gene, named GILZ1-4 (4). Present with varying abundance in mouse and rat tissues, data suggested that the four isoforms are not functionally redundant but rather involved in distinct aspects of cellular physiology and might therefore modulate distinct signaling pathways (4). Furthermore, due its multiple protein interaction in a variety of cell types, TSC22D3-2 was proposed to be implicated mechanisms, like apoptosis and cell proliferation, but also in more specialized functions, like e.g., the modulation of T lymphocyte activation and Il2-production (5-7) and in dendritic cell function (8, 9). Furthermore, TSC22D3-2 was shown to control malignant transformation through inhibition of Ras-driven tumorigenesis (6) to mediate renal sodium transport (10, 11) or adipogenesis (12).

In order to investigate the role and implication of TSC22D3-2 in these processes, we generated a mouse model constitutively lacking the main isoforms 1, 3 and 4 (4). Surprisingly, male null mutant mice are viable, but sterile but do not present severe dysfunctioning in the immune system, in adipogenesis or sodium reabsorption. Our data demonstrate that TSC22D3-deficiency alone does not play the important role as proposed from the in vitro studies. Immune reponses, adipogenesis and sodium handling are not dependent on TSC22D3, but may be the result of interplay amongst various proteins most likely of the same TSC22 family. In contrary, the male TSC22D3 mutant mice develop sterility and this only depends on the presence of TSC22D3.

Results

Generation of *Tsc22d3* knockout mice

To generate mice with a floxed *Tsc22d3* allele, we constructed the targeting vector shown in **Suppl.Fig. 1**. This contained two loxP sites flanking exon three to six that encode for the leucine zipper, TSC22, proline-rich and PDZ domains and the flirted neomycin cassette 3'. The structure of the recombined floxed allele before and following removal of the neomycin cassette and the knockout allele (Δ) is indicated in **Suppl.Fig. 1A**. For homologous recombination of the *Tsc22d3* gene, the targeting vector was electroporated into ES cells, and

5 independent correctly targeted clones were obtained. **Suppl.Fig. 1B** shows representative Southern blot analyses from correctly targeted ES cell clones digested with *Eco*RV (5' probe) and *Eco*RI (3' probe) that reveal diagnostic fragments of 7.8kb and 2kb, respectively. Three recombined ES cell clones were injected into blastocysts of C57BL6/N mice. Chimeric mice that transmitted the floxed allele to their offspring were obtained ($Tsc22d3^{loxneo/+}$; **Suppl.Fig. 1C**), and further crossed with the Flp mice in order to obtain mice harbouring a floxed ($Tsc22d3^{lox/+}$) allele (**Suppl.Fig. 1D**). Following breeding $Tsc22d3^{loxneo/+}$ mice with the germline deleter strain Nestin-Cre (13), we obtained male mice lacking exons 3-6 including the neomycin cassette, also termed $Tsc22d3^{\Delta/y}$ as identified by PCR analysis (**Suppl.Fig. 1D**). **Suppl.Fig. 1E** illustrates that at the mRNA transcript level, the $Tsc22d3^{lox}$ allele was as expressed as the wildtype allele whereas the $Tsc22d3^{\Delta}$ allele did not show any expression. Following crossing of heterozygous mutant females resulted in null mutant male mice that are born according to expected Mendelian distribution.

To ensure that the *Tsc22d3* expression is abolished in the $Tsc22d3^{\Delta/y}$ mice, we quantitatively analyzed mRNA transcript expression in various organs (**Suppl.Fig 2A**). In $Tsc22d3^{+/y}$ wildtype mice, we found the highest expression levels in kidney, brain, lung and heart, moderate expression in thymus, liver and skin and relatively low expression levels in testis and spleen (**Suppl.Fig. 2A**). In contrary, qRT-PCR analyses from organs from $Tsc22d3^{\Delta/y}$ mice unveiled near-complete abolishment of *Tsc22d3* mRNA transcript expression. This deficiency was further confirmed using a TSC22D3 polyclonal antibody that predominantly detects isoforms GILZ1 and GILZ2. Kidney protein lysates from *Tsc22d3* control and knockout mice subjected or not to previous dexamethasone stimulation, revealed GILZ1 and GILZ2 isoform expression in the control, but not in the knockout group (**Suppl.Fig. 2B**). Following stimulation with dexamethasone increased the expression of these two isoforms, but still revealed absence in the knockout animals (**Suppl.Fig. 2B**). We identified an organ-specific distribution of isoforms GILZ1 that is predominantly present in kidney, thymus, spleen and lung, whereas GILZ2 isoform expression is rather found in testis liver, skin, brain and brain (**Suppl.Fig. 2C**). Altogether, these data demonstrated that the *Tsc22d3* gene locus is efficiently deleted in $Tsc22d3^{\Delta/y}$ mice and affected the major Gilz isoforms.

$Tsc22d3^{\Delta/y}$ mice show mild metabolic alterations that changes with age

Knockout mice were born with normal body weight and gained weight normally till about 3 months of age (**Fig. 1A**). 15-month-old mice are significantly lighter (**Table II**; $P < 0.05$). To understand this difference, we found no change in body length, lean or fluids, but significant

reduced fat values in old knockout mice (**Table II**; $P < 0.05$). Plasma insulin and glucose levels from knockout and control mice measured on fed, fasted and refed states revealed a significant higher plasma insulin level upon normal feeding (**Table II**; $P < 0.05$), while plasma glucose levels were unchanged. Upon fasted and refed conditions, knockout and control mice did not exhibit significant changes in plasma insulin and levels (**Table II**). Furthermore, knockout mice did not show a significant impairment in the glucose and insulin tolerance test, although the recovery of plasma glucose concentration was slowed down (**Fig. 1B and C**). Interestingly, pancreas sections stained for insulin and glucagon revealed significant more glucagon secreting α-cells in the knockout group per islet although the plasma glucagon level are not increased (**Fig. 1D and E**; $P < 0.01$).

Since *Tsc22d3* is proposed to inhibit the *Pparγ2* gene expression by binding to the promoter, we addressed whether deficiency of *Tsc22d3* impairs differentiation of mouse embryonic fibroblasts (MEFs) when exposed to an adipogenic cocktail. Following Oil-Red O-staining, the percentage of differentiated MEFs into adipocytes was not different between knockout and control groups (**Fig. 1F and G**). In parallel, quantitative RT-PCR measurements revealed no difference in basal *Pparγ2* mRNA expression on nondifferentiated fibroblasts from control and knockout mice, while the basal *FABP4* mRNA transcript expression level was already significant increased in the knockout mice (**Fig. 1H**). Upon differentiation into adipocytes, both *Pparγ2* and *FABP4* mRNA transcript expression levels increased in both group, being even significant elevated in the knockout group (**Fig. 1H**). *Tsc22d3* (Gilz) mRNA transcript expression levels were significantly 4-fold induced in the control group upon differentiation while its expression was as expected absent in the knockout group (**Fig. 1H**). In summary, Tsc22d3-deficient mice exhibit a mild metabolic phenotype although they showed higher insulin levels. Quantitative RT-PCR analyses on adipose tissue from control and knockout mice did furthermore not reveal any difference in the expression of *Pparg, Tsc22d1*, adiponectin, aP2 and KlF15 (**Fig. 1I**). When control and knockout mice were put for 18 weeks under high fat diet and normal diet in parallel, we observed that the knockouts gained significantly less weight and less body fat content as confirmed by Echo MRI analysis compared to the control group and both group upon normal diet (**Suppl.Fig. 4A and Table V**). Insulin levels were not different in the groups except a higher insulin level in the knockout group upon normal diet (**Suppl.Fig. 4B**). Interestingly, liver histology of these groups revealed that knockout mice are more protected to develop hepatic steatosis than the corresponding control group upon high fat diet (**Suppl. Fig. 4C**). Our data demonstrate, that

lack of TSC22D3 did not result in the predicted inhibition of *Pparγ2*, but rather increased its mRNA expression, but this effect had no apparent consequences for the *in vitro* adipogenesis. Upon high fat diet, *Tsc22d3*-deficient mice are more protected from developing hepatic steatosis.

***Tsc22d3* is not required for the development of the immune system, inflammatory response or implicated in sepsis**

To test the implication of *Tsc22d3* in the immune system, we first measured thymus weight at P10, P20 and following puberty. With the exception of a significant lighter thymus in the oldest knockout group, younger animals did not show lower absolute cell numbers between the two groups (**Fig. 2A;** $P < 0.05$). More detailed FACS analysis of thymocyte subsets unveiled no major change in single cell populations with the exception of a reduced absolute cell number for DN3 positive cells and an increase in DN4 positive thymocytes (**Fig. 2B**; $P < 0.05$). Surprisingly, the glucocorticoid-senstitive thymocyte DP subset was unaffected in Tsc22d3-knockout mice (**Fig. 2B**). Equally, in spleen, with the exception of an increased cell number of erythroblasts, the absolute cell number of spleen subsets is not altered in the knockout groups (**Fig. 2C**; $P < 0.05$). And furthermore, the cell number of lymph node subsets is not different in knockout compared to control littermates (**Fig. 2D**). Overall, the architecture and cell distribution in thymus and spleen from knockout mice is preserved (**Fig. S3**).

To further test whether the inflammatory immune response is altered in mice lacking TSC22D3, we studied the cytokine secretion from peritoneal and bone marrow-derived macrophages upon stimulation with various inflammatory stimuli supplemented or not with LPS or dexamethasone (**Fig. 3**). In all stimulatory conditions tested, we found a tendency for increased RANTES secretion in knockouts, although the overall response was not strikingly different (**Fig. 3A-C**). In a second series of experiments performed on marrow-derived dendritic cells (BMDCs) upon treatment with various stimuli (LPS, MSU, ATP, Candida and CpG), we tested the inflammasome activation and found overall no difference in the secretion of IL-1β, TNF or RANTES between the knockout and the control littermates (**Fig. 4A-C**). Dexamethasone treatment leads to an equally reduced cytokine production that is not altered in the absence of *Tsc22d3* (**Fig. 4A-C**).

Furthermore, we tested whether *Tsc22d3* is implicated in a sepsis model and analysed cytokine secretion of IL-6, IL-12, TNF- and IL-2 in bone marrow-derived macrophages upon various stimuli (**Fig. 5**). No significant difference could be observed in knockout mice, that

responded equally in a dose-dependent manner to dexamethasone administration (**Fig. 5A-C**). In addition, experiments performed on splenocytes stimulated by anti-CD3 plus anti-CD28 or concanavalin A, exibit a dexamethasone dose-dependent response independent on the absence of presence of Tsc22d3 (**Fig. 5D, E**). Altogether, our experiments did not reveal a crucial involvement of Tsc22d3 in immunology or inflammatory responses upon various stimuli.

Mild impairment of renal sodium and water handling in TSC22D3-deficient mice

Previous data suggested that *Tsc22d3* is a regulator of ENaC-mediated sodium absorption and might thereby play an important role in renal sodium and water handling. We therefore investigated plasma and urinary sodium, potassium electrolyte as well as aldosterone levels and osmolarity upon standard and salt-deprived diet. With the exception of a significantly increased plasma potassium level upon standard salt diet, *Tsc22d3*-deficient mice did not show major alterations in plasma and urinary electrolyte and aldosterone levels (**Table IV**; $P < 0.05$). Plasma and urinary osmolarity was conserved upon standard and sodium-deprived diet, and following water-deprivation (**Table IV**). Upon sodium-deprived diet for 10 consecutive days, knockout mice exhibit the same water and food intake with no change in body weight (**Suppl.Fig. 5A-C**). These mice showed significant increased plasma sodium and decreased potassium levels (**Table IV**; $P < 0.05$), although plasma aldosterone levels were not different in the knockout versus the control group. In summary, upon standard and sodium-deprived diet as well as under water deprivation conditions, *Tsc22d3* knockout mice are generally able to adapt to these conditions and reveal, if any, only a mild phenotype in renal sodium and water handling.

Tsc22d3-deficiency causes male sterility

Knockout males ($Tsc22d3^{\Delta/y}$), 3-6 months old, were bred with at least 4-6 females (C57BL/6N) for 3-4 months, but no offspring was born, suggesting that the knockout males are sterile. Gross histopathological examination of all organs revealed differences neither in development, nor architecture of most organs with the exception of the testis (**Suppl.Fig. S3**). To obtain $Tsc22d3^{\Delta/y}$ mice, we therefore crossed $Tsc22d3^{+/y}$ males with heterozygous $Tsc22d3^{\Delta/+}$ females. Mendelian distribution of the obtained genotypes was normal and male $Tsc22d3^{\Delta/y}$ (knockout) mice are viable. In adult male mice, the testicular mass and size is strikingly reduced (**Fig. 6A**; $P < 0.001$). Till the age of 10 days, the histology is nearly indistinguishable between the knockout and control group. At the age of 6 months, no germ cells or mature spermatozoa could be identified (**Fig. 6B**). Plasma levels of corticosterone

were significantly decreased, while FSH and testosterone were significantly increased (**Fig. 6D**). In 20-day-old knockout mice, the total cell number per seminiferous tubule decreased by about 60% mainly due to the increased number of TUNEL-positive cells while the portion of proliferating cells as measured by Ki67-positive cells remained constant (**Fig. 6E**; $P < 0.001$). Interestingly, this was paralleled by an increased amount of interstitial Leydig cells (**Fig. 6B**). The mRNA transcript level of several genes tested was altered, and while *Pparγ2,* GR, and KLF5 were significantly downregulated, those of *Tsc22d1*, AR and KLF15 were significantly upregulated (**Fig. 6I**). This downregulation was confirmed for the direct target gene *Pparγ2* on the protein expression level (**Fig. 6F,G**). Althogether, we identified a novel and crucial role for TSC22D3 in testis development and sterility. Unexpectectly, the target gene *Pparγ2* is downregulated at the RNA and protein level, which seems to be unique to this organ.

Discussion

Tsc22d3 is constitutively expressed in a variety of mouse, rat or human tissues and a key role role has been predicted for the glucocorticoid-induced leucine zipper in e.g., the immune system, adipogenesis or sodium homeostasis. Although multiple protein-protein interaction of TSC22D3 with important signaling proteins, like e.g., NF-kB, c-Fos, Raf-1, Ras, ERK1/2, C/EPP, histone deactylase 1 (HDAC1) have been identified (see for review Ayroldi and Riccardi, 2009 (1)), little is known about the regulation and the in vivo physiological implication of this gene since the mouse knockout model for TSC22D3 was not available to proof it experimentally. In this study, we therefore generated floxed and male mice harboring null mutant allele for the *Tsc22d3* gene locus and analyzed the mice in detail with respect to their immune system and immune responses, their implication in growth and metabolism, and in their capacity to regulate ENaC-mediated sodium reabsorption in the kidney following salt- and water-deprived challenges/constraints. While we were not able to confirm a crucial role for TSC22D3 neither in the immune system, metabolism or sodium handling, we unveiled in contrary an important novel role for GIlZ in male sterility.

Mild phenotype in metabolism, adipogenesis and sodium handling in knockout mice

There is a large body of evidence that glucocorticoids are implicated in the differentiation of mesenchymal progenitor cells, and that factors that block adipogenesis would favor osteogenic lineage commitment (14). Generally, despite less body fat in older mice, TSC22D3-deficient mice do not present severe metabolic alterations, nor obvious bone

abnormalities (**Suppl.Fig. 3, Table II and III**). The presence of an increased number of glucagon-positive Langerhans cells in the pancreas may explain the higher plasma insulin levels suggesting a certain insulin resistance in the knockout animals (**Fig. 1**), although the animals react in the normal range in glucose and insulin tolerance tests and to fasted and refed conditions and the glucacon level is in the normal range (**Fig. 3**). Furthermore, adipocyte differentiation was not severely modified in our *Tsc22d3*-knockout mice although (**Fig. 3**). This was surprising as *Tsc22d3* was reported to normally bind to the tandem repeat of CCAAT/enhancer-binding protein (C/EBP) binding sites in the PPAR-γ2 promoter thereby blocking PPAR- γ2 transcription and consequently inducing PPAR-γ2 adipogenesis ((12), **Fig.3**). Indeed, in adipocytes we even found a significant increase in the PPAR-γ2 and *FABP4* mRNA transcript expression levels (**Fig. 3**). Our findings are also in contrary to findings where ectopic expression of GILZ inhibited glucocorticoid-induced adipocyte differentiation in 3T3-L1 pre-adipocyte cells (12, 15). Even more surprisingly, in liver and testis from *Tsc22d3* knockout mice, this increase of PPARγ2 promoter activation as a consequence of *Tsc22d3*-deficiency could not be confirmed and *Pparγ2* mRNA transcript and protein expression levels were downregulated in testis (**Fig. 6**). Thus, tissue-specific factors may additionally modulate the transcription level of PPARγ2. Indeed, following a high fat diet for 18 weeks clearly not only revealed that the TSC22D3 knockout mice are significant protected to gain weight in comparison to the control group, but also develop less hepatic steatosis (**Suppl.Fig. 4**). This is in contrary to the in vivo data that would have predicted an increase in hepatic steatosis in TSC22D3 knockout mice. As PPARγ agonists induce sodium and water retention in type II diabetes-treated patients (16, 17) and GILZ was shown be implicated in the induction of ENaC-mediated transport in a cortical collecting duct cell line (mpkCCDc14; (11)), *Tsc22d3* was proposed to be an important mediator of aldosterone action (18). TSC22D3, earlier identified as an early aldosterone-induced gene (19) could modify sodium and water handling in TSC22D3-deficient mice. Overall, even upon various challenges like salt- and water-deprivation, we were not able to note remarkably changes compared to the control group, suggesting that TSC22D3 by itself plays a minor role in water or sodium handling mediated by the amiloride-sensitive epithelial sodium channel (ENaC), and thus is consequently not implicated in the control of blood pressure and blood volume. In this context, it is interesting to note that in an *in vivo* mouse model, fluid retention induced by thiazolidinedione, an agonist of PPARγ is independent of collecting duct ENaC activity (20). Equally, we cannot exclude compensatory mechanisms to be implicated. Our findings

therefore highly support the hypothesis that in vivo ENaC-regulation by GILZ does not play a crucial role in the kidney homeostasis.

Immune system and immune responses are not dependent on TSC22D3

Glucocorticoids are potent modulators of the immune system, and are therefore applied as anti-inflammatory and immunosuppressive drugs. They act through glucocorticoid receptor activation and inhibition of gene expression. In the immune system, glucocorticoids induce apoptosis of $CD4^+CD8^+$ double positive (DP) cells by a mechanism not yet completely understood, but which apparently requires gene transcription and coordinated activation of caspases (21, 22). TSC22D3 is strongly up-regulated by glucocorticoids in thymus (2) and a dual role in inducing apoptosis of thymocytes and rescuing them from T-cell receptor (TCR)-induced cell death was proposed (see for review Ashwell et al, 2000 (23)). Surprisingly, despite the predicted *Tsc22d3*-dependent negative regulation of T-cell function, male *Tsc22d3* knockout mice do not present severe impairment of thymus development and all single cell populations including the thymocyte $CD4^+CD8^+$ double positive cells are unaffected with the exception of reduced absolute cell number for DN3 and DN4 positive thymocytes (**Fig. 2**). Our data also do not support an anti-proliferative activity of TSC22D3 on T-lymphocytes, as found in concanavalin A-activated T-lymphocytes (6), but this difference may be due to specific *in vitro* experimental conditions. Equally, in spleen and lymph nodes, *Tsc22d3* knockout mice do not exhibit differences in cell distribution of cell subsets (**Fig. 2**). Even the finding by Kolbus and coworkers that TSC22D3 negatively regulates erythroid progenitor differentiation could not be confirmed in our knockout mice. Albeit, we found a significant increase in erythroblasts, erythroid progenitor differentiation was not negatively regulated (**Fig. 2**).

We then asked the question whether TSC22D3 also presents immunosuppressive activities and whether the deficiency of TSC22D3 significantly alters the cytokine secretion. Overall, our findings demonstrate that stimulation of peritoneal and bone marrow-derived macrophages from TSC22D3 knockout mice using inflammatory stimuli supplemented or not with LPS or dexamethasone did not reveal a significant difference in the secretion of TNF, RANTES, MIP-2 and interleukin-6 compared to the control group (**Fig. 3**). This is in contrary to transgenic mice that overexpressed GILZ in all thymocyte subsets and mature peripheral $CD4^+$ and $CD8^+$ T cells. Transgenic $CD4^+$ T cells secreted more Th-2 cytokines like interleukin-4, -5, -13, and -10, and GILZ was shown to be implicated in the T helper-2 (Th-2) response development cells (24). Our TSC22D3-deficient bone marrow-derived cells exhibit

normal cytokine production and inflammasome activation. Even upon dexamethasone pretreatment, these cells equally secrete time- and dose-dependent reduced interleukin-1, TNF and RANTES levels in both experimental and control group (**Fig. 4**). Furthermore, it has been reported that *Tsc22d3* mRNA transcript expression levels were up-regulated in spleen and peritoneal macrophages of mice that received restraint stress (25). In the treatment of severe sepsis and septic shock, low-dose glucocorticoids exhibit anti-inflammatory effects as demonstrated by a decrease in inflammatory response and increase in anti-inflammatory cytokines (26). Because sepsis is associated with the alteration of cytokine expression and cytokine response is modulated by glucocorticoids (27), we examined whether lack of TSC22D3 affects the proinflammatory cytokine secretion and the dexamethasone response. Unexpectedly, in our *in vitro* model of sepsis, bone marrow-derived macrophages from *Tsc22d3*-deficient mice post-LPS, -Pam3 or -E. coli infection do not secrete less proinflammatory cytokines and are not more resistant to dose-dependent dexamethasone treatment as control cells (**Fig. 5**). Our findings rather suggest the in the *in vitro* sepsis model, that glucocorticoid action is not mediated or dependent on TSC22D3.

TSC22D3 exhibit a crucial and novel role in testis development and sterility

The most striking and obvious phenotype was the male sterility as evident by the significant reduced testis size and weight, the absence of germ cells and the increased apoptosis in adult seminiferous tubules (**Fig. 6**). Normal spermatogenesis requires both pituitary gonadotrophins, namely the luteinizing hormone LH and the follicle stimulating hormone FSH and the testicular androgen testosterone (see for review Steinberger et al, 1991 (28)). In our TSC22D3 knockout mice, we observed that LH levels are normal while FSH and testosterone plasma levels were increased (**Fig. 6**). Lack of TSC22D3 might result in an impaired feedback inhibition of LH secretion by the pituitary (Steinberger et al, 1991), since high FSH levels stimulated androgen production in the Leydig cells, but the secretion FSH and LH by the pituitary was not downregulated or for FSH even upregulated (**Fig. 6**).

The phenotype of our male mice also strikingly ressembled that of *Six5*- and *c-kit*-deficient mice (29, 30). Sarkar and colleagues proposed that *Six5* via reduced *c-kit* levels contributed to the male reproductive defects in Myotonic dystrophy 1 (DM1), a multisystem disorder characterized by endocrine defects that include testicular and tubular atrophy, oligospermia, Leydig cell hyperproliferation and increased FSH levels (31). Interestingly, albeit significantly lower plasma cortisol levels, high testosterone levels in the TSC22D3 knockout mice could furthermore modify cortisol activity by downregulation of glucocorticoid receptor

expression (**Fig. 6**; (32, 33)). At the same time, mRNA transcript expression level of the androgen receptor, present in several stages of spermatogenic and Sertoli cells (34) is upregulated (**Fig. 6**). It has been proposed that testosterone exerts its regulating function on spermatogenesis by modifying the cortisol-dependent apoptosis (35) that would coicidence well with the significantly high cell-apoptosis observed in our mice (**Fig. 6**). In this context, it is interesting to note that androgen receptor knockout mice showed a severe disruption onto spermatogenesis with the failure of germ cells to progress beyond the early stages of meiosis (36). Although the mechanism is not yet fully understood, Leydig cell hyperproliferation was proposed to present a compensatory mechanism to increase testicular steridogenesis induced by testosterone insufficiency (37). LH seemed to be most effective in increasing the number of interstitial cells (38), but FSH might exert a proliferative effet on precursor mesenchymal cells that form Leydig cells postnatally (39-41). In summary, TSC22D3 is essential for male gametogenesis and exerts a crucial role in the interplay between endocrine stimulation, somatic cell activity and spermatogenesis. The use of germ cell- and sertoli-cell specific conditional knockouts will further help to dissect this crucial role of Gilz in germ via somatic cells.

Does TSC22D3 really mediate glucocorticoid functions?

Due to its abundance in several cell types and its potential protein interactions, TSC22D3 or Gilz has been proposed to mediate several glucocorticoid functions (see for review Ayroldi and Riccardi, 2009 (1)). The generation of constitutive and conditional knockout models now allows proofing its implication in glucocorticoid-dependent processes. Mice lacking TSC22D3 are viable and exhibit a significant decrease in plasma cortisol. Our in vivo data clearly do not confirm a crucial involvement of TSC22D3 in immunity, immune responses or adipogenesis. And functional redundancy by other members of the same family could compensate for this loss, and indeed we found upregulation of TSC22D1 mRNA transcript expression in the testis, although surprisingly, this was this only organ that showed a glucocorticoid-deficient phenotype. All other glucocorticoid-dependent organs and tissues analyzed in this study exhibit if any only minor defects or a default that might only get visible under challenging conditions. In this context, the TSC22D3-deficient mice might be useful to dissect these glucocorticoid-dependent and –independent processes in the future.

Acknowledgements

This work has been supported by the Emma Muschamp Foundation, the Swiss National Science Foundation to EH, the Leducq Foundation to EH and BR.

We thank the Transgenic Animal Facility, the Mouse Metabolic Evaluation (Fréderic Preitner and Bernard Thorens) and the Mouse Pathology platform, and the Cellular Imaging Facility (UNIL, Switzerland) for their help and services.

Figure legends

Figure 1. Metabolic parameters in *Tsc22d3*$^{+/y}$ and *Tsc22d3*$^{\Delta/y}$ mice. (***A***) Body weight values of control (black) and knockout mice (white circles; $n \geq 8$ per group; $^{*}P < 0.05$). (***B***), glucose and (***C***) insulin tolerance tests; plasma glucose concentration was measured 30 min. before and during 120 min. following intraperitoneal administration of 1.5 mg/g glucose (***B***) or 0.8 mU/g insulin (***C***; $n \geq 6$ per group). (***D***), Glucagon (brown, α cells) and insulin (rose, β cells) expression in pancreatic islets of Langerhans from control (left) and knockout (right) mice. (n = 3 mice per group; bar = 50 μm). (***E***), Ratio of glucagon-positive Langerhans cells per islet (left) and plasma glucagons levels (right panel; N = 15-18 images, n = 3 mice per group) in control (black) and knockout mice (white columns; $^{**}P < 0.001$). (***F***, ***G***) Two days after confluence, MEF cells were ± induced to differentiate into adipocytes (ND, not differentiated; D, differentiated MEFs). Cells from control (ctrl) and knockout (ko) mice were stained with Oil-Red O at 8 days post-induction. (***F***), Overview and (***G***), higher magnification on Oil-Red O-stained cells from control (ctrl) and knockout (ko) mice exposed (D, differentiated) and not exposed to adipogenic medium (ND, not differentiated). Note that there is no obvious difference between the two groups. (***H***) and (***I***), Quantitative RT-PCR of (***H***), GILZ, PPARγ2 and FABP4 from non-differentiated (ND) and differentiated (D) MEF cells from control and knockout mice; (***I***), Tsc22d1, adiponectin, aP2, GR and AR in fat tissue from control (black) and knockout (white columns). Tsc22d1 mRNA transcript expression was in parallel tested in testis and kidney. Experiments were performed in triplicate; $^{*}P < 0.05$, $^{***}P < 0.001$.

Figure 2. Flow cytometric analyses of thymus, spleen and lymph nodes from 10-week-old male control (black) and knockout (white columns) mice. (***A***), Absolute cell numbers ($x10^6$) for the following thymocyte subsets: DN1 ($CD117^+CD44^+CD25^-$), DN2 ($CD117^+CD44^+CD25^+$), DN3 ($CD117^-CD44^-CD25^+$), DN4 ($CD117^-CD44^-CD25^-$), ISP ($CD4^-CD8^+TCR\beta^-$), γδT cells, DP (double positive, $CD4^+CD8^+$), CD8 SP (single positive, $CD4^-$

$CD8^+$), CD4 SP ($CD4^-CD8^+$) in 10, 20 and between 56-146 days old control (black) and knockout (white columns) mice. (***B***), Absolute cell numbers ($x10^6$) for the following splenocyte subsets: B cells, CD8 SP, CD4 SP, RBC (erythrocytes) and EBs (Erythroblasts, $Ter119^+CD71^+$), Mega (Megakaryocytes), Gran (Granulocytes), Mac (Macrophages). (***C***), Absolute cell numbers ($x10^6$) for the following lymph node subsets: CD8 SP and CD4 SP cells, B cells. Black bars: control; white bars: knockout mice, data represent average ± SEM. At least 3 mice per group were analyzed. $*P < 0.05$ when compared to control.

Figure 3. Analysis of peritoneal and bone marrow-derived cytokine secretion. (***A-C***), ELISA for TNF, RANTES, MIP-2 and IL-6 following (***A***), stimulation of peritoneal macrophages for 6 hours with LPS supplemented by MSU, Nig, ATP, R837 or with Pam3, zymo, pIC, TNF or PGN alone. (***B***), stimulation of peritoneal macrophages for 24 hours with LPS, zymo, R837, pIC, TNF or Pam3 and (***C***), stimulation of bone marrow-derived macrophages with zymo, R837, PGN and LPS with or without dexamethsasone (0.2 μM). Data is shown as mean values of duplicated stimulations ± SEM from 3 mice per group.

Figure 4. Normal cytokine production by *Tsc22d3*-deficient bone marrow-derived cells. (***A***), To test inflammasome activation, cells were primed with 10 ng/ml of ultra-pure LPS for the indicated periods prior to inflammasome activation by 100 ng/ml of MSU (for 5h) or 5 mM of ATP (for 1h). Inflammasome activation was quantified by measuring the amount of IL-1β in cell-free supernatants. An influence of dexamethasone on inflammasome activation was addressed by adding dexamethasone to the cells at three different time points prior to ATP or MSU stimulation as indicated. (***B***, ***C***) cells as in (***A***) were pretreated for the indicated periods with dexamethasone and stimulated for 6h with $5x10^6$ heat inactivated Candida cells per ml or 1μM CpG. TNF and RANTES secretion into the medium was measured by ELISA. Data is shown as mean values of triplet stimulations ± SEM and representative for three independent experiments with a total of 6 control and 6 knockout mice.

Figure 5. *Tsc22d3*-deficient bone marrow-derived macrophages (BMDMs) are not particularly susceptible to the immunosuppressive effects of dexamethasone. Control and knockout (***A-C***) and splenocytes (***D-E***) were incubated with or without (med) increasing concentrations of dexamethasone (DEX, 10^{-10}-10^{-7} M) and stimulated with LPS, Pam_3CSK_4 (Pam3), *Escherichia coli* (J5), CpG oligodeoxynucleotide (CpG), anti-CD3 plus anti-CD28 or concanavalin A., IL-6 (***A***), IL-12p40 (***B***), TNF (***C***) and IL-2 concentrations were quantified in

cell-culture supernatants collected 4 h (TNF) or 18 h (IL-6, IL-12p40, IL-2) after stimulation. Cytokine concentrations in cells stimulated without dexamethasone were set at 1 for normalization. Data are means ± SD of triplicates samples from one experiment comprising two mice per experimental condition and are representative of two experiments.

Figure 6. *Tsc22d3* knockout males are sterile. (***A***), Representative pictures from control (left) and knockout (right) adult testes. Note the significant decrease in testicular mass in adult knockout. (***B, C***), H&E-stained paraffin sections from control (ctrl) and knockout (ko) testes reveal increased spermatogenic cell apoptosis, absence of mature sperms and hyperproliferation of Leydig cells (black arrow). (***C***), Immunohistochemistry of Sertoli cells (rabbit anti-CTCF antibody; black arrowhead) and counterstaining with hematoxylin reveals blue nuclei. Note the presence of elongated spermatids (white arrowhead) in the control testis, which is absent in the knockout. (***D***), Corticosterone (cort), follicle stimulating (FSH), luteinizing hormone (LH) and testosterone (testo) hormone levels in plasma [ng/mL] from control and knockout males ($n \geq 10$ animals per group). (***E***), Total number of cells per seminiferous tubule ($N \geq 20$ tubules per group) in control and knockout mice (left). Ratio of Ki-67 positive cells divided by total cell number, middle) and ratio of TUNEL positive cells divided by total cell number per seminiferous tubule, $N = 18$ tubules, right). (***F***), Semi-quantitative RT-PCR (upper panel) and qRT-PCR (lower panel) of PPARγ2 mRNA transcript expression in testis from control (black) and knockout (white column) mice. Note the significant decrease in PPARγ2 mRNA transcript expression. (***G***), Western blot analysis using a PPARγ2 antibody on testis lysates. The arrow indicates the PPARγ2 protein (56 kDa). As loading control β–actin was used. (***I***), qRT-PCR of PPARγ2, Tsc22d1, GR, AR, KLF5, KLF15 in testis from control (black) and knockout (white columns). Data represent average ± SEM. Statistical analysis was performed using the unpaired Student's t-test, where $*P < 0.05$, $**P < 0.01$ and $***P < 0.001$ when compared to control. (Scale bar: (***A***), 1 mm; (***B***), 100 µm and (***C***) 50 µm).

Supplementary Figure 1. Generation of conditional *Tsc22d3* mice. (***A***), Scheme of the *Tsc22d3* wild type allele, the targeting vector and recombined floxed ($Tsc22d3^{loxneo}$ and $Tsc22d3^{lox}$) and null allele ($Tsc22d3^{\Delta}$). Relevant restriction enzymes for cloning and diagnosis are indicated. Exons 3 to 6 and the neomycin cassette (flanked by frt sites) are flanked by two loxP sites. 5' and 3' probes as well as PCR primers (s1, s2 and as) used for genotyping are

shown. (***B, C)***, Southern blot analysis from targeted ES cell clones (***B***) and *Tsc22d3*$^{+/loxneo}$ and *Tsc22d3*$^{+/+}$ mice (***C***) following digestion with *Eco*RV and *Eco*RI showing the mutant 7.8kb (5') and 2kb (3' probe) and the 7.8kb (5') and 5.4kb (3' probe) in *Tsc22d3*$^{+/loxneo}$ mice, respectively. The 12.1kb (*Eco*RV; 5' probe) and the 2kb endogenous (*Eco*RI; 3' probe) fragment are detected in *Tsc22d3*$^{+/loxneo}$ and *Tsc22d3*$^{+/+}$ mice. (***D)***, PCR-based genotyping of wild type (*Tsc22d3*$^{+/+}$, *Tsc22d3*$^{+/y}$*) and knockout (Tsc22d3*$^{\Delta/y}$), heterozygous mutant (*Tsc22d3*$^{lox/\Delta}$) and control (*Tsc22d3*$^{lox/+}$) mice identifying the wild type (+; 270 bp), Δ (300 bp) and lox (400 bp) alleles. (***E***), Comparison of mRNA transcript expression in lung and testis of *Tsc22d3*-deficient, lox and wild type mice using SYBR green. Lung and testis (black and dark grey columns, respectively) in control and knockout mice; $n = 3$ mice per group, analysis performed in triplicate; NS, non significant. Note that the mRNA transcript expression levels between *Tsc22d3*$^{+/y}$ and *Tsc22d3*$^{lox/y}$ do not differ.

Supplementary Figure 2. Knockout mice lack Tsc22d3 expression (***A***), Quantitative RT-PCR analysis of kidney, thymus, spleen, testis, liver, skin, brain, lung and heart from *Tsc22d3*$^{lox/y}$ or *Tsc22d3*$^{+/y}$ (control; gray and black columns) and *Tsc22d3*$^{\Delta/y}$ (ko; white columns; $n = 3$ per group; $P < 0.05$) determined by SYBR Green (gray) and TaqMan PCR (black columns). (***B, C***) Western blot analyses of kidneys from knockout and control mice (***B***) ± treated with vehicle or dexamethasone (± DEX) and (***C***) kidney, thymus, spleen, testis, liver, skin, brain, lung, heart and colon following dexamethasone stimulation. The polyclonal Tsc22d3 antibody identifies isoform 1 (15 kDa) and 2 (30 kDa). GAPDH (35 kDa) was used as loading control; $n = 2$ per genotype.

Supplementary Figure 3. Histopathological analyses of control and TSC22D3-deficient mice on Hematoxylin and eosin stained sections (bar size of each panel is indicated in µm). Representative pictures from 6-month-old control and knockout mice are shown.

Supplementary Figure 4. Metabolic parameters in *Tsc22d3*$^{+/y}$ and *Tsc22d3*$^{\Delta/y}$ mice following a consecutive 18 weeks high fat diet. (***A***) Body weight values of control (black) and knockout mice (white circles; $n \geq 11$ per group). (***B***), Plasma insulin concentration in control and knockout mice upon normal (chow; black: control; white: knockout) and high fat (control: grey; knockout: red columns) diet in fed, fasted and refed conditions; $n \geq 10$ per group. (***C***), Representative pictures of H&E stained liver sections from control (ctrl, left) and knockout

(ko, right panel) upon chow (upper) and high fat diet (lower panel) for 18 consecutive weeks (n = 3 mice per group; bar size indicated).

Supplementary Figure 5. Physiological parameters upon salt-deprived diet. Six-month-old control and knockout mice were analyzed with respect to their (***A***) body weight, (***B***) food and (***C***) water intake before and following 12 consecutive days of sodium-deprived diet ($n \geq 7$).

Material and Methods

Generation of conditional and null mutant *Tsc22d3* mice

The *Tsc22d3* gene was cloned from a 129/Sv mouse genomic BAC library (Incite Genomics, Inc., USA). For *Tsc22d3* gene information, see GenBank accession number NM_010286.3. The following fragments were then subcloned into a modified lox-targeting vector containing 2 loxP and 2 Frt sites. First, a 10kb (5' region, haboring exon 3) and a 5kb *Eco*RI fragments (3' region, harboring exons 4 to 6), were subcloned into pBSII KS(-) and extracted using *Pac*I and *Stu*I restriction sites. The neomycin resistance gene cassette flanked by *frt* sites and followed by one *loxP* site (pAT-FRT-K13; (42)) was cloned into *Eco*RV (3' of the polyA region). The second *loxP* sequence was introduced in a *Sma*I restriction site created by PCR-based mutagenesis, along with a new diagnostic *Eco*RV restriction site 5' of the third exon. Finally, the thymidine kinase cassette (HSV-tK) was inserted 3' of the homologous region. Further details of cloning are available on request. The targeting vector was linearized with *Pac*I, and transfected into A2 embryonic stem cells (ES cells) of the 129Sv/EV background (43, 44) as described previously (45). G418 and ganciclovir-resistant colonies were expanded and screened by PCR using the following primers; 5' recombination: sense 5'-ATAGCCTGTGCTCTGGAACT-3', antisense, 5'-TTATGGCGCGGGGATATCTA-3' and 3' recombination: sense 5'-GCCTCCGAGGTTGCAGTGTTT-3', antisense 5'-TCGCCTTCTTGACGAGTTCTTC-3'. Targeted clones were confirmed by Southern blot analysis using two external probes (3' probe: 315 bp fragment isolated from the 3' *Eco*RI clone by *Stu*I and *Bgl*II on *Eco*RI-digested DNA, and 5' probe: 1085 bp fragment isolated from the 5' *Eco*RI clone by *Dra*I on *Eco*RV-digested genomic DNA). PCR-amplified neomycin sequences were used as internal probe. Correctly targeted clones were injected into C57BL/6N blastocyts as described (46). Breeding of $Tsc22d3^{loxneo}$ mice with Flp mice (47) allowed the excision of the neomycin cassette and with (nestin-CRE mice (13)) mice to generate mice harbouring the Δ allele. To obtain knockout males ($Tsc22d3^{\Delta/y}$), heterozygous

mutant *Tsc22d3*$^{\Delta/+}$ females were crossed with wildtype males. *Tsc22d3*$^{\Delta/+}$ and *Tsc22d3*$^{+/+}$ females, as well as *Tsc22d3*$^{+/y}$ and *Tsc22d3*$^{\Delta/y}$ males were genotyped by PCR (sense (s1): 5'-CAGGTCTGAGTAACTTGTCC-3', antisense (as): 5'-CAGTCTGTGGTGACCGTTTC-3', sense (s2): 5'-TGACAGCTGCGTTTCTCAGTG-3'); s1, s2 and as were used for genotyping of lox and wt alleles, and s1 and as for the Δ allele.

All animals were housed in a controlled environment with a 14 h light/10 h dark cycle with free access to water and standard laboratory diet. Males were aged from 3 to 6 months, and were backcrossed to C57BL/6N mice (N4-N6). The control group consisted of age-matched *Tsc22d3*$^{+/y}$ and *Tsc22d3*$^{lox/y}$ littermates. Mouse experiments were conducted under authorization of local authorities and followed Swiss guidelines.

Histology and immunohistochemistry

2-(*n*=2) and 6-(*n*=1) month-old mice were dissected and organs fixed with buffered formalin (pH 7.2) for 12 hours. Tissues were embedded in paraffin (Leica Microsystems, Wetzlar, Germany) and 2-3 µm sections were stained with haematoxylin and eosin (H&E). Testis cellular proliferation was assessed by Ki-67 antibody (monoclonal rat anti-mouse, Dako M7249, Carpinteria, CA, USA; dilution 1:50) with goat anti-rat HRP secondary antibody (Biosource ALI 3404, Camarillo, CA, USA). Apoptosis was analysed using terminal transferase and Biotin-16-dUTP (TUNEL Enzyme, Roche 11 767 305 001; dilution 1:250 and Biotin-16-dUTP, dilution 1:250; Roche 11 093 070 910, Roche Diagnostics GmbH, Mannheim, Germany). Sertoli cells were labelled with the rabbit anti-CTCF (#06–917; Upstate cell signaling, Millipore, Billerica, MA, USA; dilution 1:100); secondary antibody used was EnVision (DakoCytomation, Glostrup, Denmark) as previously described (48). Pancreas sections were incubated with antibodies against insulin (Linco 4011-01, Linco Research Inc., St. Charles, MO, USA; dilution 1:6000) and glucagon (Linco 4030-01F, Linco Research Inc., St. Charles, MO, USA; dilution 1:6000), and then revealed with Fuchsin (Kit DAKO K0625, Dako, Denmark; dilution 1:50) and DAB (Kit DAKO K3468, Dako, Denmark; dilution 1:50), respectively. GILZ1 and GILZ2 proteins were labelled with the polyclonal Tsc22d3 antibody as described (4).

Quantitative real-time PCR

Following sacrifice, tissues were collected and quickly snap frozen in liquid nitrogen and kept at -80° C until used. Total RNA was extracted from tissues with the RNeasy Mini Kit or

Qiazol (Qiagen, Valencia, CA, USA). RNA quality was verified on an agarose gel and the concentration was determined by a ND-1000 Spectrophotometer (NanoDrop, Wilmington, DE, USA). Total RNA (1 μg) was subjected to reverse transcription using the SuperScript II First-Strand Synthesis System for RT–PCR (Invitrogen/Life Technologies Corporation, Carlsbad, CA, USA) following the manufacturer's instructions. The resulting cDNA was used as a template for quantitative PCR (qPCR). Results were normalized using the reference genes glyceraldehyde 3-phosphate dehydrogenase (GAPDH) or RNA polymerase II. Quantitative real-time analysis of selected genes was performed using the ABI Prism 7500 Fast Real-Time PCR System, SYBR Green as DNA binding dye for the detection of PCR products or the TaqMan probe technology (Applied Biosystems/Life Technologies Corporation, Carlsbad, CA, USA). Intron-spanning primers were designed (Microsynth AG, Switzerland) (see **Table I** list for oligonucleotides). The cycling conditions were 95 °C for 10 min, followed by 40 cycles of 95 °C for 15 s, and 60 °C for 1 min. To detect and eliminate possible primer–dimer artifacts, the dissociation curve was generated by adding a cycle of 95 °C for 15 s, 60 °C for 1 min and 95 °C for 15 s. All primer sets produced amplicons of the expected size and their identity was also verified by migration of the PCR products on agarose gel. The quantification was done by measuring the ΔΔCt normalized to the reference gene. All measurements were done at least in triplicate, n = 3 mice per group, analysis performed in triplicate, data represent average ± SEM, in all tissues tested.

Western blot analyses

Mice were sacrificed according to standard procedures and various tissue samples were collected from dexamethasone (55 μg/100g body weight)-treated and non-treated, control and knockout mice. The dexamethasone was administred intraperitoneally 3-4 hours before euthanasia. Tissue lysis was performed in ice-cold urea (8M) using the TissueLyser (Qiagen, Valencia, CA, USA). Protein levels were quantified using the Pierce BCA Protein Assay Reagent (Thermo Fisher Scientific, Waltham, MA, USA) with BSA as a standard. Equal amounts of protein extracts were resolved by 12% SDS-PAGE and electro-transferred onto a Protran nitrocellulose membrane (Whatman/GE Healthcare, Piscataway, NJ, USA). Blots were blocked in tris-buffered saline containing 0.1% Tween (TBS-T) supplemented with 4% milk powder and immunoblotted using anti-TSC22d3 antibody, as described previously (4). The blots were stripped and reprobed with GAPDH antibody (Chemicon/Millipore, Billerica, MA, USA) as a loading control; n = 2 mice per genotype.

Hormone measurements

For plasma aldosterone and corticosterone measurements, mice (n ≥ 7, 3-4-month-old) were killed by rapid decapitation between 4-6 pm. Blood was collected in EDTA tubes, immediately centrifuged and stored at -20 °C until assayed for hormone level determination. Plasma aldosterone levels were measured according to standard procedure using a radioimmunoassay (RIA) using the Coat-A-Count RIA kit (Siemens Medical Solutions Diagnostics, Ballerup, Denmark). Mice samples exhibiting values greater than 1200 pg/ml were previously diluted using a serum pool with a low aldosterone concentration (<50 pg/ml). Corticosterone was measured by RIA (IBL, Hamburg, Germany), FSH was measured by IRMA (IBL, Hamburg, Germany), and LH was measured by RIA (IDS, Liège, Belgium). Testosterone levels were assayed using a kit from MP Biomedicals (Testo DA Kit, Eschwege, Germany). The standard curves ranged between 2 and 200 ng/ml for FSH, 0.25 and 15 ng/ml for LH, and 0.1 and 10 ng/ml for testosterone. Intra- and inter-assay coefficients of variation (CVs) of all three assays were less than 5% and 10%, respectively, $n = 10$ mice per genotype.

Metabolic parameters

Body weight was measured on a weekly basis over the whole study. Body composition was analyzed on individual 2.5- and 15-month-old mice under light gaz anesthesia (1-2 % isoflurane), by quantitative nuclear magnetic resonance using an EchoMRI Whole Body Composition Analyzer (EchoMedical Systems, Houston, TX, USA). Data for individual mice were obtained by averaging results from two consecutive measurements. Plasma glucose levels in the fed, 15h fasted or 6h-refed states were measured with a glucometer (Ascensia Breeze2, Bayer, Switzerland). Plasma insulin levels were determined from tail-tip bleedings by ELISA (Ultrasensitive Mouse insulin ELISA, Mercodia AB, Uppsala, Sweden).

Glucose tolerance test; after a 15-hour overnight fast period, 6-month-old mice were injected i.p. with 1.5 mg/g glucose. Plasma glucose levels were measured 30 minutes before and punctually during 120 minutes after administration ($n \geq 6$ per group).

Insulin tolerance test; following 4 hours of food removal (9am-1pm), age-matched 7 months old mice were injected i.p. with 0.8 mU/g insulin by intraperitoneal injections. Blood samples were obtained from tail-tip bleedings, and plasma glucose levels were measured with a glucometer (Ascensia Breeze 2, Bayer, Switzerland).

Adipocyte differentiation ; Mouse embryonic fibroblasts (MEFs) were generated from 13.5-day-old embryos obtained from heterozygous mutant female *Tsc22d3*$^{+/\Delta}$ mated to wild type malese (49). Briefly, after removal of head and visceral organs (used for genotyping),

embryos were minced and trypsinized for 30 minutes at 37°C. Embryonic fibroblasts were then plated and maintained in DMEM (with 10% foetal calf serum (FCS) (Life Technologies), 100 U/ml penicillin and 100 µg/ml streptomycin) at 37°C in an atmosphere of 5% CO_2. All experiments were performed with Tsc22d3 wild-type and knockout MEFs after 15-20 passages. For adipocyte differentiation, 2-day-postconfluent cells (day 0) were transferred to DMEM supplemented with 10% FCS, 8 µg/ml biotin, 4 µg/ml pantothenate, 0.5 mM 3-isobutyl-1-methylxanthine, 1 µM dexamethasone and 10 µg/ml insulin for 2 days (all from Sigma). Medium was renewed every 2 days with DMEM containing 10% FCS, 8 µg/ml biotin, 4 µg/ml pantothenate and 10 µg/ml insulin. LY294002 (Calbiochem) was prepared in dimethyl sulfoxide (DMSO) and added at a final concentration of 50 µM in the medium 20 minutes before, and, every 12 hours after addition of the adipose cocktail. To visualize lipid accumulation, cells were stained with Oil Red O (50). Briefly, cells were washed with phosphate-buffered saline (PBS), fixed with 3.7% formaldehyde solution for 1 hour and stained with Oil Red O for 1 hour using a 60:40 (v/v) dilution in water of a 0.5% stock solution (in isopropanol). Cells were then washed twice with PBS and twice with water. MEFs were pooled from $n = 2$ per genotype. Experiments were performed in triplicate.

Sodium-restriction diet and water deprivation

Mice (20–24 weeks old) were fed with a standard salt diet (0.17% sodium, Ssniff Spezialdiäten GmbH, Soest, Germany) followed by 12 days with a sodium-deficient diet (<0.01% sodium, Ssniff Spezialdiäten GmbH, Germany). The 23 hours water deprivation was performed under normal-salt diet. Body weight, food and water intake were measured during the experiment. Spot urine and serum/blood samples were collected before and after each experiment, and osmolarity as well as sodium, potassium and creatinine composition were analyzed at the Laboratoire Central de Chimie Clinique of the University Hospital (CHUV, Lausanne, Switzerland).

Flow Cytometry and Monoclonal Antibodies

Thymocyte, lymph node and spleen single cell suspensions were prepared by standard methods and stained for FACS analysis at 4°C as follows. Cells were preincubated in 50% anti-mouse FcR (CD16/32; clone 2.4.G.2) culture supernatant and then stained with the following monoclonal antibody conjugates: CD4 (RM-4.5 or GK1.5)-FITC, -PE-Cy5 or PE-Cy7; CD8α (53.6.7)-FITC or Alexa 647; CD11b (M1/70)-FITC, PE-Cy5 or Alexa 647; CD24 (M1/69)-PE; CD25 (PC61.5)-Alexa 700 or APC-Alexa 750; CD41 (MWReg30)-FITC or -PE;

CD44 (IM781)-PE-Cy7 or Pacific Blue; CD45R/B220 (RA3-6B2)-FITC, PE-Texas Red or PE-Cy7; CD62L (Mel14)-FITC; CD71 (R17217)-PE; CD122 (5H4)-PE; CD117 (2B8)-APC; F4/80 (BM8)-APC Alexa750, Gr1 (RB6-8C5)-FITC, Alexa 647 or Alexa 700; Ter119-FITC or APC-Alexa 750; TCRβ (H57)-FITC, PE-Cy5 or APC-Alexa750; TCRγδ (GL3)-FITC or PE-Cy5. DN1 ($CD117^+CD44^+CD25^-$), DN2 ($CD117^+CD44^+CD25^+$), DN3 ($CD117^-CD44^-CD25^+$), DN4 ($CD117^-CD44^-CD25^-$), ISP ($CD4^-CD8^+TCR\beta^-$), γδT cells, DP (double positive, $CD4^+CD8^+$), CD8 SP (single positive, $CD4^-CD8^+$), CD4 SP ($CD4^-CD8^+$). All FITC conjugates were purified and conjugated in the Ludwig Institute with the exception of CD41-FITC, which was purchased from BD Biosciences (San Jose, CA, USA). All Alexa 647 conjugates were prepared in the Ludwig Institute using the Alexa 647 conjugation kit from Invitrogen (Carlsbad, CA, USA). All other monoclonal antibody conjugates were purchased from eBioscience (San Diego, CA, USA). Intracellular staining for TCRβ was performed after first surface staining with all monoclonal antibodies. After fixation and permeabilization in Cytofix/Cytoperm (BD Biosciences, San Jose, CA, USA), the cells were incubated overnight at 4°C in 1x Permwash solution (BD Biosciences, San Jose, CA, USA) containing TCRβ-PE-Cy5 and then washed in 1x Permwash and resuspended in PBS/3% FCS for FACS analysis. Samples were analyzed on either a FACS Canto™ or a FACS LSR II™ (both Becton Dickinson, San Jose, CA, USA) and the data analyzed with FlowJo™ software (TreeStar, Ashland, OR, USA).

Inflammation experiments

Three-month-old mice were sacrificed ($n = 3$, each group) and bone marrow-derived dendritic cells (BMDC), bone marrow-derived macrophages (BMDM) and thioglycolate-elicited peritoneal macrophages (TEPM) were prepared and stimulated as previously described (51-53). Briefly, LPS, MSU, ATP, Candida and CpG stimuli were obtained from InvivoGen (San Diego, CA, USA), ELISA kits from R&D Systems (Minneapolis, MN, USA). Bone marrow-derived macrophages (BMDMs) were obtained as previously described (54) and cultured in IMDM containing 10% FCS (Sigma-Aldrich), 100 UI/ml penicillin, 100 µg/ml streptomycin and 50 µM 2-mercaptoethanol. Cells were preincubated for 1 h with dexamethasone (Sigma-Aldrich) prior to stimulation with 10 ng/ml of *Salmonella minnesota* Ultra Pure lipopolysaccharide (LPS) (List Biologicals Laboratories), 10 µg/ml Pam_3CSK_4 lipopeptide (EMC microcollections), 5x 10^7 heat-inactivated *Escherichia coli* (*E. coli*) J5 or 0.1 µM CpG oligodeoxynucleotide (CpG ODN, Coley Pharmaceutical Group). Cell culture supernatants

were collected to measure the concentrations of IL-12p40 by ELISA (BD Biosciences) and the concentrations TNF and IL-6 by bioassay (55). Splenocytes (5 x 10^5 cells in 200 µl) were seeded in 96-well plates coated with 1µg/ml anti-CD3 and anti-CD28 antibodies (BD Biosciences) or stimulated with 2.5µg/ml concanavalin A (Con A, Sigma-Aldrich) in the presence or the absence of dexamethasone. IL-2 in cell culture supernatants collected after 24 h was measured by ELISA (BD Biosciences).

Statistical analysis

Data were analyzed using the Student's *t* test for comparison between the groups. Results are expressed as the mean ± SEM. A P value < 0.05 was considered as statistically significant.

References

1. Ayroldi E & Riccardi C (2009) Glucocorticoid-induced leucine zipper (GILZ): a new important mediator of glucocorticoid action. *FASEB J* 23(11):3649-3658.
2. D'Adamio F, *et al.* (1997) A new dexamethasone-induced gene of the leucine zipper family protects T lymphocytes from TCR/CD3-activated cell death. *Immunity* 7(6):803-812.
3. Mittelstadt PR & Ashwell JD (2001) Inhibition of AP-1 by the glucocorticoid-inducible protein GILZ. *J Biol Chem* 276(31):29603-29610.
4. Soundararajan R, Wang J, Melters D, & Pearce D (2007) Differential activities of glucocorticoid-induced leucine zipper protein isoforms. *J Biol Chem* 282(50):36303-36313.
5. Ayroldi E, *et al.* (2001) Modulation of T-cell activation by the glucocorticoid-induced leucine zipper factor via inhibition of nuclear factor kappaB. *Blood* 98(3):743-753.
6. Ayroldi E, *et al.* (2007) GILZ mediates the antiproliferative activity of glucocorticoids by negative regulation of Ras signaling. *J Clin Invest* 117(6):1605-1615.
7. Delfino DV, Agostini M, Spinicelli S, Vito P, & Riccardi C (2004) Decrease of Bcl-xL and augmentation of thymocyte apoptosis in GILZ overexpressing transgenic mice. *Blood* 104(13):4134-4141.
8. Cohen N, *et al.* (2006) GILZ expression in human dendritic cells redirects their maturation and prevents antigen-specific T lymphocyte response. *Blood* 107(5):2037-2044 .
9. Hamdi H, *et al.* (2007) Glucocorticoid-induced leucine zipper: A key protein in the sensitization of monocytes to lipopolysaccharide in alcoholic hepatitis. *Hepatology* 46(6):1986-1992 .
10. Muller OG, *et al.* (2003) Mineralocorticoid effects in the kidney: correlation between alphaENaC, GILZ, and Sgk-1 mRNA expression and urinary excretion of Na+ and K+. *J Am Soc Nephrol* 14(5):1107-1115 .
11. Soundararajan R, Zhang TT, Wang J, Vandewalle A, & Pearce D (2005) A novel role for glucocorticoid-induced leucine zipper protein in epithelial sodium channel-mediated sodium transport. *J Biol Chem* 280(48):39970-39981.
12. Shi X, *et al.* (2003) A glucocorticoid-induced leucine-zipper protein, GILZ, inhibits adipogenesis of mesenchymal cells. *EMBO Rep* 4(4):374-380 .
13. Buchholz F, Refaeli Y, Trumpp A, & Bishop JM (2000) Inducible chromosomal translocation of AML1 and ETO genes through Cre/loxP-mediated recombination in the mouse. *EMBO Rep* 1(2):133-139 .
14. Beresford JN, Bennett JH, Devlin C, Leboy PS, & Owen ME (1992) Evidence for an inverse relationship between the differentiation of adipocytic and osteogenic cells in rat marrow stromal cell cultures. *J Cell Sci* 102 (Pt 2):341-351 .

15. Batchvarova N, Wang XZ, & Ron D (1995) Inhibition of adipogenesis by the stress-induced protein CHOP (Gadd153). *EMBO J* 14(19):4654-4661 .
16. Guan HP, Ishizuka T, Chui PC, Lehrke M, & Lazar MA (2005) Corepressors selectively control the transcriptional activity of PPARgamma in adipocytes. *Genes Dev* 19(4):453-461 .
17. Zhang H, *et al.* (2005) Collecting duct-specific deletion of peroxisome proliferator-activated receptor gamma blocks thiazolidinedione-induced fluid retention. *Proc Natl Acad Sci U S A* 102(26):9406-9411 .
18. Soundararajan R, Melters D, Shih IC, Wang J, & Pearce D (2009) Epithelial sodium channel regulated by differential composition of a signaling complex. *Proc Natl Acad Sci U S A* 106(19):7804-7809 .
19. Robert-Nicoud M, *et al.* (2001) Transcriptome of a mouse kidney cortical collecting duct cell line: effects of aldosterone and vasopressin. *Proc Natl Acad Sci U S A* 98(5):2712-2716 .
20. Vallon V, *et al.* (2009) Thiazolidinedione-induced fluid retention is independent of collecting duct alphaENaC activity. *J Am Soc Nephrol* 20(4):721-729 .
21. Cifone MG, *et al.* (1999) Dexamethasone-induced thymocyte apoptosis: apoptotic signal involves the sequential activation of phosphoinositide-specific phospholipase C, acidic sphingomyelinase, and caspases. *Blood* 93(7):2282-2296 .
22. Marchetti MC, Di Marco B, Cifone G, Migliorati G, & Riccardi C (2003) Dexamethasone-induced apoptosis of thymocytes: role of glucocorticoid receptor-associated Src kinase and caspase-8 activation. *Blood* 101(2):585-593 .
23. Ashwell JD, Lu FW, & Vacchio MS (2000) Glucocorticoids in T cell development and function*. *Annu Rev Immunol* 18:309-345 .
24. Cannarile L, *et al.* (2006) Increased GILZ expression in transgenic mice up-regulates Th-2 lymphokines. *Blood* 107(3):1039-1047 .
25. Wang Y, *et al.* (2008) Enhanced resistance of restraint-stressed mice to sepsis. *J Immunol* 181(5):3441-3448 .
26. Briegel J, *et al.* (1994) Low-dose hydrocortisone infusion attenuates the systemic inflammatory response syndrome. The Phospholipase A2 Study Group. *Clin Investig* 72(10):782-787 .
27. Prigent H, Maxime V, & Annane D (2004) Science review: mechanisms of impaired adrenal function in sepsis and molecular actions of glucocorticoids. *Crit Care* 8(4):243-252 .
28. Steinberger A (1991) Effects of temperature on the biochemistry of the testis. *Adv Exp Med Biol* 286:33-47 .
29. Rothschild G, *et al.* (2003) A role for kit receptor signaling in Leydig cell steroidogenesis. *Biol Reprod* 69(3):925-932 .
30. Sarkar PS, Paul S, Han J, & Reddy S (2004) Six5 is required for spermatogenic cell survival and spermiogenesis. *Hum Mol Genet* 13(14):1421-1431 .
31. Vazquez JA, *et al.* (1990) Hypothalamic-pituitary-testicular function in 70 patients with myotonic dystrophy. *J Endocrinol Invest* 13(5):375-379 .
32. Chen S, Wang J, Yu G, Liu W, & Pearce D (1997) Androgen and glucocorticoid receptor heterodimer formation. A possible mechanism for mutual inhibition of transcriptional activity. *J Biol Chem* 272(22):14087-14092 .
33. Kerr JE, Beck SG, & Handa RJ (1996) Androgens modulate glucocorticoid receptor mRNA, but not mineralocorticoid receptor mRNA levels, in the rat hippocampus. *J Neuroendocrinol* 8(6):439-447 .
34. Kimura N, Mizokami A, Oonuma T, Sasano H, & Nagura H (1993) Immunocytochemical localization of androgen receptor with polyclonal antibody in paraffin-embedded human tissues. *J Histochem Cytochem* 41(5):671-678 .
35. Russell LD & Clermont Y (1977) Degeneration of germ cells in normal, hypophysectomized and hormone treated hypophysectomized rats. *Anat Rec* 187(3):347-366 .
36. De Gendt K, *et al.* (2004) A Sertoli cell-selective knockout of the androgen receptor causes spermatogenic arrest in meiosis. *Proc Natl Acad Sci U S A* 101(5):1327-1332 .
37. Mylchreest E, Sar M, Wallace DG, & Foster PM (2002) Fetal testosterone insufficiency and abnormal proliferation of Leydig cells and gonocytes in rats exposed to di(n-butyl) phthalate. *Reprod Toxicol* 16(1):19-28 .

38. Dombrowicz D, Sente B, Reiter E, Closset J, & Hennen G (1996) Pituitary control of proliferation and differentiation of Leydig cells and their putative precursors in immature hypophysectomized rat testis. *J Androl* 17(6):639-650 .
39. Benton L, Shan LX, & Hardy MP (1995) Differentiation of adult Leydig cells. *J Steroid Biochem Mol Biol* 53(1-6):61-68 .
40. Hardy MP, Zirkin BR, & Ewing LL (1989) Kinetic studies on the development of the adult population of Leydig cells in testes of the pubertal rat. *Endocrinology* 124(2):762-770 .
41. Saez JM (1994) Leydig cells: endocrine, paracrine, and autocrine regulation. *Endocr Rev* 15(5):574-626 .
42. Trumpp A, *et al.* (2001) c-Myc regulates mammalian body size by controlling cell number but not cell size. *Nature* 414(6865):768-773 .
43. Hummler E, Merillat AM, Rubera I, Rossier BC, & Beermann F (2002) Conditional gene targeting of the Scnn1a (alphaENaC) gene locus. *Genesis* 32(2):169-172 .
44. Reis LF, Ruffner H, Stark G, Aguet M, & Weissmann C (1994) Mice devoid of interferon regulatory factor 1 (IRF-1) show normal expression of type I interferon genes. *EMBO J* 13(20):4798-4806 .
45. Hummler E, *et al.* (1996) Early death due to defective neonatal lung liquid clearance in alpha-ENaC-deficient mice. *Nat Genet* 12(3):325-328 .
46. Porret A, Merillat AM, Guichard S, Beermann F, & Hummler E (2006) Tissue-specific transgenic and knockout mice. *Methods Mol Biol* 337:185-205 .
47. Rodriguez CI, *et al.* (2000) High-efficiency deleter mice show that FLPe is an alternative to Cre-loxP. *Nat Genet* 25(2):139-140 .
48. Jelinic P, Stehle JC, & Shaw P (2006) The testis-specific factor CTCFL cooperates with the protein methyltransferase PRMT7 in H19 imprinting control region methylation. *PLoS Biol* 4(11):e355 .
49. Yang YC, Hsu HK, Hwang JH, & Hong SJ (2003) Enhancement of glucose uptake in 3T3-L1 adipocytes by Toona sinensis leaf extract. *Kaohsiung J Med Sci* 19(7):327-333 .
50. Ramirez-Zacarias JL, Castro-Munozledo F, & Kuri-Harcuch W (1992) Quantitation of adipose conversion and triglycerides by staining intracytoplasmic lipids with Oil red O. *Histochemistry* 97(6):493-497 .
51. Gross O, *et al.* (2006) Card9 controls a non-TLR signalling pathway for innate anti-fungal immunity. *Nature* 442(7103):651-656 .
52. Gross O, *et al.* (2009) Syk kinase signalling couples to the Nlrp3 inflammasome for anti-fungal host defence. *Nature* 459(7245):433-436 .
53. Muruve DA, *et al.* (2008) The inflammasome recognizes cytosolic microbial and host DNA and triggers an innate immune response. *Nature* 452(7183):103-107 .
54. Roger T, *et al.* (2009) Protection from lethal gram-negative bacterial sepsis by targeting Toll-like receptor 4. *Proc Natl Acad Sci U S A* 106(7):2348-2352 .
55. Roger T, David J, Glauser MP, & Calandra T (2001) MIF regulates innate immune responses through modulation of Toll-like receptor 4. *Nature* 414(6866):920-924 .

Figure 1

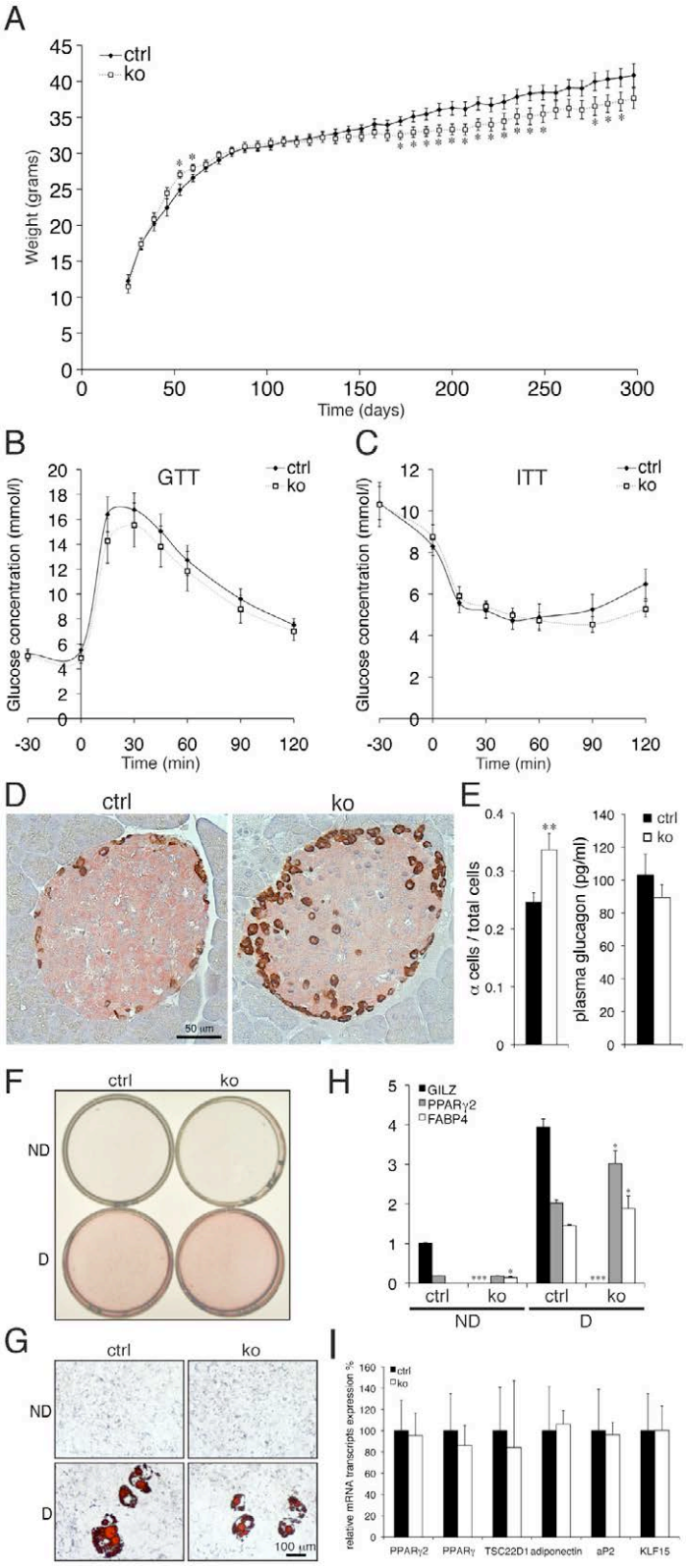
A
ctrl
ko
Weight (grams)
Time (days)
B
GTT
Glucose concentration (mmol/l)
Time (min)
C
ITT
Glucose concentration (mmol/l)
Time (min)
D
ctrl
ko
50 µm
E
α cells / total cells
plasma glucagon (pg/ml)
F
ctrl
ko
ND
D
H
GILZ
PPARγ2
FABP4
ctrl
ko
ND
D
G
ctrl
ko
ND
D
100 µm
I
relative mRNA transcripts expression %
PPARγ2
PPARγ
TSC22D1
adiponectin
aP2
KLF15

Figure 2

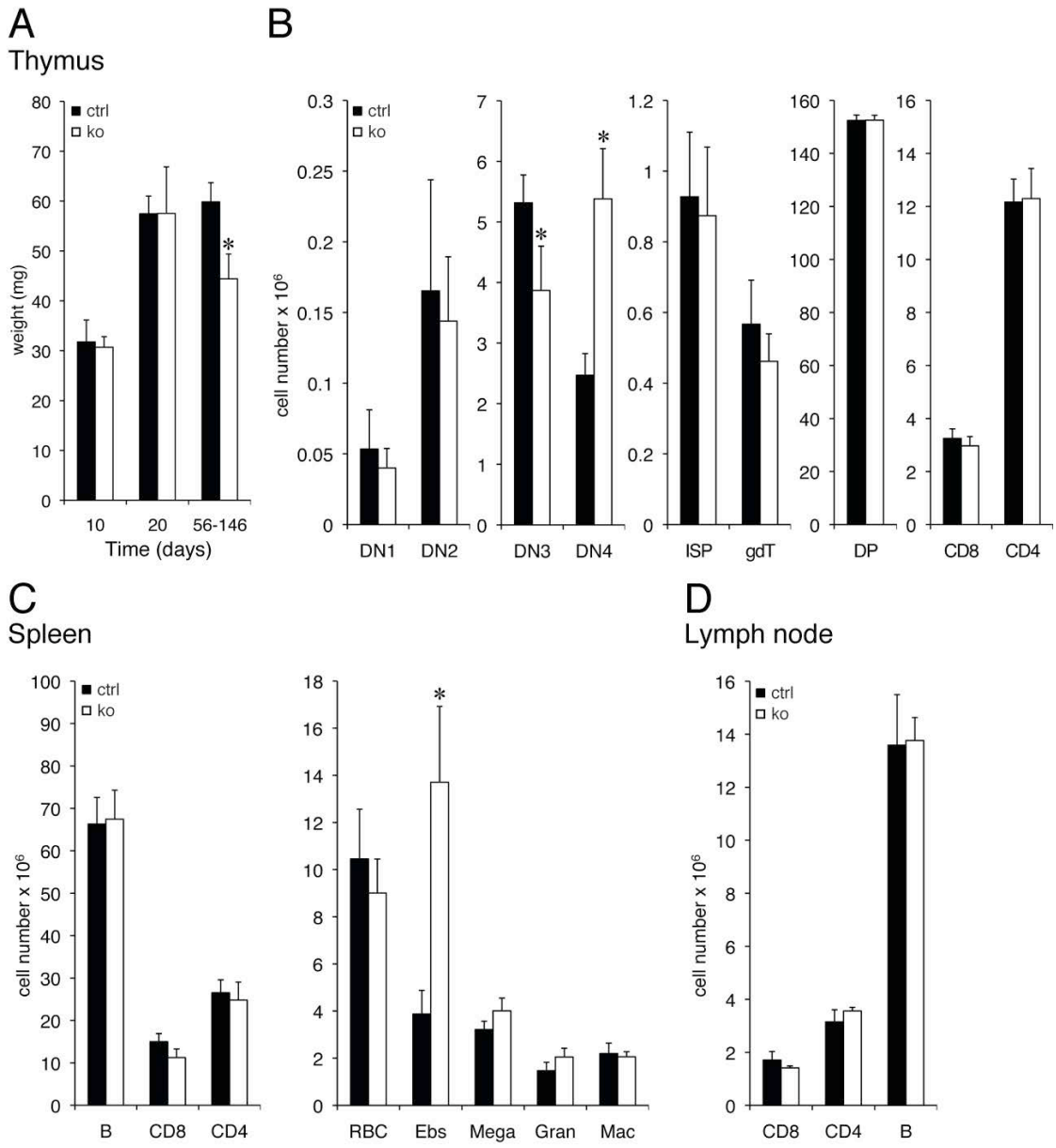
A
Thymus
ctrl
ko
weight (mg)
10
20
56-146
Time (days)
B
cell number x 10⁶
DN1
DN2
DN3
DN4
ISP
gdT
DP
CD8
CD4
C
Spleen
B
CD8
CD4
RBC
Ebs
Mega
Gran
Mac
D
Lymph node
CD8
CD4
B

Figure 3

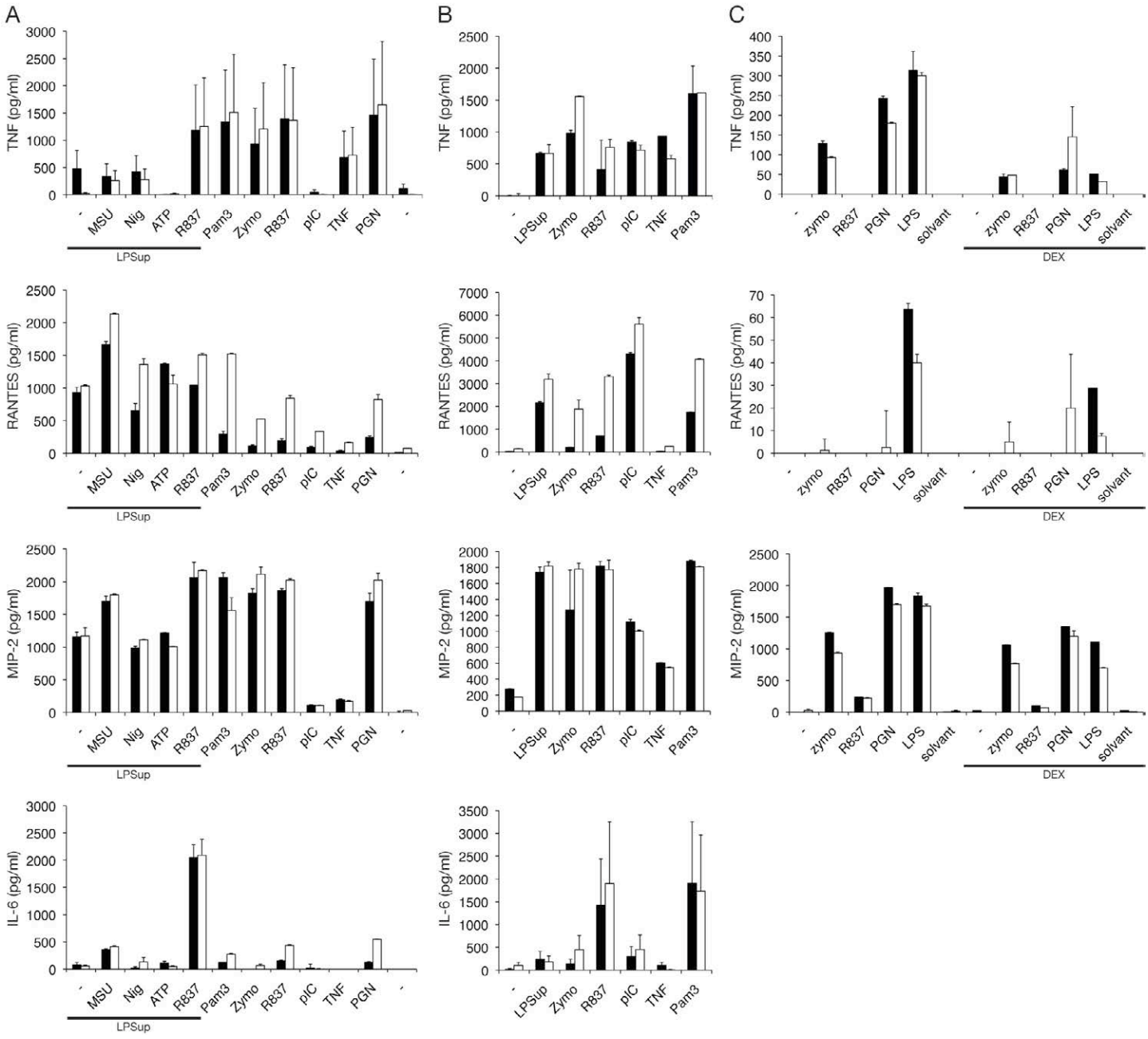
A
B
C
TNF (pg/ml)
RANTES (pg/ml)
MIP-2 (pg/ml)
IL-6 (pg/ml)
-
MSU
Nig
ATP
R837
Pam3
Zymo
pIC
TNF
PGN
LPSup
LPS
solvant
DEX

Figure 4

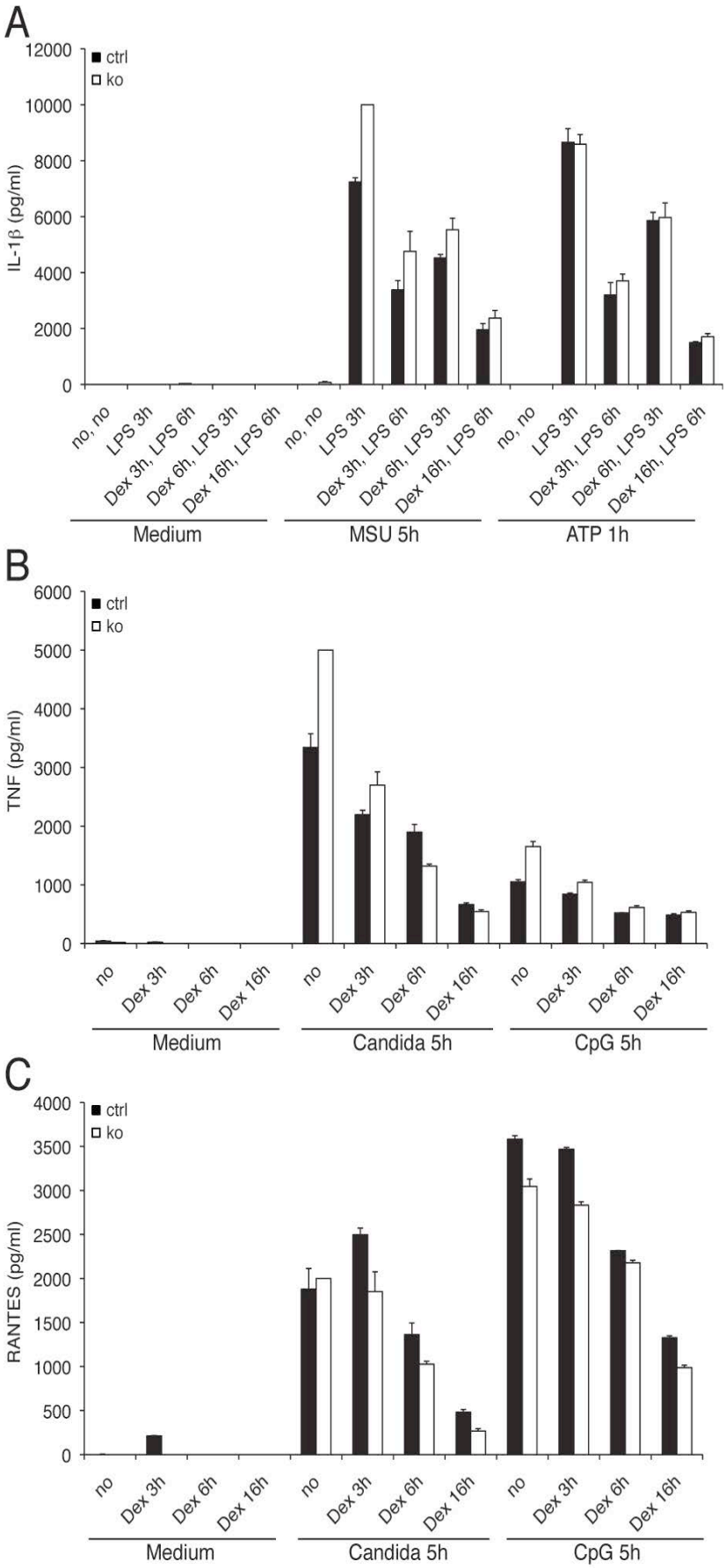
A
ctrl
ko
IL-1β (pg/ml)
12000
10000
8000
6000
4000
2000
0
no, no
LPS 3h
LPS 3h, LPS 6h
Dex 3h, LPS 3h
Dex 6h, LPS 3h
Dex 16h, LPS 6h
Medium
MSU 5h
ATP 1h
B
TNF (pg/ml)
6000
5000
4000
3000
2000
1000
0
no
Dex 3h
Dex 6h
Dex 16h
Medium
Candida 5h
CpG 5h
C
RANTES (pg/ml)
4000
3500
3000
2500
2000
1500
1000
500
0

Figure 5

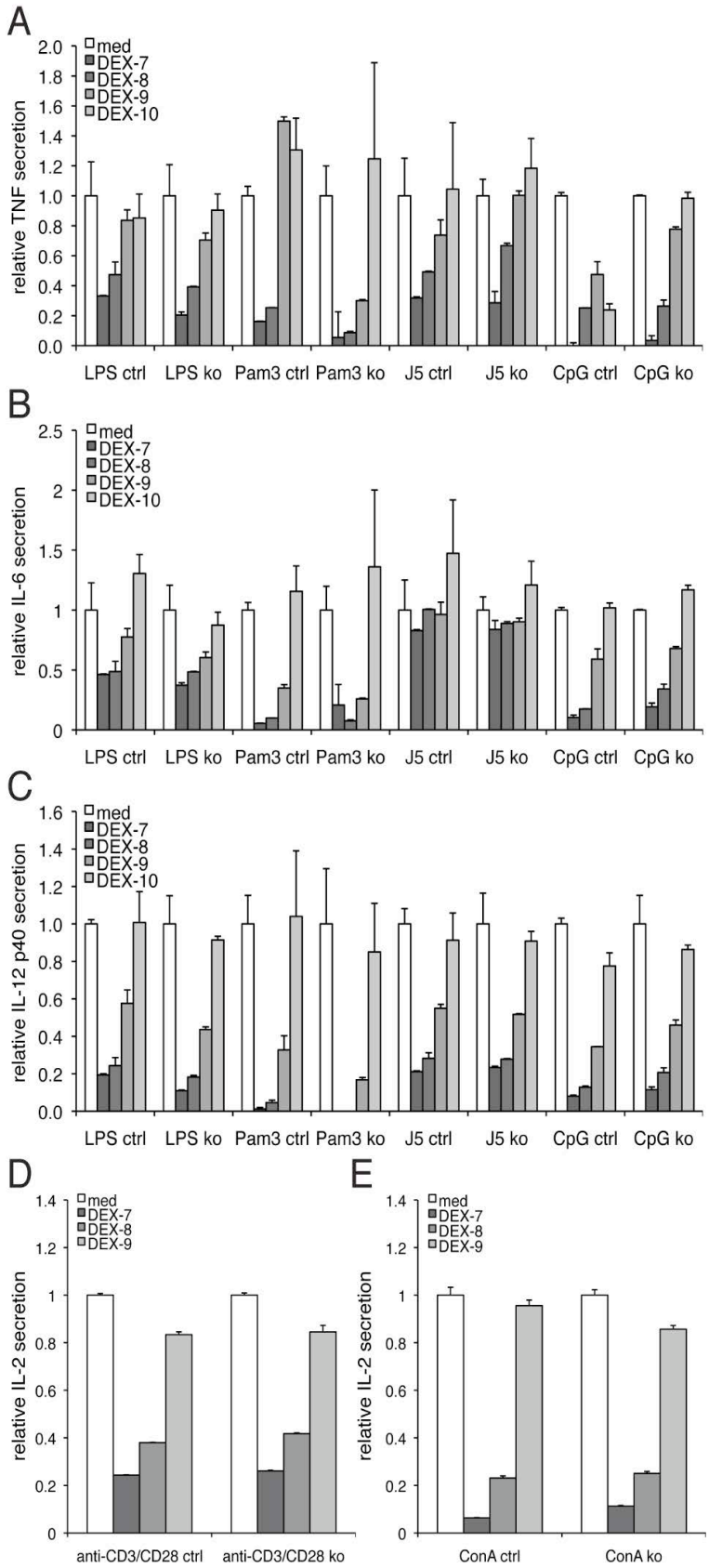
A
med
DEX-7
DEX-8
DEX-9
DEX-10
relative TNF secretion
2.0
1.8
1.6
1.4
1.2
1.0
0.8
0.6
0.4
0.2
0.0
LPS ctrl
LPS ko
Pam3 ctrl
Pam3 ko
J5 ctrl
J5 ko
CpG ctrl
CpG ko
B
relative IL-6 secretion
2.5
2
1.5
1
0.5
0
C
relative IL-12 p40 secretion
1.6
1.4
1.2
1.0
0.8
0.6
0.4
0.2
0.0
D
relative IL-2 secretion
1.4
1.2
1
0.8
0.6
0.4
0.2
0
anti-CD3/CD28 ctrl
anti-CD3/CD28 ko
E
relative IL-2 secretion
ConA ctrl
ConA ko

Figure 6

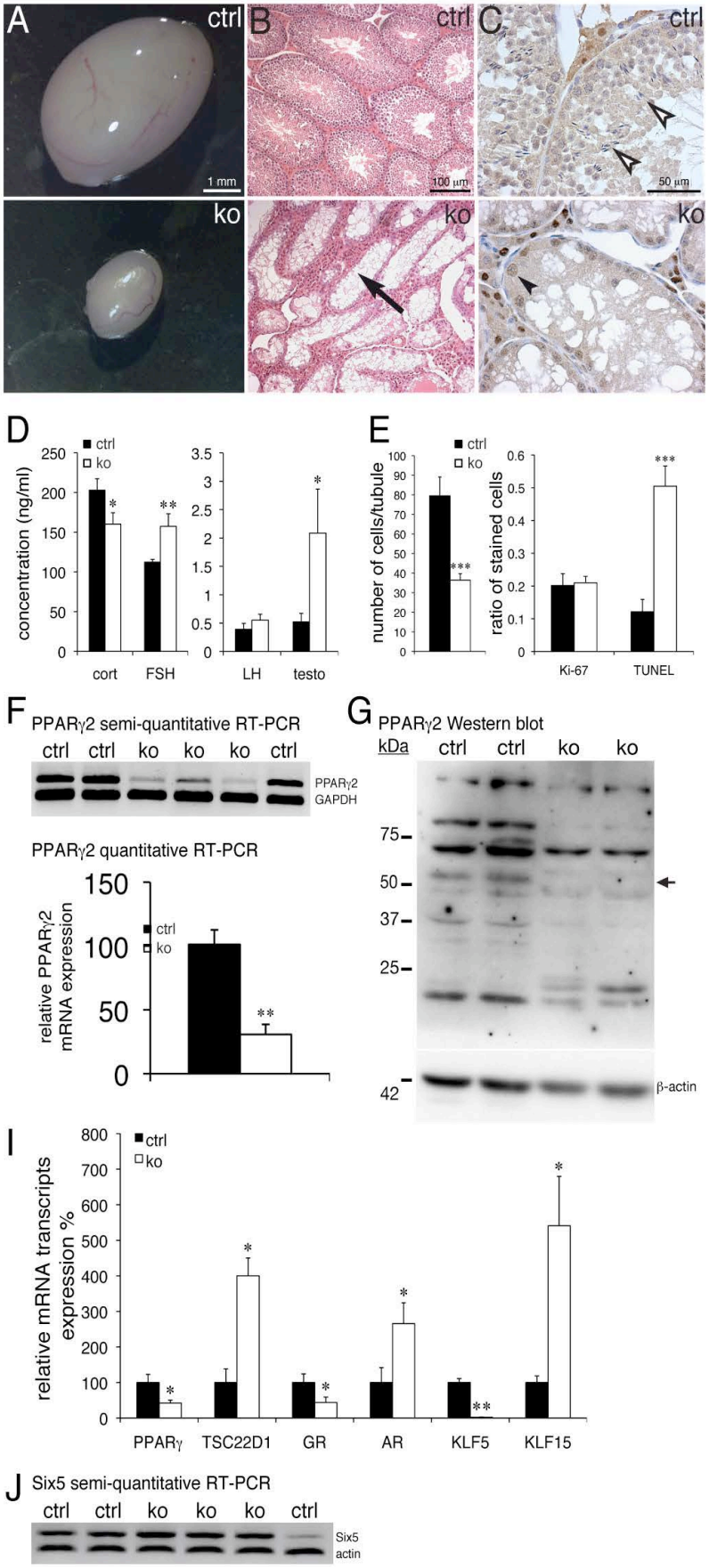
A
ctrl
1 mm
ko
B
ctrl
100 µm
ko
C
ctrl
50 µm
ko
D
ctrl
ko
concentration (ng/ml)
cort
FSH
LH
testo
E
ctrl
ko
number of cells/tubule
ratio of stained cells
Ki-67
TUNEL
F
PPARγ2 semi-quantitative RT-PCR
ctrl ctrl ko ko ko ctrl
PPARγ2
GAPDH
PPARγ2 quantitative RT-PCR
relative PPARγ2 mRNA expression
G
PPARγ2 Western blot
kDa
ctrl ctrl ko ko
75
50
37
25
42
β-actin
I
relative mRNA transcripts expression %
PPARγ
TSC22D1
GR
AR
KLF5
KLF15
J
Six5 semi-quantitative RT-PCR
ctrl ctrl ko ko ko ctrl
Six5
actin

Supplementary Figure 1

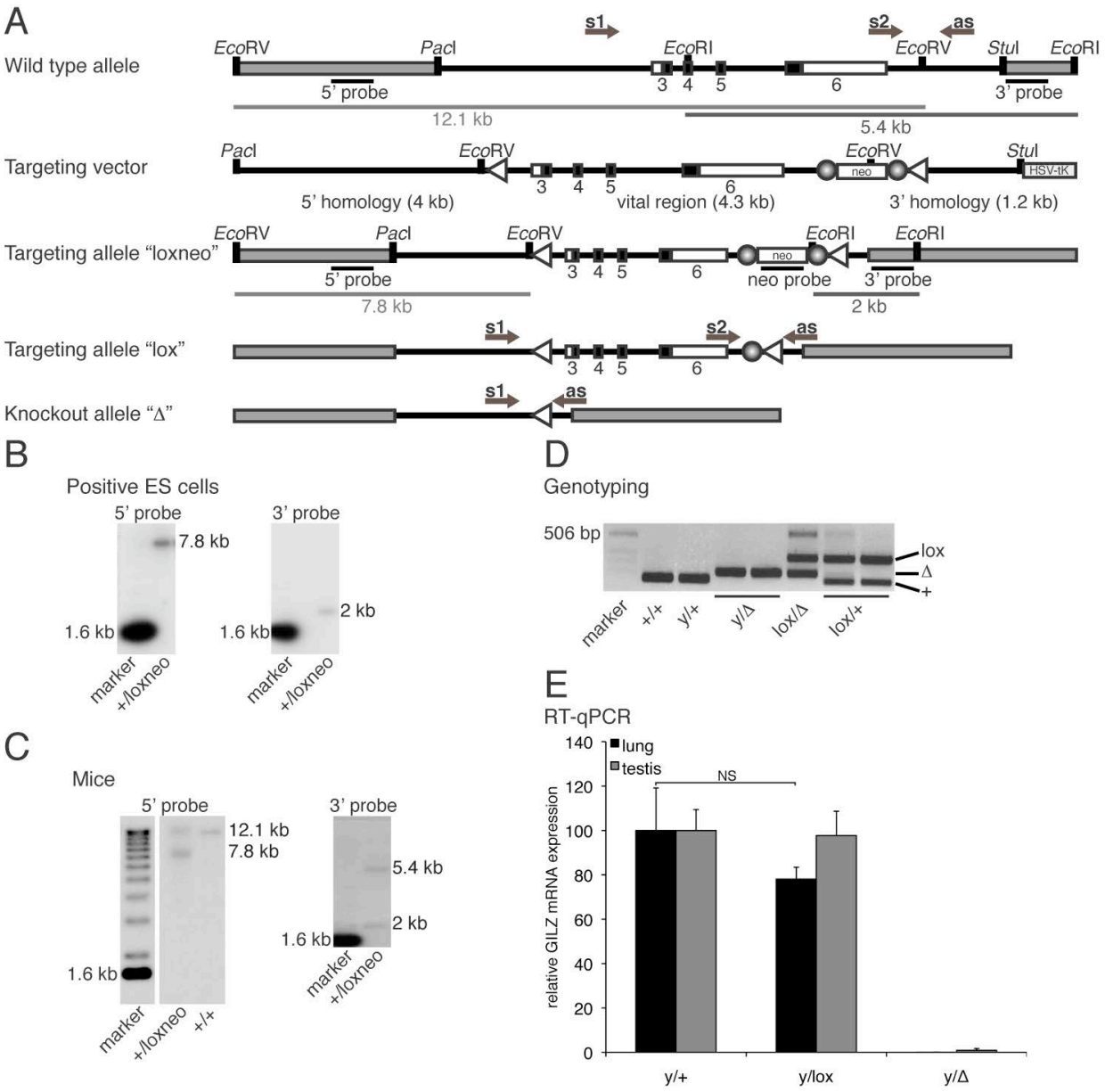

Supplementary Figure 2

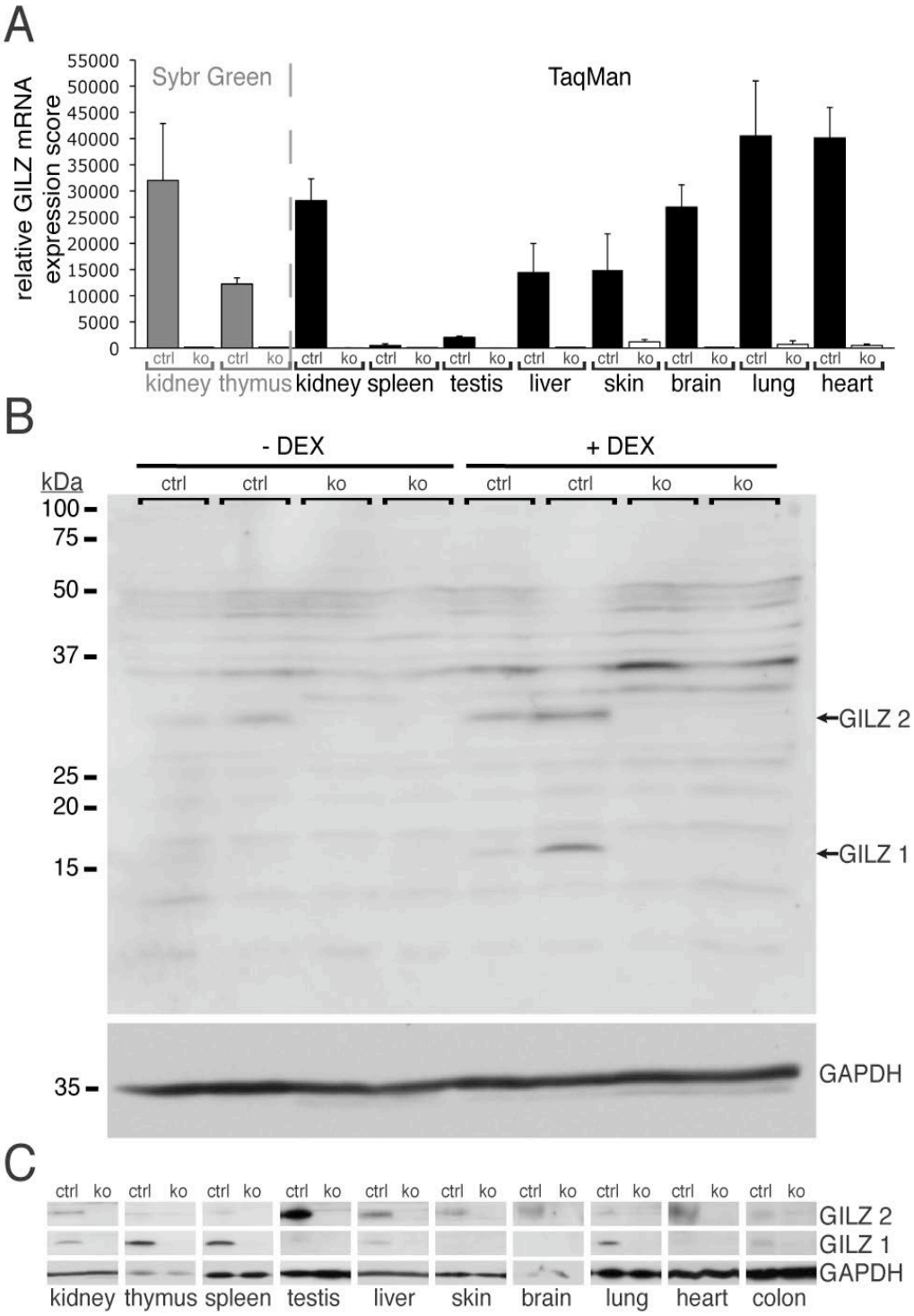

Supplementary Figure 3

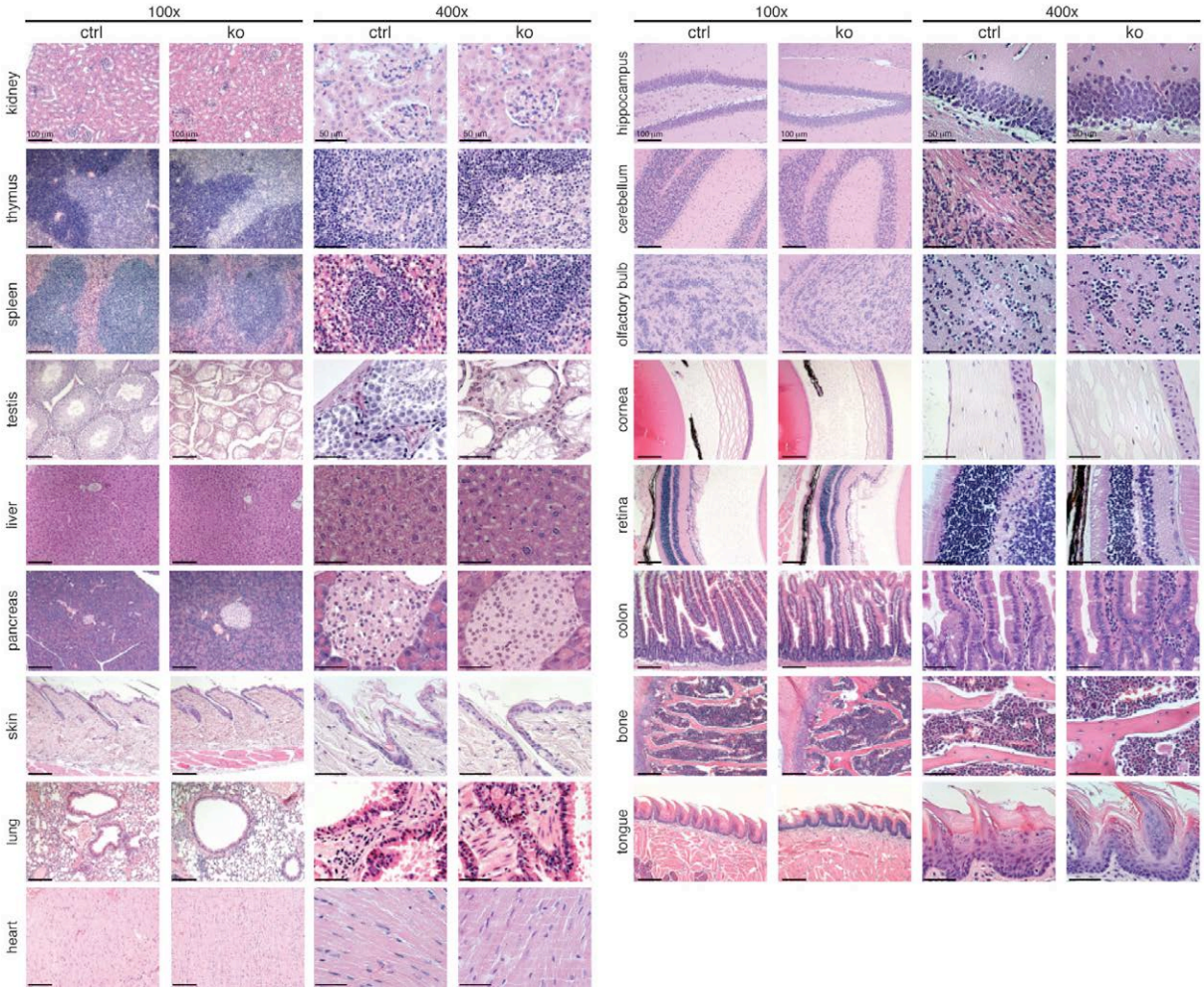

Supplementary Figure 4

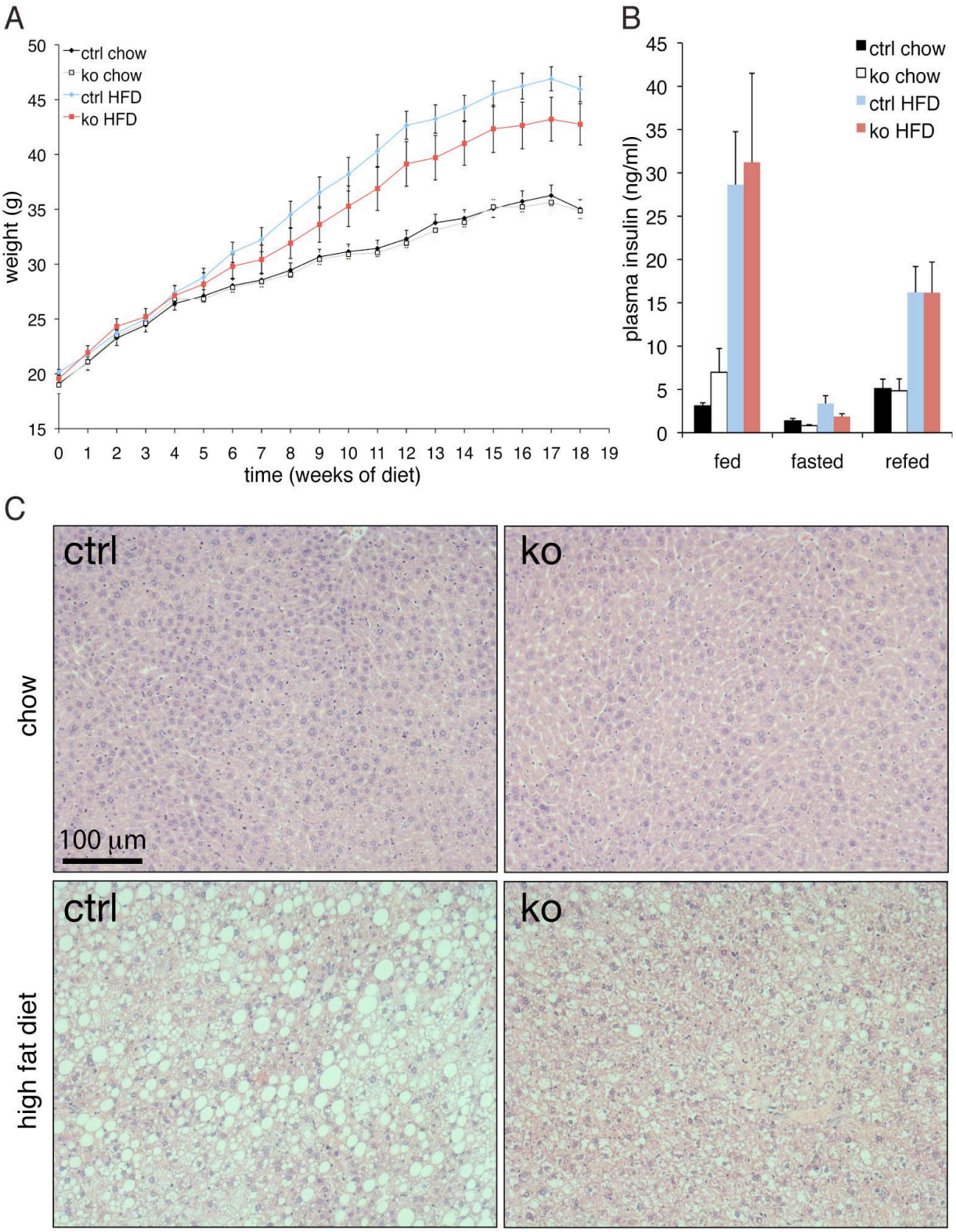

Supplementary Figure 5

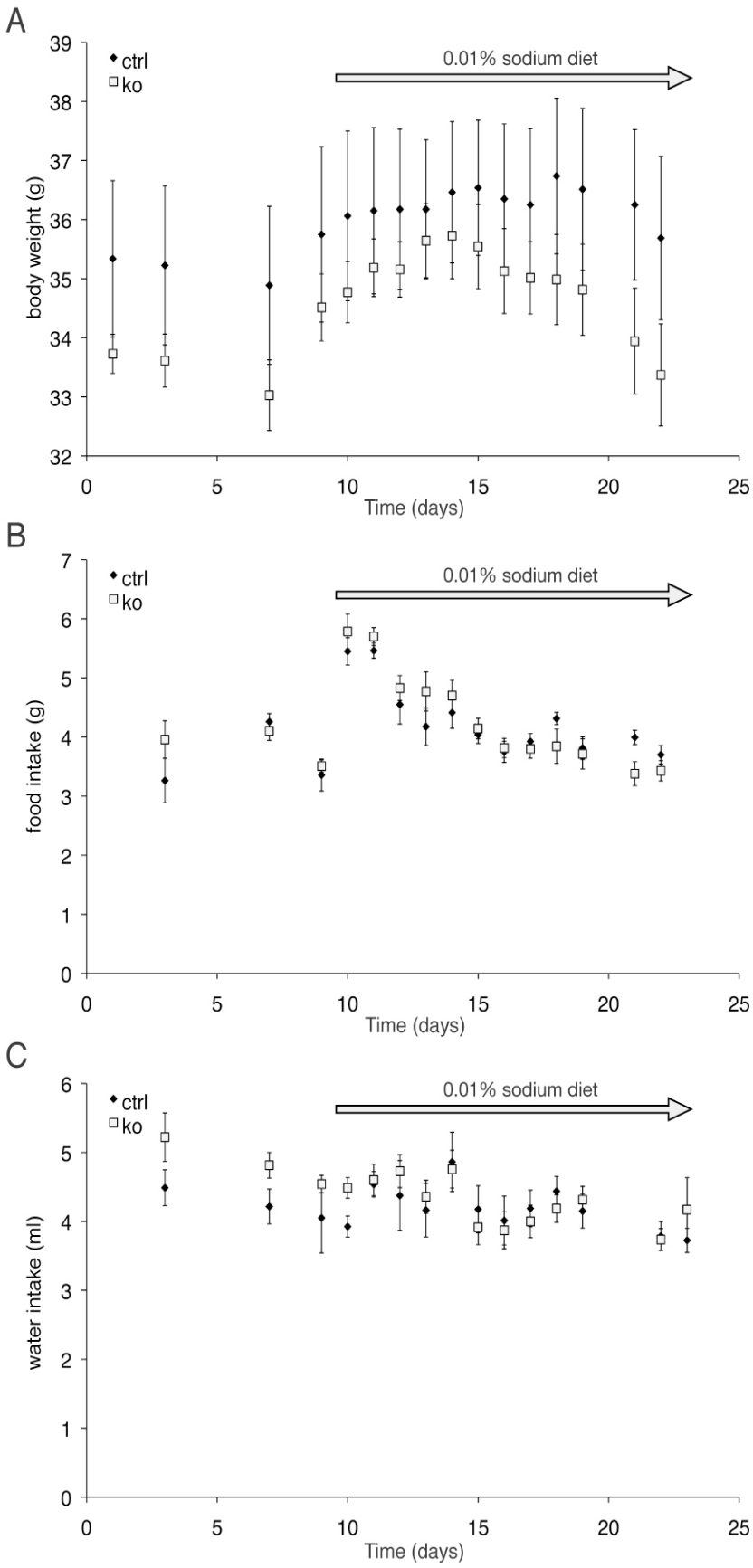

Supplementary Figure 6

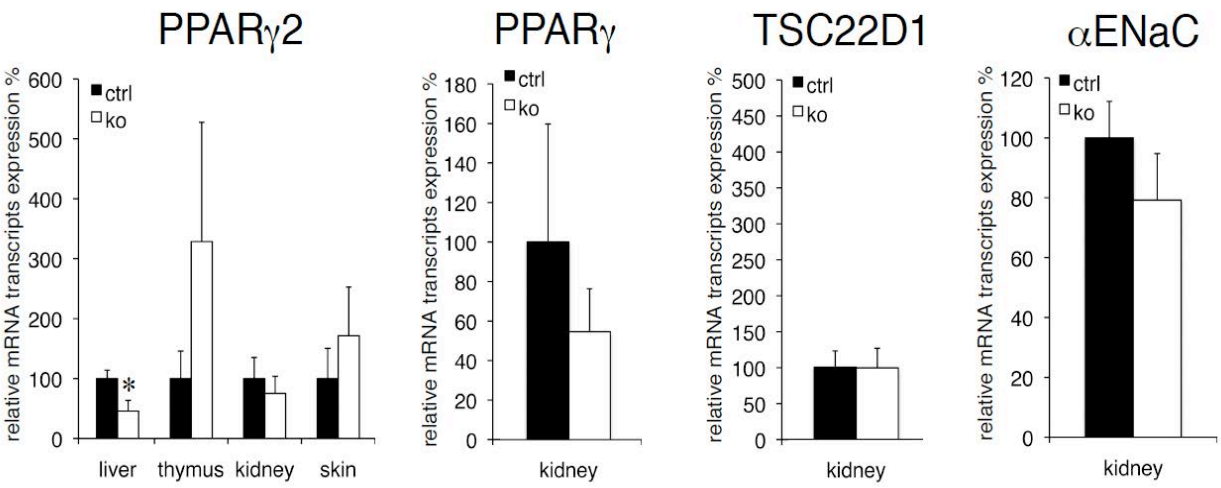

Table I

Table I. *Primers used for genotyping and quantitative RT-PCR*

Genotyping	Forward	Reverse
GILZ lox	5'-CAG GTC TGA GTA ACT TGT CC-3'	5'-CAG TCT GTG GTG ACC GTT TC-3'
GILZ KO	5'-TGA CAG CTG CGT TTC TCA GTG-3'	
cre-recombinase	5'-CCT GGA AAA TGC TTC TGT CCG-3'	5'-CAG GGT GTT ATA AGC AAT CCC-3'
myogenin	5'-TTA CGT CCA TCG TGG ACA GC-3'	5'-TGG GCT GGG TGT TAG TCT TA-3'
Sybr Green (or RT-PCR)		
GILZ	5'-TGA CTG CAA CGC CAA AGC-3'	5'-CTG ATA CAT TTC GGT GTT CAT GGT T-3'
RNA pol II	5'-GAG GAA ACG GTG GAT GTC CTT-3'	5'-AAG CAG GAG GTC AAA ACA GCC-3'
GAPDH	5'-GAC ATC AAG AAG GTG GTG AA-3'	5'-TGT CAT ACC AGG AAA TGA GC-3'
actinβ	5'-CTG GCT CCT AGC ACC ATG A-3'	5'-AGG CAC CAA TCC ACA CAG A-3'
αENaC	5'-CGG AGT TGC TAA ACT CAA CAT C-3'	5'-TGG AGA CCA GTA CCG GCT-3'
PPARγ2	5'-CGA TCT TGA CAG GAA AGA CA-3'	5'-TAG GCT CCA TAA AGT CAC CA-3'
PPARγ	5'-CAG GCT TCC ACT ATG GAG TT-3'	5'-TCC GGC AGT TAA GAT CAC AC-3'
KLF5	5'-GGT CCA GAC AAG ATG TGA AA-3'	5'-ACT AGT GAA CTC GGG GAG AG-3'
KLF15	5'-CCC AAT GCC GCC AAA CCT AT-3'	5'-GAG GTG GCT GCT CTT GGT GTA CAT C-3'
adiponectin	5'-AAG AAG GAC AAG GCC GTT CTC TT-3'	5'-GCT ATG GGT AGT TGC AGT CAG TT-3'
aP2 (FABP4)	5'-TGC CAC AAG GAA AGT GGC AG-3'	5'-CTT CAC CTT CCT GCT GTC TG-3'
AR	5'-TAC AGC CAG TGT GTG AGG AT-3'	5'-CCA CTG GAA TAA TGC TGA AG-3'
GR	5'-GGT CTG AAG AGC CAA GAG TT-3'	5'-GGA GAT TTT CAA CCA CAT CA-3'
TSC22D1	5'-GCG ATG GAT CTA GGA GTT TAC-3'	5'-GCA CCA GAG CTA TTG TCA AG-3'
Six5	5'-AGG AGA GGT TCG ACT GGA T-3'	5'-GCA GTC ACT CCC ACA CTA GA-3'
TaqMan		
GILZ	5'-TGG ATA ACA GTG CCT CCG G-3'	5'-AGG TCC ATG GCC TGC TCA-3'
GILZ probe	*5'-CCA GTG TGG TGG CCC TAG ACA ACA AGA-3'*	
PPARγ2	5'-GCC GGA TCC ACA AAA AAA GT-3'	5'-CGC CAA CAG CTT CTC CTT CT-3'
PPARγ2 probe	*5'-ATG CCA TCA GGT TTG GGC GG-3'*	
actinβ	5'-AGG TCA TCA CTA TTG GCA ACG A-3'	5'-CAC TTC ATG ATG GAA TTG AAT GTA GTT-3'
actinβ probe	*5'-TGC CAC AGG ATT CCA TAC CCA AGA AGG-3'*	

Table II

Table II. *Insulin and glucose measurements upon fasting and refeeding*

feeding state		ctrl (n=7)	ko (n=8)	p-value
fed	insulin (ng/ml)	1.5 ± 0.3	3.5 ± 0.7	0.036*
	glucose (mM)	7.7 ± 0.5	7.7 ± 0.3	0.976
fasted	insulin (ng/ml)	0.6 ± 0.1	0.8 ± 0.3	0.487
	glucose (mM)	3.8 ± 0.1	3.5 ± 0.1	0.052
refed	insulin (ng/ml)	3.9 ± 0.6	4.2 ± 0.8	0.786
	glucose (mM)	10.7 ± 0.5	9.5 ± 0.6	0.129

Table III

Table III. *Mouse body weight and length, echo MRI values*

	2.5 month old mice			15 month old mice		
	ctrl (n=7)	ko (n=8)	*p*-value	ctrl (n=7)	ko (n=9)	*p*-value
Body weight (g)	29.83 ± 0.60	29.98 ± 0.50	0.427	39.57 ± 1.56	35.27 ± 0.10	0.014*
Body length (cm)	9.87 ± 0.10	9.86 ± 0.10	0.454	10.73 ± 0.10	10.53 ± 0.09	0.082
Fat (g)	2.94 ± 2.65	3.37 ± 1.79	0.207	8.31 ± 0.94	6.34 ± 0.44	0.030*
Lean (g)	23.21 ± 0.40	22.73 ± 0.60	0.265	25.95 ± 0.80	24.82 ± 0.57	0.129
Fluids (g)	0.17 ± 0.04	0.12 ± 0.01	0.114	0.47 ± 0.08	0.46 ± 0.06	0.429

Table IV

Table IV. *Renal sodium and water handling*

Mice upon normal diet					
Plasma	ctrl	n	ko	n	*p*-value
sodium (mmol/l)	148.6 ± 0.90	7	150.3 ± 0.06	7	0.063
potassium (mmol/l)	5.5 ± 0.13	7	5.9 ± 0.18	7	0.046*
osmolarity (mmol/kg H_2O)	318.9 ± 2.65	7	321.9 ± 1.79	7	0.176
aldosterone (pg/ml)	183.9 ± 43.8	8	159.8 ± 44.4	8	0.352
Urine					
sodium (mmol/l)	54.7 ± 8.2	7	59.7 ± 8.75	7	0.684
potassium (mmol/l)	318.6 ± 28.65	7	290 ± 23.95	7	0.46
osmolarity (mmol/kg H_2O)	1911 ± 152	7	1880 ± 183	7	0.897
creatinine (µmol/l)	4887 ± 462	7	5102 ± 529	7	0.765
sodium/creatinine ratio	0.011 ± 0.0008	7	0.0118 ± 0.0011	7	0.6
potassium/creatinine ratio	0.0657 ± 0.0029	7	0.0579 ± 0.0026	7	0.069
Mice upon no sodium diet					
Plasma					
sodium (mmol/l)	147 ± 1	3	150.7 ± 0.33	3	0.013*
potassium (mmol/l)	8.5 ± 0.44	3	7.4 ± 0.21	3	0.043*
osmolarity (mmol/kg H_2O)	327 ± 2.31	3	327.3 ± 0.88	3	0.45
aldosterone (pg/ml)	601.3 ± 125.5	8	543.6 ± 161.6	7	0.39
Urine					
sodium (mmol/l)	19.5 ± 1.5	8	19.3 ± 2.2	7	0.468
potassium (mmol/l)	325 ± 12.90	8	297.9 ± 19	7	0.124
osmolarity (mmol/kg H_2O)	2588 ± 107	8	2445 ± 66	7	0.146
creatinine (µmol/l)	4013 ± 309	8	3577 ± 232	7	0.145
sodium/creatinine ratio	0.0051 ± 0.0001	8	0.0054 ± 0.0005	7	0.32
potassium/creatinine ratio	0.0855 ± 0.0091	8	0.0853 ± 0.0071	7	0.492
Mice upon normal diet, after water deprivation (23h)					
Plasma					
sodium (mmol/l)	167 ± 1.21	6	167.2 ± 1.35	6	0.464
potassium (mmol/l)	5.7 ± 0.21	6	5.83 ± 0.13	6	0.3
osmolarity (mmol/kg H_2O)	357.5 ± 1.98	6	359.0 ± 4.06	6	0.373
Urine					
sodium (mmol/l)	84.4 ± 18.81	5	76.5 ± 13.09	4	0.377
potassium (mmol/l)	474 ± 42.64	5	525 ± 36.57	4	0.204
osmolarity (mmol/kg H_2O)	2110 ± 247	5	2452 ± 124	4	0.146

Table V

Table V. *Mouse body weight and echo MRI values following chow and high fat diets*

	chow			high fat diet		
	ctrl (n=12)	ko (n=12)	*p*-value	ctrl (n=11)	ko (n=11)	*p*-value
Body weight (g)	35.44 ± 0.92	35.14 ± 0.92	0.819	46.62 ± 1.11	42.88 ± 2.11	0.124
Fat (g)	7.00 ± 0.68	6.66 ± 0.67	0.731	17.27 ± 1.03	13.36 ± 1.74	0.061
Fat / BW %	19.44 ± 1.60	18.70 ± 1.59	0.747	36.74 ± 1.55	29.81 ± 3.17	0.057
Lean (g)	25.06 ± 0.53	24.99 ± 0.63	0.930	24.76 ± 0.40	25.48 ± 0.57	0.309
Lean / BW %	70.99 ± 1.61	71.33 ± 1.65	0.885	53.41 ± 1.40	60.71 ± 2.94	0.031*
Water (g)	22.79 ± 0.48	22.73 ± 0.58	0.946	22.30 ± 0.37	23.06 ± 0.57	0.271
Water / BW %	64.55 ± 1.51	64.88 ± 1.48	0.880	48.08 ± 1.25	54.91 ± 2.65	0.026*

Protocols

Extraction of tail DNA

First part: digestion
1. Cut 3 to 5 mm of tail (at least 2 weeks old mice)
2. Add 750 µL of a mix of Tail Buffer and Proteinase K
3. Incubate overnight at 56°C

During digestion, the plasma membrane and the nuclear membrane of the cells get disrupted.

Second part: extraction
4. Spin down 1 min. at Room Temperature (RT), full speed (13'000 rpm on Mirko 20 Hettisch Zentrifugen)
5. Mix 5 min. at RT, full speed (on eppendorf mixer 5432)
6. Add 250 µL NaCl saturated (about 6M - *The role of NaCl is to precipitate DNA and get rid of proteins.)*
7. Mix 5 min. at RT, full speed. The solution has to become opaque; otherwise more NaCl has to be added.
8. Spin down 10 min. at RT, full speed
9. Take 750 µL of the liquid phase, without top and pellet, and transfer it into a new tube
10. Add 500 µL isopropanol *(Isopropanol is used to crystallize DNA.)*
11. Mix 2 min. at RT, full speed
12. Spin down 1 min. at RT, full speed
13. Discard the supernatant
14. Wash the pellet with 1.5 mL EtOH 70% *(EtOH crystallizes and precipitates DNA.)*
15. Spin down 1 min. at RT, full speed
16. Discard the supernatant taking great care of the pellet
17. Let dry the tubes upside down for 5 min. at RT
18. Add 120 µL TE (see annex) to re-suspend DNA
19. Incubate 2 hours at 37°C with shaking (eppendorf mixer, 400 rpm)

Genomic DNA can be stored at -20°C.

Tail Buffer + Proteinase K Mix (per tail):
712.5 µL Tail Buffer
37.5 µL Proteinase K

Proteinase K (10 mg/mL) is a serine protease that digests proteins and removes contamination from preparations of nucleic acids. Addition of proteinase K to these preparations rapidly inactivates nucleases that might otherwise degrade the DNA during purification. The enzyme is active in the presence of chemicals that denature proteins (SDS), chelating agents (EDTA), and other reagents and inhibitors.

Tail Buffer
Compounds: Role(s) of compounds:
1/20 Tris-HCl (Tris hydrochloride) 1M pH8 pH regulator
1/50 NaCl 5M
1/5 EDTA (ethylenediaminetetraacetic
acid) 0.5M
Limitation of proteins hydrolysis in cell extracts and inhibition of polymerases activity, thus purifying nucleic acids.
1/20 SDS (sodium dodecyl sulfate) 20% Denaturation of proteins by deleting non-covalent bindings. Conferring a negative global charge on the proteins.
17/25 ddH_2O

TE Buffer
Compounds: Role(s) of compounds:
Tris-HCl *See Tail Buffer*
EDTA *See Tail Buffer*
TE buffer protects DNA from degradation, used for storage of nucleic acids.

Isolation of DNA via NaOH digestion

1. Cut a 2-3 mm piece of tail
2. Add 600 µL NaOH 50mM *(sodium hydroxide breaks chemical bonds keeping the tissues intact - digestion).*
3. Incubate at 95°C for 30 min. agitating (500 rpm). Shake well once or twice during this time.
4. Let cool down and neutralize with 100 µL Tris-HCl 1M pH8 (*Tris-HCl keeps pH stable*).
5. Spin down 5 min. at RT, full speed

DNA can be stored at 4°C for a short time (otherwise store it at -20°C).

RNA extraction protocol

The tissues or organs isolated from the organism have to be stored at -80°C or in liquid nitrogen for short storage.

1. Put a steal bead into the tube containing the tissue
2. Under the hood, add 400 µL of Trizol (Invitrogen)
3. Put the tubes into the TissueLyser machine (Qiagen) and homogenize for 30 sec.
4. Under the hood, add 600 µL more of Trizol
5. Re-homogenize for 30 sec.
6. Spin down at 1000 g for 1 min.
7. Collect the supernatant an transfer it into a new tube
8. Incubate 5 min. at RT
9. Under the hood, add 200 µL of chloroform (1/5 volume of Trizol)
10. Shake the tubes for 15 sec. and incubate 3 min. at RT
11. Spin down at 4°C at 12'000 g for 15 min.
12. Transfer the colorless aqueous upper phase into a new tube
13. Add 250 µL of isopropanol (1/4 volume of Trizol)
14. Incubate 10 min. at RT
15. Spin down at 4°C at 12'000 g for 10 min.
16. Discard the supernatant
17. Wash the pellet with 500 µL of EtOH 75% DEPC and vortex
18. Spin down at 4°C at 7500 g for 5 min.
19. Discard the supernatant
20. Air-dry the pellet for 1 hour
21. Re-suspend RNA into H_2O DEPC

Reverse transcription protocol

After RNA extraction, the concentration has to be measured with the NanoDrop.
1. Calculate the volume of extraction to take, in order to have 1 ng of RNA:

$$if\ [RNA] = x[ng\ /\ \mu L] \Rightarrow V = 1000/x\ [\mu L]$$

2. Calculate the volume of H2O DEPC to add to have a volume of 10 µL
3. Mix 1:
    Oligo(dT): 1 µL * number of samples (+ error margin)
    dNTP mix: 1 µL * number of samples (+ error margin)
4. In new tubes, put:
    H_2O DEPC according to calculation
    RNA according to calculation
    2 µL of Mix 1
5. Incubate at 65°C for 5 min.
6. Mix 2:
    5X First-Strand Buffer: 4 µL * number of samples (+ error margin)
    0.1M DTT: 2 µL * number of samples (+ error margin)
    at very last time: SuperScript II RT: 1 µL * # of samples (+ margin)
7. Cool down the tubes in ice and spin down
8. Add 7 µL of Mix 2 and mix by pipetting
9. Incubate at 42°C for 50 min.
10. Incubate at 70°C for 15 min.
11. Dilute into 80 µL of H_2O DEPC

Protein extraction for Western blot analysis

Thiocyanate extraction: for keratins removal, extraction in thiocyanate buffer (1M NaSCN, 50mM Hepes, 10mM EDTA, 0.3M orthophenantolin, 0.1% isopropanol, 20µg/ml PMSF, pH=6.8).
1. Homogenate the samples in buffer,
2. Spin @ 27000g, 30', 0°C
3. Take the supernatant, dilute 10 times with 4°C water,
4. Spin @ 27000g, 1h, 0°C (rotor SS34, 15000 rpm)
5. Dissolve the pellet directly in laemmli buffer 1.5x
6. Heat 5' 95°C
7. Cool on ice.

Urea extraction: extraction of all the proteins of the skin. (8M Urea, 10mM EDTA, 50mM Tris-Hcl pH=8.0).
1. Homogenate the samples in buffer,
2. Incubate 30 on ice (4°C)
3. Spin @ 15000g, 30', 0°C
4. Take the supernatant
5. Add 5x laemmli buffer (final 1x)
6. Heat 5' 95°C
7. Cool on ice.

Homogenization with the TissueLyser (Qiagen):
1. In 2ml "safe-lock" Eppendorf tubes on a cold block
2. Add 2cm^2 of skin sample, 600µl of buffer, one 5mm iron bead,
3. Shake 30'' at 30Hz,
4. Turn the tube holder upside-down
5. Shake 30'' at 30Hz,
6. Proceed with the extraction

Western blot analysis

Protein quantification using the BCA Protein Assay kit (Pierce):

- in a 50ml Falcon tube:
  - 98 µl from bottle A x (number of samples + 2)
  - 2 µl from bottle B x (number of samples + 2)

  } in duplicate
- on a transparent plate, put 2 lines of BSA (10 µl) as a ladder (from 0 to 10mg of protein), then put the samples (10 µl). Quickly add 100 µl of the BCA mix over every protein well.
- Measure proteins a 540 nm wave length, the BSA scale must be between 0.1 and 1. If necessary, wait and repeat the measurement.

Plot the data as follows in excel:

A	1	2	3	4	5	6	7	8
A	0.938	0.652	0.413	0.242	0.178	0.134	0.098	0.082
B	1.114	0.627	0.402	0.235	0.176	0.129	0.105	0.083
C	1.321	1.383	0.431	0.382	1.076	1.252	0.406	0.441
D	1.484	1.406	0.428	0.447	1.105	1.257	0.413	0.446

The data obtained is then treated as shown below :

		1	2	3	4	5	6	7	8
conc (ug/ml)	A	10000	5000	2500	1250	625	312.5	156.25	0
scale	B	1.026	0.6395	0.4075	0.2385	0.177	0.1315	0.1015	0.083
scale - blank		0.9435	0.557	0.325	0.156	0.0945	0.049	0.019	0

The data obtained is then plotted as shown below :

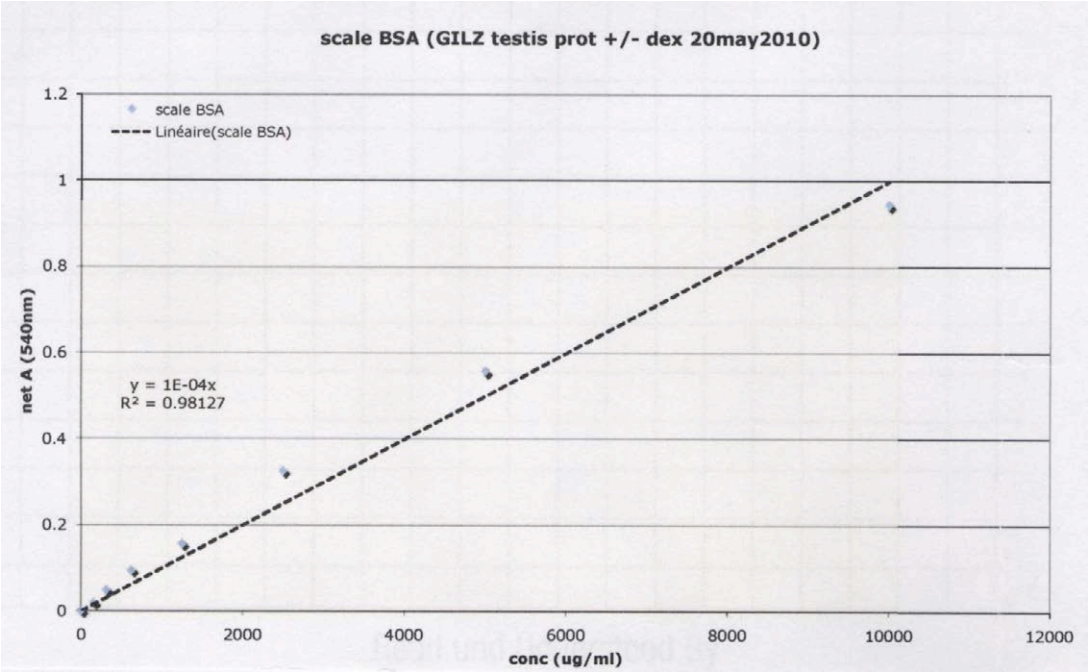

The slope allows to calculate the values for the protein concentration of the samples of interest.

sample	testis							
					dex	dex	dex	dex
dilution 1/1	+	+	-	-	+	+	-	-
mean	1.4025	1.3945	0.4295	0.4145	1.0905	1.2545	0.4095	0.444
prot conc	**14025**	**13945**	**4295**	**4145**	**10905**	**12545**	**4095**	**4435**

This is an example of the data obtained of testis protein lysates.

Gels :

Separating gel : (20 ml)	**Stacking gel : (10 ml)**
• 5 ml Tris-HCl 1.5 M, pH 8.8.	2.5 ml Tris-HCl 0.5 M, pH 6.8.
• 0.2 ml SDS 10%.	100 µl SDS 10%.
• 6.5 ml acrylamide 30%.	1.3 ml acrylamide 30%.
• 8.3 ml ddH_2O.	6.1 ml dcH_2O.
• 150 µl APS 10%.	50 µl APS 10%.
• 15 µl Temed.	20 µl Temed.

Calculate and prepare samples that manner :

Initial concentration (Ci) x Initial Volume (Vi) = Final Concentration (Cf) x Final Volume (Vf)

What we look for is the initial volume: $Vi = \frac{CfVf}{Ci}$

Cf = 2 µg/µl Vf = 100 µl

The initial concentration is divided by 1000.

Example :

Vi = (2*100)/14.025 = 14.260 µl of proteins

Water to add : 100 - Vi = 85.74 µl

Once the protein volume has been taken and put in an Eppendorf tube we must add:

- 20 µl de Laemmli buffer 5x
- Vortex and put 5 min at 95 °C
- Thermic shock bye putting on ice
- Centrifuge briefly

Migrate the proteins on the acrylamide gel, in an SDS-Page Gel box with the migration buffer 1x at 80 V for 15 min, then at 120 V until the lightest proteins join the bottom of the gel.

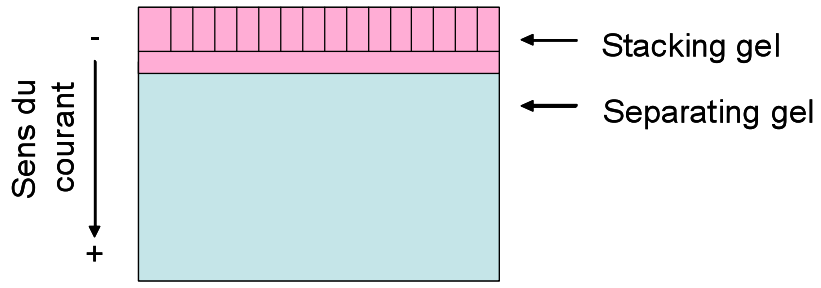

The stacking gel is used to compact proteins before entering the separating gel. The latter is used to separate the proteins in function of their size.

After the migration, transfer the proteins on a nitrocellulose membrane. Transfer buffer 1x is used and a transfer box. The gel has to be placed as shown is the following image:

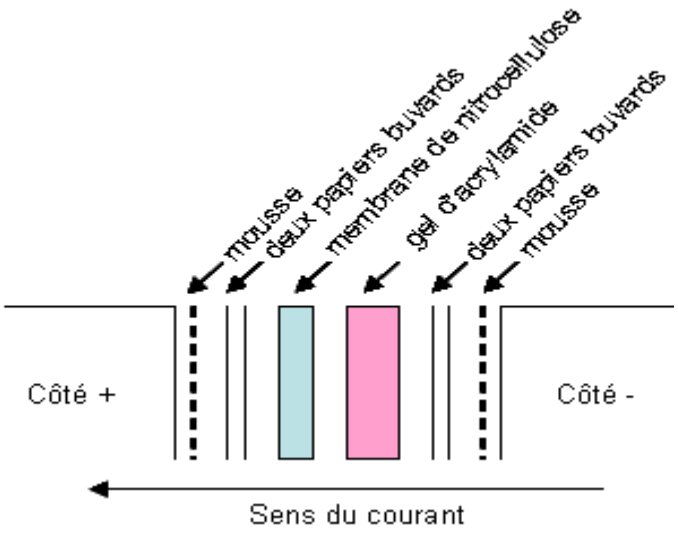

A potential must be applied, either 100 V for 1 h or 40 V for 24 h, both at 4 °C. This electrical potential drives proteins from the negative to the positive side of the membrane.

Proteins can be revealed by Ponceau S red 1% staining (2 min). Wash the membrane with distilled water.

Bloc the membrane with TBS tween + milk for 30 min (RT). This step is used to avoid unspecific binding of the primary antibody.

Incubate the membrane with the primary antibody for 1 h, then wash 3x with TBS tween and apply the secondary antibody for 1 h. The antibodies must be diluted in 2% milk. The concentration depends on the affinity of the antibody itself.

The secondary antibody is normally conjugated so to be reacting chemically or physically. The ECL kit is used to react with HRP-conjugated antibodies by bioluminescence.

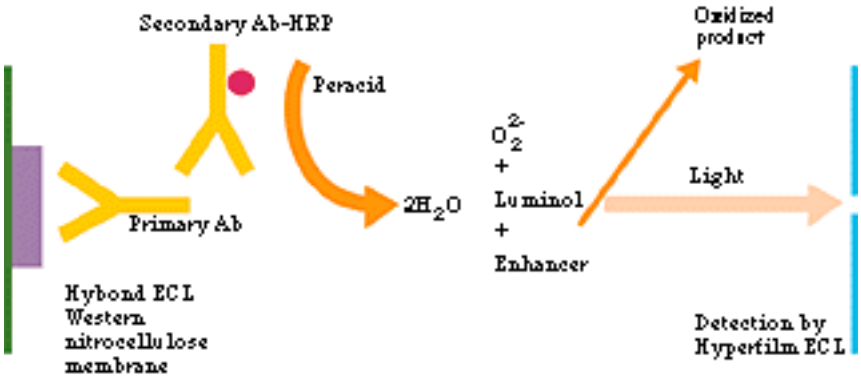

The proteins of interest on the membrane can then be revealed on a negative film in a dark room.

Cell culture of mouse embryonic fiboblasts (MEFs)

Breed 2 females with 1 male the evening and the morning after (early) separate the male and check the plug on the females.

14 days after, dissect the mother to take out the embryos:

- From the embryos, take out the head and liver (decidua).
- Perform PCR from unwanted part for genotyping. Each embryo is kept separately until genotype is known.
- The embryo is digested into trypsin.
- Once genotyped, pool cells form 3 animals together (by genotype!!), filter and put into 75 cm^2 flasks with 12 ml of medium.
- 2 days after, pass the cells into 175 cm^2 flasks with 45 ml medium.
- 2 days after, pass 1 flask into 3 of the same size.

To freeze the cells, take out the medium and rinse with PBS. Trypsinize few minutes and resuspend with 10 ml of medium in a 50 ml Falcon tube. Centrifuge at 1500 rpm and take out the supernatant. Resuspend the pellet with 12 ml of "freezing medium" (=10% DMSO, 40% FBS et 50% complete medium). Put the cells into cryovials (1 ml per tube) and store at -70 °C for one week and then store into liquid N_2 for longer periods.

To use the frozen cells, thaw cryovials at 37 °C. Pool 2 tubes per genotype into a 15 ml Falcon tube and gently add 8 ml of medium. Centrifuge at 1200 rpm for 5 min. Take out the supernatant and keep the pellet. Resuspend the cells into 4 ml of medium. Put the suspension into a 75 cm^2 flask and add 11 ml of medium. Store in the incubation oven (37 °C, 5 % CO_2).

- After 2 days, pass into 175 cm^2 flask.
- After 2 days, pass into 3x175 cm^2 flasks.
- After 2 days, pass the cells into:
    - 6x 100mm petri dishes (15 ml)
    - 6x 6-well dishes (4 ml)
    - 2x 175 cm^2 flasks (45 ml)
- After 2 days, change the medium.

MEF differentiation into adipocytes

Once cells are subconfluent (2 days after confluence), put the “differentiation medium”.

For 500 ml of “differentiation medium” mix these reagents to DMEM:

- 50 ml FBS.
- 5.5 ml Sodium Pyruvate.
- 5.5 ml L-glutamine.
- 500 µl Dexamethasone 1 µM ; prepared like this : 6.8 mg in 1 ml mQ water.
- 150 µl IBMX 0.5 mM ; prepared like this : 57.5 mg in 150 µl NaOH 2M.
- 500 µl Insulin 5 mg/ml ; prepared like this : 5 mg in 1 ml HCl 50 mM.
- 500 µl Roziglitazone 2 µM ; prepared like this : 0.25 mg in 500 µl DMSO/PBS (proportion 1:3). Prepare at the last moment (can not be kept once in solution).

Once differentiated, cells must be kept into the “maintaining medium”.

For 300 ml of “maintaining medium” mix these reagents to DMEM:

- 300 ml of DMEM.
- 30 ml FBS.
- 1/1000 Gentanamicin.
- 300 µl Insulin (same concentration as for the differentiation medium).
- 0.3 mg Roziglitazone in 200 µl DMSO.

After 2 days, change this maintaining medium, and after 2 days again.

When the cells are ready for further experiments, rinse them with PBS :

1. For Oil red O staining, put formaldehyde on the cells for 15 min (caution, do not breath or touch !) Put Oil red O stain for 4 h on the dried/fixed cells. After, rinse with distilled water and take the picture with an inverted microscope.
2. For RNA analysis, use 600 µl of RLT buffer (RNeasy kit - Qiagen) for the lysis of the cells. Scrap the cells and put them into a Qiashredder column (Qiagen) for better lysis. Then extract the RNA following standard protocols.

Primary keratinocytes cell culture

- Take pups because in adult skin there is too many fibroblasts that would invade the culture dish instead of keratinocytes.
- Decapitation of the animal.
- Cut and keep the tail for genotyping.
- Cut the fore and hind legs at the half-length.
- Incision of the back with a scalpel.
- Peel a bit the skin away from both sides.
- Take away the skin from the legs.
- Spread out the skin with dermal side in contact with a dispase (5 mg/mL in Dubelco minimal essential medium (DMEM) ie: without Ca^{++} nor Mg^{++}) solution.
- Let incubate O/N at 4 °C or at 37 °C for 1-2 h.
- Put the skin on the epidermal side on a dish and take away the dermis that should go easily due to the dispase treatment.

- To put the skins in the dishes, forceps, funnel, gauzes (tissue) to filtrate… Put everything under UV light for 10 min to disinfect, heat the coating solution and the complete culture medium at 37 °C.
- In the hood, the flux comes from upside, so avoid to pass over objects or dishes. Bacteria don't fly!
- Put the coating solution (2 mL per medium culture dish), which is used as a protein matrix for cells to adhere.

- To separate dermis and epidermis, stick the skin epidermal side on the dish. Pull softly to get rid of the dermis, which is larger. Then pool the epidermises that are thinner and whiter than the dermis, by genotype. Then add 4mL of medium.
- Then slice thinly the skins with scissors avoiding putting the hand over the dish.
- Homogenize with a pipette, then take the cells from the medium and put them on the funnel with the gauze (filtration process to get rid of "everything" else than cells). Repeat this step with new medium 10 mL.
- Centrifuge 2 min (don't touch the speed control if using the machine in the culture room of the DPT) to collect cells at the bottom of the tube.
- Recover the coating solution on the side of the dish without making traces with the pipette, because cells wouldn't grow there.
- Take the supernatant after centrifugation of the Falcon tubes. Then suspend the base (culot) with medium 2 mL (for 1 dish) on the dishes for sedimentation. Check with the microscope that there are enough cells.
- Isolated cells that are clear have more chance to grow.
- Let incubate without EGF during 2-4 h at 37 °C then change the medium with one containing EGF when cells have well adhered (when it is the case, there is less contrast viewing with the microscope, meaning that they are well alive).
- Flame a glass pipette then aspire particles (dead cells).
- To do this change of medium it is necessary to rinse first with PBS or old culture medium that is still sterile and isotonic. Avoid the contact of the pipette and the dish.
- Put the new medium 4 mL per mid sized dish.
- Add EGF 1 µL/mL, or even 2 µL/mL to boost the reaction at the start of the culture.
- Add Ca^{++} (about 40-80 µM) as defined by R.-P. Charles.
- Incubate at 37 °C until the next passage (when the medium in the dishes changes color.

REFERENCES

Abo Hegab S, Hanke W (1984) The significance of cortisol for osmoregulation in carp (Cyprinus carpio) and tilapia (Sarotherodon mossambicus). Gen Comp Endocrinol 54:409-417.

Abriel H, Loffing J, Rebhun JF, Pratt JH, Schild L, Horisberger JD, Rotin D, Staub O (1999) Defective regulation of the epithelial Na+ channel by Nedd4 in Liddle's syndrome. J Clin Invest 103:667-673.

Achermann JC, Ozisik G, Meeks JJ, Jameson JL (2002) Genetic causes of human reproductive disease. J Clin Endocrinol Metab 87:2447-2454.

Akama TO, Nakagawa H, Sugihara K, Narisawa S, Ohyama C, Nishimura S, O'Brien DA, Moremen KW, Millan JL, Fukuda MN (2002) Germ cell survival through carbohydrate-mediated interaction with Sertoli cells. Science 295:124-127.

Alberti L, Girola A, Gilardini L, Conti A, Cattaldo S, Micheletto G, Invitti C (2007) Type 2 diabetes and metabolic syndrome are associated with increased expression of 11beta-hydroxysteroid dehydrogenase 1 in obese subjects. Int J Obes (Lond) 31:1826-1831.

Alexander CM, Landsman PB, Teutsch SM, Haffner SM (2003) NCEP-defined metabolic syndrome, diabetes, and prevalence of coronary heart disease among NHANES III participants age 50 years and older. Diabetes 52:1210-1214.

Alvarez de la Rosa D, Zhang P, Naray-Fejes-Toth A, Fejes-Toth G, Canessa CM (1999) The serum and glucocorticoid kinase sgk increases the abundance of epithelial sodium channels in the plasma membrane of Xenopus oocytes. J Biol Chem 274:37834-37839.

Amasheh S, Barmeyer C, Koch CS, Tavalali S, Mankertz J, Epple HJ, Gehring MM, Florian P, Kroesen AJ, Zeitz M, Fromm M, Schulzke JD (2004) Cytokine-dependent transcriptional down-regulation of epithelial sodium channel in ulcerative colitis. Gastroenterology 126:1711-1720.

Anantharam A, Palmer LG (2007) Determination of epithelial Na+ channel subunit stoichiometry from single-channel conductances. J Gen Physiol 130:55-70.

Anantharam A, Tian Y, Palmer LG (2006) Open probability of the epithelial sodium channel is regulated by intracellular sodium. J Physiol 574:333-347.

Ando H, Yanagihara H, Hayashi Y, Obi Y, Tsuruoka S, Takamura T, Kaneko S, Fujimura A (2005) Rhythmic messenger ribonucleic acid expression of clock genes and adipocytokines in mouse visceral adipose tissue. Endocrinology 146:5631-5636.

Ashcroft GS, Yang X, Glick AB, Weinstein M, Letterio JL, Mizel DE, Anzano M, Greenwell-Wild T, Wahl SM, Deng C, Roberts AB (1999) Mice lacking Smad3 show accelerated wound healing and an impaired local inflammatory response. Nat Cell Biol 1:260-266.

Ashwell JD, Lu FW, Vacchio MS (2000) Glucocorticoids in T cell development and function*. Annu Rev Immunol 18:309-345.

Asselin-Labat ML, Biola-Vidamment A, Kerbrat S, Lombes M, Bertoglio J, Pallardy M (2005) FoxO3 mediates antagonistic effects of glucocorticoids and interleukin-2 on glucocorticoid-induced leucine zipper expression. Mol Endocrinol 19:1752-1764.

Asselin-Labat ML, David M, Biola-Vidamment A, Lecoeuche D, Zennaro MC, Bertoglio J, Pallardy M (2004) GILZ, a new target for the transcription factor FoxO3, protects T lymphocytes from interleukin-2 withdrawal-induced apoptosis. Blood 104:215-223.

Auberson M, Hoffmann-Pochon N, Vandewalle A, Kellenberger S, Schild L (2003) Epithelial Na+ channel mutants causing Liddle's syndrome retain ability to respond to aldosterone and vasopressin. Am J Physiol Renal Physiol 285:F459-471.

Ayroldi E, Zollo O, Macchiarulo A, Di Marco B, Marchetti C, Riccardi C (2002) Glucocorticoid-induced leucine zipper inhibits the Raf-extracellular signal-regulated kinase pathway by binding to Raf-1. Mol Cell Biol 22:7929-7941.

Ayroldi E, Zollo O, Bastianelli A, Marchetti C, Agostini M, Di Virgilio R, Riccardi C (2007) GILZ mediates the antiproliferative activity of glucocorticoids by negative regulation of Ras signaling. J Clin Invest 117:1605-1615.
Ayroldi E, Migliorati G, Bruscoli S, Marchetti C, Zollo O, Cannarile L, D'Adamio F, Riccardi C (2001) Modulation of T-cell activation by the glucocorticoid-induced leucine zipper factor via inhibition of nuclear factor kappaB. Blood 98:743-753.
Barak Y, Liao D, He W, Ong ES, Nelson MC, Olefsky JM, Boland R, Evans RM (2002) Effects of peroxisome proliferator-activated receptor delta on placentation, adiposity, and colorectal cancer. Proc Natl Acad Sci U S A 99:303-308.
Bargiello TA, Jackson FR, Young MW (1984) Restoration of circadian behavioural rhythms by gene transfer in Drosophila. Nature 312:752-754.
Barker PM, Nguyen MS, Gatzy JT, Grubb B, Norman H, Hummler E, Rossier B, Boucher RC, Koller B (1998) Role of gammaENaC subunit in lung liquid clearance and electrolyte balance in newborn mice. Insights into perinatal adaptation and pseudohypoaldosteronism. J Clin Invest 102:1634-1640.
Barmeyer C, Harren M, Schmitz H, Heinzel-Pleines U, Mankertz J, Seidler U, Horak I, Wiedenmann B, Fromm M, Schulzke JD (2004) Mechanisms of diarrhea in the interleukin-2-deficient mouse model of colonic inflammation. Am J Physiol Gastrointest Liver Physiol 286:G244-252.
Barnes PJ (2010) Mechanisms and resistance in glucocorticoid control of inflammation. J Steroid Biochem Mol Biol 120:76-85.
Barsoum I, Yao HH (2006) The road to maleness: from testis to Wolffian duct. Trends Endocrinol Metab 17:223-228.
Baschant U, Tuckermann J The role of the glucocorticoid receptor in inflammation and immunity. J Steroid Biochem Mol Biol 120:69-75.
Bastie C, Holst D, Gaillard D, Jehl-Pietri C, Grimaldi PA (1999) Expression of peroxisome proliferator-activated receptor PPARdelta promotes induction of PPARgamma and adipocyte differentiation in 3T3C2 fibroblasts. J Biol Chem 274:21920-21925.
Beato M, Herrlich P, Schutz G (1995) Steroid hormone receptors: many actors in search of a plot. Cell 83:851-857.
Belot A, Ranchin B, Fichtner C, Pujo L, Rossier BC, Liutkus A, Morlat C, Nicolino M, Zennaro MC, Cochat P (2008) Pseudohypoaldosteronisms, report on a 10-patient series. Nephrol Dial Transplant 23:1636-1641.
Berrebi D, Bruscoli S, Cohen N, Foussat A, Migliorati G, Bouchet-Delbos L, Maillot MC, Portier A, Couderc J, Galanaud P, Peuchmaur M, Riccardi C, Emilie D (2003) Synthesis of glucocorticoid-induced leucine zipper (GILZ) by macrophages: an anti-inflammatory and immunosuppressive mechanism shared by glucocorticoids and IL-10. Blood 101:729-738.
Beyer TA, Auf dem Keller U, Braun S, Schafer M, Werner S (2007) Roles and mechanisms of action of the Nrf2 transcription factor in skin morphogenesis, wound repair and skin cancer. Cell Death Differ 14:1250-1254.
Bhalla V, Soundararajan R, Pao AC, Li H, Pearce D (2006) Disinhibitory pathways for control of sodium transport: regulation of ENaC by SGK1 and GILZ. Am J Physiol Renal Physiol 291:F714-721.
Bhalla V, Daidie D, Li H, Pao AC, LaGrange LP, Wang J, Vandewalle A, Stockand JD, Staub O, Pearce D (2005) Serum- and glucocorticoid-regulated kinase 1 regulates ubiquitin ligase neural precursor cell-expressed, developmentally down-regulated protein 4-2 by inducing interaction with 14-3-3. Mol Endocrinol 19:3073-3084.
Bhat MA, Izaddoost S, Lu Y, Cho KO, Choi KW, Bellen HJ (1999) Discs Lost, a novel multi-PDZ domain protein, establishes and maintains epithelial polarity. Cell 96:833-845.

Bhoumik A, Fichtman B, Derossi C, Breitwieser W, Kluger HM, Davis S, Subtil A, Meltzer P, Krajewski S, Jones N, Ronai Z (2008) Suppressor role of activating transcription factor 2 (ATF2) in skin cancer. Proc Natl Acad Sci U S A 105:1674-1679.
Bilder D, Perrimon N (2000) Localization of apical epithelial determinants by the basolateral PDZ protein Scribble. Nature 403:676-680.
Blanpain C, Fuchs E (2009) Epidermal homeostasis: a balancing act of stem cells in the skin. Nat Rev Mol Cell Biol 10:207-217.
Bonny O, Hummler E (2000) Dysfunction of epithelial sodium transport: from human to mouse. Kidney Int 57:1313-1318.
Boron W, Boulpaep E (2004) Medical Physiology, Updated Edition.
Botero-Velez M, Curtis JJ, Warnock DG (1994) Brief report: Liddle's syndrome revisited--a disorder of sodium reabsorption in the distal tubule. N Engl J Med 330:178-181.
Boulais N, Misery L (2007) Merkel cells. Journal of the American Academy of Dermatology 57:147-165.
Boulais N, Misery L (2008) The epidermis: a sensory tissue. Eur J Dermatol 18:119-127.
Braissant O, Foufelle F, Scotto C, Dauca M, Wahli W (1996) Differential expression of peroxisome proliferator-activated receptors (PPARs): tissue distribution of PPAR-alpha, -beta, and -gamma in the adult rat. Endocrinology 137:354-366.
Brenner M, Hearing VJ (2008) The protective role of melanin against UV damage in human skin. Photochemistry and photobiology 84:539-549.
Bressler RS, Bressler CH (1989) Functional anatomy of the skin. Clin Podiatr Med Surg 6:229-246.
Brouard M, Casado M, Djelidi S, Barrandon Y, Farman N (1999) Epithelial sodium channel in human epidermal keratinocytes: expression of its subunits and relation to sodium transport and differentiation. J Cell Sci 112 (Pt 19):3343-3352.
Brown RL, Ormsby I, Doetschman TC, Greenhalgh DG (1995) Wound healing in the transforming growth factor-beta-deficient mouse. Wound Repair Regen 3:25-36.
Bruns JB, Carattino MD, Sheng S, Maarouf AB, Weisz OA, Pilewski JM, Hughey RP, Kleyman TR (2007) Epithelial Na+ channels are fully activated by furin- and prostasin-dependent release of an inhibitory peptide from the gamma-subunit. J Biol Chem 282:6153-6160.
Bugaj V, Pochynyuk O, Stockand JD (2009) Activation of the epithelial Na+ channel in the collecting duct by vasopressin contributes to water reabsorption. Am J Physiol Renal Physiol 297:F1411-1418.
Candi E, Schmidt R, Melino G (2005) The cornified envelope: a model of cell death in the skin. Nat Rev Mol Cell Biol 6:328-340.
Canessa CM, Schafer JA (1992) AVP stimulates Na+ transport in primary cultures of rabbit cortical collecting duct cells. Am J Physiol 262:F454-461.
Canessa CM, Horisberger JD, Rossier BC (1993) Epithelial sodium channel related to proteins involved in neurodegeneration. Nature 361:467-470.
Canessa CM, Schild L, Buell G, Thorens B, Gautschi I, Horisberger JD, Rossier BC (1994) Amiloride-sensitive epithelial Na+ channel is made of three homologous subunits. Nature 367:463-467.
Cannarile L, Zollo O, D'Adamio F, Ayroldi E, Marchetti C, Tabilio A, Bruscoli S, Riccardi C (2001) Cloning, chromosomal assignment and tissue distribution of human GILZ, a glucocorticoid hormone-induced gene. Cell Death Differ 8:201-203.
Carattino MD, Sheng S, Bruns JB, Pilewski JM, Hughey RP, Kleyman TR (2006) The epithelial Na+ channel is inhibited by a peptide derived from proteolytic processing of its alpha subunit. J Biol Chem 281:18901-18907.

Carreau S, Genissel C, Bilinska B, Levallet J (1999) Sources of oestrogen in the testis and reproductive tract of the male. Int J Androl 22:211-223.
Carreau S, Delalande C, Silandre D, Bourguiba S, Lambard S (2006) Aromatase and estrogen receptors in male reproduction. Mol Cell Endocrinol 246:65-68.
Carreau S, Silandre D, Bois C, Bouraima H, Galeraud-Denis I, Delalande C (2007) Estrogens: a new player in spermatogenesis. Folia Histochem Cytobiol 45 Suppl 1:S5-10.
Cartharius K, Frech K, Grote K, Klocke B, Haltmeier M, Klingenhoff A, Frisch M, Bayerlein M, Werner T (2005) MatInspector and beyond: promoter analysis based on transcription factor binding sites. Bioinformatics 21:2933-2942.
Chalfie M, Wolinsky E (1990) The identification and suppression of inherited neurodegeneration in Caenorhabditis elegans. Nature 345:410-416.
Chalmel F, Rolland AD, Niederhauser-Wiederkehr C, Chung SS, Demougin P, Gattiker A, Moore J, Patard JJ, Wolgemuth DJ, Jegou B, Primig M (2007) The conserved transcriptome in human and rodent male gametogenesis. Proc Natl Acad Sci U S A 104:8346-8351.
Chandra V, Huang P, Hamuro Y, Raghuram S, Wang Y, Burris TP, Rastinejad F (2008) Structure of the intact PPAR-gamma-RXR-alpha nuclear receptor complex on DNA. Nature:350-356.
Chang SS, Grunder S, Hanukoglu A, Rosler A, Mathew PM, Hanukoglu I, Schild L, Lu Y, Shimkets RA, Nelson-Williams C, Rossier BC, Lifton RP (1996) Mutations in subunits of the epithelial sodium channel cause salt wasting with hyperkalaemic acidosis, pseudohypoaldosteronism type 1. Nat Genet 12:248-253.
Charles RP (2007) Role of the epithelial sodium channel (ENaC) in the epidermal barrier function of the skin. PhD Thesis, University of Lausanne.
Charles RP, Guitard M, Leyvraz C, Breiden B, Haftek M, Haftek-Terreau Z, Stehle JC, Sandhoff K, Hummler E (2008) Postnatal requirement of the epithelial sodium channel for maintenance of epidermal barrier function. J Biol Chem 283:2622-2630.
Chawla A, Schwarz EJ, Dimaculangan DD, Lazar MA (1994) Peroxisome proliferator-activated receptor (PPAR) gamma: adipose-predominant expression and induction early in adipocyte differentiation. Endocrinology 135:798-800.
Chen SY, Bhargava A, Mastroberardino L, Meijer OC, Wang J, Buse P, Firestone GL, Verrey F, Pearce D (1999) Epithelial sodium channel regulated by aldosterone-induced protein sgk. Proc Natl Acad Sci U S A 96:2514-2519.
Chifflet S, Hernandez JA, Grasso S (2005) A possible role for membrane depolarization in epithelial wound healing. Am J Physiol Cell Physiol 288:C1420-1430.
Chmielowiec J, Borowiak M, Morkel M, Stradal T, Munz B, Werner S, Wehland J, Birchmeier C, Birchmeier W (2007) c-Met is essential for wound healing in the skin. J Cell Biol 177:151-162.
Chraibi A, Horisberger JD (2002) Na self inhibition of human epithelial Na channel: temperature dependence and effect of extracellular proteases. J Gen Physiol 120:133-145.
Chraibi A, Vallet V, Firsov D, Hess SK, Horisberger JD (1998) Protease modulation of the activity of the epithelial sodium channel expressed in Xenopus oocytes. J Gen Physiol 111:127-138.
Christensen BM, Mercier Zuber A, Loffing J, Stehle JC, Deen PM, Rossier BC, Hummler E (2010a) {alpha}ENaC-Mediated Lithium Absorption Promotes Nephrogenic Diabetes Insipidus. J Am Soc Nephrol.
Christensen BM, Perrier R, Wang Q, Zuber AM, Maillard M, Mordasini D, Malsure S, Ronzaud C, Stehle JC, Rossier BC, Hummler E (2010b) Sodium and potassium balance

depends on alphaENaC expression in connecting tubule. J Am Soc Nephrol 21:1942-1951.
Clark AR, Lasa M (2003) Crosstalk between glucocorticoids and mitogen-activated protein kinase signalling pathways. Curr Opin Pharmacol 3:404-411.
Cohen N, Mouly E, Hamdi H, Maillot MC, Pallardy M, Godot V, Capel F, Balian A, Naveau S, Galanaud P, Lemoine FM, Emilie D (2006) GILZ expression in human dendritic cells redirects their maturation and prevents antigen-specific T lymphocyte response. Blood 107:2037-2044.
Cooke HJ, Saunders PT (2002) Mouse models of male infertility. Nat Rev Genet 3:790-801.
Coviello AD, Kaplan B, Lakshman KM, Chen T, Singh AB, Bhasin S (2008) Effects of graded doses of testosterone on erythropoiesis in healthy young and older men. J Clin Endocrinol Metab 93:914-919.
Craven SE, Bredt DS (1998) PDZ proteins organize synaptic signaling pathways. Cell 93:495-498.
D'Adamio F, Zollo O, Moraca R, Ayroldi E, Bruscoli S, Bartoli A, Cannarile L, Migliorati G, Riccardi C (1997) A new dexamethasone-induced gene of the leucine zipper family protects T lymphocytes from TCR/CD3-activated cell death. Immunity 7:803-812.
de Rooij DG, Grootegoed JA (1998) Spermatogonial stem cells. Curr Opin Cell Biol 10:694-701.
de Rooij DG, Mizrak SC (2008) Deriving multipotent stem cells from mouse spermatogonial stem cells: a new tool for developmental and clinical research. Development 135:2207-2213.
Debonneville C, Flores SY, Kamynina E, Plant PJ, Tauxe C, Thomas MA, Munster C, Chraibi A, Pratt JH, Horisberger JD, Pearce D, Loffing J, Staub O (2001) Phosphorylation of Nedd4-2 by Sgk1 regulates epithelial Na(+) channel cell surface expression. EMBO J 20:7052-7059.
Delbes G, Levacher C, Habert R (2006) Estrogen effects on fetal and neonatal testicular development. Reproduction 132:527-538.
Denda M, Fujiwara S, Hibino T (2006) Expression of voltage-gated calcium channel subunit alpha1C in epidermal keratinocytes and effects of agonist and antagonists of the channel on skin barrier homeostasis. Exp Dermatol 15:455-460.
Despres JP, Lemieux I (2006) Abdominal obesity and metabolic syndrome. Nature 444:881-887.
Desvergne B, Wahli W (1999) Peroxisome proliferator-activated receptors: nuclear control of metabolism. Endocr Rev 20:649-688.
Diakov A, Bera K, Mokrushina M, Krueger B, Korbmacher C (2008) Cleavage in the {gamma}-subunit of the epithelial sodium channel (ENaC) plays an important role in the proteolytic activation of near-silent channels. J Physiol 586:4587-4608.
Diamond JM (1978) Channels in epithelial cell membranes and junctions. Fed Proc 37:2639-2643.
Dinchev D, Janda B, Evstatieva L, Oleszek W, Aslani MR, Kostova I (2008) Distribution of steroidal saponins in Tribulus terrestris from different geographical regions. Phytochemistry 69:176-186.
Dobens LL, Hsu T, Twombly V, Gelbart WM, Raftery LA, Kafatos FC (1997) The Drosophila bunched gene is a homologue of the growth factor stimulated mammalian TSC-22 sequence and is required during oogenesis. Mech Dev 65:197-208.
Dohrmann CE, Belaoussoff M, Raftery LA (1999) Dynamic expression of TSC-22 at sites of epithelial-mesenchymal interactions during mouse development. Mech Dev 84:147-151.

Dong M, Feng XZ, Wu LJ, Wang BX, Ikejima T (2001) Two new steroidal saponins from the rhizomes of Dioscorea panthaica and their cytotoxic activity. Planta Med 67:853-857.
Doyle DA, Lee A, Lewis J, Kim E, Sheng M, MacKinnon R (1996) Crystal structures of a complexed and peptide-free membrane protein-binding domain: molecular basis of peptide recognition by PDZ. Cell 85:1067-1076.
Dreyer C, Krey G, Keller H, Givel F, Helftenbein G, Wahli W (1992) Control of the peroxisomal beta-oxidation pathway by a novel family of nuclear hormone receptors. Cell 68:879-887.
Dubois NC, Hofmann D, Kaloulis K, Bishop JM, Trumpp A (2006) Nestin-Cre transgenic mouse line Nes-Cre1 mediates highly efficient Cre/loxP mediated recombination in the nervous system, kidney, and somite-derived tissues. Genesis 44:355-360.
Dymecki SM (1996) Flp recombinase promotes site-specific DNA recombination in embryonic stem cells and transgenic mice. Proc Natl Acad Sci U S A 93:6191-6196.
Eddleston J, Herschbach J, Wagelie-Steffen AL, Christiansen SC, Zuraw BL (2007) The anti-inflammatory effect of glucocorticoids is mediated by glucocorticoid-induced leucine zipper in epithelial cells. J Allergy Clin Immunol 119:115-122.
Eddy EM, Washburn TF, Bunch DO, Goulding EH, Gladen BC, Lubahn DB, Korach KS (1996) Targeted disruption of the estrogen receptor gene in male mice causes alteration of spermatogenesis and infertility. Endocrinology 137:4796-4805.
Edwards CR, Stewart PM, Burt D, Brett L, McIntyre MA, Sutanto WS, de Kloet ER, Monder C (1988) Localisation of 11 beta-hydroxysteroid dehydrogenase--tissue specific protector of the mineralocorticoid receptor. Lancet 2:986-989.
Ellestad LE, Malkiewicz SA, Guthrie HD, Welch GR, Porter TE (2009) Expression and regulation of glucocorticoid-induced leucine zipper in the developing anterior pituitary gland. J Mol Endocrinol 42:171-183.
Eming SA, Werner S, Bugnon P, Wickenhauser C, Siewe L, Utermohlen O, Davidson JM, Krieg T, Roers A (2007) Accelerated wound closure in mice deficient for interleukin-10. Am J Pathol 170:188-202.
Ergonul Z, Frindt G, Palmer LG (2006) Regulation of maturation and processing of ENaC subunits in the rat kidney. Am J Physiol Renal Physiol 291:F683-693.
Eskandari S, Snyder PM, Kreman M, Zampighi GA, Welsh MJ, Wright EM (1999) Number of subunits comprising the epithelial sodium channel. J Biol Chem 274:27281-27286.
Fakitsas P, Adam G, Daidie D, van Bemmelen MX, Fouladkou F, Patrignani A, Wagner U, Warth R, Camargo SM, Staub O, Verrey F (2007) Early aldosterone-induced gene product regulates the epithelial sodium channel by deubiquitylation. J Am Soc Nephrol 18:1084-1092.
Falin R, Veizis IE, Cotton CU (2005) A role for ERK1/2 in EGF- and ATP-dependent regulation of amiloride-sensitive sodium absorption. Am J Physiol Cell Physiol 288:C1003-1011.
Falin RA, Cotton CU (2007) Acute downregulation of ENaC by EGF involves the PY motif and putative ERK phosphorylation site. J Gen Physiol 130:313-328.
Fanning AS, Anderson JM (1999) Protein modules as organizers of membrane structure. Curr Opin Cell Biol 11:432-439.
Fejes-Toth G, Frindt G, Naray-Fejes-Toth A, Palmer LG (2008) Epithelial Na+ channel activation and processing in mice lacking SGK1. Am J Physiol Renal Physiol 294:F1298-1305.
Fiol DF, Kultz D (2005) Rapid hyperosmotic coinduction of two tilapia (Oreochromis mossambicus) transcription factors in gill cells. Proc Natl Acad Sci U S A 102:927-932.

Fiol DF, Mak SK, Kultz D (2007) Specific TSC22 domain transcripts are hypertonically induced and alternatively spliced to protect mouse kidney cells during osmotic stress. FEBS J 274:109-124.
Firsov D, Gautschi I, Merillat AM, Rossier BC, Schild L (1998) The heterotetrameric architecture of the epithelial sodium channel (ENaC). EMBO J 17:344-352.
Firsov D, Schild L, Gautschi I, Merillat AM, Schneeberger E, Rossier BC (1996) Cell surface expression of the epithelial Na channel and a mutant causing Liddle syndrome: a quantitative approach. Proc Natl Acad Sci U S A 93:15370-15375.
Fraser R, Ingram MC, Anderson NH, Morrison C, Davies E, Connell JM (1999) Cortisol effects on body mass, blood pressure, and cholesterol in the general population. Hypertension 33:1364-1368.
Frateschi S (2009) Functional analysis of altered channel-activating protease-1 (CAP1) expression in the skin. PhD Thesis, University of Lausanne.
Frindt G, Masilamani S, Knepper MA, Palmer LG (2001) Activation of epithelial Na channels during short-term Na deprivation. Am J Physiol Renal Physiol 280:F112-118.
Froment P, Gizard F, Defever D, Staels B, Dupont J, Monget P (2006) Peroxisome proliferator-activated receptors in reproductive tissues: from gametogenesis to parturition. J Endocrinol 189:199-209.
Fu L, Lee CC (2003) The circadian clock: pacemaker and tumour suppressor. Nat Rev Cancer 3:350-361.
Fuchs E (2008) Skin stem cells: rising to the surface. J Cell Biol 180:273-284.
Fuchs W, Larsen EH, Lindemann B (1977) Current-voltage curve of sodium channels and concentration dependence of sodium permeability in frog skin. J Physiol 267:137-166.
Fuh G, Pisabarro MT, Li Y, Quan C, Lasky LA, Sidhu SS (2000) Analysis of PDZ domain-ligand interactions using carboxyl-terminal phage display. J Biol Chem 275:21486-21491.
Funder JW, Pearce PT, Smith R, Smith AI (1988) Mineralocorticoid action: target tissue specificity is enzyme, not receptor, mediated. Science 242:583-585.
Gachon F, Olela FF, Schaad O, Descombes P, Schibler U (2006) The circadian PAR-domain basic leucine zipper transcription factors DBP, TEF, and HLF modulate basal and inducible xenobiotic detoxification. Cell Metab 4:25-36.
Gallardo T, Shirley L, John GB, Castrillon DH (2007) Generation of a germ cell-specific mouse transgenic Cre line, Vasa-Cre. Genesis 45:413-417.
Galon J, Franchimont D, Hiroi N, Frey G, Boettner A, Ehrhart-Bornstein M, O'Shea JJ, Chrousos GP, Bornstein SR (2002) Gene profiling reveals unknown enhancing and suppressive actions of glucocorticoids on immune cells. FASEB J 16:61-71.
Garner CC, Nash J, Huganir RL (2000) PDZ domains in synapse assembly and signalling. Trends Cell Biol 10:274-280.
Gavrila A, Peng CK, Chan JL, Mietus JE, Goldberger AL, Mantzoros CS (2003) Diurnal and ultradian dynamics of serum adiponectin in healthy men: comparison with leptin, circulating soluble leptin receptor, and cortisol patterns. J Clin Endocrinol Metab 88:2838-2843.
Geller DS, Rodriguez-Soriano J, Vallo Boado A, Schifter S, Bayer M, Chang SS, Lifton RP (1998) Mutations in the mineralocorticoid receptor gene cause autosomal dominant pseudohypoaldosteronism type I. Nat Genet 19:279-281.
Ghadessy FJ, Lim J, Abdullah AA, Panet-Raymond V, Choo CK, Lumbroso R, Tut TG, Gottlieb B, Pinsky L, Trifiro MA, Yong EL (1999) Oligospermic infertility associated with an androgen receptor mutation that disrupts interdomain and coactivator (TIF2) interactions. J Clin Invest 103:1517-1525.
Gilbert SF (2006) Developmental Biology.

Golubovic A, Kuhn A, Williamson M, Kalbacher H, Holstein TW, Grimmelikhuijzen CJ, Grunder S (2007) A peptide-gated ion channel from the freshwater polyp Hydra. J Biol Chem 282:35098-35103.
Gomez M, Raju SV, Viswanathan A, Painter RG, Bonvillain R, Byrne P, Nguyen DH, Bagby GJ, Kolls JK, Nelson S, Wang G (2010) Ethanol upregulates glucocorticoid-induced leucine zipper expression and modulates cellular inflammatory responses in lung epithelial cells. J Immunol 184:5715-5722.
Gonzales EB, Kawate T, Gouaux E (2009) Pore architecture and ion sites in acid-sensing ion channels and P2X receptors. Nature 460:599-604.
Grifoni SC, Gannon KP, Stec DE, Drummond HA (2006) ENaC proteins contribute to VSMC migration. Am J Physiol Heart Circ Physiol 291:H3076-3086.
Gross O, Gewies A, Finger K, Schafer M, Sparwasser T, Peschel C, Forster I, Ruland J (2006) Card9 controls a non-TLR signalling pathway for innate anti-fungal immunity. Nature 442:651-656.
Gross O, Poeck H, Bscheider M, Dostert C, Hannesschlager N, Endres S, Hartmann G, Tardivel A, Schweighoffer E, Tybulewicz V, Mocsai A, Tschopp J, Ruland J (2009) Syk kinase signalling couples to the Nlrp3 inflammasome for anti-fungal host defence. Nature 459:433-436.
Grossmann C, Freudinger R, Mildenberger S, Krug AW, Gekle M (2004) Evidence for epidermal growth factor receptor as negative-feedback control in aldosterone-induced Na+ reabsorption. Am J Physiol Renal Physiol 286:F1226-1231.
Guan Y, Hao C, Cha DR, Rao R, Lu W, Kohan DE, Magnuson MA, Redha R, Zhang Y, Breyer MD (2005) Thiazolidinediones expand body fluid volume through PPARgamma stimulation of ENaC-mediated renal salt absorption. Nat Med 11:861-866.
Guitard M, Leyvraz C, Hummler E (2004) A nonconventional look at ionic fluxes in the skin: lessons from genetically modified mice. News Physiol Sci 19:75-79.
Gupta RA, Sarraf P, Brockman JA, Shappell SB, Raftery LA, Willson TM, DuBois RN (2003) Peroxisome proliferator-activated receptor gamma and transforming growth factor-beta pathways inhibit intestinal epithelial cell growth by regulating levels of TSC-22. J Biol Chem 278:7431-7438.
Gurtner GC, Werner S, Barrandon Y, Longaker MT (2008) Wound repair and regeneration. Nature 453:314-321.
Hamm LL, Feng Z, Hering-Smith KS (2010) Regulation of sodium transport by ENaC in the kidney. Curr Opin Nephrol Hypertens 19:98-105.
Hansson JH, Schild L, Lu Y, Wilson TA, Gautschi I, Shimkets R, Nelson-Williams C, Rossier BC, Lifton RP (1995a) A de novo missense mutation of the beta subunit of the epithelial sodium channel causes hypertension and Liddle syndrome, identifying a proline-rich segment critical for regulation of channel activity. Proc Natl Acad Sci U S A 92:11495-11499.
Hansson JH, Nelson-Williams C, Suzuki H, Schild L, Shimkets R, Lu Y, Canessa C, Iwasaki T, Rossier B, Lifton RP (1995b) Hypertension caused by a truncated epithelial sodium channel gamma subunit: genetic heterogeneity of Liddle syndrome. Nat Genet 11:76-82.
Harada S, Rodan GA (2003) Control of osteoblast function and regulation of bone mass. Nature 423:349-355.
Hardy MH (1992) The secret life of the hair follicle. Trends Genet 8:55-61.
Harris M, Firsov D, Vuagniaux G, Stutts MJ, Rossier BC (2007) A novel neutrophil elastase inhibitor prevents elastase activation and surface cleavage of the epithelial sodium channel expressed in Xenopus laevis oocytes. J Biol Chem 282:58-64.

Harris M, Garcia-Caballero A, Stutts MJ, Firsov D, Rossier BC (2008) Preferential assembly of epithelial sodium channel (ENaC) subunits in Xenopus oocytes: role of furin-mediated endogenous proteolysis. J Biol Chem 283:7455-7463.
Hata Y, Nakanishi H, Takai Y (1998) Synaptic PDZ domain-containing proteins. Neurosci Res 32:1-7.
Herold MJ, McPherson KG, Reichardt HM (2006) Glucocorticoids in T cell apoptosis and function. Cell Mol Life Sci 63:60-72.
Hess RA, Cooke PS, Hofmann MC, Murphy KM (2006) Mechanistic insights into the regulation of the spermatogonial stem cell niche. Cell Cycle 5:1164-1170.
Hince M, Sakkal S, Vlahos K, Dudakov J, Boyd R, Chidgey A (2008) The role of sex steroids and gonadectomy in the control of thymic involution. Cell Immunol 252:122-138.
Hong G, Lockhart A, Davis B, Rahmoune H, Baker S, Ye L, Thompson P, Shou Y, O'Shaughnessy K, Ronco P, Brown J (2003) PPARgamma activation enhances cell surface ENaCalpha via up-regulation of SGK1 in human collecting duct cells. Faseb J 17:1966-1968.
Houben E, De Paepe K, Rogiers V (2007) A Keratinocyte's Course of Life. Skin pharmacology and physiology 20:122-132.
Howard BV, Howard WJ (1994) Dyslipidemia in non-insulin-dependent diabetes mellitus. Endocr Rev 15:263-274.
Huang JC (2008) The role of peroxisome proliferator-activated receptors in the development and physiology of gametes and preimplantation embryos. PPAR Res 2008:732303.
Huelsken J, Vogel R, Erdmann B, Cotsarelis G, Birchmeier W (2001) beta-Catenin controls hair follicle morphogenesis and stem cell differentiation in the skin. Cell 105:533-545.
Hughey RP, Bruns JB, Kinlough CL, Harkleroad KL, Tong Q, Carattino MD, Johnson JP, Stockand JD, Kleyman TR (2004) Epithelial sodium channels are activated by furin-dependent proteolysis. J Biol Chem 279:18111-18114.
Hummler E, Merillat AM, Rubera I, Rossier BC, Beermann F (2002) Conditional gene targeting of the Scnn1a (alphaENaC) gene locus. Genesis 32:169-172.
Hummler E, Barker P, Gatzy J, Beermann F, Verdumo C, Schmidt A, Boucher R, Rossier BC (1996) Early death due to defective neonatal lung liquid clearance in alpha-ENaC-deficient mice. Nat Genet 12:325-328.
Issemann I, Green S (1990) Activation of a member of the steroid hormone receptor superfamily by peroxisome proliferators. Nature 347:645-650.
Ivanova A, Serly J, Dinchev D, Ocsovszki I, Kostova I, Molnar J (2009) Screening of some saponins and phenolic components of Tribulus terrestris and Smilax excelsa as MDR modulators. In Vivo 23:545-550.
Jasti J, Furukawa H, Gonzales EB, Gouaux E (2007) Structure of acid-sensing ion channel 1 at 1.9 A resolution and low pH. Nature 449:316-323.
Jelinic P, Stehle JC, Shaw P (2006) The testis-specific factor CTCFL cooperates with the protein methyltransferase PRMT7 in H19 imprinting control region methylation. PLoS Biol 4:e355.
Johanssen S, Allolio B (2007) Mifepristone (RU 486) in Cushing's syndrome. Eur J Endocrinol 157:561-569.
Joiner WJ, Wang LY, Tang MD, Kaczmarek LK (1997) hSK4, a member of a novel subfamily of calcium-activated potassium channels. Proc Natl Acad Sci U S A 94:11013-11018.
Kajava AV, Kobe B (2002) Assessment of the ability to model proteins with leucine-rich repeats in light of the latest structural information. Protein Sci 11:1082-1090.
Kakihana R, Moore JA (1976) Circadian rhythm of corticosterone in mice: the effect of chronic consumption of alcohol. Psychopharmacologia 46:301-305.

Kalsbeek A, Fliers E, Romijn JA, La Fleur SE, Wortel J, Bakker O, Endert E, Buijs RM (2001) The suprachiasmatic nucleus generates the diurnal changes in plasma leptin levels. Endocrinology 142:2677-2685.
Kanai F, Marignani PA, Sarbassova D, Yagi R, Hall RA, Donowitz M, Hisaminato A, Fujiwara T, Ito Y, Cantley LC, Yaffe MB (2000) TAZ: a novel transcriptional co-activator regulated by interactions with 14-3-3 and PDZ domain proteins. EMBO J 19:6778-6791.
Kaplan DH, Kissenpfennig A, Clausen BE (2008) Insights into Langerhans cell function from Langerhans cell ablation models. European journal of immunology 38:2369-2376.
Kasturi SS, Tannir J, Brannigan RE (2008) The metabolic syndrome and male infertility. J Androl 29:251-259.
Katzmarzyk PT, Leon AS, Wilmore JH, Skinner JS, Rao DC, Rankinen T, Bouchard C (2003) Targeting the metabolic syndrome with exercise: evidence from the HERITAGE Family Study. Med Sci Sports Exerc 35:1703-1709.
Kellenberger S, Schild L (2002) Epithelial sodium channel/degenerin family of ion channels: a variety of functions for a shared structure. Physiol Rev 82:735-767.
Kellenberger S, Gautschi I, Schild L (2002) An external site controls closing of the epithelial Na+ channel ENaC. J Physiol 543:413-424.
Kellenberger S, Gautschi I, Schild L (2003) Mutations in the epithelial Na+ channel ENaC outer pore disrupt amiloride block by increasing its dissociation rate. Mol Pharmacol 64:848-856.
Kester HA, van der Leede BM, van der Saag PT, van der Burg B (1997) Novel progesterone target genes identified by an improved differential display technique suggest that progestin-induced growth inhibition of breast cancer cells coincides with enhancement of differentiation. J Biol Chem 272:16637-16643.
Kester HA, Blanchetot C, den Hertog J, van der Saag PT, van der Burg B (1999) Transforming growth factor-beta-stimulated clone-22 is a member of a family of leucine zipper proteins that can homo- and heterodimerize and has transcriptional repressor activity. J Biol Chem 274:27439-27447.
Khoury CM, Yang Z, Li XY, Vignali M, Fields S, Greenwood MT (2008) A TSC22-like motif defines a novel antiapoptotic protein family. FEMS Yeast Res 8:540-563.
Kirby ED, Geraghty AC, Ubuka T, Bentley GE, Kaufer D (2009) Stress increases putative gonadotropin inhibitory hormone and decreases luteinizing hormone in male rats. Proc Natl Acad Sci U S A 106:11324-11329.
Kliewer SA, Forman BM, Blumberg B, Ong ES, Borgmeyer U, Mangelsdorf DJ, Umesono K, Evans RM (1994) Differential expression and activation of a family of murine peroxisome proliferator-activated receptors. Proc Natl Acad Sci U S A 91:7355-7359.
Kobayashi A, Behringer RR (2003) Developmental genetics of the female reproductive tract in mammals. Nat Rev Genet 4:969-980.
Kobe B, Deisenhofer J (1995) Proteins with leucine-rich repeats. Curr Opin Struct Biol 5:409-416.
Koehl GE, Spitzner M, Ousingsawat J, Schreiber R, Geissler EK, Kunzelmann K (2010) Rapamycin inhibits oncogenic intestinal ion channels and neoplasia in APC(Min/+) mice. Oncogene 29:1553-1560.
Kosari F, Sheng S, Li J, Mak DO, Foskett JK, Kleyman TR (1998) Subunit stoichiometry of the epithelial sodium channel. J Biol Chem 273:13469-13474.
Krege JH, Hodgin JB, Couse JF, Enmark E, Warner M, Mahler JF, Sar M, Korach KS, Gustafsson JA, Smithies O (1998) Generation and reproductive phenotypes of mice lacking estrogen receptor beta. Proc Natl Acad Sci U S A 95:15677-15682.

Krug AW, Grossmann C, Schuster C, Freudinger R, Mildenberger S, Govindan MV, Gekle M (2003) Aldosterone stimulates epidermal growth factor receptor expression. J Biol Chem 278:43060-43066.
Kuenzli S, Saurat JH (2003) Peroxisome proliferator-activated receptors in cutaneous biology. Br J Dermatol 149:229-236.
Kunzelmann K (2005) Ion channels and cancer. J Membr Biol 205:159-173.
Lambard S, Galeraud-Denis I, Saunders PT, Carreau S (2004) Human immature germ cells and ejaculated spermatozoa contain aromatase and oestrogen receptors. J Mol Endocrinol 32:279-289.
Lansdown AB (2002) Calcium: a potential central regulator in wound healing in the skin. Wound Repair Regen 10:271-285.
Lecureuil C, Fontaine I, Crepieux P, Guillou F (2002) Sertoli and granulosa cell-specific Cre recombinase activity in transgenic mice. Genesis 33:114-118.
Lemberger T, Staels B, Saladin R, Desvergne B, Auwerx J, Wahli W (1994) Regulation of the peroxisome proliferator-activated receptor alpha gene by glucocorticoids. J Biol Chem 269:24527-24530.
Leposavic G, Perisic M (2008) Age-associated remodeling of thymopoiesis: role for gonadal hormones and catecholamines. Neuroimmunomodulation 15:290-322.
Levine B, Jean-Francois M, Bernardi F, Gargiulo G, Dobens L (2007) Notch signaling links interactions between the C/EBP homolog slow border cells and the GILZ homolog bunched during cell migration. Dev Biol 305:217-231.
Liang X, Butterworth MB, Peters KW, Frizzell RA (2010) AS160 modulates aldosterone-stimulated epithelial sodium channel forward trafficking. Mol Biol Cell 21:2024-2033.
Lingueglia E, Champigny G, Lazdunski M, Barbry P (1995) Cloning of the amiloride-sensitive FMRFamide peptide-gated sodium channel. Nature 378:730-733.
Loffing J, Pietri L, Aregger F, Bloch-Faure M, Ziegler U, Meneton P, Rossier BC, Kaissling B (2000) Differential subcellular localization of ENaC subunits in mouse kidney in response to high- and low-Na diets. Am J Physiol Renal Physiol 279:F252-258.
Loffing J, Zecevic M, Feraille E, Kaissling B, Asher C, Rossier BC, Firestone GL, Pearce D, Verrey F (2001) Aldosterone induces rapid apical translocation of ENaC in early portion of renal collecting system: possible role of SGK. Am J Physiol Renal Physiol 280:F675-682.
Lupas A (1996) Coiled coils: new structures and new functions. Trends Biochem Sci 21:375-382.
Lynch HE, Goldberg GL, Chidgey A, Van den Brink MR, Boyd R, Sempowski GD (2009) Thymic involution and immune reconstitution. Trends Immunol 30:366-373.
Mack JA, Anand S, Maytin EV (2005) Proliferation and cornification during development of the mammalian epidermis. Birth Defects Res C Embryo Today 75:314-329.
MacNeil S (2007) Progress and opportunities for tissue-engineered skin. Nature 445:874-880.
Mandard S, Muller M, Kersten S (2004) Peroxisome proliferator-activated receptor alpha target genes. Cell Mol Life Sci 61:393-416.
Marieb EN (2009) Human Anatomy & Physiology.
Martin-Fontecha A, Lanzavecchia A, Sallusto F (2009) Dendritic cell migration to peripheral lymph nodes. Handbook of experimental pharmacology:31-49.
Masilamani S, Kim GH, Mitchell C, Wade JB, Knepper MA (1999) Aldosterone-mediated regulation of ENaC alpha, beta, and gamma subunit proteins in rat kidney. J Clin Invest 104:R19-23.
Mata M, Merritt SE, Fan G, Yu GG, Holzman LB (1996) Characterization of dual leucine zipper-bearing kinase, a mixed lineage kinase present in synaptic terminals whose

phosphorylation state is regulated by membrane depolarization via calcineurin. J Biol Chem 271:16888-16896.
Matzuk MM, Lamb DJ (2008) The biology of infertility: research advances and clinical challenges. Nat Med 14:1197-1213.
Mauro T, Dixon DB, Hanley K, Isseroff RR, Pappone PA (1995) Amiloride blocks a keratinocyte nonspecific cation channel and inhibits Ca(++)-induced keratinocyte differentiation. J Invest Dermatol 105:203-208.
Mauro T, Dixon DB, Komuves L, Hanley K, Pappone PA (1997) Keratinocyte K+ channels mediate Ca2+-induced differentiation. J Invest Dermatol 108:864-870.
Mauro T, Guitard M, Behne M, Oda Y, Crumrine D, Komuves L, Rassner U, Elias PM, Hummler E (2002) The ENaC channel is required for normal epidermal differentiation. J Invest Dermatol 118:589-594.
McDonald FJ, Yang B, Hrstka RF, Drummond HA, Tarr DE, McCray PB, Jr., Stokes JB, Welsh MJ, Williamson RA (1999) Disruption of the beta subunit of the epithelial Na+ channel in mice: hyperkalemia and neonatal death associated with a pseudohypoaldosteronism phenotype. Proc Natl Acad Sci U S A 96:1727-1731.
McKinley C, Thong KJ, Baird DT (1993) The effect of dose of mifepristone and gestation on the efficacy of medical abortion with mifepristone and misoprostol. Hum Reprod 8:1502-1505.
Michael AE, Thurston LM, Rae MT (2003) Glucocorticoid metabolism and reproduction: a tale of two enzymes. Reproduction 126:425-441.
Michalik L, Desvergne B, Tan NS, Basu-Modak S, Escher P, Rieusset J, Peters JM, Kaya G, Gonzalez FJ, Zakany J, Metzger D, Chambon P, Duboule D, Wahli W (2001) Impaired skin wound healing in peroxisome proliferator-activated receptor (PPAR)alpha and PPARbeta mutant mice. J Cell Biol 154:799-814.
Michlig S, Mercier A, Doucet A, Schild L, Horisberger JD, Rossier BC, Firsov D (2004) ERK1/2 controls Na,K-ATPase activity and transepithelial sodium transport in the principal cell of the cortical collecting duct of the mouse kidney. J Biol Chem 279:51002-51012.
Miesfeld R, Okret S, Wikstrom AC, Wrange O, Gustafsson JA, Yamamoto KR (1984) Characterization of a steroid hormone receptor gene and mRNA in wild-type and mutant cells. Nature 312:779-781.
Misery L (2004) Nicotine effects on skin: are they positive or negative? Exp Dermatol 13:665-670.
Mittelstadt PR, Ashwell JD (2001) Inhibition of AP-1 by the glucocorticoid-inducible protein GILZ. J Biol Chem 276:29603-29610.
Moll JR, Olive M, Vinson C (2000) Attractive interhelical electrostatic interactions in the proline- and acidic-rich region (PAR) leucine zipper subfamily preclude heterodimerization with other basic leucine zipper subfamilies. J Biol Chem 275:34826-34832.
Moller DE (2001) New drug targets for type 2 diabetes and the metabolic syndrome. Nature 414:821-827.
Moller DE, Kaufman KD (2005) Metabolic syndrome: a clinical and molecular perspective. Annu Rev Med 56:45-62.
Montell C (2000) A PDZ protein ushers in new links. Nat Genet 26:6-7.
Moyer BD, Duhaime M, Shaw C, Denton J, Reynolds D, Karlson KH, Pfeiffer J, Wang S, Mickle JE, Milewski M, Cutting GR, Guggino WB, Li M, Stanton BA (2000) The PDZ-interacting domain of cystic fibrosis transmembrane conductance regulator is required for functional expression in the apical plasma membrane. J Biol Chem 275:27069-27074.

Moyle WR, Ramachandran J (1973) Effect of LH on steroidogenesis and cyclic AMP accumulation in rat Leydig cell preparations and mouse tumor Leydig cells. Endocrinology 93:127-134.
Mruk DD, Cheng CY (2004) Sertoli-Sertoli and Sertoli-germ cell interactions and their significance in germ cell movement in the seminiferous epithelium during spermatogenesis. Endocr Rev 25:747-806.
Muller BM, Kistner U, Veh RW, Cases-Langhoff C, Becker B, Gundelfinger ED, Garner CC (1995) Molecular characterization and spatial distribution of SAP97, a novel presynaptic protein homologous to SAP90 and the Drosophila discs-large tumor suppressor protein. J Neurosci 15:2354-2366.
Muller MB, Uhr M, Holsboer F, Keck ME (2004) Hypothalamic-pituitary-adrenocortical system and mood disorders: highlights from mutant mice. Neuroendocrinology 79:1-12.
Muruve DA, Petrilli V, Zaiss AK, White LR, Clark SA, Ross PJ, Parks RJ, Tschopp J (2008) The inflammasome recognizes cytosolic microbial and host DNA and triggers an innate immune response. Nature 452:103-107.
Muth TR, Ahn J, Caplan MJ (1998) Identification of sorting determinants in the C-terminal cytoplasmic tails of the gamma-aminobutyric acid transporters GAT-2 and GAT-3. J Biol Chem 273:25616-25627.
Naray-Fejes-Toth A, Canessa C, Cleaveland ES, Aldrich G, Fejes-Toth G (1999) sgk is an aldosterone-induced kinase in the renal collecting duct. Effects on epithelial Na+ channels. J Biol Chem 274:16973-16978.
Nicod M, Michlig S, Flahaut M, Salinas M, Fowler Jaeger N, Horisberger JD, Rossier BC, Firsov D (2002) A novel vasopressin-induced transcript promotes MAP kinase activation and ENaC downregulation. EMBO J 21:5109-5117.
Nitta H, Bunick D, Hess RA, Janulis L, Newton SC, Millette CF, Osawa Y, Shizuta Y, Toda K, Bahr JM (1993) Germ cells of the mouse testis express P450 aromatase. Endocrinology 132:1396-1401.
O'Shaughnessy PJ, Monteiro A, Verhoeven G, De Gendt K, Abel MH Effect of FSH on testicular morphology and spermatogenesis in gonadotrophin-deficient hypogonadal mice lacking androgen receptors. Reproduction 139:177-184.
O'Shaughnessy PJ, Monteiro A, Verhoeven G, De Gendt K, Abel MH (2010) Effect of FSH on testicular morphology and spermatogenesis in gonadotrophin-deficient hypogonadal mice lacking androgen receptors. Reproduction 139:177-184.
O'Shea EK, Rutkowski R, Kim PS (1989) Evidence that the leucine zipper is a coiled coil. Science 243:538-542.
Oakes ND, Kennedy CJ, Jenkins AB, Laybutt DR, Chisholm DJ, Kraegen EW (1994) A new antidiabetic agent, BRL 49653, reduces lipid availability and improves insulin action and glucoregulation in the rat. Diabetes 43:1203-1210.
Oda Y, Imanzahrai A, Kwong A, Komuves L, Elias PM, Largman C, Mauro T (1999) Epithelial sodium channels are upregulated during epidermal differentiation. J Invest Dermatol 113:796-801.
Ohta S, Shimekake Y, Nagata K (1996) Molecular cloning and characterization of a transcription factor for the C-type natriuretic peptide gene promoter. Eur J Biochem 242:460-466.
Oishi K, Ohkura N, Kadota K, Kasamatsu M, Shibusawa K, Matsuda J, Machida K, Horie S, Ishida N (2006) Clock mutation affects circadian regulation of circulating blood cells. J Circadian Rhythms 4:13.
Olsen NJ, Viselli SM, Fan J, Kovacs WJ (1998) Androgens accelerate thymocyte apoptosis. Endocrinology 139:748-752.

Ousingsawat J, Spitzner M, Schreiber R, Kunzelmann K (2008) Upregulation of colonic ion channels in APC (Min/+) mice. Pflugers Arch 456:847-855.
Ovaere P, Lippens S, Vandenabeele P, Declercq W (2009) The emerging roles of serine protease cascades in the epidermis. Trends Biochem Sci 34:453-463.
Palmer LG (1984) Voltage-dependent block by amiloride and other monovalent cations of apical Na channels in the toad urinary bladder. J Membr Biol 80:153-165.
Palmer LG, Frindt G (1986) Amiloride-sensitive Na channels from the apical membrane of the rat cortical collecting tubule. Proc Natl Acad Sci U S A 83:2767-2770.
Palmer LG, Andersen OS (2008) The two-membrane model of epithelial transport: Koefoed-Johnsen and Ussing (1958). J Gen Physiol 132:607-612.
Pasquali R, Patton L, Gambineri A (2007) Obesity and infertility. Curr Opin Endocrinol Diabetes Obes 14:482-487.
Paus R, Cotsarelis G (1999) The biology of hair follicles. The New England journal of medicine 341:491-497.
Payvar F, Wrange O, Carlstedt-Duke J, Okret S, Gustafsson JA, Yamamoto KR (1981) Purified glucocorticoid receptors bind selectively in vitro to a cloned DNA fragment whose transcription is regulated by glucocorticoids in vivo. Proc Natl Acad Sci U S A 78:6628-6632.
Perretti M, D'Acquisto F (2009) Annexin A1 and glucocorticoids as effectors of the resolution of inflammation. Nat Rev Immunol 9:62-70.
Peters JM, Lee SS, Li W, Ward JM, Gavrilova O, Everett C, Reitman ML, Hudson LD, Gonzalez FJ (2000) Growth, adipose, brain, and skin alterations resulting from targeted disruption of the mouse peroxisome proliferator-activated receptor beta(delta). Mol Cell Biol 20:5119-5128.
Phillips WD, Maimone MM, Merlie JP (1991) Mutagenesis of the 43-kD postsynaptic protein defines domains involved in plasma membrane targeting and AChR clustering. J Cell Biol 115:1713-1723.
Pittendrigh CS (1954) On Temperature Independence in the Clock System Controlling Emergence Time in Drosophila. Proc Natl Acad Sci U S A 40:1018-1029.
Poduje S, Sjerobabski-Masnec I, Ozanic-Bulic S (2008) Vitamin D--the true and the false about vitamin D. Collegium antropologicum 32 Suppl 2:159-162.
Ponce A, Vega-Saenz de Miera E, Kentros C, Moreno H, Thornhill B, Rudy B (1997) K+ channel subunit isoforms with divergent carboxy-terminal sequences carry distinct membrane targeting signals. J Membr Biol 159:149-159.
Pradervand S, Wang Q, Burnier M, Beermann F, Horisberger JD, Hummler E, Rossier BC (1999) A mouse model for Liddle's syndrome. J Am Soc Nephrol 10:2527-2533.
Proksch E, Brandner JM, Jensen JM (2008) The skin: an indispensable barrier. Exp Dermatol 17:1063-1072.
Pui CH, Relling MV, Downing JR (2004) Acute lymphoblastic leukemia. N Engl J Med 350:1535-1548.
Raja, Sivamani K, Garcia MS, Isseroff RR (2007) Wound re-epithelialization: modulating keratinocyte migration in wound healing. Front Biosci 12:2849-2868.
Rajala MW, Qi Y, Patel HR, Takahashi N, Banerjee R, Pajvani UB, Sinha MK, Gingerich RL, Scherer PE, Ahima RS (2004) Regulation of resistin expression and circulating levels in obesity, diabetes, and fasting. Diabetes 53:1671-1679.
Rajewsky K, Gu H, Kuhn R, Betz UA, Muller W, Roes J, Schwenk F (1996) Conditional gene targeting. J Clin Invest 98:600-603.
Reddy P, Zehring WA, Wheeler DA, Pirrotta V, Hadfield C, Hall JC, Rosbash M (1984) Molecular analysis of the period locus in Drosophila melanogaster and identification of a transcript involved in biological rhythms. Cell 38:701-710.

Rees JL (2003) Genetics of hair and skin color. Annual review of genetics 37:67-90.
Reis LF, Ruffner H, Stark G, Aguet M, Weissmann C (1994) Mice devoid of interferon regulatory factor 1 (IRF-1) show normal expression of type I interferon genes. EMBO J 13:4798-4806.
Riccardi C, Bruscoli S, Ayroldi E, Agostini M, Migliorati G (2001) GILZ, a glucocorticoid hormone induced gene, modulates T lymphocytes activation and death through interaction with NF-kB. Adv Exp Med Biol 495:31-39.
Riccardi C, Zollo O, Nocentini G, Bruscoli S, Bartoli A, D'Adamio F, Cannarile L, Delfino D, Ayroldi E, Migliorati G (2000) Glucocorticoid hormones in the regulation of cell death. Therapie 55:165-169.
Robert-Nicoud M (2001) The control of sodium balance. In: Lausanne.
Robert-Nicoud M, Flahaut M, Elalouf JM, Nicod M, Salinas M, Bens M, Doucet A, Wincker P, Artiguenave F, Horisberger JD, Vandewalle A, Rossier BC, Firsov D (2001) Transcriptome of a mouse kidney cortical collecting duct cell line: Effects of aldosterone and vasopressin. Proc Natl Acad Sci U S A 98:2712-2716.
Rodriguez CI, Buchholz F, Galloway J, Sequerra R, Kasper J, Ayala R, Stewart AF, Dymecki SM (2000) High-efficiency deleter mice show that FLPe is an alternative to Cre-loxP. Nat Genet 25:139-140.
Roger T, David J, Glauser MP, Calandra T (2001) MIF regulates innate immune responses through modulation of Toll-like receptor 4. Nature 414:920-924.
Roger T, Froidevaux C, Le Roy D, Reymond MK, Chanson AL, Mauri D, Burns K, Riederer BM, Akira S, Calandra T (2009) Protection from lethal gram-negative bacterial sepsis by targeting Toll-like receptor 4. Proc Natl Acad Sci U S A 106:2348-2352.
Rogiers V (2001) EEMCO guidance for the assessment of transepidermal water loss in cosmetic sciences. Skin Pharmacol Appl Skin Physiol 14:117-128.
Rossier BC, Stutts MJ (2009) Activation of the epithelial sodium channel (ENaC) by serine proteases. Annu Rev Physiol 71:361-379.
Rossier BC, Pradervand S, Schild L, Hummler E (2002) Epithelial sodium channel and the control of sodium balance: interaction between genetic and environmental factors. Annu Rev Physiol 64:877-897.
Roudier-Pujol C, Rochat A, Escoubet B, Eugene E, Barrandon Y, Bonvalet JP, Farman N (1996) Differential expression of epithelial sodium channel subunit mRNAs in rat skin. J Cell Sci 109 (Pt 2):379-385.
Rowell LB (1974) Human cardiovascular adjustments to exercise and thermal stress. Physiological reviews 54:75-159.
Rubera I, Hummler E, Beermann F (2009) Transgenic mice and their impact on kidney research. Pflugers Arch 458:211-222.
Rubera I, Loffing J, Palmer LG, Frindt G, Fowler-Jaeger N, Sauter D, Carroll T, McMahon A, Hummler E, Rossier BC (2003) Collecting duct-specific gene inactivation of alphaENaC in the mouse kidney does not impair sodium and potassium balance. J Clin Invest 112:554-565.
Sahar S, Sassone-Corsi P (2009) Metabolism and cancer: the circadian clock connection. Nat Rev Cancer 9:886-896.
Sasagawa I, Yazawa H, Suzuki Y, Nakada T (2001) Stress and testicular germ cell apoptosis. Arch Androl 47:211-216.
Sasaki H, Matsui Y (2008) Epigenetic events in mammalian germ-cell development: reprogramming and beyond. Nat Rev Genet 9:129-140.
Saunders PT, Fisher JS, Sharpe RM, Millar MR (1998) Expression of oestrogen receptor beta (ER beta) occurs in multiple cell types, including some germ cells, in the rat testis. J Endocrinol 156:R13-17.

Schafer M, Werner S (2007) Transcriptional control of wound repair. Annu Rev Cell Dev Biol 23:69-92.
Schild L (2010) The epithelial sodium channel and the control of sodium balance. Biochim Biophys Acta:1159-1165.
Schild L, Canessa CM, Shimkets RA, Gautschi I, Lifton RP, Rossier BC (1995) A mutation in the epithelial sodium channel causing Liddle disease increases channel activity in the Xenopus laevis oocyte expression system. Proc Natl Acad Sci U S A 92:5699-5703.
Schild L, Lu Y, Gautschi I, Schneeberger E, Lifton RP, Rossier BC (1996) Identification of a PY motif in the epithelial Na channel subunits as a target sequence for mutations causing channel activation found in Liddle syndrome. EMBO J 15:2381-2387.
Schmitz G, Muller G (1991) Structure and function of lamellar bodies, lipid-protein complexes involved in storage and secretion of cellular lipids. Journal of lipid research 32:1539-1570.
Seckl JR, Walker BR (2001) Minireview: 11beta-hydroxysteroid dehydrogenase type 1- a tissue-specific amplifier of glucocorticoid action. Endocrinology 142:1371-1376.
Seidel G, Adermann K, Schindler T, Ejchart A, Jaenicke R, Forssmann WG, Rosch P (1997) Solution structure of porcine delta sleep-inducing peptide immunoreactive peptide A homolog of the shortsighted gene product. J Biol Chem 272:30918-30927.
Sharpe RM (1994) Regulation of spermatogenesis. In: The Physiology of Reproduction, 2nd edn Edition: Raven Press, New York.
Shen JP, Cotton CU (2003) Epidermal growth factor inhibits amiloride-sensitive sodium absorption in renal collecting duct cells. Am J Physiol Renal Physiol 284:F57-64.
Shi PP, Cao XR, Sweezer EM, Kinney TS, Williams NR, Husted RF, Nair R, Weiss RM, Williamson RA, Sigmund CD, Snyder PM, Staub O, Stokes JB, Yang B (2008) Salt-sensitive hypertension and cardiac hypertrophy in mice deficient in the ubiquitin ligase Nedd4-2. Am J Physiol Renal Physiol 295:F462-470.
Shi X, Hamrick M, Isales CM (2007) Energy Balance, Myostatin, and GILZ: Factors Regulating Adipocyte Differentiation in Belly and Bone. PPAR Res 2007:92501.
Shi X, Shi W, Li Q, Song B, Wan M, Bai S, Cao X (2003) A glucocorticoid-induced leucine-zipper protein, GILZ, inhibits adipogenesis of mesenchymal cells. EMBO Rep 4:374-380.
Shibanuma M, Kuroki T, Nose K (1992) Isolation of a gene encoding a putative leucine zipper structure that is induced by transforming growth factor beta 1 and other growth factors. J Biol Chem 267:10219-10224.
Shimba S, Ishii N, Ohta Y, Ohno T, Watabe Y, Hayashi M, Wada T, Aoyagi T, Tezuka M (2005) Brain and muscle Arnt-like protein-1 (BMAL1), a component of the molecular clock, regulates adipogenesis. Proc Natl Acad Sci U S A 102:12071-12076.
Shimkets RA, Warnock DG, Bositis CM, Nelson-Williams C, Hansson JH, Schambelan M, Gill JR, Jr., Ulick S, Milora RV, Findling JW, et al. (1994) Liddle's syndrome: heritable human hypertension caused by mutations in the beta subunit of the epithelial sodium channel. Cell 79:407-414.
Sillard R, Schulz-Knappe P, Vogel P, Raida M, Bensch KW, Forssmann WG, Mutt V (1993) A novel 77-residue peptide from porcine brain contains a leucine-zipper motif and is recognized by an antiserum to delta-sleep-inducing peptide. Eur J Biochem 216:429-436.
Sinha MK, Ohannesian JP, Heiman ML, Kriauciunas A, Stephens TW, Magosin S, Marco C, Caro JF (1996) Nocturnal rise of leptin in lean, obese, and non-insulin-dependent diabetes mellitus subjects. J Clin Invest 97:1344-1347.

Smit P, Russcher H, de Jong FH, Brinkmann AO, Lamberts SW, Koper JW (2005) Differential regulation of synthetic glucocorticoids on gene expression levels of glucocorticoid-induced leucine zipper and interleukin-2. J Clin Endocrinol Metab 90:2994-3000.
Snyder PM (2009) Down-regulating destruction: phosphorylation regulates the E3 ubiquitin ligase Nedd4-2. Sci Signal 2:pe41.
Snyder PM, Cheng C, Prince LS, Rogers JC, Welsh MJ (1998) Electrophysiological and biochemical evidence that DEG/ENaC cation channels are composed of nine subunits. J Biol Chem 273:681-684.
Snyder PM, Olson DR, Kabra R, Zhou R, Steines JC (2004) cAMP and serum and glucocorticoid-inducible kinase (SGK) regulate the epithelial Na(+) channel through convergent phosphorylation of Nedd4-2. J Biol Chem 279:45753-45758.
Snyder PM, Price MP, McDonald FJ, Adams CM, Volk KA, Zeiher BG, Stokes JB, Welsh MJ (1995) Mechanism by which Liddle's syndrome mutations increase activity of a human epithelial Na+ channel. Cell 83:969-978.
Soundararajan R, Wang J, Melters D, Pearce D (2007) Differential activities of glucocorticoid-induced leucine zipper protein isoforms. J Biol Chem 282:36303-36313.
Soundararajan R, Pearce D, Hughey RP, Kleyman TR (2010) Role of epithelial sodium channels and their regulators in hypertension. J Biol Chem:30363-30369.
Soundararajan R, Zhang TT, Wang J, Vandewalle A, Pearce D (2005) A novel role for glucocorticoid-induced leucine zipper protein in epithelial sodium channel-mediated sodium transport. J Biol Chem 280:39970-39981.
Soundararajan R, Melters D, Shih IC, Wang J, Pearce D (2009) Epithelial sodium channel regulated by differential composition of a signaling complex. Proc Natl Acad Sci U S A 106:7804-7809.
Sternberg EM (2006) Neural regulation of innate immunity: a coordinated nonspecific host response to pathogens. Nat Rev Immunol 6:318-328.
Sun J, Tadokoro S, Imanaka T, Murakami SD, Nakamura M, Kashiwada K, Ko J, Nishida W, Sobue K (1998) Isolation of PSD-Zip45, a novel Homer/vesl family protein containing leucine zipper motifs, from rat brain. FEBS Lett 437:304-308.
Thorey IS, Hinz B, Hoeflich A, Kaesler S, Bugnon P, Elmlinger M, Wanke R, Wolf E, Werner S (2004) Transgenic mice reveal novel activities of growth hormone in wound repair, angiogenesis, and myofibroblast differentiation. J Biol Chem 279:26674-26684.
Tonko M, Ausserlechner MJ, Bernhard D, Helmberg A, Kofler R (2001) Gene expression profiles of proliferating vs. G1/G0 arrested human leukemia cells suggest a mechanism for glucocorticoid-induced apoptosis. FASEB J 15:693-699.
Tontonoz P, Hu E, Graves RA, Budavari AI, Spiegelman BM (1994a) mPPAR gamma 2: tissue-specific regulator of an adipocyte enhancer. Genes Dev 8:1224-1234.
Tontonoz P, Graves RA, Budavari AI, Erdjument-Bromage H, Lui M, Hu E, Tempst P, Spiegelman BM (1994b) Adipocyte-specific transcription factor ARF6 is a heterodimeric complex of two nuclear hormone receptors, PPAR gamma and RXR alpha. Nucleic Acids Res 22:5628-5634.
Treisman JE, Lai ZC, Rubin GM (1995) Shortsighted acts in the decapentaplegic pathway in Drosophila eye development and has homology to a mouse TGF-beta-responsive gene. Development 121:2835-2845.
Tripathi A, King C, de la Morenas A, Perry VK, Burke B, Antoine GA, Hirsch EF, Kavanah M, Mendez J, Stone M, Gerry NP, Lenburg ME, Rosenberg CL (2008) Gene expression abnormalities in histologically normal breast epithelium of breast cancer patients. Int J Cancer 122:1557-1566.

Tynan SH, Lundeen SG, Allan GF (2004) Cell type-specific bidirectional regulation of the glucocorticoid-induced leucine zipper (GILZ) gene by estrogen. J Steroid Biochem Mol Biol 91:225-239.
Uchida D, Kawamata H, Omotehara F, Miwa Y, Hino S, Begum NM, Yoshida H, Sato M (2000) Over-expression of TSC-22 (TGF-beta stimulated clone-22) markedly enhances 5-fluorouracil-induced apoptosis in a human salivary gland cancer cell line. Lab Invest 80:955-963.
Vainio S, Lin Y (2002) Coordinating early kidney development: lessons from gene targeting. Nat Rev Genet 3:533-543.
Vallet V, Chraibi A, Gaeggeler HP, Horisberger JD, Rossier BC (1997) An epithelial serine protease activates the amiloride-sensitive sodium channel. Nature 389:607-610.
Vallon V, Hummler E, Rieg T, Pochynyuk O, Bugaj V, Schroth J, Dechenes G, Rossier B, Cunard R, Stockand J (2009) Thiazolidinedione-induced fluid retention is independent of collecting duct alphaENaC activity. J Am Soc Nephrol 20:721-729.
Verdier-Sevrain S, Bonte F (2007) Skin hydration: a review on its molecular mechanisms. Journal of cosmetic dermatology 6:75-82.
Verrey F, Fakitsas P, Adam G, Staub O (2008) Early transcriptional control of ENaC (de)ubiquitylation by aldosterone. Kidney Int 73:691-696.
Vogel P, Magert HJ, Cieslak A, Adermann K, Forssmann WG (1996) hDIP--a potential transcriptional regulator related to murine TSC-22 and Drosophila shortsighted (shs)--is expressed in a large number of human tissues. Biochim Biophys Acta 1309:200-204.
Vuagniaux G, Vallet V, Jaeger NF, Hummler E, Rossier BC (2002) Synergistic activation of ENaC by three membrane-bound channel-activating serine proteases (mCAP1, mCAP2, and mCAP3) and serum- and glucocorticoid-regulated kinase (Sgk1) in Xenopus Oocytes. J Gen Physiol 120:191-201.
Vuagniaux G, Vallet V, Jaeger NF, Pfister C, Bens M, Farman N, Courtois-Coutry N, Vandewalle A, Rossier BC, Hummler E (2000) Activation of the amiloride-sensitive epithelial sodium channel by the serine protease mCAP1 expressed in a mouse cortical collecting duct cell line. J Am Soc Nephrol 11:828-834.
Wajchenberg BL (2000) Subcutaneous and Visceral Adipose Tissue: Their Relation to the Metabolic Syndrome. Endocr Rev 21:697-738.
Waldmann R, Champigny G, Bassilana F, Heurteaux C, Lazdunski M (1997) A proton-gated cation channel involved in acid-sensing. Nature 386:173-177.
Wang JC, Derynck MK, Nonaka DF, Khodabakhsh DB, Haqq C, Yamamoto KR (2004) Chromatin immunoprecipitation (ChIP) scanning identifies primary glucocorticoid receptor target genes. Proc Natl Acad Sci U S A 101:15603-15608.
Wang S, Yue H, Derin RB, Guggino WB, Li M (2000) Accessory protein facilitated CFTR-CFTR interaction, a molecular mechanism to potentiate the chloride channel activity. Cell 103:169-179.
Watanabe H, Suzuki A, Kobayashi M, Takahashi E, Itamoto M, Lubahn DB, Handa H, Iguchi T (2003) Analysis of temporal changes in the expression of estrogen-regulated genes in the uterus. J Mol Endocrinol 30:347-358.
Weisberg SP, McCann D, Desai M, Rosenbaum M, Leibel RL, Ferrante AW, Jr. (2003) Obesity is associated with macrophage accumulation in adipose tissue. J Clin Invest 112:1796-1808.
Widen C, Zilliacus J, Gustafsson JA, Wikstrom AC (2000) Glucocorticoid receptor interaction with 14-3-3 and Raf-1, a proposed mechanism for cross-talk of two signal transduction pathways. J Biol Chem 275:39296-39301.
Wilhelm D, Koopman P (2006) The makings of maleness: towards an integrated view of male sexual development. Nat Rev Genet 7:620-631.

Willis WD, Jr. (2007) The somatosensory system, with emphasis on structures important for pain. Brain Res Rev 55:297-313.
Wilson A, Laurenti E, Oser G, van der Wath RC, Blanco-Bose W, Jaworski M, Offner S, Dunant CF, Eshkind L, Bockamp E, Lio P, Macdonald HR, Trumpp A (2008) Hematopoietic stem cells reversibly switch from dormancy to self-renewal during homeostasis and repair. Cell 135:1118-1129.
Wu X, Yamada-Mabuchi M, Morris EJ, Tanwar PS, Dobens L, Gluderer S, Khan S, Cao J, Stocker H, Hafen E, Dyson NJ, Raftery LA (2008) The Drosophila homolog of human tumor suppressor TSC-22 promotes cellular growth, proliferation, and survival. Proc Natl Acad Sci U S A 105:5414-5419.
Wulff P, Vallon V, Huang DY, Volkl H, Yu F, Richter K, Jansen M, Schlunz M, Klingel K, Loffing J, Kauselmann G, Bosl MR, Lang F, Kuhl D (2002) Impaired renal Na(+) retention in the sgk1-knockout mouse. J Clin Invest 110:1263-1268.
Xiao J, Wang NL, Sun B, Cai GP (2010) Estrogen receptor mediates the effects of pseudoprotodiocsin on adipogenesis in 3T3-L1 cells. Am J Physiol Cell Physiol 299:C128-138.
Yachi K, Inoue K, Tanaka H, Yoshikawa H, Tohyama M (2007) Localization of glucocorticoid-induced leucine zipper (GILZ) expressing neurons in the central nervous system and its relationship to the stress response. Brain Res 1159:141-147.
Yamazaki M, Ishidoh K, Suga Y, Saido TC, Kawashima S, Suzuki K, Kominami E, Ogawa H (1997) Cytoplasmic processing of human profilaggrin by active mu-calpain. Biochem Biophys Res Commun 235:652-656.
Yang H, Charles RP, Hummler E, Isseroff RR (2007) The Epithelial Sodium Channel (ENaC) is Involved in the Galvanotaxis of Mouse and Human Keratinocytes. Gordon Conference abstract.
Yang YH, Aeberli D, Dacumos A, Xue JR, Morand EF (2009) Annexin-1 regulates macrophage IL-6 and TNF via glucocorticoid-induced leucine zipper. J Immunol 183:1435-1445.
Yang Z, Khoury C, Jean-Baptiste G, Greenwood MT (2006) Identification of mouse sphingomyelin synthase 1 as a suppressor of Bax-mediated cell death in yeast. FEMS Yeast Res 6:751-762.
Yazawa H, Sasagawa I, Nakada T (2000) Apoptosis of testicular germ cells induced by exogenous glucocorticoid in rats. Hum Reprod 15:1917-1920.
Yazawa H, Sasagawa I, Ishigooka M, Nakada T (1999) Effect of immobilization stress on testicular germ cell apoptosis in rats. Hum Reprod 14:1806-1810.
Yen PM, Liu Y, Palvimo JJ, Trifiro M, Whang J, Pinsky L, Janne OA, Chin WW (1997) Mutant and wild-type androgen receptors exhibit cross-talk on androgen-, glucocorticoid-, and progesterone-mediated transcription. Mol Endocrinol 11:162-171.
Yuji Yamaguchi VJH (2009) Physiological factors that regulate skin pigmentation. BioFactors 35:193-199.
Zhang FP, Poutanen M, Wilbertz J, Huhtaniemi I (2001) Normal prenatal but arrested postnatal sexual development of luteinizing hormone receptor knockout (LuRKO) mice. Mol Endocrinol 15:172-183.
Zhang H, Zhang A, Kohan DE, Nelson RD, Gonzalez FJ, Yang T (2005) Collecting duct-specific deletion of peroxisome proliferator-activated receptor gamma blocks thiazolidinedione-induced fluid retention. Proc Natl Acad Sci U S A 102:9406-9411.
Zhang W, Yang N, Shi XM (2008) Regulation of mesenchymal stem cell osteogenic differentiation by glucocorticoid-induced leucine zipper (GILZ). J Biol Chem 283:4723-4729.

Zhao B, Koon D, Bethin KE (2006) Identification of transcription factors at the site of implantation in the later stages of murine pregnancy. Reproduction 131:561-571.
Zhao M (2009) Electrical fields in wound healing-An overriding signal that directs cell migration. Semin Cell Dev Biol 20:674-682.
Zhu Y, Qi C, Korenberg JR, Chen XN, Noya D, Rao MS, Reddy JK (1995) Structural organization of mouse peroxisome proliferator-activated receptor gamma (mPPAR gamma) gene: alternative promoter use and different splicing yield two mPPAR gamma isoforms. Proc Natl Acad Sci U S A 92:7921-7925.
Zuber AM, Centeno G, Pradervand S, Nikolaeva S, Maquelin L, Cardinaux L, Bonny O, Firsov D (2009) Molecular clock is involved in predictive circadian adjustment of renal function. Proc Natl Acad Sci U S A 106:16523-16528.